USE OF NEURAL NETWORKS FOR THE IDENTIFICATION OF DAMAGE IN SHIP STRUCTURES

ACHMAD ZUBAYDI

INFORMATION TO USERS

This manuscript has been reproduced from the microfilm master. UMI films the text directly from the original or copy submitted. Thus, some thesis and dissertation copies are in typewriter face, while others may be from any type of computer printer.

The quality of this reproduction is dependent upon the quality of the copy submitted. Broken or indistinct print, colored or poor quality illustrations and photographs, print bleedthrough, substandard margins, and improper alignment can adversely affect reproduction.

In the unlikely event that the author did not send UMI a complete manuscript and there are missing pages, these will be noted. Also, if unauthorized copyright material had to be removed, a note will indicate the deletion.

Oversize materials (e.g., maps, drawings, charts) are reproduced by sectioning the original, beginning at the upper left-hand corner and continuing from left to right in equal sections with small overlaps.

Photographs included in the original manuscript have been reproduced xerographically in this copy. Higher quality 6" x 9" black and white photographic prints are available for any photographs or illustrations appearing in this copy for an additional charge. Contact UMI directly to order.

ProQuest Information and Learning
300 North Zeeb Road, Ann Arbor, MI 48106-1346 USA
800-521-0600

USE OF NEURAL NETWORKS FOR THE IDENTIFICATION OF DAMAGE IN SHIP STRUCTURES

by

°Achmad Zubaydi

A thesis submitted to the School of Graduate Studies in partial fulfillment of the requirements for the degree of Doctor of Philosophy

Faculty of Engineering and Applied Science
Memorial University of Newfoundland
April 2001

St. John's Newfoundland Canada

In the Name of Allah, the Beneficent, the Merciful

To my wife: Emmy, and my daughters: Evvy, Essy, Erry, and Ekky

ABSTRACT

The occurrence of damage in a ship's structure especially at the connection between a longitudinal and a heavy transverse members of the side shell is unavoidable under all operating conditions. The damage does not generally result in the loss of ships, nevertheless, it is often the cause of costly repairs and replacements of hull structures. Therefore, damage should be identified at an early stage in order to prevent the development of a more significant damage. This study presents a procedure for the identification of damage occurrence in the side shell of a ship's structure using a neural network technique. The structure is modeled as a stiffened plate.

An experimental study using modal testing techniques was carried out for measuring the time history of the random response of undamaged and damaged models. The damage was made using a hacksaw at several locations on the longitudinal faceplate near the transverse member. The random decrement signatures, and the auto and cross-correlation functions were obtained from the random response.

A finite element model was developed to generate numerical acceleration frequency response functions for the model. Excellent agreement was obtained between the numerical and the experimental acceleration frequency response functions. The numerical and the experimental data were used for validating an identification technique using neural networks.

The results of the present study show that one can use the random signature or the

autocorrelation function for the random response to identify the extent and location of damage.

ACKNOWLEDGMENTS

First of all, I would like to thank Dr. M. R. Haddara, my thesis supervisor, for his constant support, guidance, willingness, and the challenging technical discussion during the course of my doctoral program. Despite his heavy responsibilities as the Associate Dean, Graduate Studies and Research, of the Faculty of Engineering and Applied Science, Dr. Haddara had always been available for discussions, both as a supervisor and also as a well-wisher. I will be indebted to him.

My co-supervisor, Dr. A. S. J. Swamidas offered many valuable suggestions. His participation, insight, and standard of excellence have been a very positive influence on my education at Memorial University of Newfoundland. It has been a pleasure for working with such a truly kind and cordial person. My special thanks to Dr. M. Booton, for his support, encouragement, and also for serving on the supervisory committee.

I express my appreciation to the members of the Technical Service, Structures, Fluid, and Wave Tank Laboratories. Many thanks are due to Mr. J. Andrew, Mr. H. Dye and their staff for fabricating the stiffened plate models. My sincere thanks to Mr. A. Bursey, Mr. A. Kuczora, and Mr. D. Sparkes for their invaluable assistance in preparing, installing, and calibrating the equipments and the experimental models. I also thank the manager and staffs of the Center for Computer Aided Engineering for their support during the computational portion of my research.

Financial support provided by the Government of Indonesia through the High Education Project (HEP), Ministry of Education and Culture is gratefully acknowledged. An additional funding provided by the Central Grant URGE Project, Marine Technology Post-Graduate Program, Faculty of Marine Technology ITS, and Dr. Haddara are also thankfully acknowledged.

The Indonesian Student Community and The Muslim Student Association of MUN in St. John's helped me in various ways during my stay in Canada. My sincere thank to them. Finally, I would like to acknowledgment the great and continuous moral support of my wife, Emmy, and my daughters, Evvy, Essy, Erry, and Ekky.

Contents

List of Tables

List of Figures

List of Symbols

Symbol	Description
$[A_r]$	Residual Matrix
AMF	Added Mass Factor
$[B]$	Strain-Displacement Matrix
$[B(s)]$	System Matrix
$[C]$	Viscous Damping Matrix
$[\bar{C}]$	Constitutive Matrix
E	Young's Modulus
Er	Error
$F(x, \dot{x})$	Function of the Damping and the Nonlinear Part of the Restoring Forces
$f(\cdot)$	Squashing Function
$\{f(t)\}$	Force Vector
G_{xx}	Input Auto-Spectrum
G_{xy}	Cross-Spectrum

G_{yx}	Cross-Spectrum
G_{yy}	Output Auto-Spectrum
$[H(s)]$	Transfer Function Matrix
$[H(j\omega)]$	Frequency Response Function
I	Input
J	Number of Sample Functions
$[J]$	Jacobian Matrix
$[K]$	Stiffness Matrix
L	Lagrangian
M	Output from a Hidden Layer
M_i^*	Added Mass of the i^{th} Mode of the Model
$M_{i\,air}$	Mass of the i^{th} Mode of the Model in Air
$M_{i\,fluid}$	Mass of the i^{th} Mode of the Model in Water
m	Number of the Independent Equations
$[M]$	Mass Matrix
N	Number of Segments
$[N]$	Shape Function
O	Output of a Single Neuron
O_N	Network Output
O_T	Target Output

$P_{ik}(j\omega)$	Lower Residual
$[p]$	Modal Matrix
$\{Q\}$	Nodal Load Vector
$Q_{ik}(j\omega)$	Upper Residual
$R_{yy}(\tau)$	Autocorrelation Function
$R_{y_1y_2}(\tau)$	Crosscorrelation Function
$S_{yy}(\omega)$	Power Spectral Density
T	Kinetic Energy
$\overline{T}$	Period of the Damped Oscillation
t	Time
U	Strain Energy
$\{v(t)\}$	Displacement Vector
W_I	Synapses Weights applied to Inputs to the Neurons in the Hidden Layer
W_{IB}	Threshold applied to Neurons in the Hidden Layer (Unity)
W_{IM}	Threshold applied to Neurons in the Hidden Layer (Input)
W_O	Synapses Weights applied to Inputs to the Neurons in the Output Layer
W_{OB}	Threshold applied to Neurons in the Output Layer (Unity)
W_{OM}	Threshold applied to Neurons in the Output Layer (Input)
$\{x(\tau)\}$	Randomdec Signature

$\{y(t)\}$	Displacement Vector
$\{z(t)\}$	Displacement Vector
$\{\epsilon\}$	Strain Matrix
ϵ_1	Relative Amount of Noise at Input
ϵ_2	Relative Amount of Noise at Output
ζ	Viscous Damping Factor
γ	Coherence Function
K	Parameter
μ	Poisson's Ratio
Φ	Phase Angle
Π	Total Potential Energy
ρ	Mass Density
$\{\sigma\}$	Stress Matrix
τ	Time Length of Response
τ_1	The Length of the Random Record
ω	Natural Frequency
ω_d	Frequency of the Damped Free Vibration
ψ_y^2	Mean Square Value

Chapter 1

Introduction

1.1 General

During operation, a ship's structure is affected by cyclic regular and irregular loads due to waves. Cyclic wave loads on a ship's structure may produce fatigue damage, especially at locations where there are high stress concentrations such as at the connection between a longitudinal and a heavy transverse member of the side shell. Although, in many cases, this damage may not lead to the loss of the ship, it should be identified at an early stage as to prevent the ship from developing a more significant damage. This will save on costly repairs and replacements of expensive hull structure components.

Many analytical and experimental techniques for damage identification have been reported in the literature. Non-Destructive Evaluation (NDE) techniques using parametric identification methods are widely used to detect the occurrence of damage. These methods use the changes in the vibration characteristics of the structure which results as a

consequence of the structural damage.

NDE techniques can identify a suitable mathematical model corresponding to the change of the physical properties of the structure based on the measurement of the modal parameters. However, the range of damage identification scenarios, likely to be encountered in realistic application to all physical systems, is extensive. Therefore, it is necessary to find methods which can cope with the various specific applications.

In recent years, many researchers have developed non-parametric identification approaches for assessing structural damage using a new computing architecture, called neural networks. These methods were inspired by the knowledge gained from the study of human brain and nerve cells. The basic approach of this method is to identify the changes in the modal parameters and/or in the physical properties of the structure which are related to various damage states.

There are many types of neural networks which can be developed by changing the network topology, node characteristics and learning procedures to identify structural damage. Most of the available methods have been used to detect the damage in trusses, frames, beams, and plates used for applications in civil, mechanical and aerospace engineering. These methods have not yet been used to identify the damage in component structures (such as stiffened panels, transverse frames, etc) used in ship structures.

For these reasons, the present study extends the work of other researchers by dealing with the structural damage identification of ship structures at the location of high stress concentrations such as at the connections of longitudinal to heavy transverse members of the

side shell. The structure was modeled as a stiffened plate.

1.2 Scope of the Present Study

The present study is carried out to develop a technique for identifying damage occurrence in the side shell of a ship's structure. This technique does not only determine the existence of the damage, but also its location and its extent. The technique is based on the use of the autocorrelation function of the random response of the structure as a mathematical model.

Neural networks are utilized to identify the changes occurring in the model as a result of damage occurrence. Experimental data obtained from the testing of four physical models as well as numerically generated data using a finite element model were used to develop the technique and to validate it. Physical models were tested both in air and water and data was analyzed using modal testing techniques as well as the technique developed in the present study.

1.3 Methodology

In order to identify the damage occurrence in the structure, four stiffened plate models were tested. Each model consisted of a plate, an unequal angle longitudinal, and a T-section transverse member. The models were designed and fabricated to represent the side shell of a ship's structure. The dynamic responses of the undamaged and damaged models were

investigated experimentally and numerically.

A modal testing procedure was used for carrying out the experimental study of the models in air and water. In order to investigate the effect of water on the stiffened plate models, the models were placed in a water tank. Fast sine sweep and random excitations were selected for exciting the model. The damage was simulated by saw cuts of 0.01 inches (0.025 cm) width and of different lengths ($\leq$ 1.20 inches = 3.048 cm) at several locations of the longitudinal faceplate near the transverse member. The fast sine sweep signal and its dynamics were used for obtaining the acceleration frequency response functions of the undamaged and damaged model. From the vibrating models due to the random excitation, the acceleration random time responses of the undamaged models as well as the models with progressive damage were measured.

A finite element model was developed and used for generating the acceleration frequency response functions, the acceleration free vibration responses, and the acceleration auto- and cross-correlation functions of the undamaged and damaged stiffened plate models subjected to an impulse and random excitations. The presence of damage was represented by introducing a gap of 0.01 inches between identified elements of the faceplate of the longitudinal. The effect of water on the models was modeled using an added mass factor. The results of the numerical frequency response functions were compared to those of the experimental ones for validation.

The random responses were filtered around the predominant mode using a wide-band filter, and the results were averaged using the random decrement technique for obtaining an

estimate of the free-vibration responses, called the random decrement signatures. The random decrement signatures along with the free vibration responses were used for identifying the location and extent of damage in models.

In addition to the random decrement technique, the filtered random responses were also analyzed using a statistical procedure for obtaining the auto- and cross-correlation functions. The experimental and numerical auto- and cross-correlation functions were also utilized for detecting the presence of damage in models.

The results indicated that the randomdec signature, the free vibration response, and the autocorrelation function can be used to identify the presence of damage as well as its extent and its location. However, the change in the natural frequencies of the structure as a result of damage was very small. Also, the randomdec signatures, the free vibration responses, and the autocorrelation functions had similar shapes for undamaged and damaged conditions. On the other hand, it was found that damage alters the shape of the crosscorrelation function, which can be used to detect the onset of damage.

Because of the above reasons, the identification of the damage in the model was carried out using a neural network technique. Input to the network consisted of the autocorrelation functions resulting from the experimental and numerical studies of Model #1 and their first derivative. The output consisted of a single function which was formed by adding together the damping force and the nonlinear part of the restoring force. This function was then used to identify not only the damage occurrence in the model, but also its extent and location.

1.4 Organization of the Dissertation

The research study reported in this dissertation contains three parts, viz., (i) the experimental study using a modal testing procedure; (ii) the analytical modal analysis using finite element procedure; and (iii) the analytical study using neural network technique. The study employed a combination of the experimental and analytical data. The organization of the dissertation is given as follows:

Chapter 1 addresses the general idea of using neural network for identification of damage in the structure. The scope and methodology used in the present study as well as the organization of the dissertation are also presented in this Chapter.

Chapter 2 contains a review of literature to provide an overview of the procedures for damage detection and identification in the area of floating bodies using parametric identification methods. The limitations of the existing methods are analyzed and the need for neural network analysis is brought out.

The theoretical background pertaining to the research reported in this dissertation is explained in Chapter 3. This includes the basic theories of finite element analysis, random decrement technique, auto- and cross-correlation functions, modal analysis and testing, neural networks, and their application to the problem at hand.

The experimental study of the stiffened plate models is described in Chapter 4. This includes the fabrication of the models, the experimental setup, details of instrumentation and

their calibration, the placement of the load cell and accelerometers, and the experimental procedure used in modal testing.

The analyses of the experimental and analytical results are given in Chapter 5. Changes in the frequency response functions and the free vibration responses that resulted from inducing the damage on the stiffened plate models are presented and discussed in this Chapter. This includes validation of the results of the finite element analysis by comparing the analytical results with experimental ones. The identification of damage occurrence in the model using the randomdec signature is also discussed in this Chapter. The effect of added mass on the frequency, the free vibration responses and the randomdec signature is also explored.

Chapter 6 presents the results of using the experimental autocorrelation functions for identifying the presence of damage in the model. A comparison between the randomdec signatures and the autocorrelation function is given. Analytical results are also presented to complement the experimental ones. In addition to autocorrelation functions, the identification of damage occurrence using crosscorrelation functions is also discussed.

The use of neural networks for damage identification in the stiffened plate model is demonstrated in Chapter 7. The training of neural networks using the training set data resulting from experimental and numerical autocorrelation functions is analyzed and discussed in this Chapter. Also, the capability of the trained neural networks to identify the extent and location of damage in the stiffened plate model is demonstrated.

Finally, the conclusions drawn from this research investigation are summarized in

Chapter 8. In this Chapter, the problem areas that need to be further investigated are also proposed.

Chapter 2

Literature Review

2.1 Introduction

Identification of damage in structural components in service is very important and essential to ensure the integrity of any structure. The reason being, that the damages tend to propagate and cause sudden failures which are usually very costly in terms of property damage or worse, human life. The most common method of damage identification is visual inspection using NDE techniques as pointed out in the previous chapter. However, the visual inspection of large and complex structures such as ships and offshores structures may be difficult and costly due to problems of accessibility in which the investigator needs to access the component under operating conditions. In some cases the visual inspection may prove to be unreliable and impossible when the damage is small.

Therefore, in recent years, the indirect diagnostic methodologies for damage identification, such as modal analysis and neural networks, have attracted the attention of

many researchers. The basic approach is to detect changes in the dynamic characteristics of the structure. These changes are subsequently related to various damage states. The objective of any damage identification is to determine whether structural damage has occurred and if so, to determine the location and the extent of the damage.

This chapter reviews the studies on the damage identification using NDE techniques and indirect diagnostic methodologies, which were carried out by earlier researchers, which can be applied to floating bodies such as ships and offshore structures.

2.2 Ship's Damage Identification

Recently, High Tensile Steel (HTS) has been extensively used in hull constructions for reducing a ship's weight. The welded HTS structures have a higher operational stress level; however, there is no improvement in fatigue properties compared with that of mild steel structures. Thus, the fatigue of component structures made with HTS causes most of the damage in ship structures, especially for component structures with high stress concentrations such as connections and details. For this reason, several analytical and experimental studies relating to ship damage, in particular on the side shell of tankers, satisfying regulatory requirements, have been published in recent years. These articles, which are directly related to the present study, are reviewed briefly.

Strathaus and Bea (1992) carried out a study on structural maintenance of new and existing ships. The objectives of the study were: (i) to develop practical tools and procedures

for analysis of proposed ship structure repairs, and (ii) to provide guidelines for cost effective design and construction of lower-maintenance ship structures. One of the important results from this study was that about 42% of all the fatigue damage in ships have occurred in the side shell, especially in the connections between longitudinal and heavy transverse members of the side shell as shown in Figure 2.1.

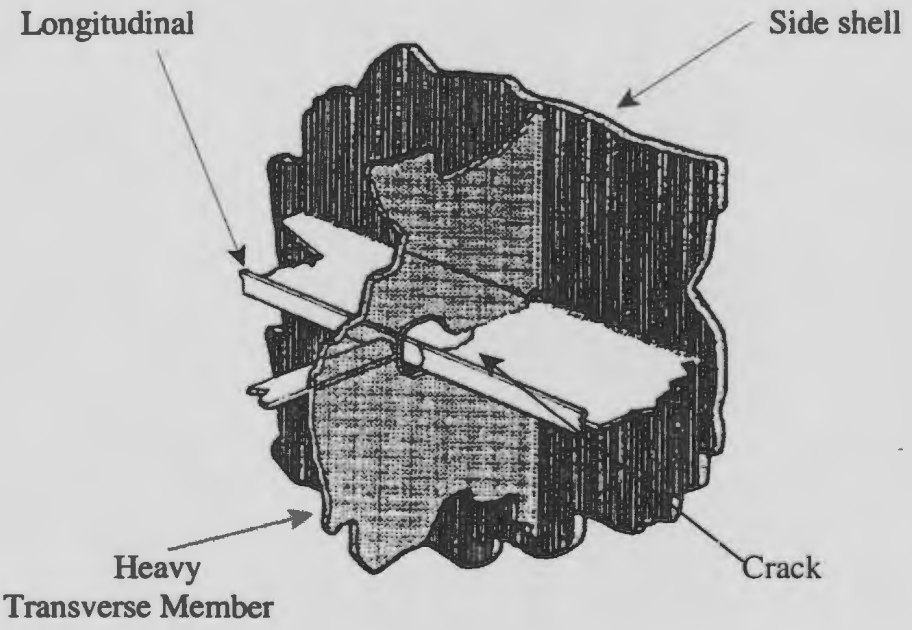

Figure 2.1 Crack in the Connection between the Longitudinal and the Heavy Transverse Member

A procedure for evaluating fatigue damage in the longitudinal of the side shell of tankers due to external wave pressure was developed by Cramer *et al.* (1993). The procedure used the stress response, generated by external water pressure due to relative wave heights, to initiate and grow fatigue damage. A numerical study of 25 stiffeners having six different sizes was carried out to investigate the fatigue damage. The mean pressure and stress

variation in ballast, laden, and combined ballast/laden conditions for each stiffener were studied. The results showed that the highest fatigue damage was experienced for stiffeners located at mean water lines.

Hansen and Winterstein (1995) predicted the fatigue damage, along the side shell, that was caused partly by a combination of vertical and horizontal wave-induced hull bending, and partly by outside water pressure. The fatigue damage was calculated in laden and ballast conditions using longitudinals of segregated ballast tankers. They reported that the outside water pressure accounted for the majority of fatigue damages, and that the combination of stresses due to vertical and horizontal wave-induced hull bending resulted in a significant increase in fatigue damage.

Sucharski (1995), identified typical fractures in tankers, the probable effects and responses due to such damages, and gave a strategy for their prevention. He identified the fractures that were found in four classes of eight crude oil tankers operating between Alaska and the U.S. West Coast and observed that fatigue was the main cause for fractures that occurred in various tankers. He found that at least two-thirds of the fractures occurred in the connection between longitudinal members of the bottom or the side shell and significant transverse structures such as transverse bulkheads and web frames.

From the literature reviewed above, it appears that most of the fatigue damage in ship structures tend to be located at the longitudinals of the side shell near their connections with the transverse members and bulkheads. Because of the location of longitudinals is in cargo

holds or tanks, it is difficult to get access to the location of damage for evaluating the extent of damage under operating conditions,. For this reason, some researchers have used numerical methods to evaluate the extent of damage.

Ghoneim and Tadros (1992) examined the damage existing in the side shell structures of M.V. Robert LeMeur and M.V. Arctic due to ice loads. They examined the indentation damage at the frame where maximum deformation had occurred, predicted the forces causing damage, and enhanced the understanding of the behavior of structure based on measured indentation using FE analysis. Based on the evaluation of experimental results of M.V. Robert LeMeur, they concluded that damage was caused by numerous ice impacts, each occurring over relatively small areas.

Based on S-N curves and Miner's formula, Xue *et al.* (1994) developed a formula to calculate the cumulative fatigue damage (D) in longitudinals of tankers and containers due to primary wave induced loads and hydrodynamic pressures. D was designed as a function of the stress parameter (Ω_p) which represented the cumulative action of wave induced loads on structures, and incorporated the combined effects of stress levels and, its occurring frequency, such that:

$$D = \frac{T}{A}\Omega_p \tag{2.1}$$

where: T was the time over which the damage was calculated, and A was an empirical constant. Xue *et al.* (1994) used several examples of tankers and container ships with

different block coefficients and hull forms to compare the effect of ship type on Ω_p. From the example results they stated that the above formula could be applied to real ship structures to calculate the fatigue damage, provided that Ω_p was calibrated using real structural behavior.

Strathaus and Bea (1996) reviewed the results of the SSIIS (Ship Structural Integrity Information System) I project in which one of the aims was to use an integrated database system for damage identification in ship structures. They evaluated the existing database systems that could determine and represent failure location in a ship's structure. They concluded that existing database systems have powerful features to improve ship maintenance; nevertheless, it was necessary to improve the existing database systems so that they could define and develop detailed representations of the failure locations in a ship's structure.

In addition to the literature reviewed above, many other researchers have also used numerical calculations for the evaluation of damage in tankers. All investigations, however, have evaluated only the damage due to accidents such as collision and grounding.

Ito *et al.* (1994) developed the NKK energy method which could be used to analyze the strength of the side shell of tankers in collision. Kuroiwa *et al.* (1994) conducted experiments of collision, drop, and raking tests to develop numerical simulations of failure. These experiments used full scale, ½ scale, and ⅓ scale structural models to evaluate the structural damage of tankers, such as that due to plate rupture and welds failure during

collision and grounding. Paik and Lee (1995) estimated the raking length of tankers due to grounding, using semi-empirical formulae for energy. They also analyzed the damaged hull section due to vertical bending moments using a progressive collapse analysis method. De Kat *et al.* (1995) predicted the damage growth and hull strength of stranded tankers due to wave-induced loads and dynamic ship motions, using FE analysis. Rodd and Sikora (1995) conducted a series of grounding experiments using a quarter-scale hull bottom models. Their results provided vital information toward the understanding of the detailed structural failure mechanisms that lead to the inner shell rupture during grounding accidents. Rodd and Sikoras' results could also be used as a validation to develop crashworthiness systems for tankers using analytical and numerical modeling techniques.

From this literature review, it is clear that most numerical studies and the consequent formulae proposed determine the damages that occur due to collision only. Only a small number of studies have calculated the damage that occurred due to wave action during the normal operation of ships. Moreover, the main cause of ship structural damage was fatigue due to wave induced loads, especially for structures with large stress concentrations at the connection between the longitudinal and the heavy transverse members of the side shell. However, in all the literature reviewed, no study has identified this damage at an early stage nor has found the location and extent of the damage.

2.3 Damage Identification

2.3.1 Changes in Modal Parameters

As pointed out in the previous Chapter, damages that occur in a structure usually change its physical properties, i.e., stiffness and damping. These changes can be reflected in the changes of modal parameters of the structure, such as natural frequencies, damping ratios and mode shapes. Therefore, Non-Destructive Evaluation (NDE) techniques which use the changes of vibrational characteristics of the structure have been used by many researchers for damage identification. The following discussion is focused on a review of the damage identification for offshore structures, which like ship structures, are affected by external wave forces.

Yang *et al.* (1980, 1981, 1984) applied the random decrement technique for inspecting the damage in offshore structures. They used a 1:13.8 scale model of the actual Gulf of Mexico offshore oil platform for an experiment. The damage was modeled using saw cuts of the welded section of the structure on the cross beam. This technique required measurements only of the dynamic responses of the structure and not the input excitation. The results indicated that this method could identify damage by evaluating the differences between the random decrement signatures in the damaged and the undamaged situations. However, this method could not be used to locate the damage or to give an estimation of its severity.

Shahrivar and Bouwkamp (1986) detected the existing damages in structural elements of an eight-legged k-braced steel offshore oil and gas production tower by determining its

natural frequency shifts. They performed modal testing of an offshore framed platform model, with grossly cracked structural members. SAP IV, a general purpose program, was employed to model the structure mathematically. Experimental and analytical results showed that the damage caused a reduction in natural frequencies and an increase in structural responses.

Marshall (1990) used a hydro-elastic model of a typical four-legged jacket offshore platform to carry out structural integrity monitoring. Structural damage was simulated by saw cutting inclined member(s) in a k-braced panel under consideration, and responses data were analyzed using the Marple algorithm with the Maximum Entropy Method (MEM). The detection of damage was based on the changes in resonant frequencies compared with the intact structure. Marshall (1990) concluded that the resonant frequency change indicated clearly the structure had been damaged.

Roitman *et al.* (1991) used modal testing for identifying a damaged tubular joint in a fixed offshore framed structure. They examined two small scale models which were designed based on the similitude theory. The damage was modeled by cutting one of the end joints. In addition to natural frequencies and damping ratios, modal amplitude responses were also measured. Absolute differences between modal amplitude responses for the intact and damaged structures were measured. Therefore, Roitman *et al.* (1991) stated that modal analysis could be applied to offshore jacket structures for identifying the occurrence of damage in joints of tubular diagonal members. This technique, however, could not be used

to identify the location of the damage.

Damage evaluation of offshore structure models using the changes of vibration signatures was also carried out by Osegueda and D'Souza (1992). Modal testing of a jacket-type offshore structure model was conducted. The damage was caused by disconnecting one end of a diagonal member at the lower joint. Osegueda and D'Souza (1992) evaluated the damage in each member by comparing the internal modal energy distribution of the undamaged structure to that of the severed structure. Experimental results of damaged structures showed that the damage would occur at the element with high energy distribution. This technique could locate the correct member which has been affected by the damage.

Chen and Swamidas (1993) proposed a procedure of modal testing for detecting the crack growth in a tripod tower platform using global sensors (an accelerometer and a linear variable displacement transducer (LDVT)) and local sensors (strain gauges). In order to confirm the accuracy of experimental results, a numerical computation using FE analysis was also carried out. The damage was modeled as a small crack (45° inclined saw cut). Results showed that accelerometers and LDVTs could determine changes of natural frequencies in the structure. These changes indicated the possibility of a growing crack in the structure. Strain gauges located in critical areas of the structure could find out the location and magnitude of the crack.

Chen (1996) investigated vibration techniques for crack detection in fatiguing plate-type structures using the model of plated T-joints. He performed modal testing on fatigue-

cracked models of plated T-joints to measure the Frequency Response Function (FRF). Numerical calculation was also carried out using FE analysis, and results were refined by comparing the FRF from the FE and intact experimental models. A combination of the experimental and numerical procedures was then developed to find out the location, length and depth of the crack. Chen (1996) stated that this method was a promising method for crack detection in complex structures such as offshore structures, and would help in the further development of a new vibration-based NDE technique for industrial applications.

In addition to the literature reviewed above, Doebling *et al.* (1996) have reviewed many papers dealing with damage identification of structural systems due to changes in their vibration characteristics. Their report describes the development of damage identification methods and applications, and summarizes the current state-of-the art. They stated that measured vibration data could be used to identify the damage in structures. However, they noted that the literature needs to focus more on specific applications and industries, and that researchers should focus more on the testing of real structures in their operating environment.

The performance of some damage identification methods, i.e., MAC, COMAC, MSF, RD, and Change in Modal Vector Perpendicular to Predominant Modal Direction, on offshore platforms was evaluated by Viero and Roitman (1999). Two different small scale and redundant hydroelastic models, constructed based on the Similitude Theory, were tested in air. The results showed that the MAC and MSF methods had a sensitivity to the imposed damages and the deck mass changes. The COMAC method was able to clearly indicate the

damage location. The Change in Modal Vector Perpendicular to Predominant Modal Direction method was able to detect damage using a deck instrumentation only.

All the methods reviewed here could identify the existing damage, and some of them could give the location and the extent of damage in structures. The severity of damage was mostly simulated by cutting off (in physical experiment) one or more members, or by reducing the stiffness of one or more elements where the crack was located. However, these methods have evaluated only the damages that occur in trusses, frames, beams, and plates used in applications for civil, mechanical, and aerospace engineering. No available publication identifies the damage in stiffened plates and its application to ship structures.

2.3.2 Neural Network Procedures

While NDE techniques that utilize the changes in vibration characteristics of structures have been examined by many researchers, in recent years, many other researchers have developed non-parametric identification approaches for assessing structural damage. They use a new computing architecture, called neural network technique, which was inspired by the study of the behavior of human brain and nerve cells. The following discussion reviews the use of neural networks for detecting and identifying the damage in structures.

Wu *et al.* (1992) used back-propagation neural networks with a single hidden layer to simulate the damage states in structures using a three-story building frame. The structure was subjected to an earthquake excitation, and its transient response was computed in the

time domain. The damage was modeled by reducing the stiffness of its members. A neural network was used to identify the map from the Fourier spectra as input data to the level of the damage in each of the members as output data. As a pilot study, this neural network could identify any existing damage in structures with promising results.

Kudva *et al.* (1992) also used a back-propagation neural network to detect the damage in an aircraft structure which was represented as a 16-bay stiffened panel model. The damage was represented as circular holes of various sizes and at several locations. Their effects on strain values were determined using FE analysis. A neural network was utilized to identify the map from the strain gauge data as input data to the location and the size of the hole as output data. They found that a neural network could be used to determine the damage location without any appreciable error, but stated that the prediction of damage size was more difficult giving sometimes erroneous results.

The work of Kudva *et al.* (1992) motivated Worden *et al.* (1993) to locate the position of a fault in the framed structure using a multi-layer perceptron (MLP) neural network. In order to model the damage, one of the structural members was removed completely. The neural network was used to identify the map from static strain data as input data to a subjective measure of the damage as output data. Like Kudva *et al.* (1992), Worden *et al.* (1993) also trained the neural network using data from FE simulation. However, unlike Kudva *et al.* (1992), who did not test the trained neural network using data from experimental results, Worden *et al.* (1993) also compared the trained neural network with

the experimental results from a two-dimensional cantilever latticework model. The results showed that a trained neural network could successfully locate faults in an experimental structure even though the neural network was trained using FE data.

Elkordy *et al.* (1993) investigated the feasibility of using analytically generated states of damage to train neural networks. They used data obtained from two analytical models of a five-story steel frame. A neural network was utilized to identify the map from the mode shapes as input data to the percentage change in member stiffness as output data. The capability of the neural network was verified using a set of the damage state obtained from the shaking-table test of a physical model of the five-story steel frame. Elkordy *et al.* (1993) stated that a trained neural network has the strong potential for making on-line structural monitoring a practical reality.

The use of an MLP neural network, based on a training algorithm, to identify damage in a four element cantilever beam was presented by Leath and Zimmerman (1993). The damage in the beam was modeled by reducing Young's modulus up to 95%. The algorithm was able to identify damage with a maximum error of 35%.

Szewczyk and Hajela (1994) used an improved counter-propagation neural network (CPN) to detect the damage in structures. They modeled the damage as a reduction in stiffness of a structural element that was measured by its static displacement under prescribed loads. A neural network was used to identify the map from static deformation under load as input data to Young's modulus of the members as output data. Szewczyk and Hajela (1994)

observed from exercises on framed structures that a neural network performance was generally precise, with gradual deterioration in the presence of noisy and incomplete measurements.

Ceravalo and Stefano (1995) used a back-propagation neural network for identifying damage in a truss structure modeled using the FE method. In this study, damage was modeled by removing elements of the truss. The results showed that the network located the damage well. However, the authors did not discuss how noisy measurements or multiple damage would affect the results.

A neural network approach, for damage detection and identification in structures, also attracted the attention of Rhim and Lee (1995). They used a MLP neural network to identify the characteristics of damage in composite structures. Delamination in a FE model of the structure was used to model the damage. Before a neural network was applied, forces and accelerations were extracted using an auto-regressive exogenous (ARX) model as transfer function input patterns, and various types of damage were designed as output patterns. A neural network was used to identify the map from the characteristic polynomial as input data to an empirical damage scale as output data. The results from numerical simulation demonstrated that this method had potential for practical application since it was robust to measurement noise and distortion of input patterns.

Barai and Pandey (1995) also adopted a MLP neural network with a back-propagation learning paradigm to identify damage in truss structures such as railway bridges. The damage

was simulated by reducing the area of its members. The neural network was used to identify the map from various nodal time histories measured in-situ, as input data, to the changes in the cross sectional of the stiffness, as output data. FE modeling of the truss structure with a moving point force was used to train the neural network. They claimed that this method had great potential for damage identification and needed to be investigated further. They also stated that a suitable chosen location of vibration signature measurements was important, since it affected the accuracy of results.

Adaptive resonance theory (ART) neural networks were applied by Mangal *et al.* (1996) to detect the damage in the model of a jacket-offshore platform. The neural network was used to identify the map from natural frequencies and modal vectors as input data to the changes in deck mass and stiffness, respectively, as output data. FE analysis was used for numerical computations, and the results used as input and output data for training neural networks. As a comparison, the damage in the model was also detected by using a back-propagation network (BPN). Both ART and BPN gave good results for damage detection. However, while the previously trained BPN could not adapt itself to new situations, the ART could adapt itself to changed conditions and new situations. Therefore, for better performance Mangal *et al.* (1996) suggested that both ART and BPN should be used simultaneously.

Two probabilistic neural networks were used by Klenke and Paez (1996) to identify the damage in mechanical systems. The first technique used a probabilistic neural network

(PNN) that used Bayesian decision analysis, and the second one used a probabilistic pattern classifier (PPC) which was designed by Klenke and Paez (1996). PNN was used to analyze a number of undamaged and damaged systems, and the PPC was used to analyze the member location of the damaged system. An experimental measurement of an aerospace housing component using the virtual environmental for test optimization (VETO) was carried out for generating experimental data in which damage was represented by five progressive cuts in the housing. Based on the experimental results, Klenke and Paez (1996) stated that both PNN and PPC clearly offered robust methods for assisting in damage identification of structures, even in the most lightly damaged case. However, these methods could not determine the location and the extent of damage.

Masri *et al.* (1996) used a feedforward multilayer neural network to detect damage, in linear and non-linear systems. Their approach was based on the identification of a high-fidelity neural network to match the restoring forces associated with an element of the system to be monitored. The changes in stiffness and damping were used to simulate the damage. The neural network was used to identify the map from the velocity and the acceleration, as input data, to restoring forces, as output data. Vibration measurements from a healthy system were required for training the neural network using an adaptive random search algorithm. To monitor the health of the systems, the trained neural network was fed with comparable vibration measurements from the same systems under different conditions of responses. Outputs from the neural network and systems were compared, and damage in the system

could be identified by observing the output errors between them. Masri *et al.* (1996) stated that this approach provided a robust method for damage detection through monitoring of the systems' restoring forces, even for a small change in modal parameters.

The limitation of traditional neural networks (TNN) in dealing with patterns that may vary in the time domain caused Barai and Pandey (1997) to develop their investigation in the damage identification of truss structures. In this study, they applied time-delay neural networks (TDNN). In order to demonstrate the superiority of the TDNNs, they also used their previous data (Barai and Pandey 1995) to train TDNNs. Unlike the TNNs, which provided a signal to the network from a series of input channels in turn, the TDNNs provided a signal to the network from a series of input channels together. Based on the comparison results of the damage detection of railway bridges, Barai and Pandey (1997) concluded that TDNNs performed better than TNNs.

Seed and Murphy (1998) were successful in applying the multilayer perceptron neural network for modeling the chaotic behavior of the growth of short fatigue cracks in medium carbon steel. They used the Hobson short fatigue crack growth law for modeling fatigue crack growth. The neural network was used to identify the map from the number of separate crack data a, as input data, to crack growth rate da/dN, as output data. The results were then used for predicting the characteristics of microstructural threshold d and empirical constants α, and C using the following equation:

$$\frac{da}{dN} = C\,a^{\alpha}\,(d-a)^{1-\alpha}. \qquad (2.2)$$

The application of neural networks in the area of floating bodies is very limited. William (1993) discussed a general understanding of how neural network technology can be used for solving complex problems in naval and commercial ships, i.e.: on-line maintenance monitoring, diagnostics, and failure prediction systems. Roskilly and Mesbahi (1996) used artificial neural network for simulating the pipe connections in a marine system, representing the data in the Moody diagram. Haddara *et al.* (1992, 1994, 1995, 1996, 1998, and 1999) used a neural network technique for identifying ship's parameters such as ship's stability, free roll decay, free response of coupled heave-pitch and sway-yaw motions, and hydrodynamic characteristic from ship maneuvering trails.

Beyond what is mentioned in the above literature discussed review, some researchers have carried out studies on modal parameter identification using neural networks. Although these studies did not specifically refer to damage in structures, their ideas could be applied to the identification of structural damage. Lim *et al.* (1996) developed the concept of a neural network that could identify the modal parameters of structures such as natural frequency, damping ratio, and mode shape on-line. Yang and Lee (1997) developed a back-propagation neural network for system identification, on-line state estimation, and vibration suppression to control the vibration response of composite smart structures with built-in sensors and actuators.

2.4 Summary

Most of the damage in ship structures occurs at the connection between the longitudinal and heavy transverse members of the side shell. Numerical and experimental studies have been carried out for damage identification in ship structures. However, only a few numerical methods are available to identify the existing damage in ship structures where the location and the extent of damage could be identified. Moreover, all the earlier experimental methods used destructive techniques where the structural member was completely damaged and focused their attention on the identification of damage that occurred only due to accidents.

On the other hand NDE techniques, using changes in vibrational characteristics of structures via modal testing and analysis, are widely used for damage detection. With the advancement in computer performance capability, the availability of more accurate modal testing devices, and the development of FE analysis, the diagnosis of damage using these techniques could not only identify the existence of damage, but could also give the location and accurate extent of damage. However, the use of these techniques is still limited for structures such as trusses, frames, beams and plates. No available technique identifies the damage occurring in stiffened plates and its application to ship structures in which the water effect was considered.

In the meantime, the use of neural network techniques for damage identification in structures is still in its beginning stages. Although many neural network techniques could determine the existing damage without errors, their capabilities for identifying the location

and the extent of damage still lack precision. Like modal analysis, most of the available techniques using neural networks have only been applied to structures such as trusses, frames, beams, and plates.

Based on the above review, the present study as given in the subsequent Chapters extends the current techniques to the stiffened plates used for ship structures. This procedure uses a combination of current neural network techniques and modal testing to identify the existing and the location of damage. Meanwhile, numerical computation using FE analysis would also be carried out. The goal of this study would be the development of a neural network technique that could identify not only changes of the modal parameters recorded at several critical locations in the side shell due to the existing damage, but also give the precise location and the extent of damage on-line.

Chapter 3

Theoretical Background

3.1 Finite Element (FE) Analysis

The aim of the present study is to identify the change in the dynamic response of the stiffened plate models when a damage occurs. It would be preferable if one can use a large number of physical models which cover all damage scenarios. Because of cost and time constraints, only four models were fabricated and used to measure the dynamic response. In order to complement the experiments, finite element models were developed to obtain the dynamic response in cases that were not covered by the experiments. These will be referred to as FE models. The following general equation of motion for a multiple-degrees-of-freedom system was used in formulating the FE models:

$$[M]\{\ddot{v}(t)\} + [C]\{\dot{v}(t)\} + [K]\{v(t)\} = \{f(t)\} \tag{3.1}$$

where $[M]$, $[C]$, and $[K]$ are the mass, viscous damping and stiffness matrices, respectively, $\{v\}$

is the displacement vector and $\{f(t)\}$ is force vector. It is assumed that the viscous damping matrix $[C]$ or Rayleigh damping can be expressed as:

$$[C] = \alpha[M] + \beta[K]$$

where α and β are proportionality constants. The solution of Equation (3.1) is valid for any time $t > 0$ and any set of initial conditions. Details of the derivation of Equation (3.1) using FE analysis are given in Appendix A.

3.1.1 Application of FE Analysis in the Present Study

In the present study, FE analysis was used to model the stiffened plate and its supports. Unlike Satsangi and Ray (1998) who used an eight noded isoparametric plate element to model the plate and a three noded beam element to model the stiffener, the present study used an eight noded shell element (parabolic thin shell elements) for modeling both the stiffened plate and its supporting structure. The reason for modeling the supports is to simulate the vibration of the tank bottom, which occurred due to manner in which the stiffened plate model was connected to the tank bottom. The stiffened plate and its supports were discretized into 3208 elements and the results are shown in Figure 3.1.

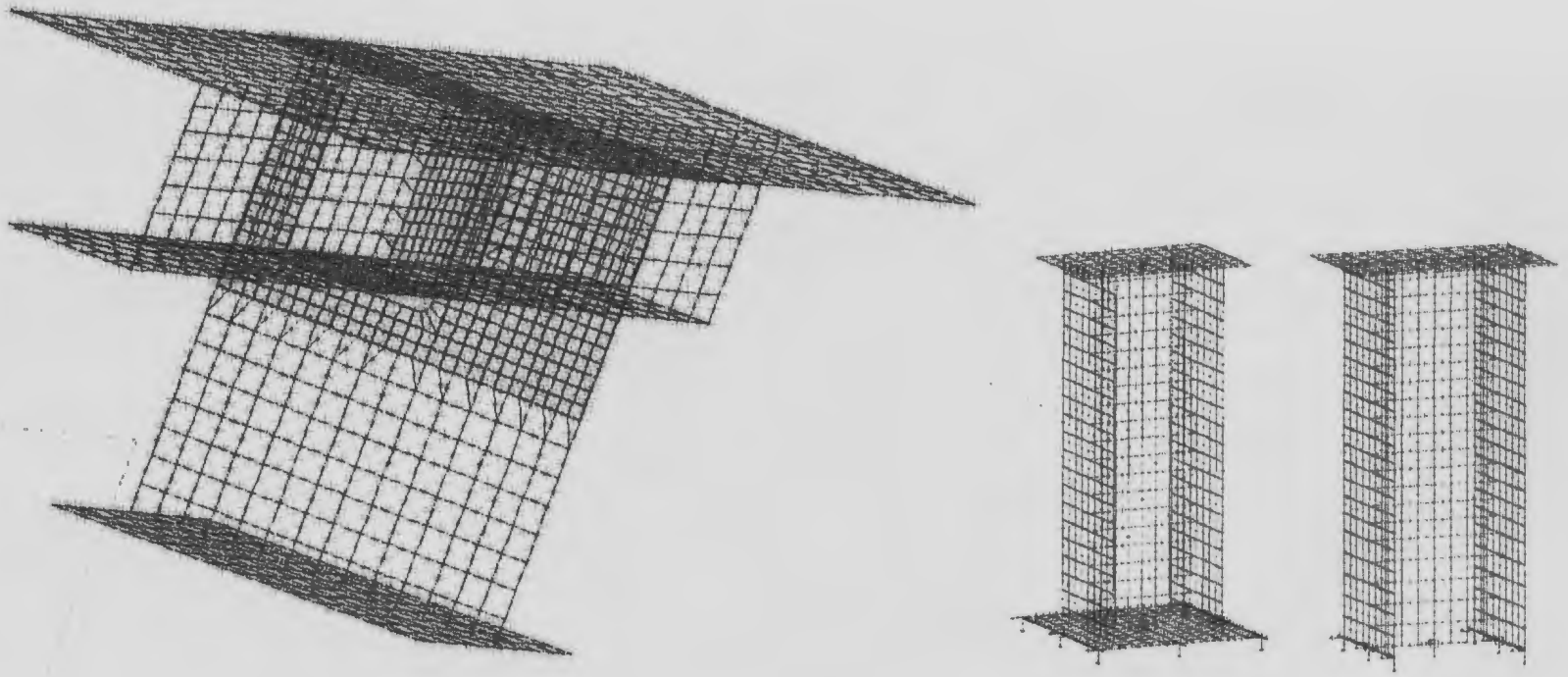

3.1.a: The stiffened plate

3.1.b: The left support 3.1.c: The right support

not to scale

Figure 3.1: FE Model of the Stiffened Plate and its Supports using Thin Shell Elements available in I-DEAS Program

In the experimental study, a crack was made in the faceplate of the longitudinal near the heavy transverse member using a saw blade. Therefore, the crack was modeled by creating a gap of 0.01 inch wide between identified elements. This represents the thickness of the saw blade. The model was used to generate the frequency response functions, the free vibration responses, the auto- and cross-correlation functions, and the modal parameters of the undamaged and the damaged stiffened plate models.

The calculations were performed using an industrial package: I-DEAS Master Series software package (Lawry, 1996). This package determines the modes of vibration characterized by the natural frequencies and mode shapes, and uses these to calculate the dynamic responses such as the frequency response functions, the free vibration responses, and the auto and cross-correlation functions. When the modes of vibration were obtained, the resulting equations of motion are:

$$[\backslash M\backslash]\{\ddot{y}\} + [\backslash C\backslash]\{\dot{y}\} + [\backslash K\backslash]\{y\} = \{f(t)\} \tag{3.2}$$

but now the mass, damping and stiffness matrices are diagonal, making the mathematics much simpler. Equation (3.2) is called the modal form of the equation of motion.

3.2 Modal Analysis

Modal analysis is the process of characterizing modal parameters of a linear, time-invariant

system either through analytical or experimental approach. In order to apply modal analysis to the system, the system is assumed to satisfy the following four basic assumptions (Allemang *et al.*, 1996):

a. The structure is assumed to be a linear. This means that the response of the system, due to any combination of forces which applied simultaneously, is equal to the sum of the individual response to each of the forces acting alone.

b. The structure is time-invariant. This implies that the system parameters such as the mass, the stiffness, and the damping ratio are constants with respect to time.

c. The structure is considered to follow Betti-Maxwell's reciprocal theorem. It states that the deformation at point j due to a force applied at point k is equal to the deformation at point k due to a force at point j. Under this condition, it is required to measure only a column or a row of the system frequency response functions.

d. The structure is observable. The input-output measurements that are made contain enough information to generate an adequate behavioral model of the structure.

The theory of modal analysis and testing used in the present study is reviewed in Appendix B.

3.2.1 Application of Modal Analysis in the Present Study

The modal analysis and testing were used to record the dynamic responses of the stiffened plate model due to a fast sine sweep excitation, from which the frequency response functions (FRFs) were obtained. Furthermore, the modal parameters, such as the natural frequencies and damping ratios were extracted from the corresponding FRFs.

A single input/single output (SISO) function was used to measure the acceleration FRF models at six different locations in the stiffened plate. The experimental FRFs were measured using the B&K 2034 signal analyzer (Bruel &Kjaer Inc., 1987). The B&K signal analyzer provided facilities to solve the problems outlined in Appendix B.2.1 - B.2.4. A Hanning window was used for signal analysis, and a linear averaging method with 75% overlap was used in which the number of averaging was 100. Also, a zoom of 50.00 Hz frequency span was used so that a better acceleration FRFs (coherence = 1.00) can be obtained. The FRFs obtained using the B&K 2034 signal analyzer were then transferred to a personal computer using the National Instruments GPIB interface. The modal parameters were extracted using The STAR STRUCT® software (Spectral Dynamics, Inc., 1994). A block diagram for the experimental procedure is given in Chapter 4.

The experimental FRFs and the corresponding modal parameters were utilized to verify the correctness of FE model. The analytical FRFs were calculated using the FE analysis performed using the I-DEAS Master Series software package (Lawry , 1996). An impulse excitation was applied to the dynamic model to obtain the numerical FRFs and their

modal parameters.

3.3 Random Vibration

3.3.1 The Random Decrement Technique

The random decrement technique, called randomdec technique hereafter, is a technique developed for averaging the time history of the random response of a structural system to obtain an estimate of its free vibration response. This response is usually referred to as the randomdec signature. The main advantage of this technique is that only the measured dynamic response of a structure is needed. Therefore, this technique can be used to identify the free vibration response of a structure on-line without disrupting the normal operation of the structure being tested.

The randomdec technique was empirically developed by Cole (1973) for detecting the failure of a space shuttle wing model. He also hypothesized that the randomdec signature is equivalent to the free vibration response of the system with initial displacement equal to the threshold level and an initial slope equal to zero.

The basic concept of the randomdec technique is based on the fact that the random response of a structural system under random excitation is composed of two components: a) a deterministic component and b) a random component (assumed to have a zero average) (Ibrahim, 1977). By averaging enough samples of the random response, the random component of the response will average out to zero, leaving the deterministic component of

the response, which gives the randomdec signature. The technique computes the average of a large number (N) of segments, each of time length τ of the random response $\{y(t)\}$ given by Equation (3.2) in the following manner:

The starting time t_i of each segment is selected such that $\{y(t_i)\} = \{y_s\}$ = constant, called threshold level or trigger level, and the slope $\{\dot{y}(t_i)\}$ has alternating positive and negative values. This process can be represented in mathematical form as follows:

$$\{x(\tau)\} = \frac{1}{N}\sum_{i=1}^{N}\{y(t_i + \tau)\} \tag{3.3}$$

where:

$\{y(t_i)\} = \{y_s\}$ $\qquad i = 1, 2, 3 \ldots .$

$\{\dot{y}(t_i)\} \geq 0$ $\qquad i = 1, 3, 5 \ldots .$

$\{\dot{y}(t_i)\} \leq 0$ $\qquad i = 2, 4, 6 \ldots .$

The function $\{x(\tau)\}$ is the randomdec signature, and is only defined in the time interval $0 \leq \tau \leq \tau_1$, where τ_1 is the length of the random record. An example of the randomdec signature $\{x(\tau)\}$ obtained using Equation (3.3) is shown in Figure 3.2.

Next, replacing time t in Equation (3.2) with $(t_i + \tau)$, summing over number of segments N, dividing by N, and using Equation (3.3), Equation (3.2) can be written as:

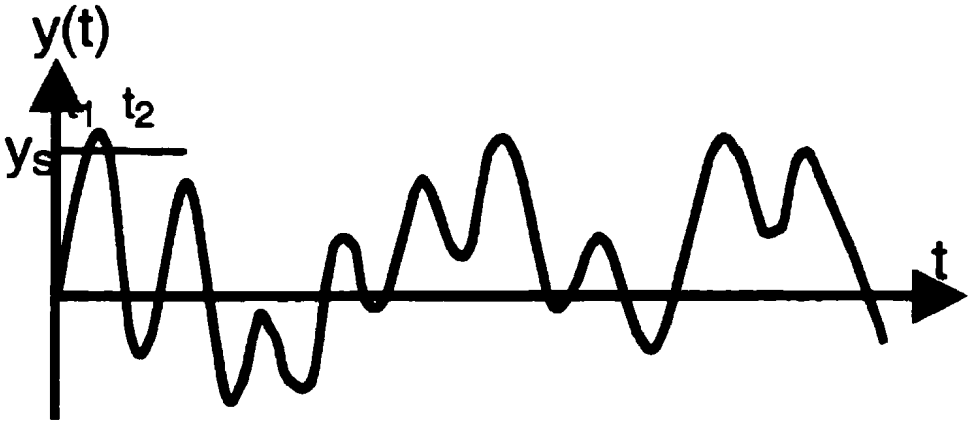

3.2.a. A random response

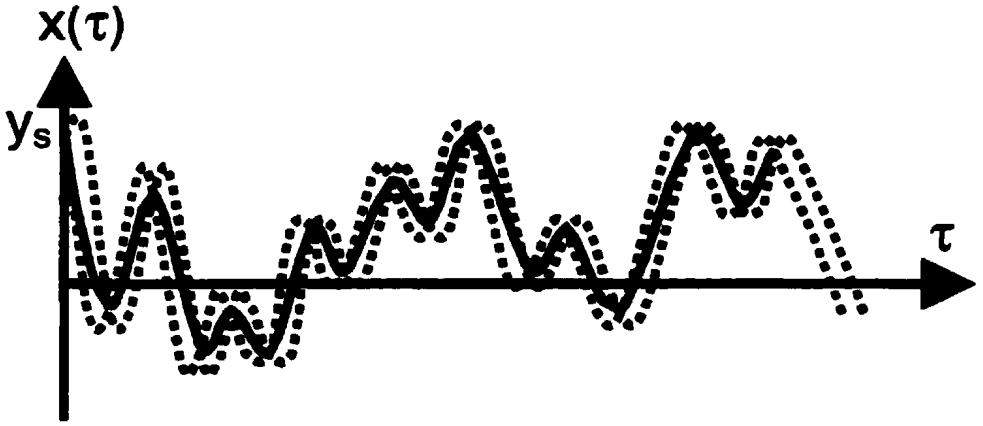

3.2.b. Signature after two averages

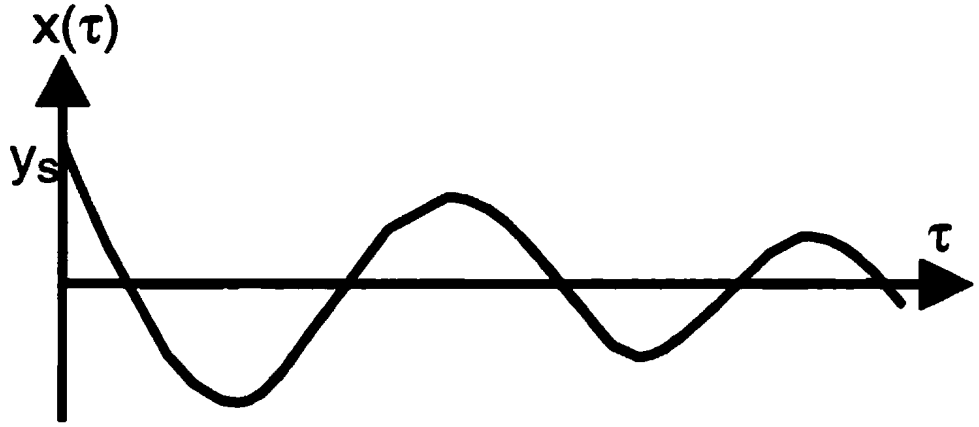

3.2.c. Signature after N averages

Figure 3.2. The Extraction of Randomdec Signature from a Random Response

$$[M]\{\ddot{x}(\tau)\} + [C]\{\dot{x}(\tau)\} + [K]\{x(\tau)\} = \frac{1}{N}\sum_{i=1}^{N}\{f(t_i+\tau)\} \qquad (3.4)$$

Now considering the right-hand side of Equation (3.4), since $\{f(t)\}$ is a stationary random input with zero mean, and Gaussian random process, then:

$$\frac{1}{N}\sum_{i=1}^{N}\{f(t_i+\tau)\} = 0 \qquad (3.5)$$

and Equation (3.4) reduces to:

$$[M]\{\ddot{x}(\tau)\} + [C]\{\dot{x}(\tau)\} + [K]\{x(\tau)\} = 0 \qquad (3.6)$$

Equation (3.6) and Figures 3.2.c. describe the free motion of the system whose forced response is described by Equation (3.2).

Vandiver *et al.* (1982) developed a mathematical basis for the relationship between the autocorrelation function and the randomdec signature. For a single-degree randomdec signature, they have shown that the randomdec signature is related to the autocorrelation function as follows:

$$x(\tau) = \frac{R_{yy}(\tau)}{R_{yy}(0)} y_s \qquad (3.7)$$

From Equation (3.7), it can be observed that the autocorrelation function of the

random response is proportional to the randomdec signature. This means that the autocorrelation function and the randomdec signature have similar behavior and properties.

3.3.2 The Auto- and Cross-correlation Functions

The correlation function defines the correlation between two parameters as a function of the time (Curtis and Lust, 1996). If the two parameters are the same except for the time of observation, i.e., $y(j)$ and $y(j + \tau)$, the function is known as an autocorrelation function. The mathematical expression of the autocorrelation function $R_{yy}(\tau)$ is given as

$$R_{yy}(\tau) = \frac{1}{J - \tau} \sum_{j=1}^{J-\tau} y(j)\, y(j+\tau) \tag{3.8}$$

If the two parameters are physically distinct, i.e., $y_1(j)$ and $y_2(j + \tau)$ the function is known as a crosscorrelation function $R_{y_1y_2}(\tau)$ as shown in Equation (3.9):

$$R_{y_1y_2}(\tau) = \frac{1}{J - \tau} \sum_{j=1}^{J-\tau} y_1(j)\, y_2(j+\tau) \tag{3.9}$$

On the other hand, the power spectral density (PSD) $S_{yy}(\omega)$ provides information of the random response in the frequency domain. PSD is the Fast Fourier Transform (FFT) of $R_{yy}(\tau)$ as shown in Equation (3.10):

$$S_{yy}(\omega) = \int_{-\infty}^{\infty} R_{yy}(\tau)\, e^{-i\omega\tau}\, d\tau \tag{3.10}$$

Therefore, the autocorrelation function can be obtained in the form of an Inverse Fast Fourier Transform (IFFT) of the PSD:

$$R_{yy}(\tau) = \frac{1}{2\pi} \int_{-\infty}^{\infty} S_{yy}(\omega)\, e^{i\omega\tau}\, d\omega \tag{3.11}$$

3.3.3 Application of Randomdec Technique, the Auto- and Cross-correlation Functions in the Present Study

The randomdec technique, and the auto- and cross-correlation functions were used to analyze the experimental random response so that an estimate of its free vibration response can be obtained. The random response of the model was obtained by applying random excitation to the model. A single input/multiple output (SIMO) procedure was used to measure the acceleration random responses at six different locations on the stiffened plate model.

The acceleration random response was filtered using a wide-band filter around the predominant frequency. The filtered results were then analyzed using Equation (3.3) to obtain the randomdec signature, and using Equations (3.8) and (3.9) to obtain the auto- and cross-correlation functions. The filtering of the random responses and the calculation of the auto and cross-correlation functions were performed using the Matlab 4.1 software package (The MathWorks, Inc, 1992). A FORTRAN program was used to calculate the randomdec

signature.

The FE model was used to obtain the free vibration response and the autocorrelation function. The free vibration response was obtained by exciting the model using an impulse. A white noise random signal was used to excite the model, and the random response was used to determine the power spectral density (PSD). The autocorrelation function was obtained by applying an Inverse Fast Fourier Transform (IFFT) to the PSD. All processes were performed using I-DEAS Master Series 6 software package (Lawry, 1996). Similar to the experimental autocorrelation functions, the numerical autocorrelation function were also filtered using the Matlab 4.1 software package mentioned earlier.

3.4 Added Mass

The stiffened plate models represent the side shell, of a ship's structure, which is always in contact with water; therefore, the influence of the water on the models must be considered. This effect can be represented as an added mass. The effect of the added mass is to cause a decrease in the natural frequency and an increase in damping ratio of the model.

There are many theoretical and experimental studies which have been carried out to determine the added mass coefficients for similar structures. Haddara and Cao (1996) developed a non-dimensional value, called an added mass factor (*AMF*) to measure the change in the natural frequencies due to the fluid-loading effect. They defined the added mass factor as:

$$AMF = \frac{M_i^*}{M_{i\,air}} \tag{3.12}$$

where:

$$M_i^* = M_{i\,fluid} - M_{i\,air} \tag{3.13}$$

and M_i^* is an added mass of the i^{th} mode of the model, $M_{i\,air}$ is mass of the i^{th} mode of the model in air, and $M_{i\,fluid}$ is the mass of the i^{th} mode of the model in water.

Since the physical stiffness $[K]$ of the models remain unchanged whether they are in air or in fluid, and the undamped natural frequencies ω_i are given by:

$$\omega_i = \sqrt{\frac{K_i}{M_i}} \tag{3.14}$$

The following relation is obtained:

$$\frac{M_{i\,fluid}}{M_{i\,air}} = \frac{\omega_{i\,air}^2}{\omega_{i\,fluid}^2} \tag{3.15}$$

or:

$$M_{i\,fluid} = \frac{\omega^2_{i\,air}}{\omega^2_{i\,fluid}} M_{i\,air} \tag{3.16}$$

By substituting Equation (3.16) into Equation (3.12), the following equation is obtained:

$$AMF = \left(\frac{\omega_{i\,air}}{\omega_{i\,fluid}}\right)^2 - 1 \tag{3.17}$$

3.4.1 Application of an Added Mass Factor in the Present Study

The natural frequencies of the stiffened plate models in air and in water obtained from the experiments were used to calculate the AMF in Equation (3.17). The AMF was used to estimate the added mass value using Equation (3.12). The added mass was then added to the mass of the stiffened plate models used in calculating the vibration responses using the FE analysis.

3.5 Artificial Neural Networks

An artificial neural network is an information processing system that is nonalgorithmic, and intensely parallel. It is not a computer in the sense people think of them as today, nor it is programmed like a computer (Caudill, *et al.*, 1994). It is inspired by the neuron architecture

and operation of the human brain, which has a capability to handle problems such as language understanding, visual processing, speech recognition, and other tasks which involve perception and induction. A basic nerve cell or neuron is composed of a processing body, transmitting axons, receiving synapses, and dendrites as shown in Figure. 3.3. It can be seen from Figure 3.3 that dendrites feed information into each neuron or nucleus. At each dendrite/ neuron interface, a synapse controls the strength of the signal fed in. Each neuron sums its inputs and sends out a signal along its single axon if the sum is above certain threshold. The axon branches into dendrites which feed into other neurons.

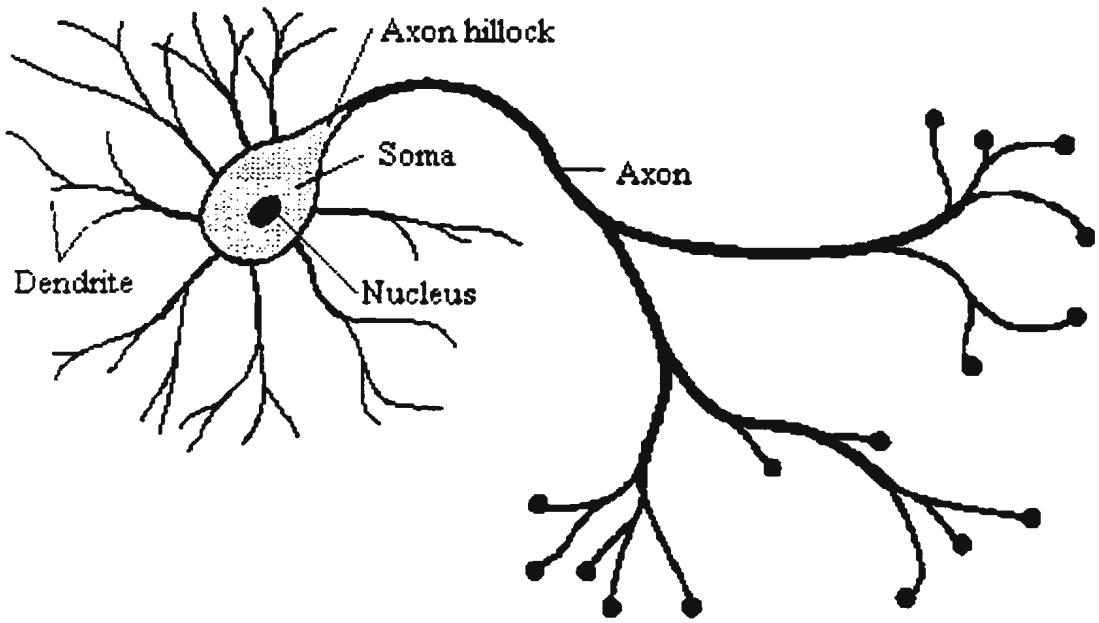

Figure 3.3: Biological Network

Based on the understanding of neurons, a computational model of a neural network was developed. For a single nerve cell, it could be modeled as an artificial neuron

(computational unit), which consists of receiving sites (synapses), receiving connections (dendrites), a processing element (cell body), and transmitting connections (axons) as shown in Figure 3.4.

Mathematically, it consists of an input layer, one or more hidden layers and an output layer of neurons. The input and hidden layers each contain one bias neuron with input unity. The summed inputs into the hidden layer neurons are processed by a transfer function when they pass through the neuron. For the nodes in the hidden layers, the most widely used type of transfer function is a sigmoid function.

The sigmoidal or the *S*-shaped function which drives its name from sigma for *S* in Greek, relates the output of a neuron to the weighted input, which the neuron receives, as follows:

$$f(i) = \frac{1 - e^{-i}}{1 + e^{-i}} \tag{3.17}$$

The $f(i)$ plays a central role in neural networks since it simulates the firing action of the biological neurons. The value of $f(i)$ in Equation (3.17) is always between -1 and +1.

For a single input-output case, the mapping equation for a single neuron as shown in Figure 3.4 (Haddara and Hinchey, 1995) is given by:

$$O = W_{OB} + W_{OM} F(W_{IM} I + W_{IB}) \tag{3.18}$$

where: O is an output of a single neuron, W_{IB} is a threshold applied to neurons in the hidden layer (unity), W_{IM} is a threshold applied to neurons in the hidden layer (input), W_{OB} is a threshold applied to neurons in the output layer (unity), and W_{OM} is a threshold applied to neurons in the output layer (input).

It can be seen from Equation (3.18) that the weights can be used in an input-output plot to scale and shift both horizontally along I and vertically along O using the transfer function.

In the present study, the creation of the neural network to model an input-output system is achieved by establishing the appropriate values of the connection weights W_I and W_O using a learning algorithm so that the response O_N of the system matches the target response O_T. The Method of Steepest Descent was used to optimize the weights using an iterative procedure. The training starts by assigning arbitrary values to the weights so that the value of the response error is determined as:

$$Er = O_N - O_T \tag{3.19}$$

where Er is an error, O_N is a network output, O_T is a target output, and

$$O_N = \Sigma\, W_O M$$

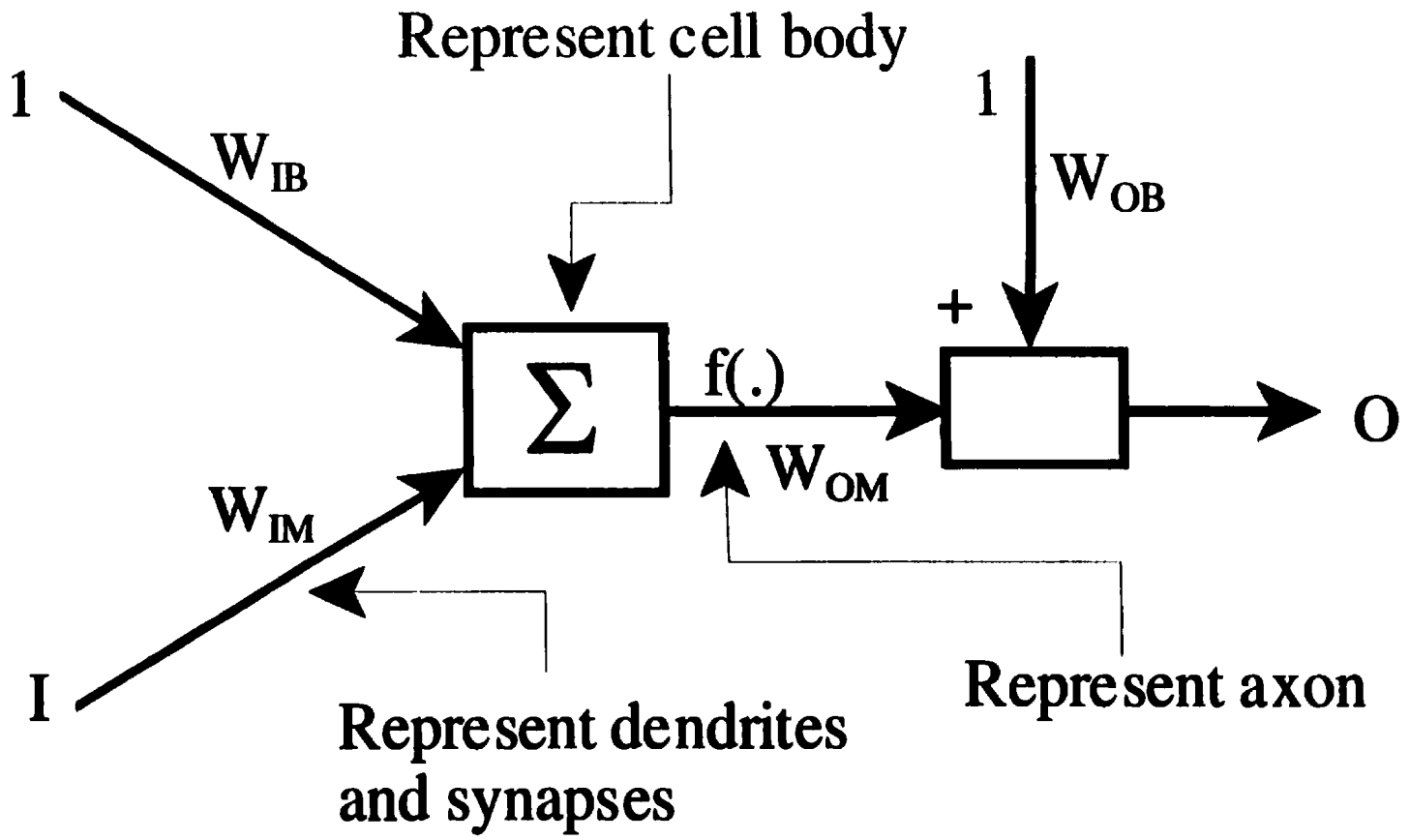

Figure 3.4: Artificial Neural Network

where W_O is synapses weights applied to inputs to the neurons in the output layer and M is output from a hidden layer.

In order to get the appropriate values of the weights, the error squared ΣEr^2 must be minimized. For small changes in W_O and M, one can write:

$$\Delta Er^2 = \Sigma \left[\frac{\partial Er^2}{\partial W_O} \right] \Delta W_O + \Sigma \left[\frac{\partial Er^2}{\partial M} \right] \Delta M \tag{3.20}$$

Since $M = f[\Sigma W_I I]$, $\Delta M = \Sigma \frac{\partial M}{\partial W_I} \Delta W_I$; therefore, the Equation (3.20) can be written as:

$$\Delta Er^2 = \Sigma \left[\frac{\partial Er^2}{\partial W_O} \right] \Delta W_O + \Sigma \left[\frac{\partial Er^2}{\partial M} \right] \Sigma \frac{\partial M}{\partial W_I} \Delta W_I \tag{3.21}$$

At each step, the next weights are calculated according to:

$$W(NEW) = W(OLD) + \Delta W \tag{3.22}$$

Therefore:

$$W_O(NEW) = W_O(OLD) - K \frac{\partial Er^2}{\partial W_O} \tag{3.23}$$

and:

$$W_I(NEW) = W_I(OLD) - \mathbf{K}[\frac{\partial Er^2}{\partial M}] \frac{\partial M}{\partial W_I} \tag{3.24}$$

where $\mathbf{K}$ is parameter. The negative of the gradient in Equations (3.23) and (3.24) shows the direction of steepest descent.

The above technique was applied to identify the extent and the location of damage in the stiffened plate models using Equation (3.1). For this purpose, Equation (3.1) is rewritten as a set of independent equations using modal analysis.

In order to obtain the independent equations form of Equation (3.1), the eigenvalue problem of the undamped system associated with matrices $[M]$ and $[K]$ is solved. The solution can be written in the general form:

$$[M][p][\omega_n^2] = [K][p] \tag{3.25}$$

The modal matrix $[p]$ can be normalized so as to satisfy

$$[p]^T[M][p] = [1] \tag{3.26}$$

$$[p]^T[K][p] = [\omega_n^2] \tag{3.27}$$

Next, the following linear transformation is considered:

$$\{v(t)\} = [p]\{z(t)\}, \tag{3.28}$$

relating the vectors $\{v(t)\}$ and $\{z(t)\}$, where the vectors represent two different sets of generalized coordinates. Because $[p]$ is a constant matrix, a transformation similar to Equation (3.28) exists between $\{\dot{v}(t)\}$, $\{\ddot{v}(t)\}$, and $\{\dot{z}(t)\}$, $\{\ddot{z}(t)\}$. Substituting Equation (3.28) into Equation (3.1), premultiplying by $[p]^T$, and considering Equations (3.26) and (3.27), one obtains

$$\{\ddot{z}(t)\} + [\hat{C}]\{\dot{z}(t)\} + [\omega_n^2]\{z(t)\} = \{G(t)\} \tag{3.29}$$

where:

$$\{G(t)\} = [p]^T \{f(t)\} \tag{3.30}$$

$$[\hat{C}] = [p]^T[C][p] \tag{3.31}$$

Matrix $[C]$ can be assumed to be a linear combination of matrices $[M]$ and $[K]$, and α and β are constants, thus the matrix $[\hat{C}]$ is diagonal. If

$$[\hat{C}] = [2\zeta\omega_n] \tag{3.32}$$

Equation (3.29) can be written in the following form.

$$\ddot{z}_r(t) + 2\zeta_r\omega_{n,r}\dot{z}_r(t) + \omega_{n,r}^2 z_r(t) = G_r(t), \qquad r = 1, 2, \ldots, m \tag{3.33}$$

Equation (3.33) is a set of m independent equations of the original Equation (3.1) and similar to Equation 3.2). Therefore, it can be written in the form of the random decrement equation.

$$\ddot{x}_r(t) + 2\zeta_r\omega_{n,r}\dot{x}_r(t) + \omega_{n,r}^2 x_r(t) = 0 \tag{3.34}$$

Introducing

$$F_r(x_r,\dot{x}_r) = \omega_{n,r}^2\,\zeta_r^2\,x_r + 2\,\zeta_r\,\omega_{n,r}\,\dot{x}_r \tag{3.35}$$

into Equation (3.34), one obtains

$$\ddot{x}_r(t) + \omega_{d,r}^2 x_r(t) + F_r(x_r,\dot{x}_r) = 0 \tag{3.36}$$

where $\omega_{d,r}$ is the frequency of the damped free vibration. The mathematical formulation given by Equation (3.36) describes the free motion of a set of models whose forced response is described by Equation (3.1). Equation (3.36) was used to identify the occurrence, extent, and location of the damage by estimating the function $F_r(x_r,\dot{x}_r)$ for the undamaged and damaged conditions at the predominant mode using a neural network technique described above.

The rationale behind using the function $F_r(x_r,\dot{x}_r)$ for damage identification is that the presence of damage causes the change of dynamic responses of the model such as

displacement x, and velocity $\dot{x}$. It can be analyzed from Equation (3.35) that the change of x, and $\dot{x}$ causes the change of the function $F_r(x_r,\dot{x}_r)$.

3.5.1 Application of the Neural Network Technique in the Present Study

In order to determine the function $F_r(x_r,\dot{x}_r)$, a block diagram of the neural network, which represents Equation (3.36) was designed as shown in Figure 3.5. The network has an input layer, a middle or hidden layer of six neurons, and an output layer of neurons. The input and hidden layers each contain one bias neuron with input unity. For the undamaged and each damaged condition, the autocorrelation function that could represent a free motion of the system (Zubaydi *et al.*, 2000), and its first derivative were used as input data to the network. $\omega_{d_r}^2$ is obtained from the autocorrelation function by measuring the period of the decaying oscillation.

The function $F_r(x_r,\dot{x}_r)$ was expressed as a nonlinear function of the displacement x, and velocity $\dot{x}$ using two sets of weights using the neural network algorithm as:

$$F(x_r, \dot{x}_r) = \sum_{k=0}^{11} W_o^{(k)} M_k \tag{3.37}$$

where:

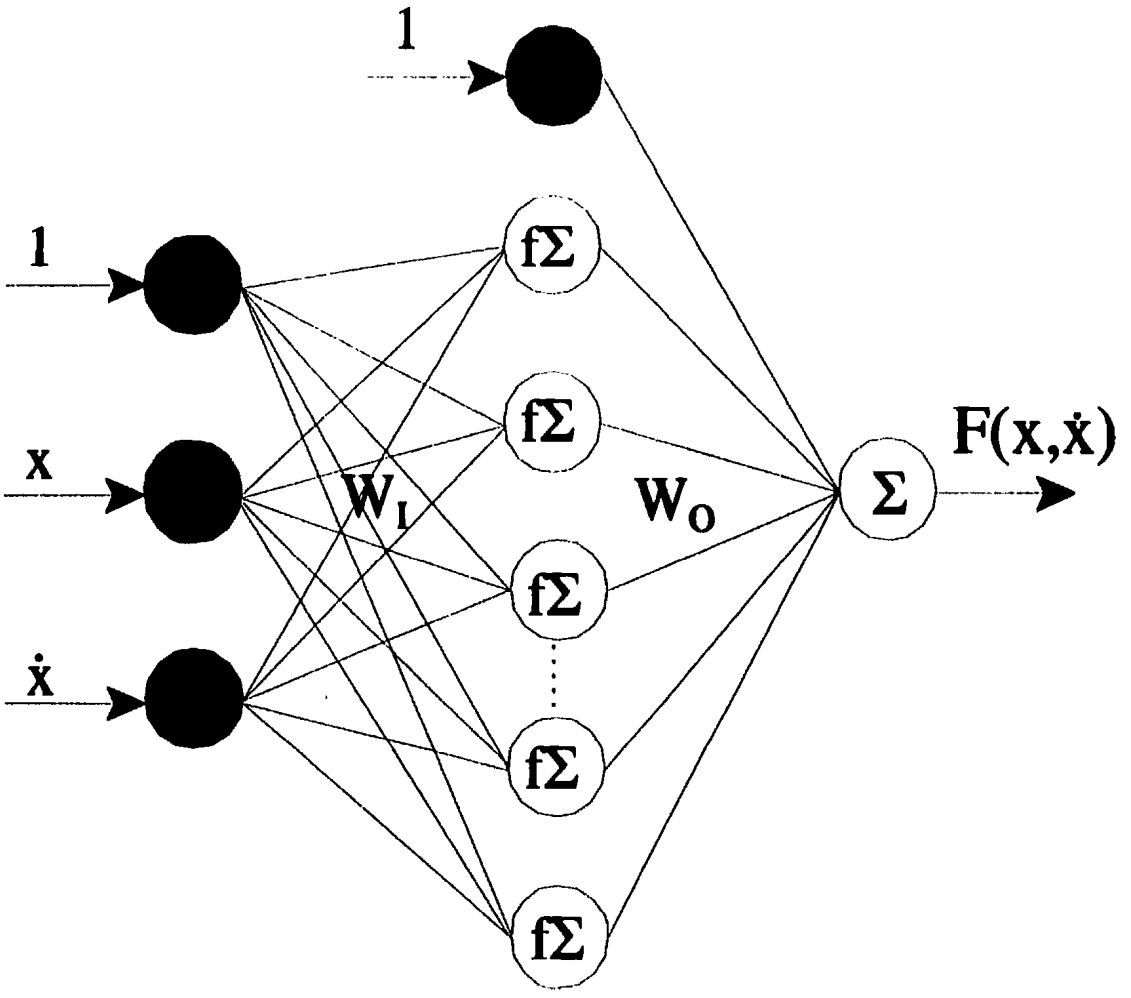

Figure 3.5: Block Diagram for the Neural Network used in Damage Identification

$$M_k = f\left(\sum_{j=0}^{2} W_I^{(j)} x_j\right) \tag{3.38}$$

and $M_0 = 1$ and $x_0 = 1$.

The weights $W_I^{(o)}$ and $W_o^{(o)}$ were applied to input and the hidden layers, whereas M_k is the output of the k^{th} neuron in the hidden layer. By obtaining the two sets of weights (W_I, W_o) and substituting them to Equation (3.37) and (3.38), the function $F_r(x_r, \dot{x}_r)$ can be obtained.

The function $F_r(x_r, \dot{x}_r)$ determined from the network is then substituted back in Equation (3.36) and the equation is integrated numerically using a fourth order Runge-Kutta technique to obtain the corresponding estimates of the average values for the autocorrelation function. The estimated autocorrelation function is then compared with the input autocorrelation function. The difference between the two is the error to be minimized in the subsequent iterations.

The experimental and numerical autocorrelation functions of Model #1, its first derivatives, and the damped frequencies for all cases were used as input data for training the neural network. The neural network technique used for damage identification was written using a FORTRAN program.

3.6 Summary

This Chapter provides an overview of the theoretical approach used in the present study. It discusses the general equation of motion of system with viscous damping in Section 3.1. Section 3.2 summarizes the theory of FE analysis used to generate an FE model, and its solution procedure for the dynamic analysis of thin shell elements. In Section 3.3, the theory of modal analysis and testing provides a basis for understanding the methodology used for the computation and for the planning of the experimental study, in which the dynamic characteristics such as FRFs and modal parameters are obtained.

Next, Section 3.4 provides the methods for interpreting the random responses using the randomdec technique, the auto- and cross-correlation functions. The calculation of added mass factors from the natural frequencies of a vibrating structure in air and in water was discussed in Section 3.5. Finally, in Section 3.6, the theory of neural network and its application for identifying the occurrence of damage in the stiffened plate models as well as its extent and location were summarized.

Chapter 4

Experimental Study

4.1 Introduction

Experimental studies are very important tools for investigating the behavior of a structure, since they make it possible to gain a direct insight into problems which are difficult to conceive analytically. Therefore, in order to investigate the behavior of an undamaged and damaged stiffened plate structure in air and in water and to make the correlation with analytical results, the experimental study of the stiffened plate models were carried out.

As pointed out in the literature review and discussed in the theoretical background, any physical change that occurs in the structure, such as a crack, will cause changes in the physical properties. These can be expressed in terms of changes in the mass, stiffness and/or damping of the structure. The change of stiffness or damping will produce changes in the modal parameters such as natural frequencies, damping ratios, and mode shapes of the structure. The change of mass as a consequence of a crack is negligible.

Among the various modal testing techniques available for damage identification, the acceleration FRFs and acceleration random responses were utilized in the present study. Accelerometers were used to measure accelerations of the stiffened plate models from which the acceleration FRFs and random responses can be obtained.

In this chapter, the details of the experimental study of the stiffened plate models are described. This includes the fabrication of the models, the experimental setup, instrumentation, calibration, and the procedure of the experiment. Data processing and analysis will be meaningful only when proper data acquisition has been made using the correct experimental methods.

Four models of the stiffened plate have been tested in the present study. One model has been tested in air, and the remaining ones have been tested in water. For convenience, the tested models will be identified as Models #1, #2, #3, and #4, respectively. In order to monitor the responses, six accelerometers were attached to each model at six different locations.

The experimental study has been carried out in the Fluids & Hydraulics Laboratory of the Faculty of Engineering and Applied Science. The details of the experimental study are given in the subsequent sections of this chapter.

4.2 Fabrication of the Stiffened Plate Models

Two pieces of 7/16 inch and one piece of ½ inch thick structural plate, along with one piece

of unequal leg angle steel section of ½ inch, were jointed together by welding to form a stiffened plate model as shown in Figure 4.1. Figure 4.2 shows the dimensions of the single stiffened plate model. The dimensions were measured when the surface of models were dry and clean. A photograph of one of the tested stiffened plate model, Model #3 is shown in Figure 4.3. The choice of dimensions was based on a combination of factors, namely, the dimensions of real ship structures, the maximum capacity of the equipment available at the laboratory, and the materials available in the Faculty of Engineering and Applied Science, Memorial University of Newfoundland, St. John's.

However, due to manufacturing errors, the actual thicknesses of plate and angle sections were different for different specimens; they were different from those given in the fabricator's data sheet. In order to have the actual dimensions of the model, the thickness of the tested specimens were measured at several locations on the Models and the average values are listed in Table 4.1.

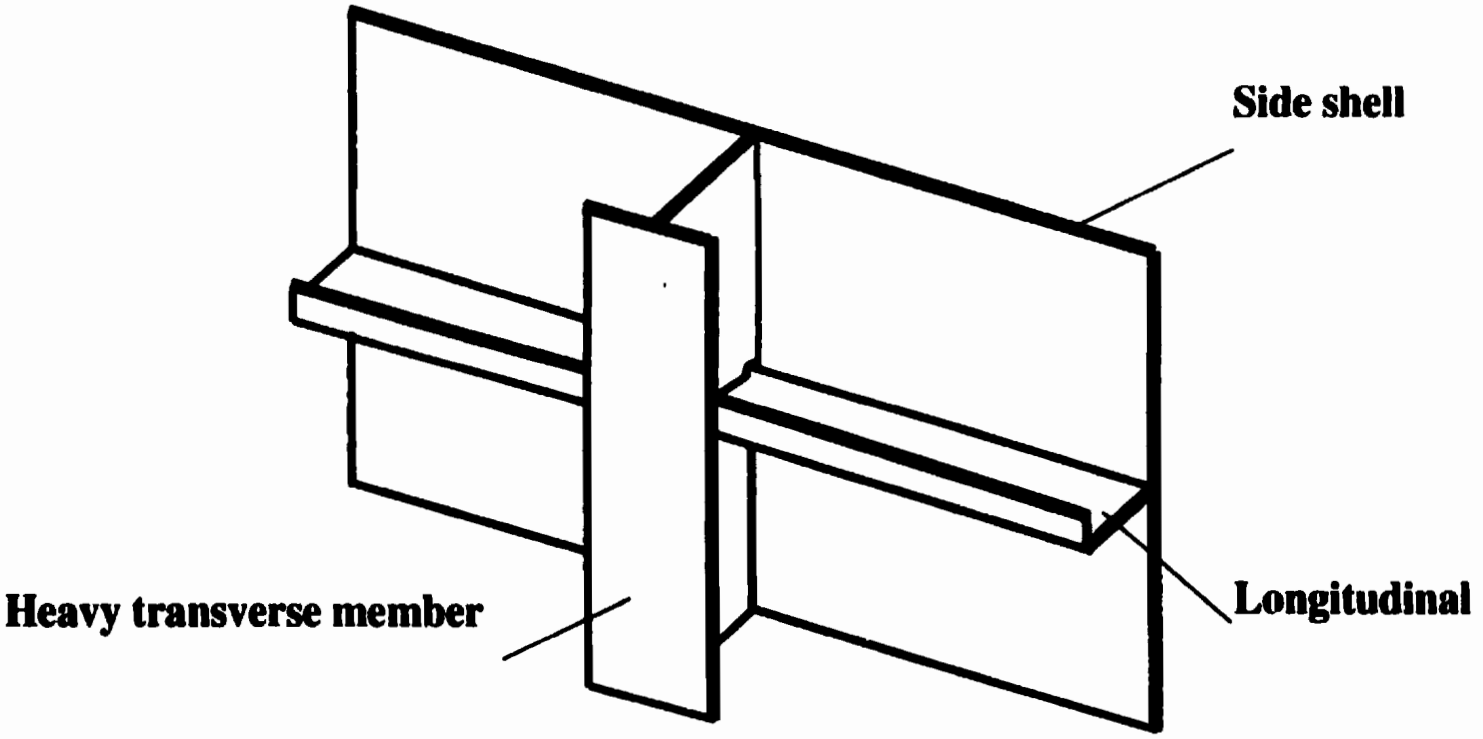

Figure 4.1. The Stiffened Plate Model

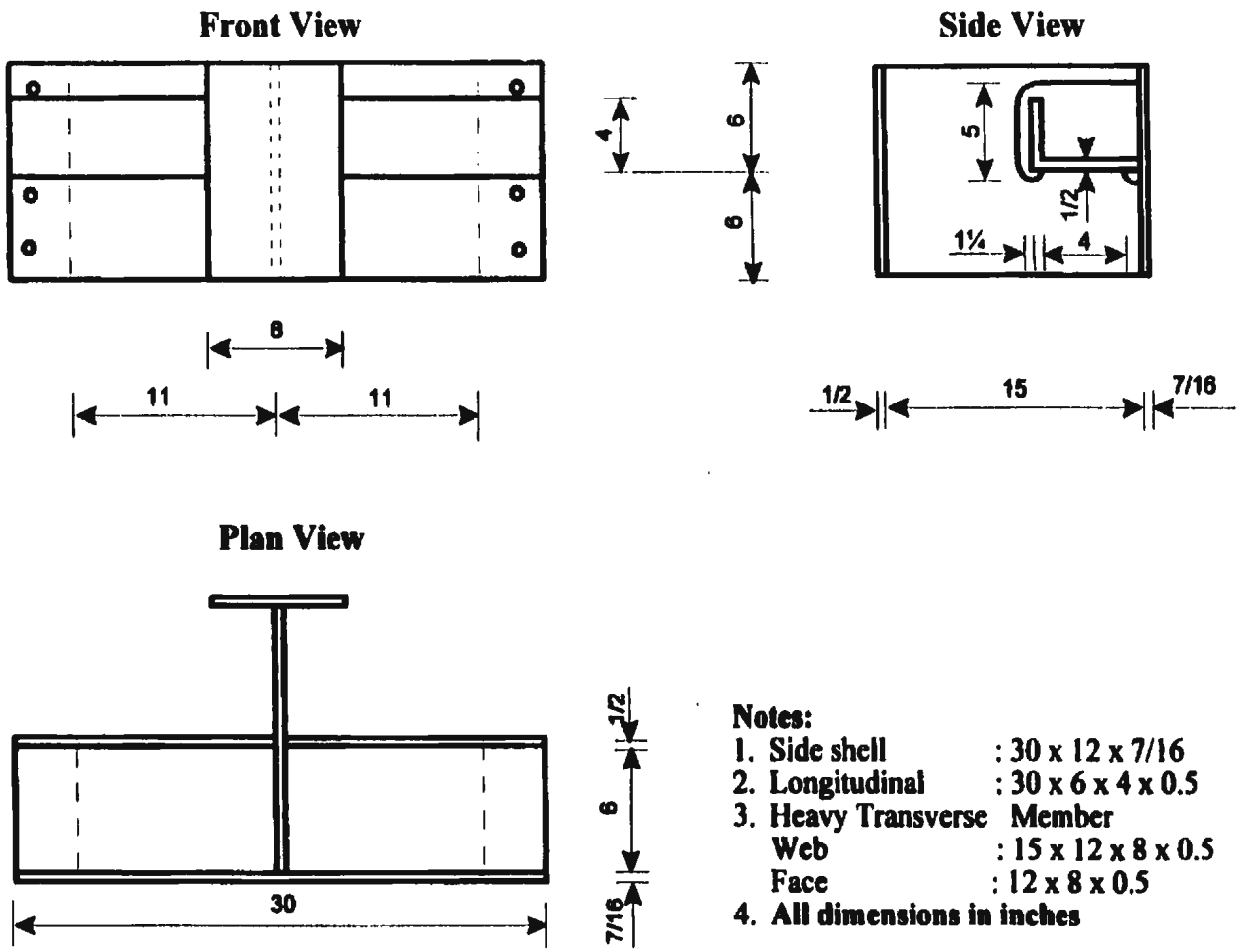

Figure 4.2. Dimensions of the Stiffened Plate Model

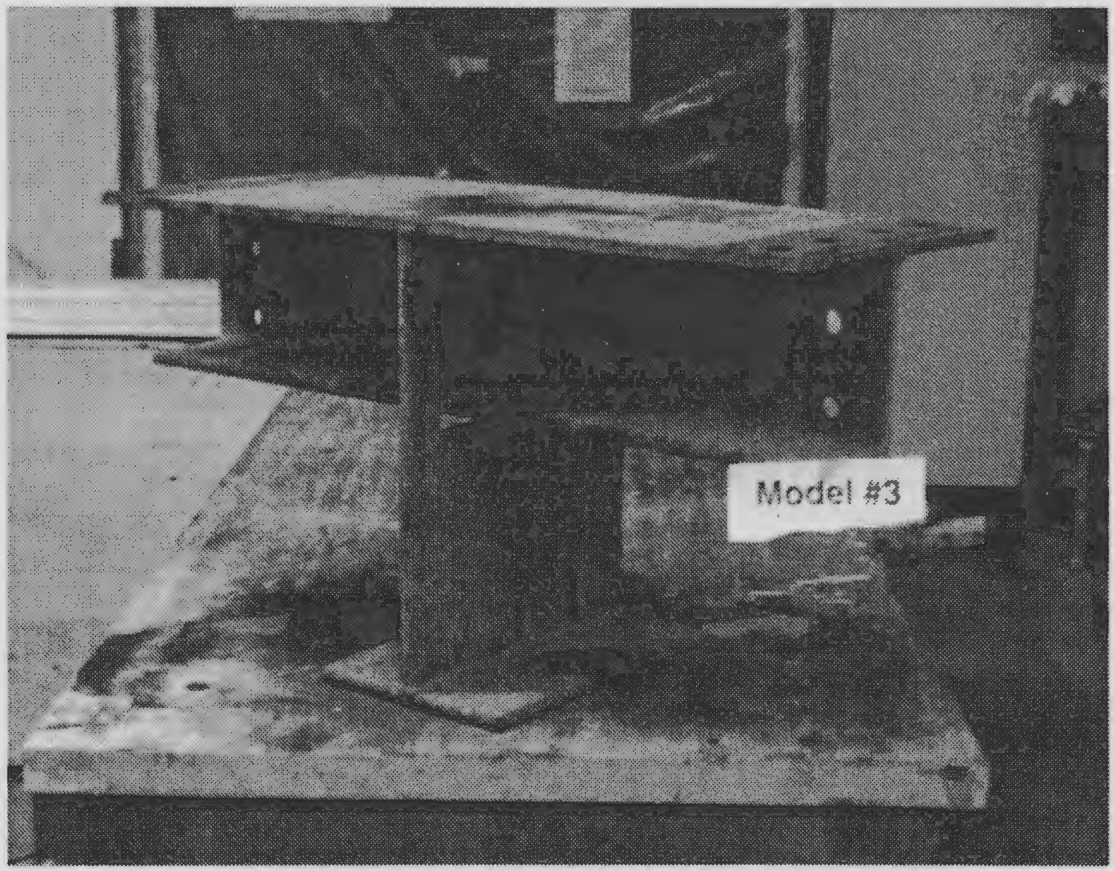

Figure 4.3 The Stiffened Plate Model (Model #3)

Table 4.1: The Thickness of Stiffened Plate Models (inches)

Geometry (thickness)	Fabrication data sheet	Experimental specimens measurements							
		Model #1	Errors (%)	Model #2	Errors (%)	Model #3	Errors (%)	Model #4	Errors (%)
Side shell plate	7/16	0.4554	4.09	0.4560	4.23	0.4570	4.46	0.4570	4.46
Unequal angle	0.50	0.4997	0.04	0.5170	3.40	0.5100	1.80	0.5080	1.60
Transverse member plate	0.50	0.5086	1.72	0.5138	2.72	0.5128	2.56	0.4980	0.40

4.3 Experimental Setup

The experimental setup for modal testing was designed as shown in Figure 4.4. Since the experiments were also carried out in water, the stiffened plate models were placed in a water tank as shown in Figure 4.5.

The dimensions of the tank were (290.00 x 30.00 x 40.00) inches. The wall of the tank was made of transparent plastic and constructed on steel frames used to strengthen the wall. The tank was fixed to five rigid supports. The fixed boundary condition of the model was obtained by clamping the side shell and the angle over a length of 22.00 inch at each end between two heavy square steel blocks (12.00 x 12.00 x 1.00) inches.

The lower block was supported by a heavy I-beam (8.00 x 8.00 x 1.00) inches, in which the right support was welded to a thick plate (30.00 x 12.00 x 0.50) inches and the left support was bolted to the same thick plate. This plate, which was used to strengthen the tank bottom, was then welded to the tank bottom. The reason for bolting the left support to the thick plate is to allow the easy replacement of the models, see Figure 4.4.

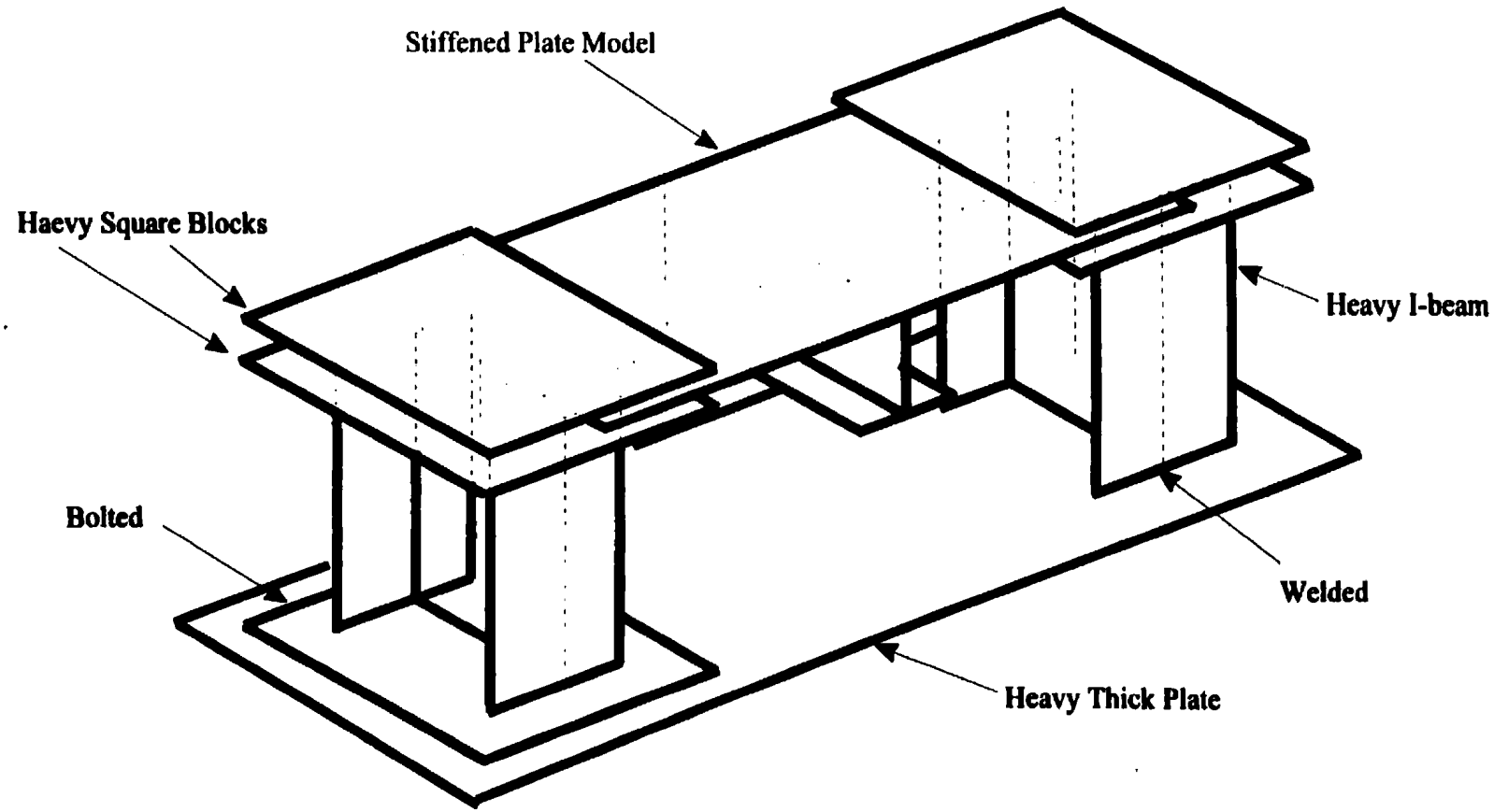

Figure 4.4 Schematic of Stiffened Plate Setup

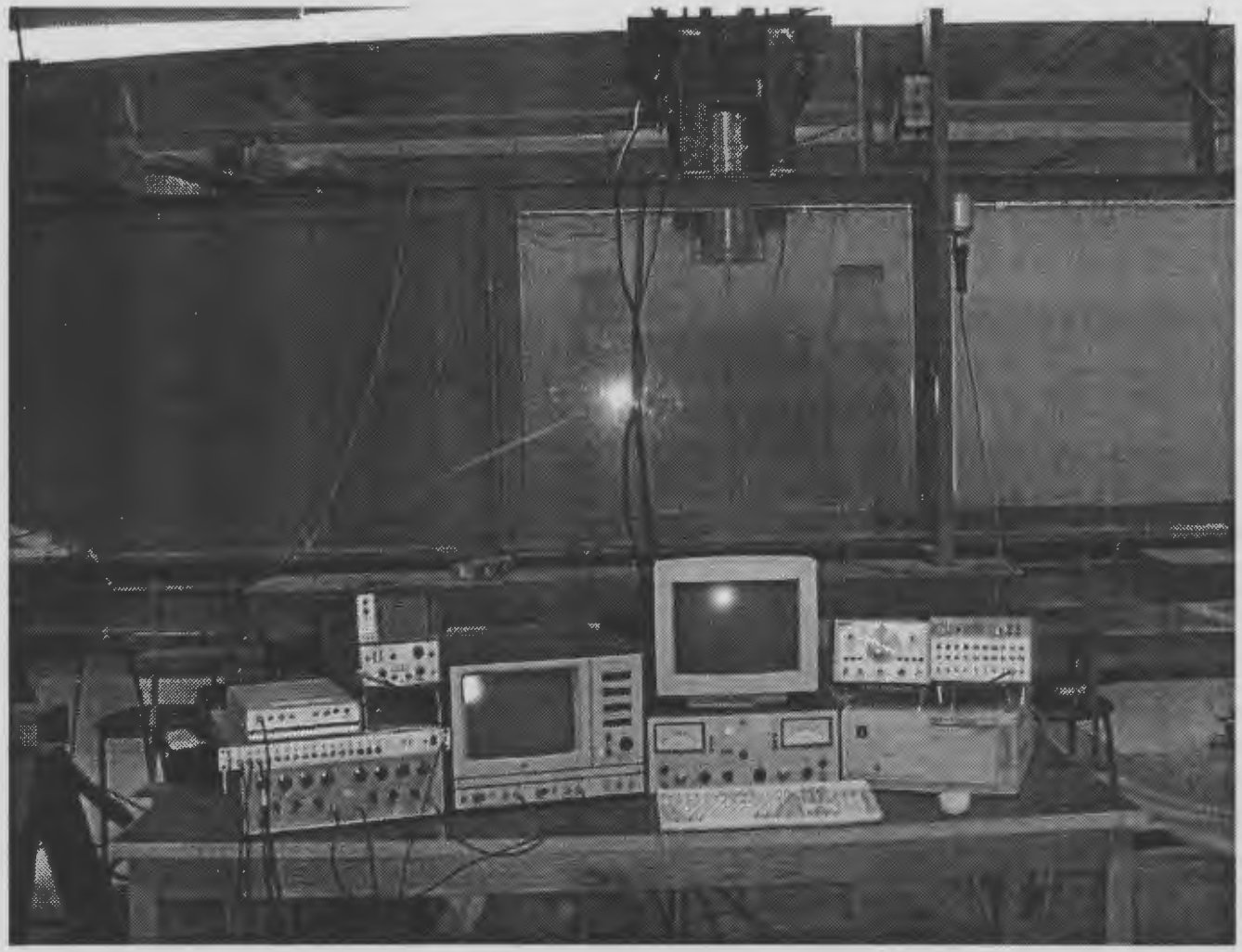

Figure 4.5 Instrumentation Setup

4.4 Instrumentation

In the present study, the SISO (single-input excitation and single-output excitation) and the SIMO (single-input excitation and multi-output data acquisition) techniques were used. Figure 4.6 shows a schematic of the measurement setup. In order to excite the stiffened plate models, a fast sine sweep and pseudo-random signals were selected for obtaining the dynamic responses.

The fast sine sweep and the random noise signals were generated by a HP 3314A function generator and a Wavetek 132 noise generator, respectively. The signals were amplified by a power amplifier B & K 27067 and sent to the vibration exciters B & K 4801 and 4802 to excite the model through a connecting rod. The excitation force applied to the model was measured using a Kistler load cell model 912 attached between the connecting rod and the model. Accelerometers type PCB 330A were used to measure the dynamic responses of the stiffened plate models from which the acceleration FRFs and the acceleration random responses could be obtained.

The fast sine sweep signals and their acceleration responses were amplified by a 504E dual mode amplifier and PCB 433A differential amplifier, and filtered through a Krohn-Hite filter model 3323. From this filter, both the force and response signals were sent to a dual channel amplifier B&K 2034 analyzer for performing a Fast Fourier Transform so that FRFs and coherence functions could be obtained, and then to a data acquisition system for storing the original and the analyzed data. At the same time, the force and response signals were

viewed through an oscilloscope (Tektronix T 922) for monitoring purposes, so that large force signals that clip the response signals could be avoided. Furthermore, FRFs and coherence data were transferred to a personal computer using the National Instruments GPIB interface for analysis. A commercial software package, STAR STRUCT® (Spectral Dynamics, Inc., 1994), was used to analyze the FRFs and the coherence so that modal parameters can be obtained.

Like the fast sine sweep signals and their acceleration responses, the random force signals and their acceleration vibration responses were also passed through a 504E dual mode amplifier and PCB 433A differential amplifier to the Krohn-Hite model 3323 filter. From this filter they were passed to a Keithley 570 data acquisition system. All the measured data were digitalized by the Keithley 570, manipulated by KDAC500, and stored on the hard disk of a personal computer. Also, the random force signals and their acceleration random responses were sent to a Tektronix T 922 oscilloscope to monitor the signals so that the large signal could be avoided. The random responses were used to obtain the randomdec signatures.

The details of the instrumentation used in the present study and the process of their calibration are reviewed in Appendix C.

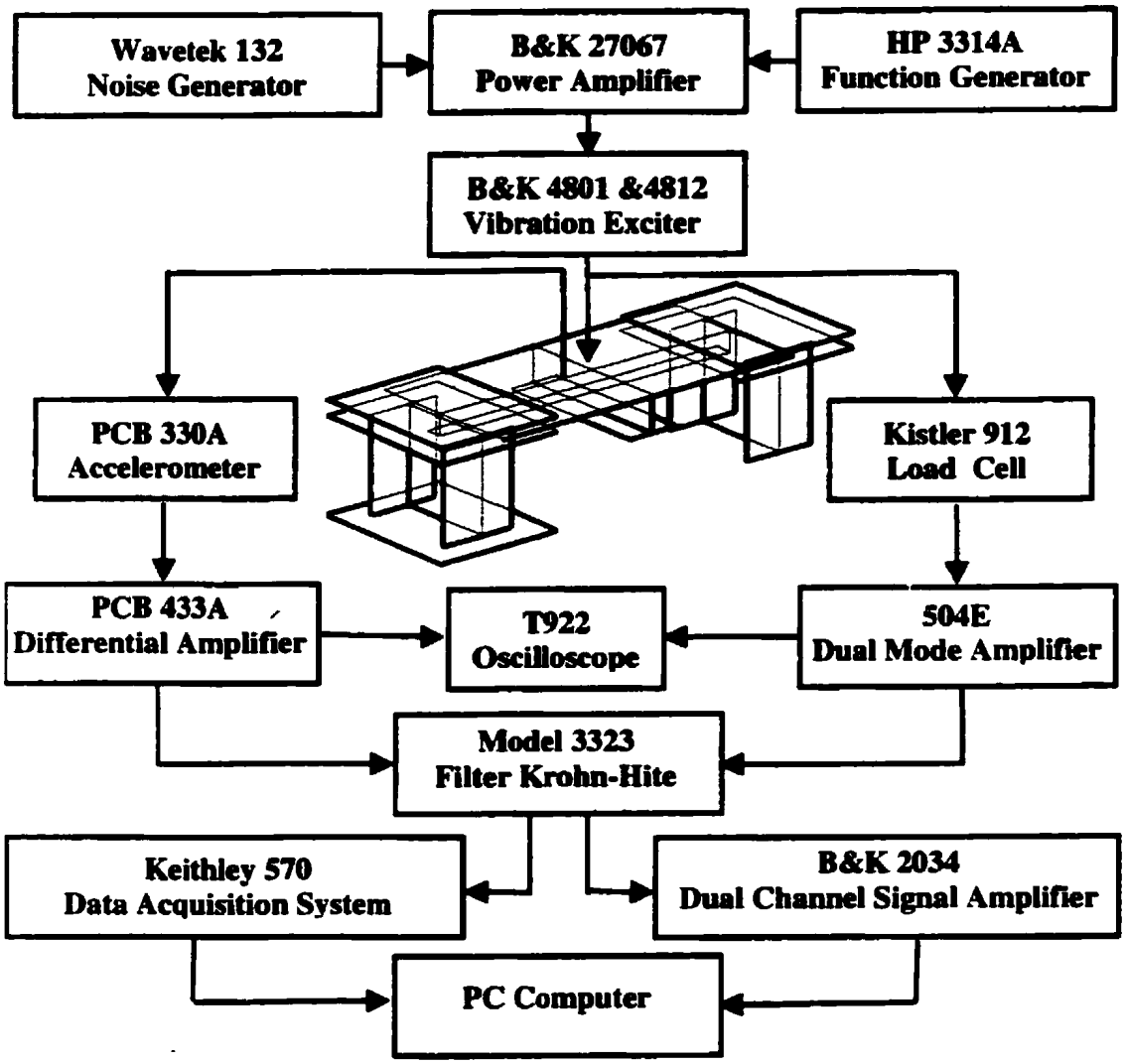

Figure 4.6 Schematic of the Measurement

4.5 Location of the Load Cell and the Accelerometers

In order to have a good understanding of the dynamic responses of the undamaged stiffened plate models as well as the models with damage of different lengths, the load cell and the accelerometers must be mounted at the proper locations.

4.5.1 Load Cell Arrangement

The load cell was mounted on that side of the shell which was without the longitudinal and heavy transverse members. The load cell was located slightly off the center of the stiffened plate model to generate all the symmetric and asymmetric vibration modes. The exciting force represented the action of the wave pressure which would cause the majority of fatigue damages (Hansen and Winterstein, 1995). The load cell was fixed vertically on the model to apply an axial load as shown in Figure 4.7.

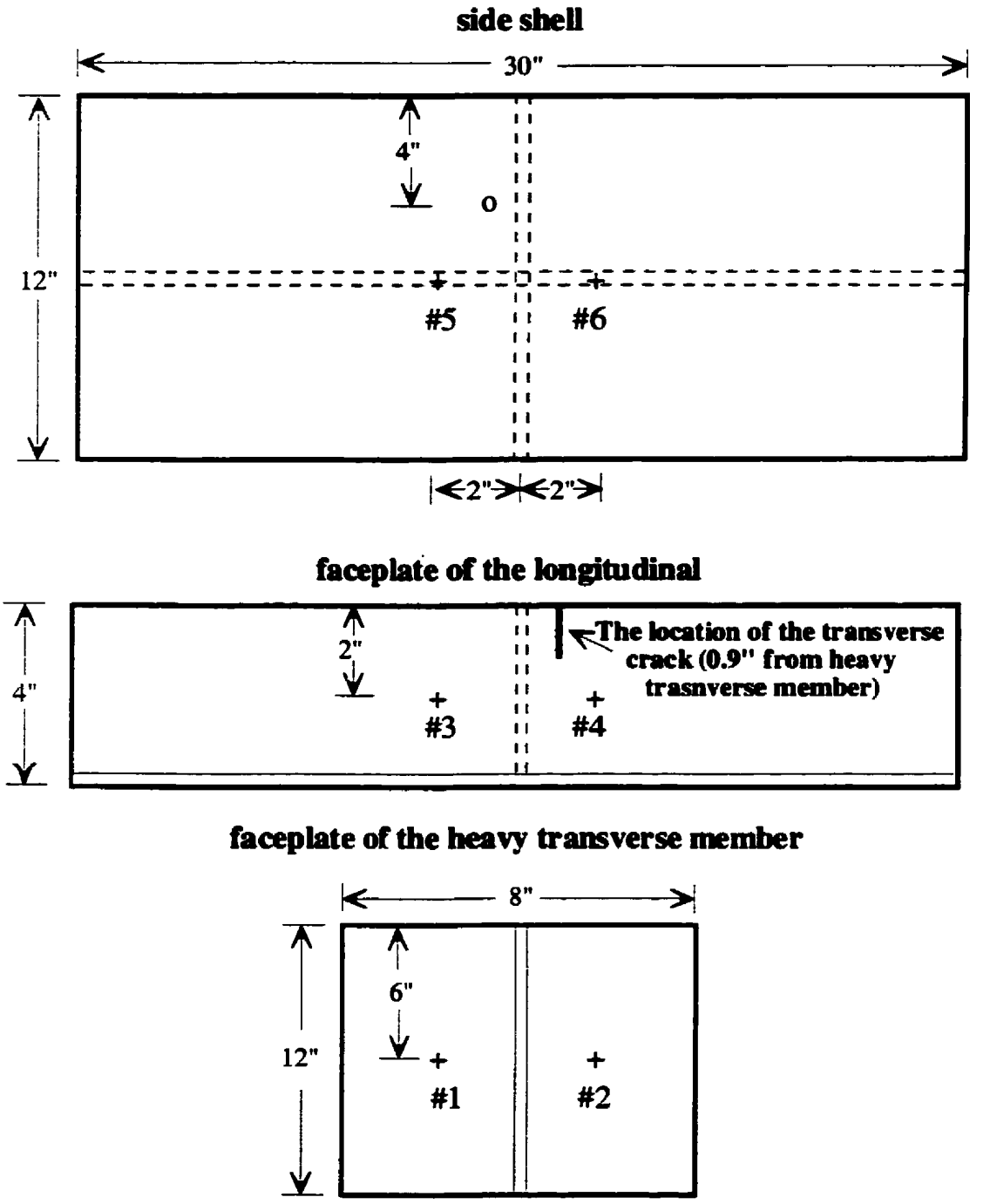

Figure 4.7. The Arrangement of the Load Cell and the Accelerometers

4.5.2 Accelerometers Arrangement

In order to determine the best positions for the points of measurement, six accelerometers were attached to each stiffened plate model at six different locations for acquiring the responses of the models. The accelerometers were placed on the models at a location near the web of the heavy transverse member at which the damage was expected to occur, based on the literature review.

Two accelerometers were located on the side shell, two were located on the faceplate of the longitudinal, and two were located on the faceplate of the heavy transverse member. Figure 4.7 shows the details of the location of the six accelerometers.

4.6 General Procedure

The experiment was carried out using a modal testing technique (Ewins, 1996). Modal testing was performed by monitoring the input excitation and the output response of the oscillating structure at the points of measurement. The details of the experimental procedure are given below.

1. The fast sine sweep signal was applied to the undamaged stiffened plate model (Model #1), and at the same time the acceleration FRFs were recorded at the location of accelerometer #1. The experiment was carried out in two steps. First, the fast sine sweep signal with a frequency span of 1000.00 Hz (1.00 - 1000.00 Hz) was used to

roughly locate the resonant frequencies of the model. Second, the signal frequencies were swept through a certain predefined frequency range. The frequency span of 50.00 Hz (between 20.00 Hz to 870.00 Hz) was selected so as to give a better acceleration FRFs and coherence. These results were sent to the computer via the National Instruments GPIB interface, and the STAR STRUCT® software was used to measure the modal parameters. This procedure was repeated for accelerometers #2,#3, #4, #5, and #6.

2. The fast sine sweep signal was disconnected, and the random signal was applied to Model #1. The acceleration random responses were recorded at the six different locations of the accelerometers using the SIMO technique. The results were then digitized, manipulated and stored on the disk. The data was analyzed using the randomdec technique and the auto- and cross-correlation functions were calculated.

3. In order to simulate the damage that occurs in the critical area of the longitudinal , a small initial saw cut of length of 0.40 inch was made at the tip of the longitudinal faceplate near the heavy transverse member (of Model #1) at a distance of 0.90 inch from the heavy transverse member (on one side only), (see Figure 4.7 for detail).

4. The fast sine sweep at a frequency span of 50.00 Hz (between 20.00 to 870.00 Hz) and random signals were applied again to Model #1 for damage identification, and at the same time the responses were recorded. In this step, the responses were recorded at the location of accelerometers #1 and #2 only. A preliminary study,

indicated in Chapter 5, demonstrated that the responses measured at the location of accelerometers #1 and #2 were much more pronounced than those measured at other locations.

5. Steps 3 and 4 were repeated for crack lengths of 0.80 inch, and 1.20 inch, respectively.

6. In order to ensure that the experiments gave accurate and complete damage results , steps 1 - 5 were repeated for Model #2. The location of crack was the same as Model #1, i.e., at a distance of 0.90 inch from the heavy transverse member (on one side only). However, the experiments were carried out by increasing the damage length by 0.20 inch.

7. The stiffened plate model represents the side shell of a ship's structure which is always in contact with water. Therefore, the experiments of Model #2 were also carried out in water. The depth of submergence above the model was 0.00 inch for partial submergence and 4.00 inch for full submergence.

8. In order to investigate the effect of the damage location on the dynamic responses, steps 1-7 were applied for other models also, viz., Models #3 and #4. The location of cracks were 1.35 inch (Model #3) and 1.80 inch (Model #4) from the heavy transverse member (on one side only).

Effect of damage growth at several locations, both in air and in water, were determined from the FRFs measurements, the randomdec signature and the auto- and cross-correlation functions calculations. The modal parameters such as natural frequencies and damping ratios were also determined.

4.7 Summary

The fabrication of stiffened plate models, experimental setup, instrumentation, calibration, placement of the load cell and accelerometers, and the procedures used for the experimental study were briefly described in this chapter. Getting accurate and reliable results require a proper experimental setup and calibration, careful test parameter identification, and intelligent and precise experimental measurement. These procedures have been meticulously followed in the present study to test the four stiffened plate models so that proper and well conditioned data could be obtained.

The results such as acceleration FRFs, acceleration random responses, randomdec signatures, auto- and cross-correlation functions, and modal parameters such as natural frequencies and damping ratios for the undamaged and damaged models were acquired in the present study. The analyses of these data are presented in the subsequent chapters with a view to identify the crack size and location.

Chapter 5

Dynamics of Stiffened Plate Models

5.1 Introduction

In this chapter, we present the results of the calculation of the acceleration frequency response functions for stiffened plate models using data obtained from experiments as well as that obtained from the FE models. Also, the results of the calculation of the free vibration response using the FE models, and the randomdec signatures using the experimental random responses are presented.

Although the calculations were made for the four models, only the results obtained using Model #1 will be presented here. Results obtained for the other three models are given in Appendix D. These results are in agreement with the results obtained for Model #1. This provided confidence in the accuracy of the conclusions derived from the present study.

5.2 Undamaged Model

5.2.1 Frequency Response Function (FRF)

Figures 5.1.a - 5.1.f show the experimental FRFs obtained at the locations of accelerometers #1, #2, #3, #4, #5, and #6, respectively. The values of the dominant experimental natural frequencies and damping ratios of FRFs are tabulated in Table 5.1. From the Figures 5.1.a - 5.1.f and Table 5.1, it can be seen that the FRFs obtained from the response measured at the six different locations have similar shapes, frequencies and damping ratios. Figures 5.1.a - 5.1.f also indicate that the fourth mode has the highest amplitude in the FRF record. This means that the fourth mode is the mode which has the most dominant frequency. The difference between the left (accelerometers #1, #3, and #5) and the right (accelerometers #2, #4, and #6) ones may be due to the fact that Model #1 was not symmetric. The asymmetry was caused by the slight difference in the dimensions caused by fabrication tolerances.

It can also be noticed that only FRFs obtained from measurements made using accelerometers #1 and #2 showed peaks corresponding to all modes up to the eighth mode. Measurements obtained from other accelerometers failed to show peaks corresponding to some modes. This is a direct consequence of the geometry of the arrangements of the accelerometers and the responses at the accelerometer locations due to model behavior. Six accelerometers have been used to identify the best location for measurements. It was, therefore, decided to use hereafter measurements obtained using accelerometers #1 and #2.

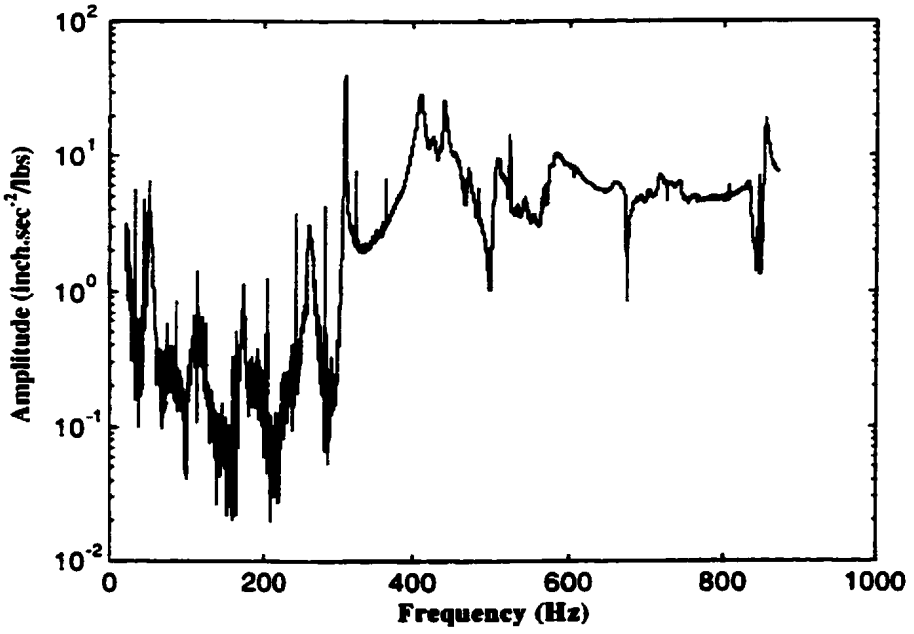

5.1.a: Experimental FRF at accelerometer #1

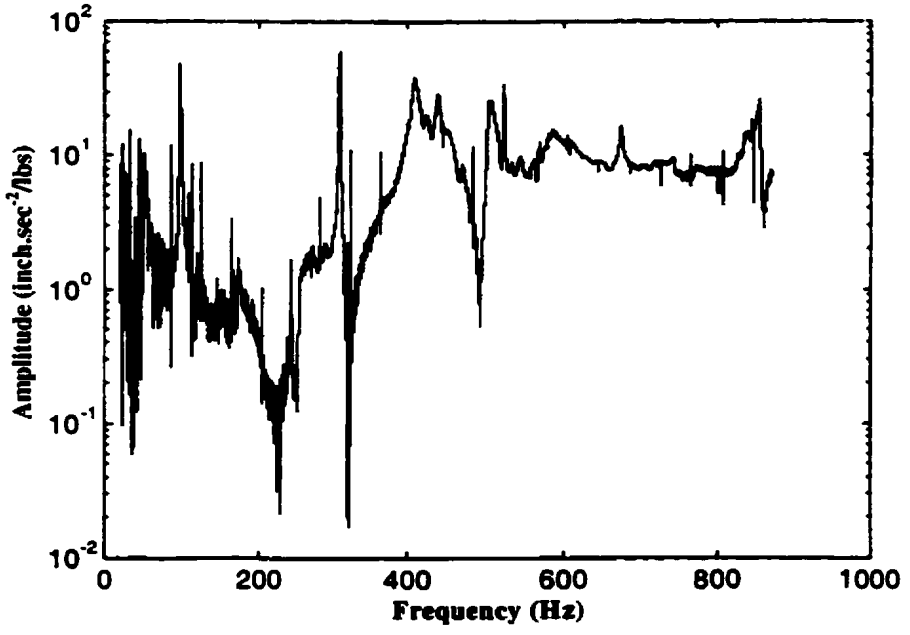

5.1.b: Experimental FRF at accelerometer #2

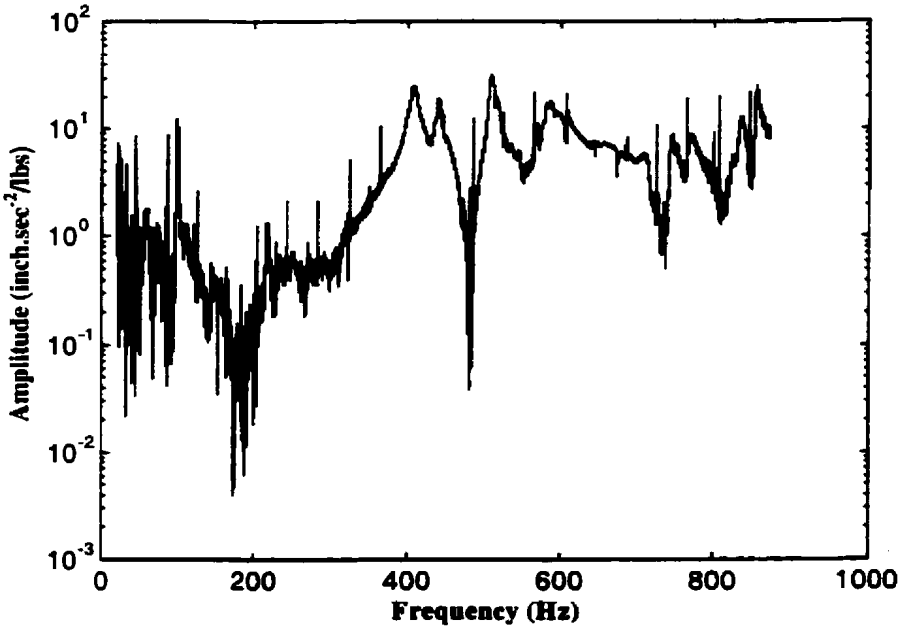

5.1.c: Experimental FRF at accelerometer #3

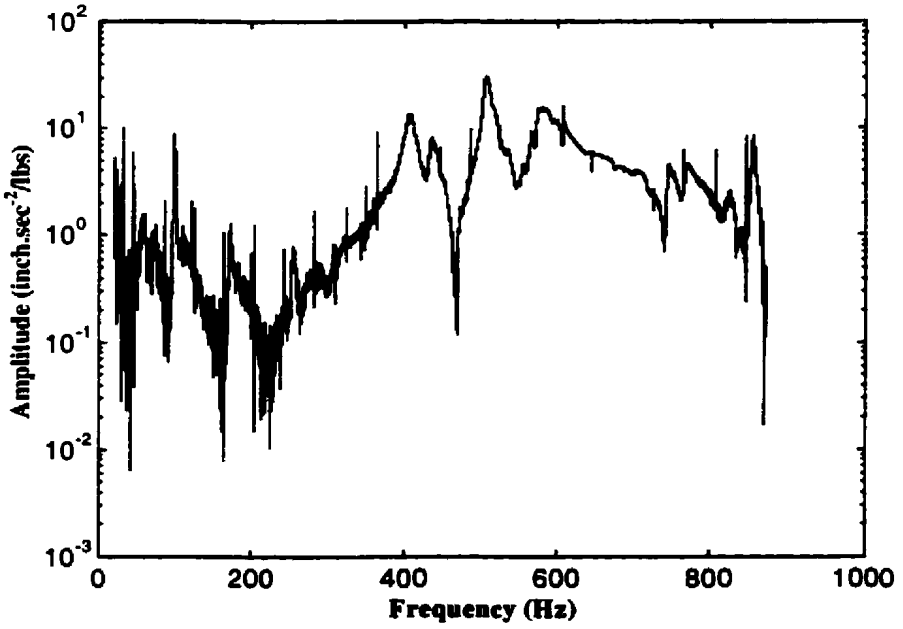

5.1.d: Experimental FRF at accelerometer #4

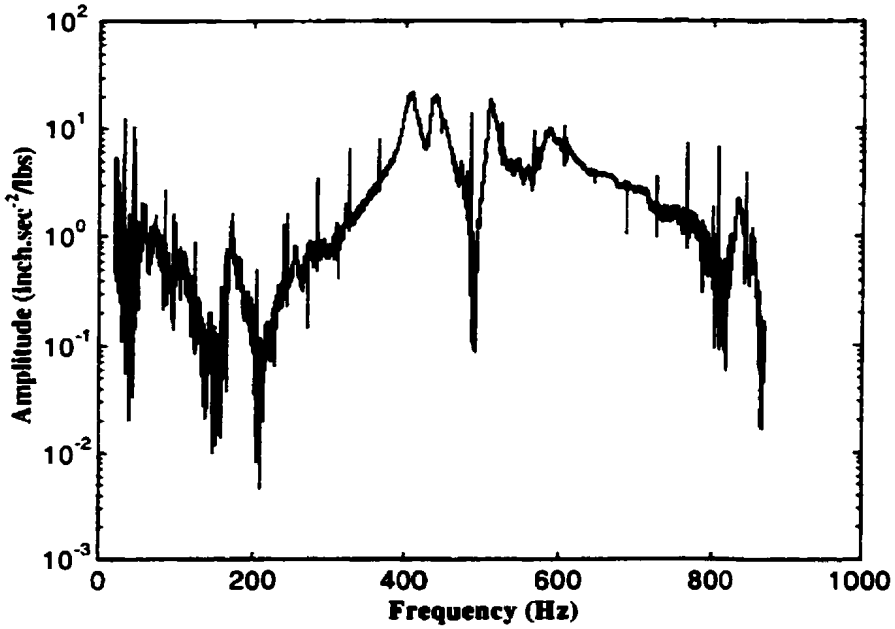

5.1.e: Experimental FRF at accelerometer #5

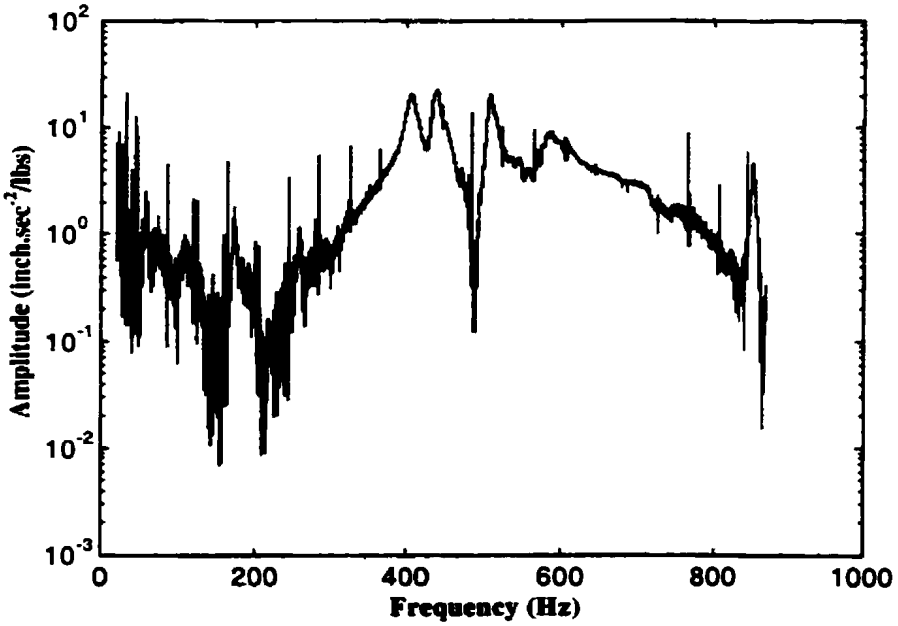

5.1.f: Experimental FRF at accelerometer #6

Figure 5.1: Experimental FRFs

Table 5.1: Comparison of Experimental Natural Frequencies and Damping Ratios of the Undamaged Model at Six Different Locations

No	Accelerometer #1		Accelerometer #2		Accelerometer #3		Accelerometer #4		Accelerometer #5		Accelerometer #6	
	Freq (Hz)	Damp. (%)	Freq (Hz)	Damp. (%)	Freq (Hz)	Damp. (%)	Freq (Hz)	Damp. (%)	Freq (Hz)	Damp. (%)	Freq (Hz)	Damp. (%)
1	50.31	1.710	50.63	1.690	50.25	0.589	50.00	0.482	49.94	1.060	50.38	0.461
2	113.31	0.214	113.13	0.185	-	-	-	-	-	-	-	-
3	310.71	0.101	310.69	0.093	309.50	0.041	310.31	0.112	310.44	0.080	310.44	0.088
4	409.19	0.865	409.50	0.930	407.13	0.963	406.69	1.150	410.06	1.430	406.88	1.480
5	525.31	0.028	525.31	0.044	-	-	-	-	-	-	-	-
6	569.38	0.181	569.94	0.185	569.88	0.245	569.13	0.245	569.94	0.182	569.56	0.226
7	741.56	0.290	742.19	0.256	744.56	0.263	745.31	0.321	-	-	-	-
8	854.38	0.214	853.56	0.225	854.25	0.225	854.19	0.197	854.19	0.186	852.67	0.227

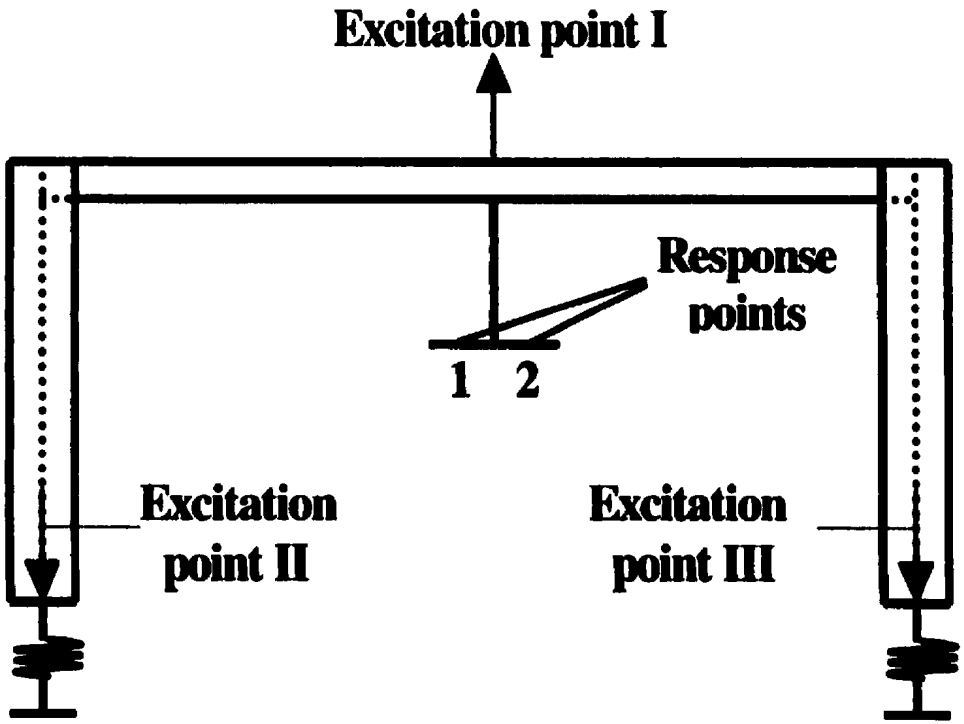

Figure 5.2: Combination of Three Single-Input Single-Output (SISO) Test Procedures

In order to compare between the FRF obtained using the FE model and the experimental FRF, we needed to modify the FE element model to take into consideration the boundary conditions resulting from the flexibility of tank bottom. For that reason, three excitations were applied to the FE models at the locations designated I, II, and III in Figure 5.2. The numerical FRF was obtained by summing up the FRFs obtained using these three excitations, see Figures 5.3.a - 5.3.c. This addition did not take into account the influence of the phase of the FRF obtained for the three-excitation at locations I, II and III. Similar to the experimental FRF, the highest peak of the numerical FRF also occurred at the fourth mode. This means that the fourth mode is the predominant natural frequency

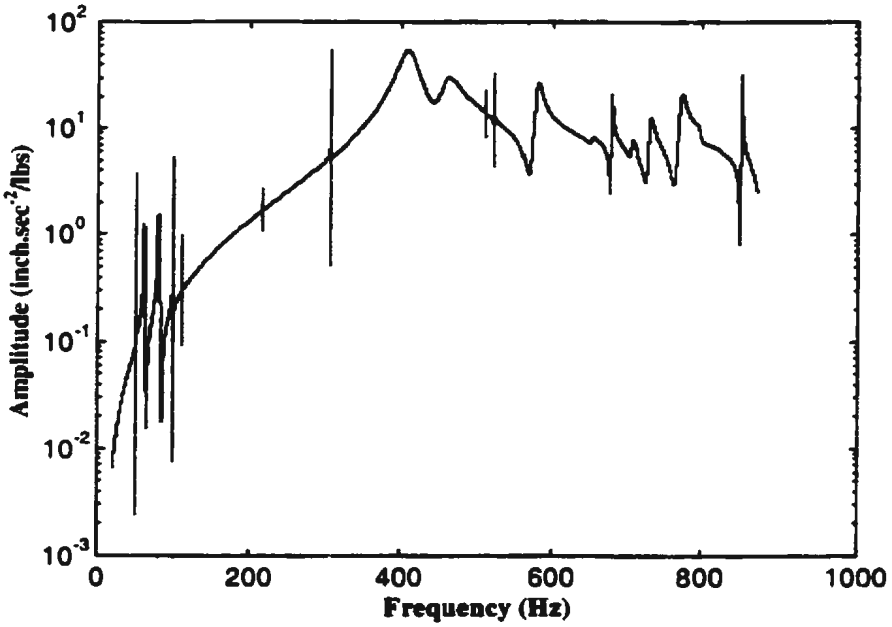

5.3.a: Numerical FRF due to excitation at location I

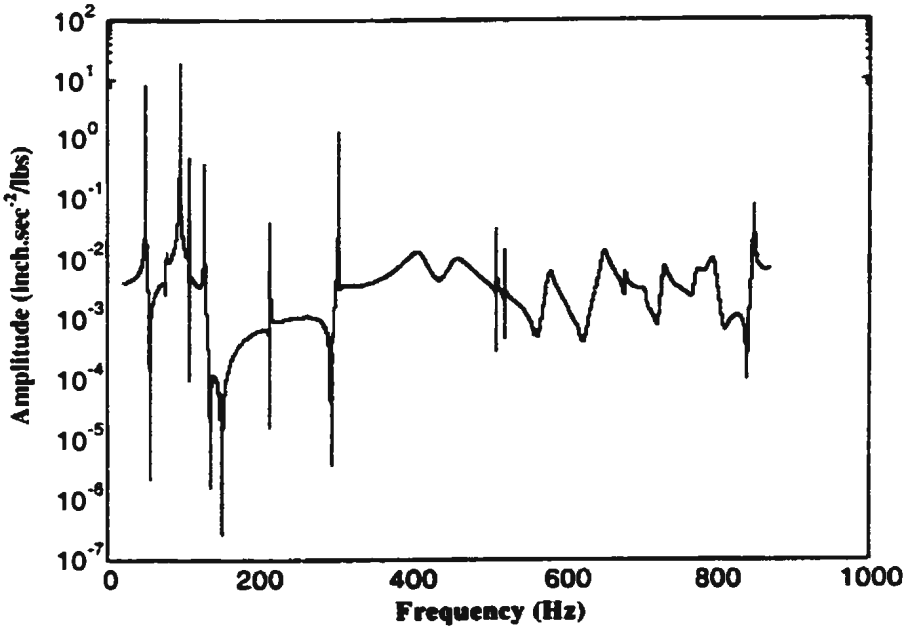

5.3.b: Numerical FRF due to excitation at location II

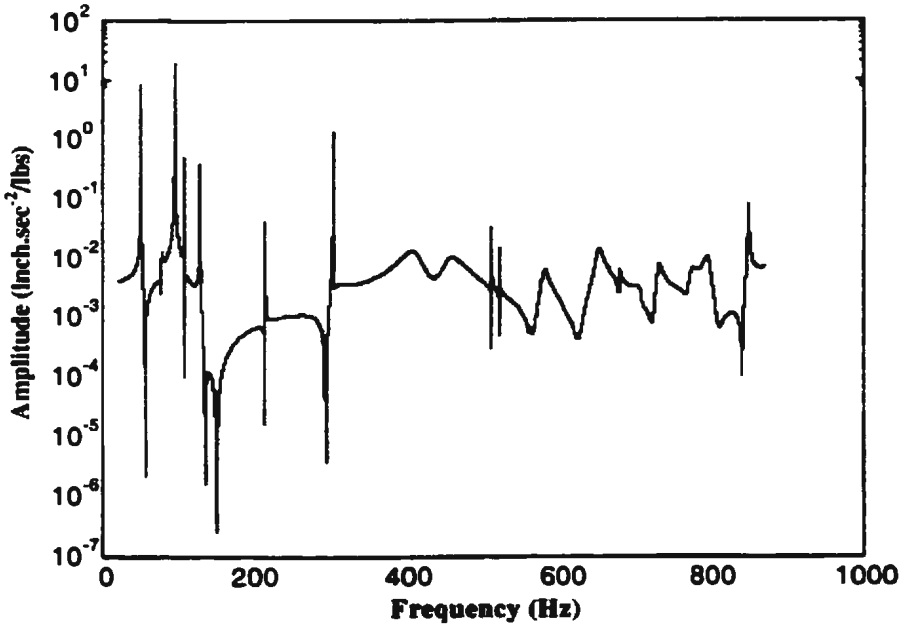

5.3.c: Numerical FRF due to excitation at location III

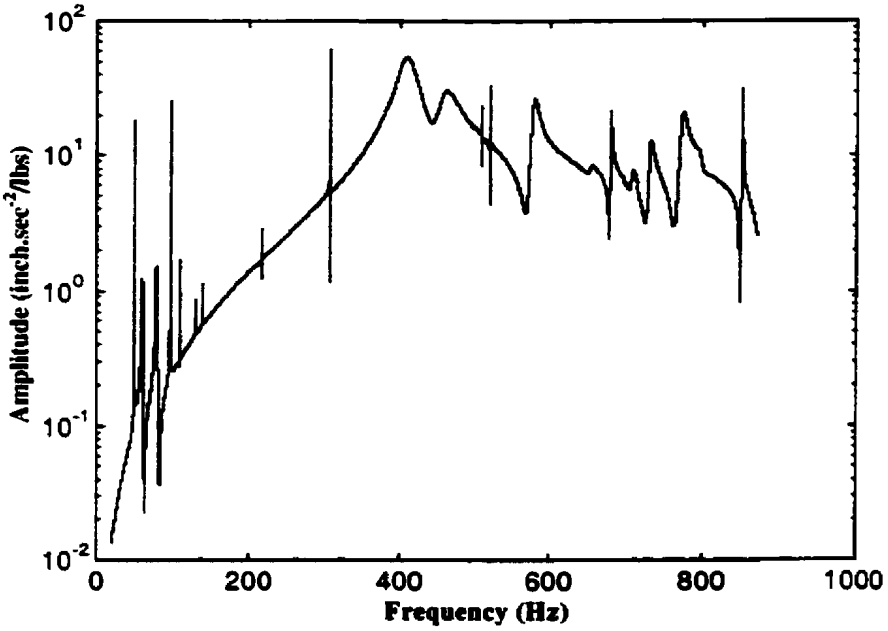

5.3.d: Numerical FRF due to excitations at location I, II, and III

Figure 5.3: Numerical FRFs

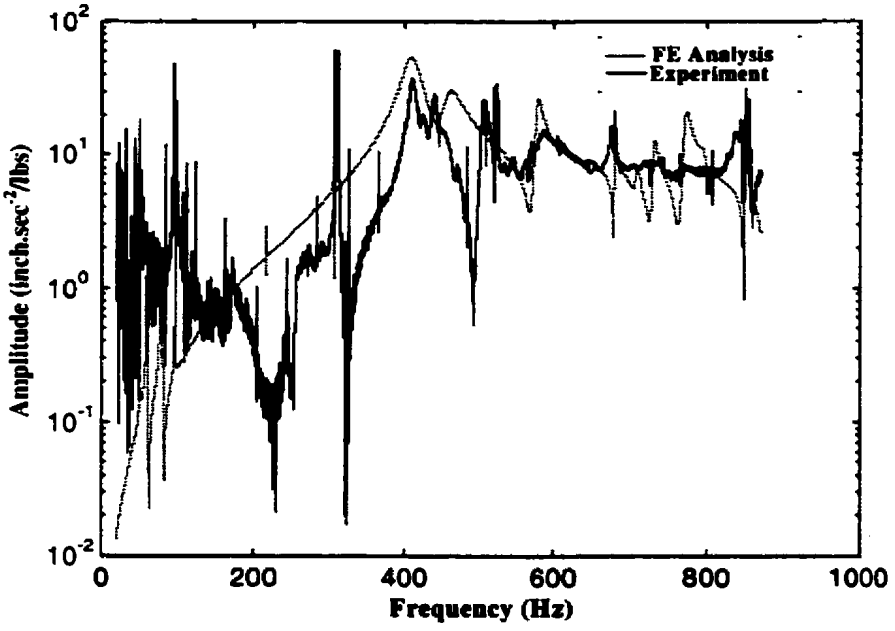

Figure 5.4: Comparison between Experimental and Numerical FRFs

Table 5.2: Comparison between Experimental and Numerical Natural Frequency and Damping Ratio of the Undamaged Stiffened Plate Model

No	Numerical Analysis		Experiment		Error between Analysis and Experiment (Hz)
	Frequency (Hz)	Damping (%)	Frequency (Hz)	Damping (%)	
1	50.95	0.005	50.63	1.690	0.32
2	110.66	0.005	113.13	0.185	-2.47
3	307.19	0.005	310.69	0.093	-3.50
4	412.31	3.00	409.50	0.930	2.81
5	521.66	0.005	525.31	0.044	-3.65
6	566.71	0.700	569.94	0.185	-3.23
7	748.33	0.400	742.19	0.256	6.14
8	860.15	0.040	853.56	0.225	6.59

Figure 5.4 shows a comparison between acceleration FRF obtained experimentally and numerically. The values of the experimental and numerical natural frequencies are listed in Table 5.2. Figure 5.4 and Table 5.2 indicate that the numerical FRF is in good agreement with the experimental one for all modes. The difference in the damping ratio is mainly due to the fact that the exciting force used in the experiment was different from that used in the analysis. The experiment used a sine sweep force, whereas the FE analysis used an impulse force.

In order to get the best results for the FRFs and coherence, the sine sweep force was swept through a certain smaller, predefined frequency range in which the FRF magnitude was

well defined; whereas the impulse force was swept through the whole frequency range. An antiresonant region was observed in the experimental FRF around 200.00 - 240.00 Hz, which could not be obtained from the numerical model. To match the amplitude and modulus of the experimental and numerical FRFs, the damping ratios were adjusted.

In order to get a better understanding of the model's behavior for each mode, the associated mode shapes are shown in Figures 5.5.a – 5.5.h. These figures show that the first mode is a bending mode in which the vibration of the heavy transverse member is dominant. The second mode is a torsional mode of the heavy transverse member, and the third mode is the second bending mode of the heavy transverse member. The fourth mode is the bending mode for the side shell and the longitudinal.

Furthermore, the fifth mode is a coupled mode with the left support vibration being dominant, and the sixth mode is a coupled mode with the right support being dominant. The seventh mode is a coupled mode of the right support and the longitudinal, whereas the eighth mode is a coupled bending and torsional mode of the side shell and the heavy transverse member. From Figures 5.4, 5.5, and Table 5.2, it is clear that the fourth mode is the mode with the most dominant natural frequency. Based on the above results, it can be concluded that the FE analysis accurately modeled the undamaged stiffened plate; hence, it was used to predict the free vibration response of the undamaged stiffened plate model and its natural frequency using the combination of the three SISO.

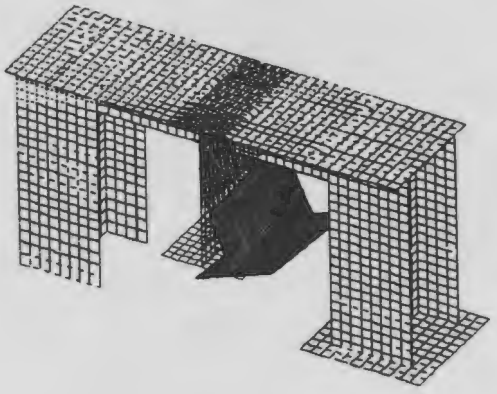

5.5.a: Mode 1 (50.95 Hz)

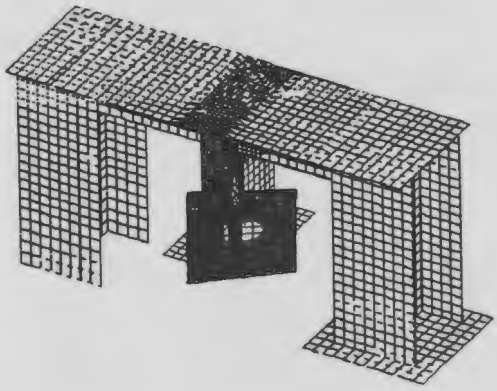

5.5.b: Mode 2 (110.66 Hz)

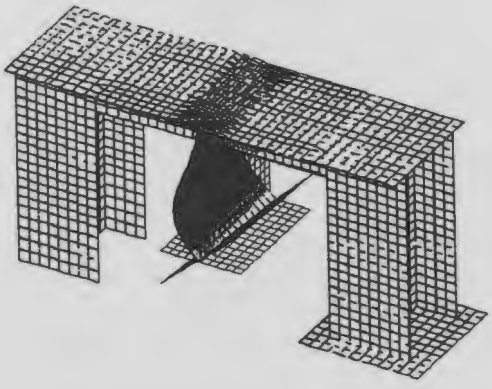

5.5.c: Mode 3 (307.19 Hz)

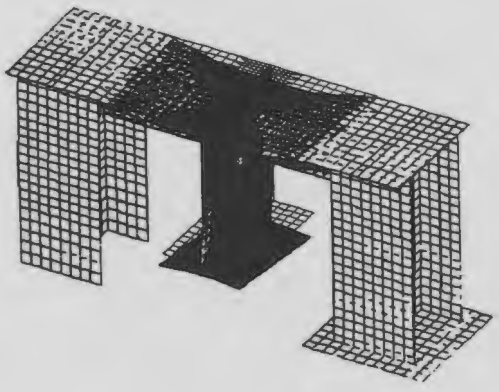

5.5.d: Mode 4 (412.31 Hz)

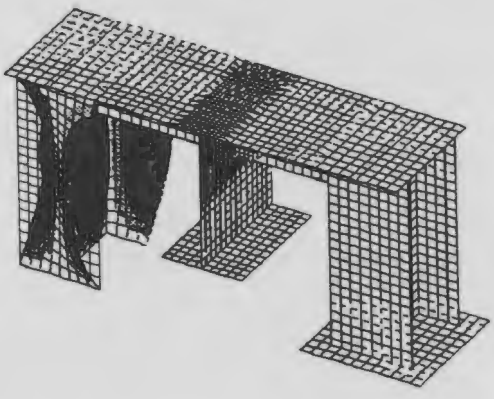

5.5.e: Mode 5 (521.66 Hz)

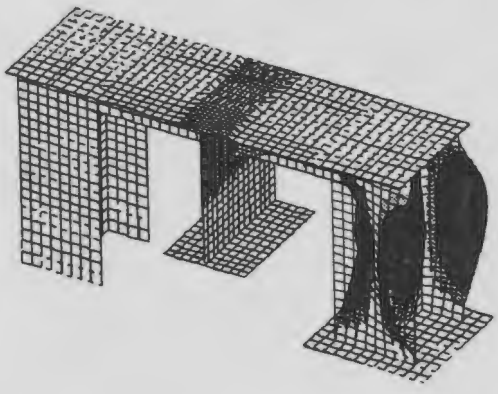

5.5.f: Mode 6 (566.71 Hz)

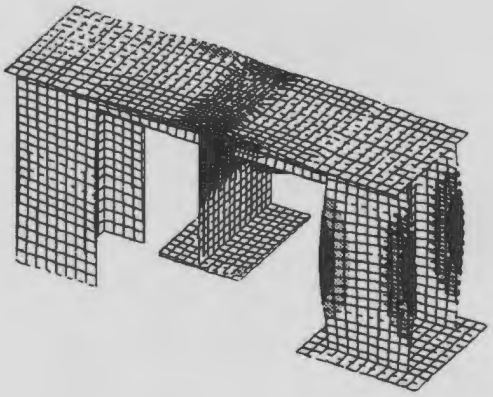

5.5.g: Mode 7 (748.33 Hz)

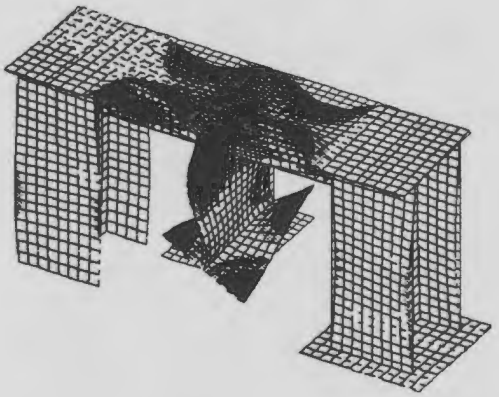

5.5.h: Mode 8 (860.15 Hz)

Figure 5.5: Dominant Mode Shapes of the Undamaged Model

5.2.2 Free Vibration Responses and Randomdec Signatures

Numerical free vibration responses due to excitations at locations I, II, and III are shown in Figures 5.6.a, b and c, respectively. These figures indicate that the free vibration response due to excitation at location I is similar to that due to excitation at location III but is completely different from that due to excitation at location II. However, the magnitude of the free vibration response due to excitation at locations III is much lower than that due to excitation at location I. The reason is that the free vibration responses represent the vibration response for the fourth mode of the model, in which the vibration of the longitudinal and the heavy transverse member was dominant, and the vibration of the left and right supports was not dominant (see Figures 5.4 and 5.5).

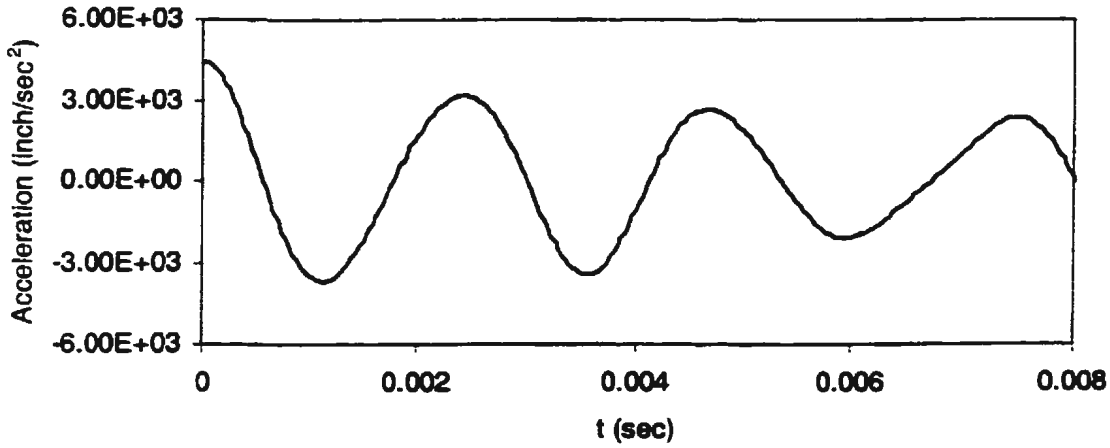

5.6.a: Numerical Free Vibration Response due to Excitation I

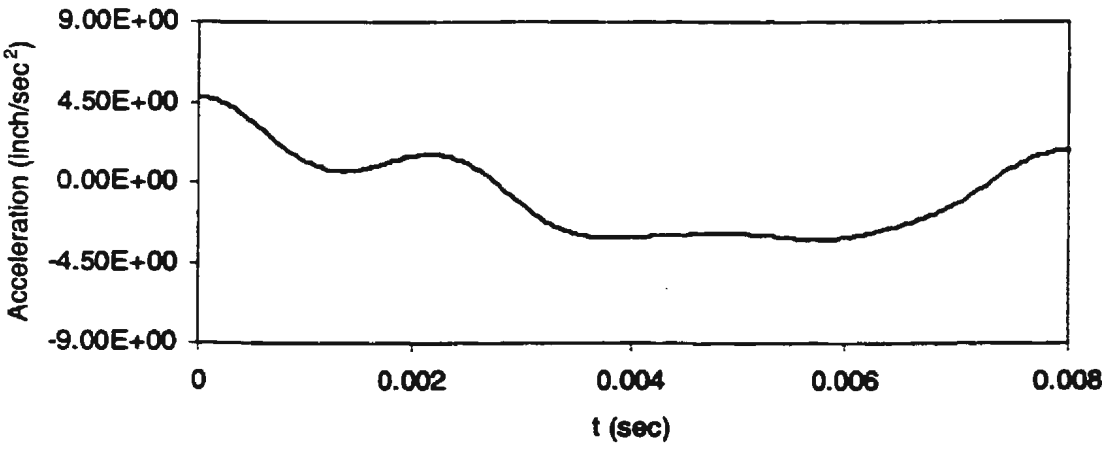

5.6.b: Numerical Free Vibration Response due to Excitation II

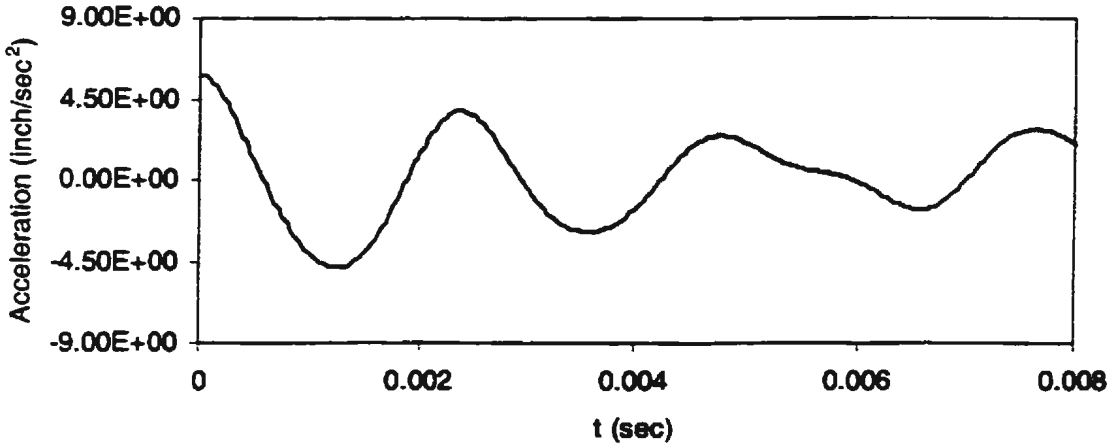

5.6.c: Numerical Free Vibration Response due to Excitation III

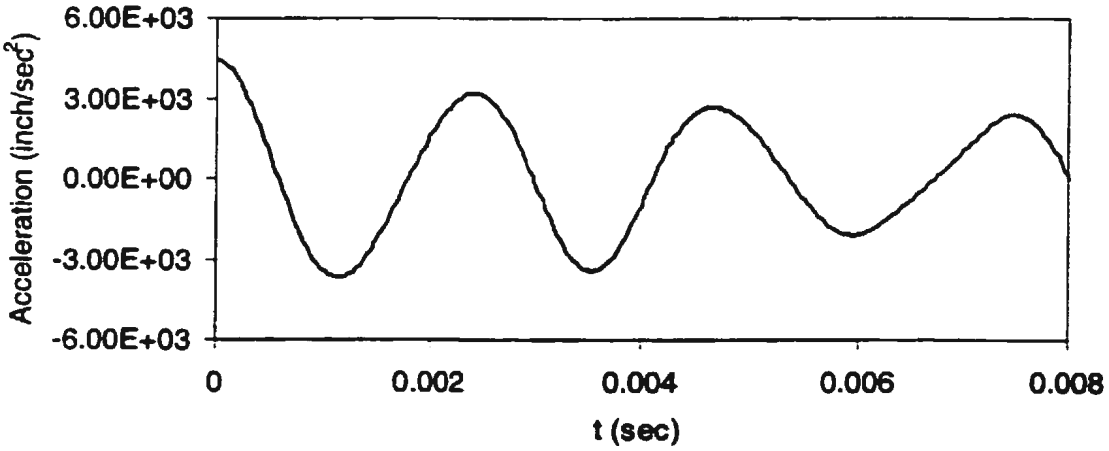

5.6.d: Numerical Free Vibration Response due to Excitations I, II, and III

Figure 5.6: Numerical Free Vibration Response

Figure 5.6.d shows the actual free vibration response for the stiffened plate model, which is the combination of the three free vibration responses obtained from the FE model. This response is similar to that shown in Figure 5.6.a. Since the contributions of the free vibration responses due to excitation at locations II and III are very small, they could be neglected while considering the numerical free vibration response of the model. The natural frequency obtained from Figure 5.6.a is 412.73 Hz. This frequency is slightly higher than that tabulated in Table 5.2, but this difference is within the experimental error. The numerical free vibration response is then used to verify the randomdec signature obtained from the experimental random response.

The experimental random response of the undamaged stiffened plate model was recorded from accelerometer #2, see Figure 5.7.a. The record was obtained over a period of 1.00 sec and contained 7000 data points. The response was filtered around the most dominant frequency using a wide-band filter, and the result is shown in Figure 5.7.b. The filtered response was then used to calculate the randomdec signature, Equation (3.3). The process of calculation is as follows:

The filtered response was divided into more than 700 overlapping segments, each having a length of 0.001 second, and starting with the same initial displacement. This gave 70 points per segment. The segments were summed up, and they yielded a record of the randomdec signature as shown in Figure 5.8. This figure indicates that the randomdec signature can be used to represent the free vibration response of the system with an initial displacement to the trigger level.

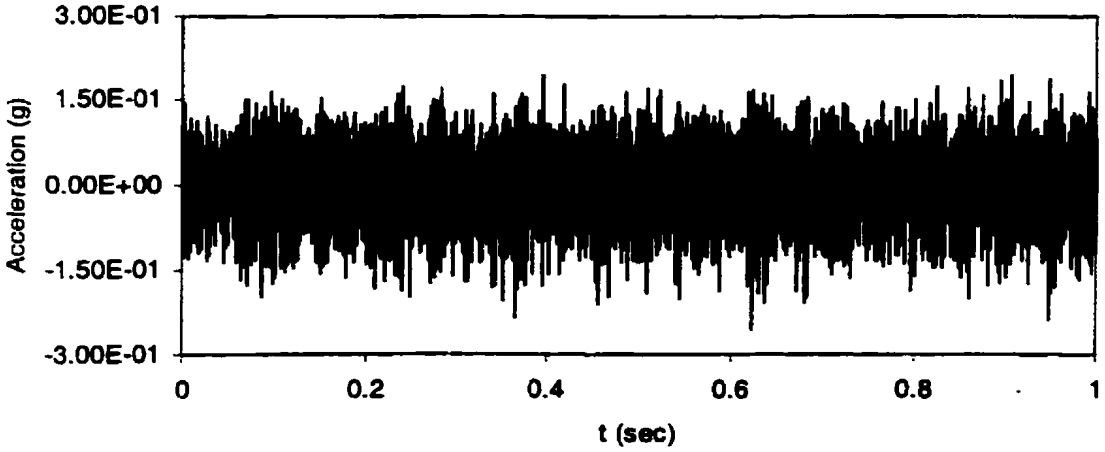

5.7.a: Before filtering

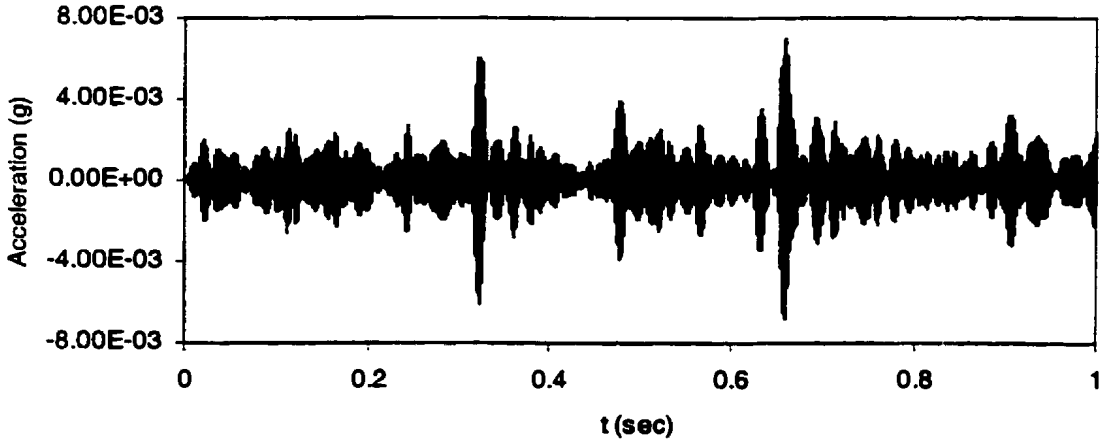

5.7.b: After filtering

Figure 5.7: The Random Response

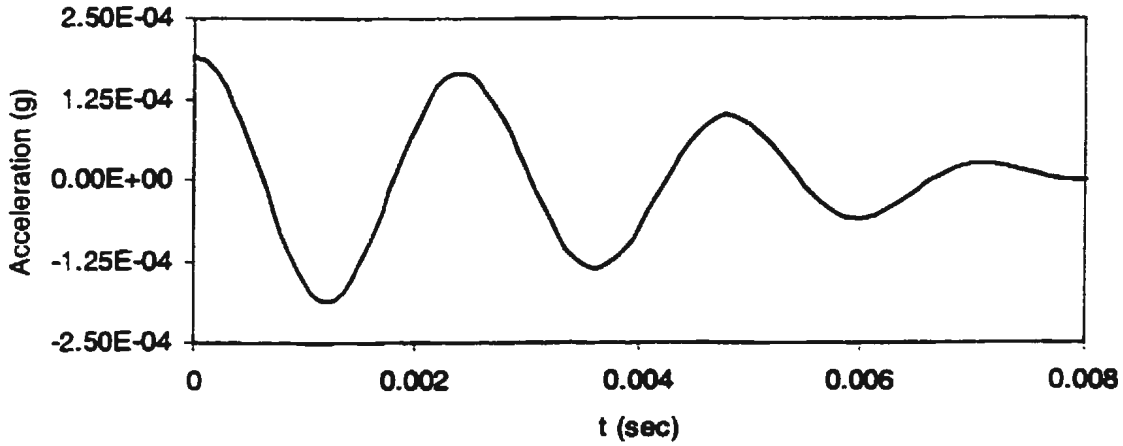

Figure 5.8: The Randomdec Signature

Figure 5.8 shows that the magnitude of the randomdec signature is very small and the natural frequency is very high. The cause is that, due to the limitation of laboratory facilities as mentioned in Chapter 4, only small part of the structure with limited dimensions could be modeled as the stiffened plate model. If the randomdec signature of the random response of a full scale model due to waves at sea is calculated, the magnitude of the randomdec signature is expected to be higher and the natural frequency is expected to be lower. The technique developed in this study will be still suitable for the analysis of this data.

The randomdec signature is then compared with the numerical free vibration response as shown in Figure 5.9. It can be observed from Figure 5.9 that the agreement between the numerical free vibration response and the experimental randomdec signature is excellent, especially for the first two cycles. The disagreement between the two records beyond the second cycle will not pose any problem, since the identification method used in

the present study does not require a long record of the response. One cycle of the response is used to identify the damage.

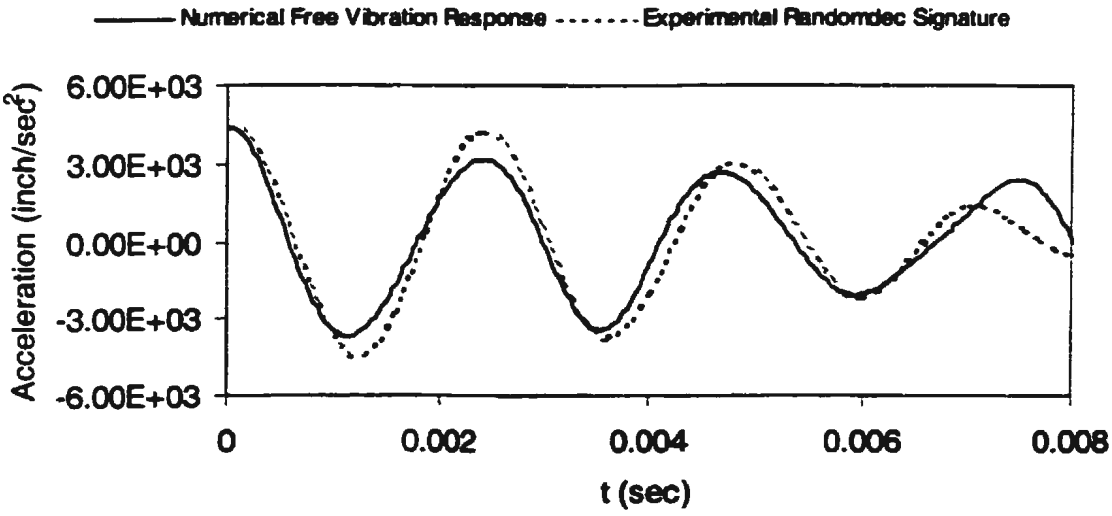

Figure 5.9: Comparison between Experimental Randomdec Signature and Numerical Free Vibration Response of Undamaged Model

Based on the above results, it can be concluded that FE analysis has accurately modeled the undamaged stiffened plate, and the numerical free vibration response can be used to verify the randomdec signature. Therefore, the model can be used to generate the dynamic behavior of the undamaged model at different conditions. The model is then used to determine the FRFs and the free vibration responses of the stiffened plate model with several damage lengths.

5.3 Effect of Damage

In order to examine the acceleration FRFs, the free vibration response, and the randomdec signature of the stiffened plate Model #1 for damaged conditions, the damage was simulated, in both the experimental and numerical studies. Experimentally, saw cuts were made in the stiffened plate for modeling the damage. Numerically, the damage in the structure was modeled by introducing a gap of 0.01 inch between certain identified elements of longitudinal's faceplate. The gap represents the thickness of the hacksaw blade used in the experiment.

5.3.1 Frequency Response Function (FRF)

The experimental and numerical acceleration FRFs for the damaged stiffened plate model with crack lengths of 0.40 inch, 0.80 inch, and 1.20 inch are drawn together in Figure 5.10.a - 5.10.d, respectively. The comparison between the dominant experimental and numerical frequencies of the damaged model along with the undamaged one is listed in Table 5.3.

As observed from Figures 5.10.a - 5.10.c and Table 5.3, the numerical acceleration FRFs are in good agreement with the experimental ones. Table 5.3 indicates that detectable changes in the frequency, due to the presence of damage, start to occur in the frequency of the fourth mode. This result was observed for the experimental as well as the numerical data. The frequency of this mode decreases as the crack length increases. This is due to the fact that the fourth mode is a bending mode with dominant vibration of the side shell and the

longitudinal in which the crack is located, see Figure 5.5.d. For the other modes, shown in Figures 5.5.a , b, c, e, f, g, and h, respectively, the longitudinal and the side shell vibrations are not dominant; consequently the changes due to the presence of damage are marginal.

Although, Figures 5.5.a – 5.5.h show dominant mode shapes of the undamaged stiffened plate model, they can also be considered as the mode shapes of the damaged stiffened plate model. The reason is that the cracks to be identified in the present study are limited to a length of 1.20 inch; therefore, the damage did not influence the mode shapes much. It has only affected the frequencies.

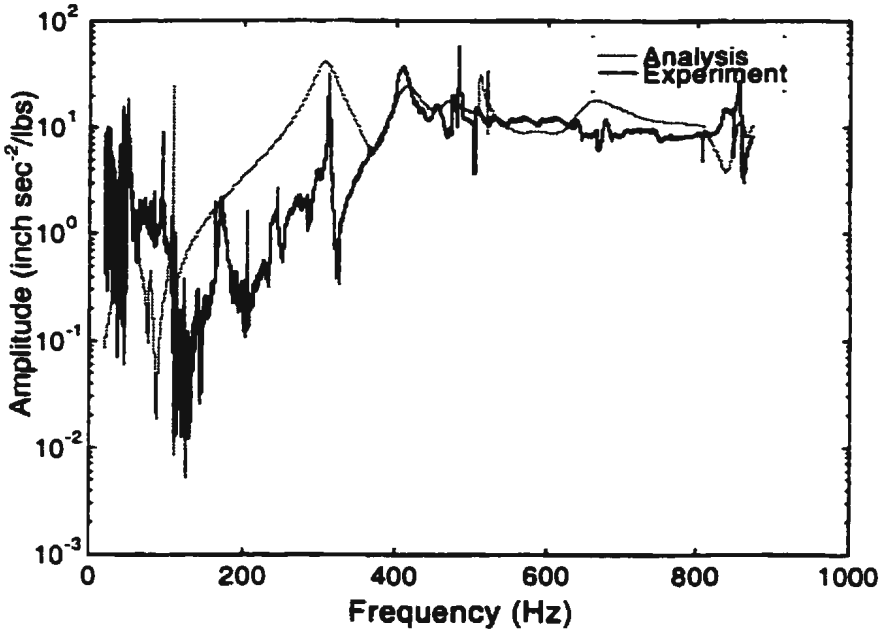

5.10.a: Crack length = 0.40 inch

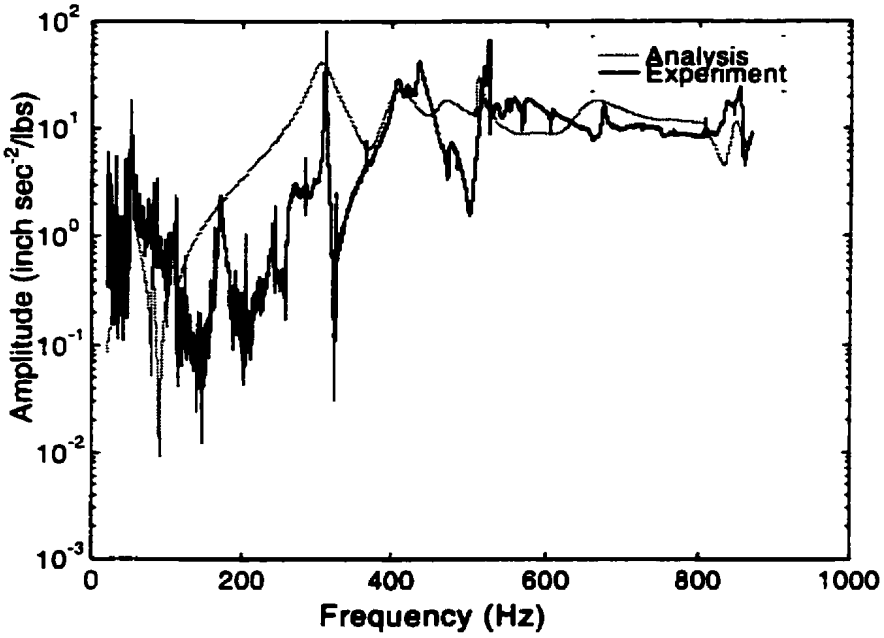

5.10.b: Crack length = 0.80 inch

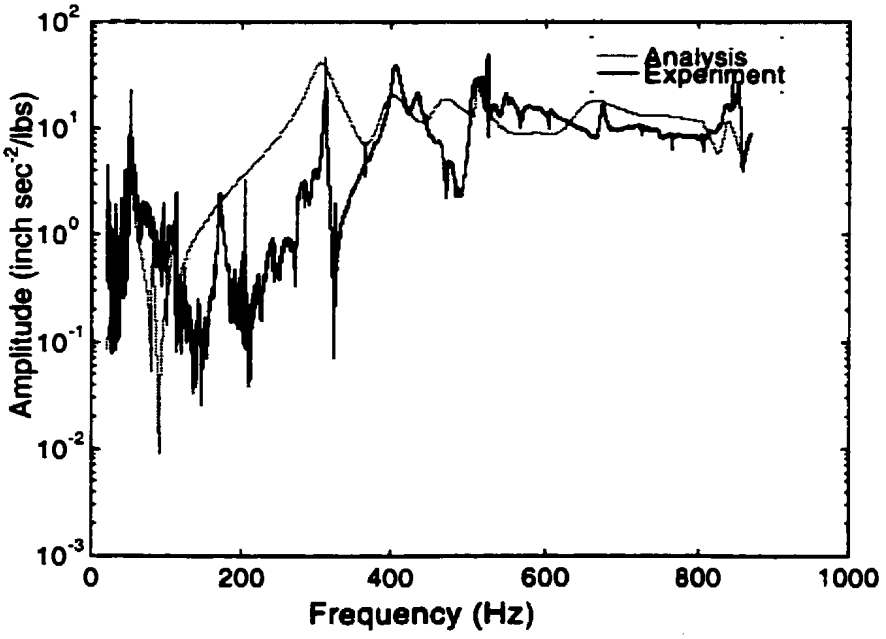

5.10.c: Crack length = 1.20 inch

Figure 5.10: Comparison between Experimental and Numerical Acceleration FRFs

Table 5.3: Comparison of Experimental and Numerical Dominant Natural Frequencies (Hz)

No	Damage with length of							
	0.00 inch		0.40 inch		0.80 inch		1.20 inch	
	Exp.	Num.	Exp.	Num.	Exp.	Num.	Exp.	Num.
1	50.63	50.95	50.19	50.95	50.56	50.95	50.25	50.94
2	113.13	110.66	113.13	110.66	113.31	110.66	113.19	110.66
3	310.69	307.19	311.50	307.19	311.38	307.18	311.94	307.17
4	409.50	412.31	408.56	410.96	406.81	406.80	406.06	399.76
5	525.31	521.66	525.38	521.60	525.50	521.60	525.50	521.60
6	569.94	566.71	568.87	566.71	-	566.71	-	566.71
7	742.19	748.33	741.94	748.11	-	747.38	-	745.59
8	853.56	860.15	853.81	859.25	853.25	859.25	853.69	858.05

Note: Exp. = Experiment; Num. = Numerical

From the above results, it can be concluded that the FE analysis has also accurately modeled the damaged stiffened plate. Hence, it could be used to characterize the damaged behavior of the stiffened plate Model #1. The model was then used to generate the free vibration responses of the damaged stiffened plate model.

5.3.2 Free Vibration Responses and Randomdec Signatures

Figures.5.11.a – 5.11.c show a comparison between experimental randomdec signatures and numerical free vibration responses for the damaged model with crack lengths of 0.40 inch, 0.80 inch, and 1.20 inch, respectively. A comparison of the experimental and the numerical frequencies obtained from Figure 5.9 for the undamaged condition and Figures. 5.11.a - 5.11.c for damaged conditions is given in Table 5.4 and plotted in Figure 5.12, respectively. Like the undamaged model, the signatures of the damaged model shown in Figures 5.11.a - 5.11.c also represent the randomdec signatures and the free vibration responses of the fourth mode.

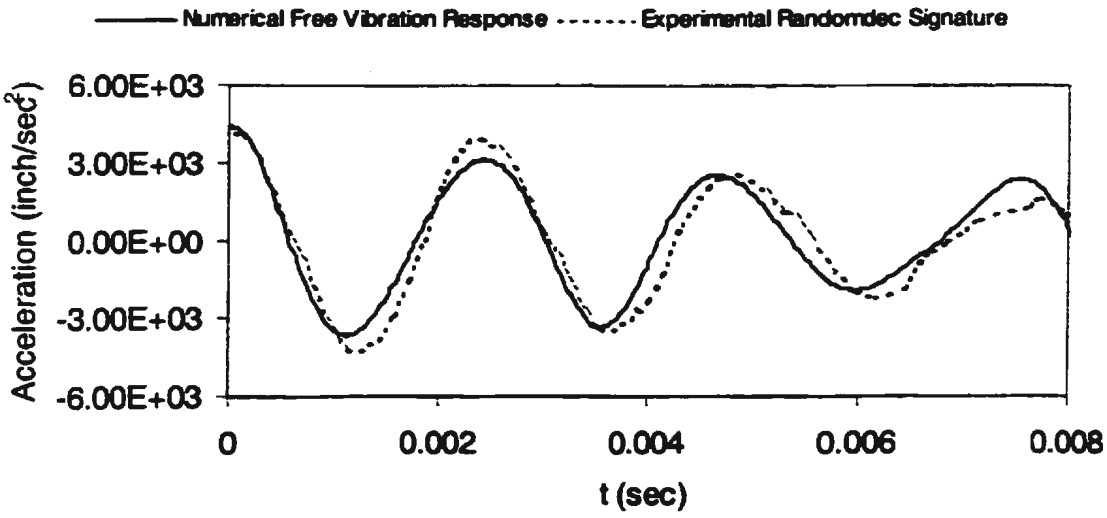

5.11.a: Crack length = 0.40 inch

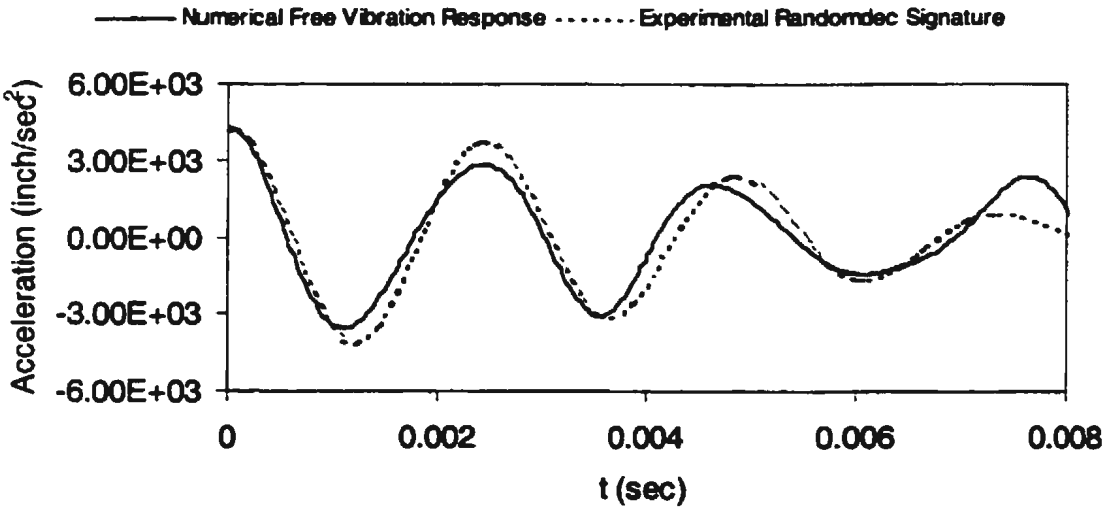

5.11.b: Crack length = 0.80 inch

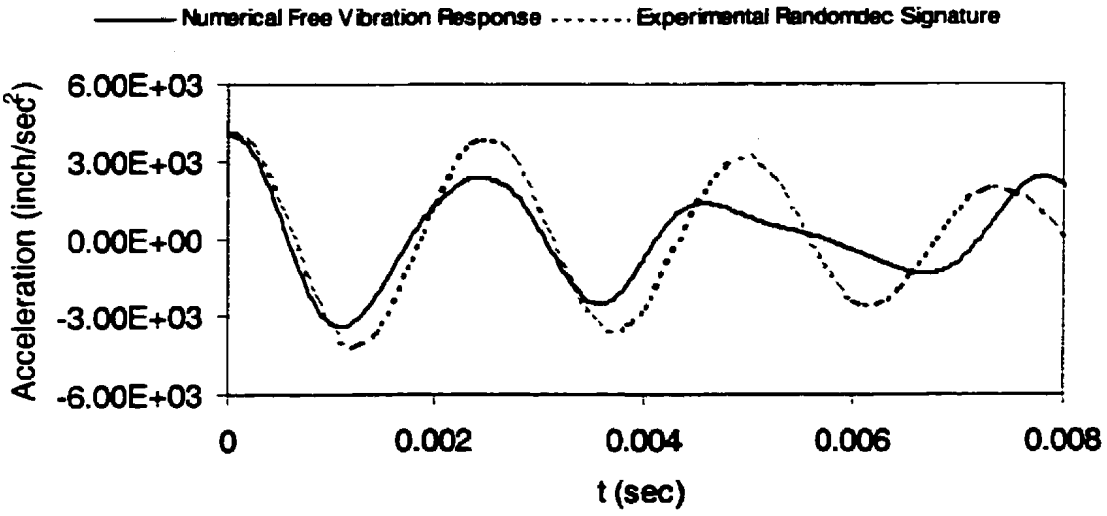

5.11.c: Crack length = 1.20 inch

Figure 5.11: Comparison between Experimental Randomdec Signatures and Numerical Free Vibration Responses (Model #1 in Air)

Table 5.4: Comparison between Natural Frequencies obtained from Experimental Randomdec Signatures and Numerical Free Vibration Responses (Hz)

Crack Length (inches)	Experimental Randomdec Signature	Numerical Free Vibration Response
0.00	412.73	412.62
0.40	411.59	411.55
0.80	408.66	408.53
1.20	404.66	404.53

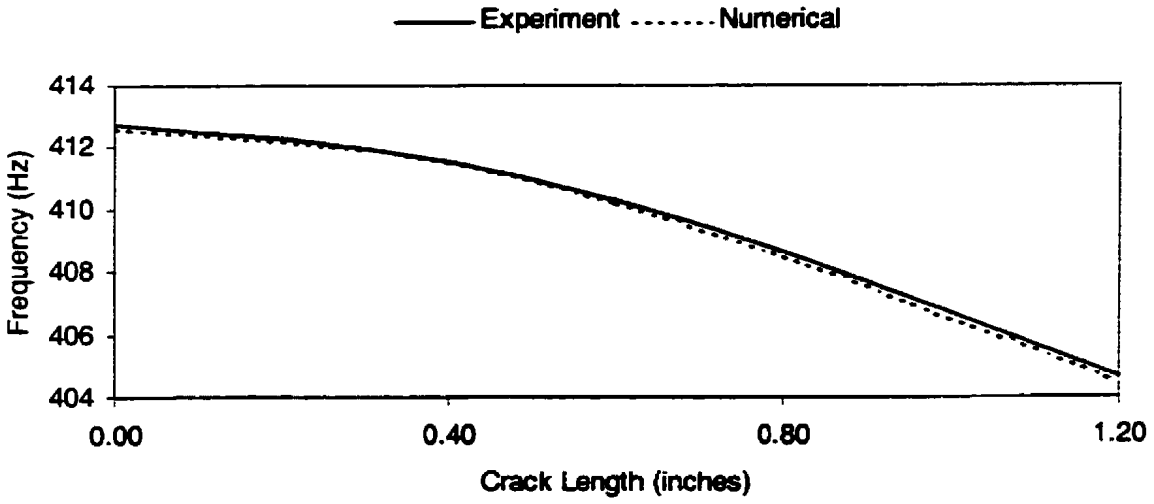

Figure 5.12: Comparison of Experimental Randomdec Signatures and Numerical Free Vibration Responses Natural Frequencies of Model #1 in Air

It can be observed from Figures 5.11.a – 5.11.c, and Table 5.4 that at least the first cycle of the experimental randomdec signatures matches closely the numerical free vibration response. As mentioned before, the identification technique uses only the first cycle. Furthermore, Figure 5.12 and Table 5.4 indicate that the frequency of the damaged model with crack length of 0.40 inch is almost the same as the undamaged one. It is also clear that the frequency decreases as the crack length increases. When compared with the frequencies in Table 5.2, the frequencies shown in Table 5.4 are slightly different, for both the experimental and the numerical ones. Frequencies in Table 5.2 were obtained from the experimental and the numerical FRFs; therefore, the results represent the actual frequency of Model #1. Frequencies shown in Table 5.4 were obtained from Figures 5.9 and 5.11. The random responses used for the randomdec signatures were filtered using a wide-band filter.

Therefore, they might contain more than one frequency, i.e., one was the predominant frequency and the others were the higher and / or the lower frequencies. The higher or the lower frequencies might affect the measured frequency. This problem also occurred for the free vibration responses that were not filtered. Nevertheless, these differences are within the allowable experimental errors.

Moreover, the higher amplitudes of the acceleration responses shown in Figures 5.11 are those of the numerical acceleration free vibration responses; this was obtained using the unit impulse response of the structure through the FE analysis. In fact, the actual magnitudes of the experimental acceleration randomdec signatures were much lower than the numerical ones, see Figure 5.8. This is due to the fact that the actual force applied to the stiffened plate model through the function/noise generator was very small. Since, the experimental acceleration randomdec signatures were verified using the numerical free vibration responses, their magnitudes were scaled up so that they have the same starting point magnitudes as the numerical ones.

From the above results, it can be concluded that the randomdec technique and the FE analysis could be used to identify the dynamic behavior of Model #1 for both the undamaged and damaged conditions. In order to ensure that these methods would give the accurate and complete results of the damage in the stiffened plate model in the process of damage identification, they were used again to identify the damage in other models, viz., Models #2, #3, and #4, which have similar dimensions and characteristics as Model #1. Since the results were similar, they are presented and discussed in Appendix D.

5.4 Summary

Application of the randomdec technique and the FE analysis in the identification of damage in the stiffened plate models in air and water have been investigated experimentally and numerically. The effects of the crack length and location and added water mass on the randomdec signatures, the free vibration responses and frequencies were analyzed. The randomdec signatures were able to identify the damage occurrence along with its extent and location and the presence of water by changing their signatures and frequencies. The FE analysis was also successful in modeling the stiffened plate so that the frequencies and the free vibration responses in air and water could be obtained.

The results obtained using randomdec signature and free vibration responses indicated that the signatures and responses for all cases have similar shapes, especially for the first cycle. Also, the change in frequencies due to the presence of damage was very small. In the field, this may cause the detection of small cracks in a structure to be a difficult task using the randomdec technique or the FE model. In order that the damage occurrence could be detected in its earliest stage of development, the random responses as well as the FE model used in this Chapter are analyzed using another method called the auto- and cross-correlation function approach in the next Chapter. The randomdec signatures obtained in this Chapter are used for verifying the results.

Chapter 6

Use of Auto- and Cross-correlation Functions for Damage Detection

6.1 Introduction

The dynamic response of the undamaged and damaged models are identified using another form of the vibration response: the auto and cross-correlation functions. The advantage of using the auto and cross-correlation functions is that they can be easily obtained from the stationary random responses of the structure using statistical methods. In the present study, the experimental and numerical auto and cross-correlation functions obtained for Model #1 in air are calculated and analyzed.

6.2 Autocorrelation Functions

6.2.1 Experimental Data

The experimental randomdec signatures and autocorrelation functions for the undamaged stiffened plate model, as well as the damaged model with different crack lengths, are compared, and the results are shown in Figures 6.1.a – 6.1.d. As can be observed from Figures 6.1.a – 6.1.d, the experimental autocorrelation functions match the experimental randomdec signatures closely. Figures 6.1.a – 6.1.d also indicate that only the first two cycles in randomdec signatures may be reliable. After the first two cycles the transient solution that is assumed to be represented by the randomdec signature decays and noise will predominate. However, these differences should not affect the results, since only the first cycle is used in the method of analysis adopted in the present study.

Table 6.1 shows the magnitudes obtained for the frequency of the predominant mode, i.e., the fourth mode. It can be seen from Table 6.1 that the frequencies obtained from the experimental autocorrelation functions are in good agreement with those obtained from the experimental randomdec signatures. Table 6.1 also indicates that the frequency of the damaged model with a crack length of 0.40 inch is very close to the undamaged one. It is also clear that the frequency decreases as the crack length increases.

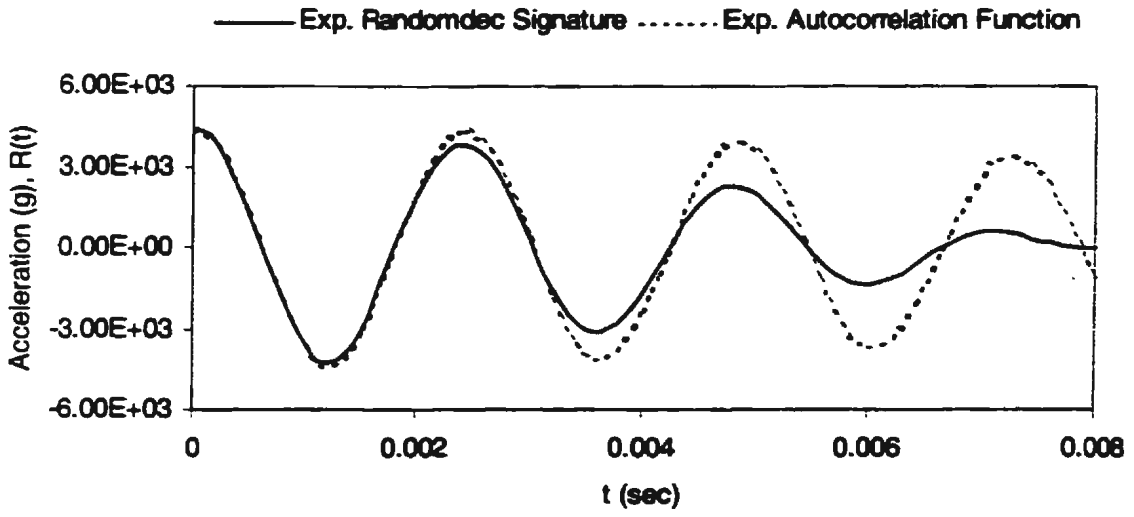

6.1.a: Undamaged

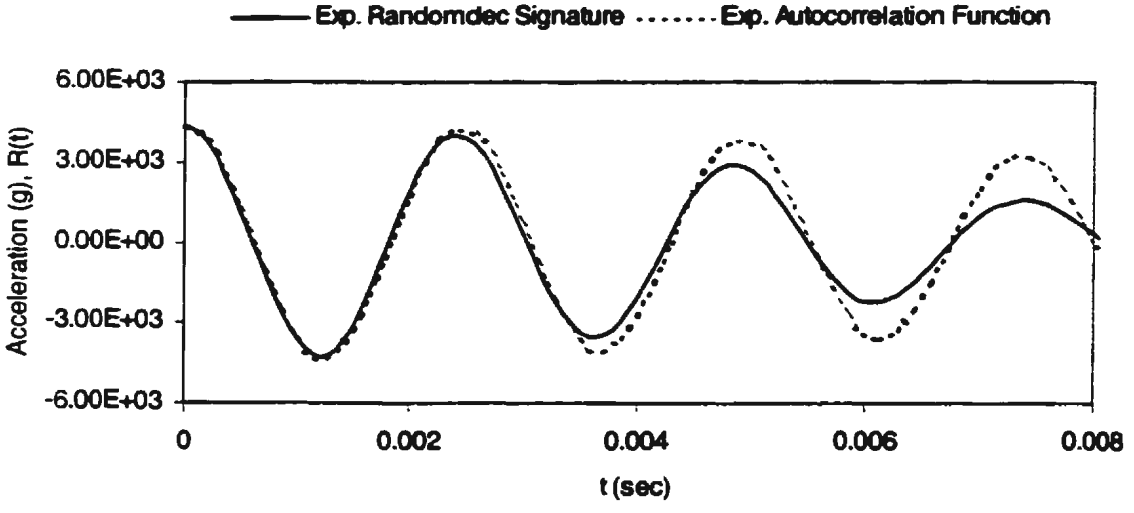

6.1.b: Crack length = 0.40 inch

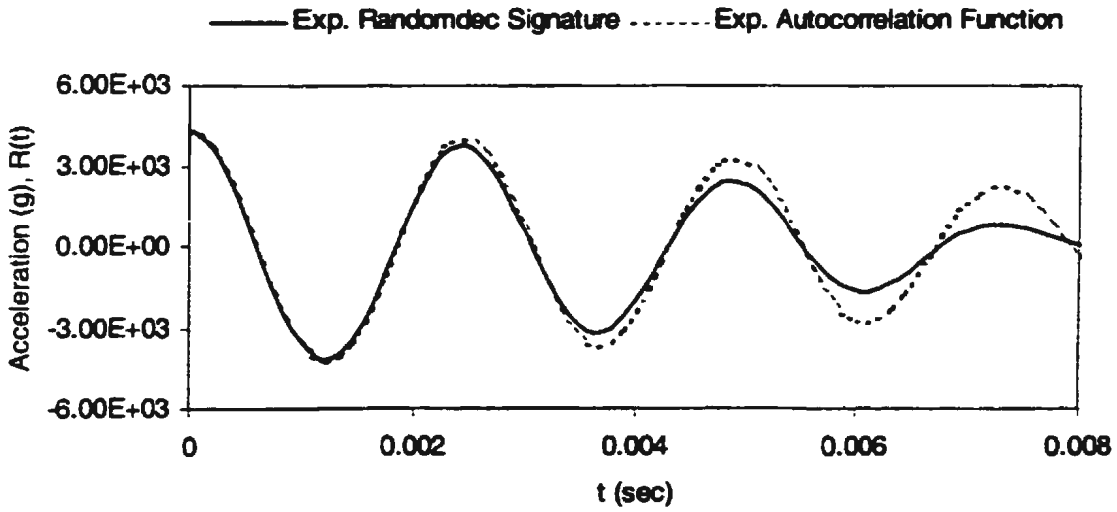

6.1.c: Crack length = 0.80 inch

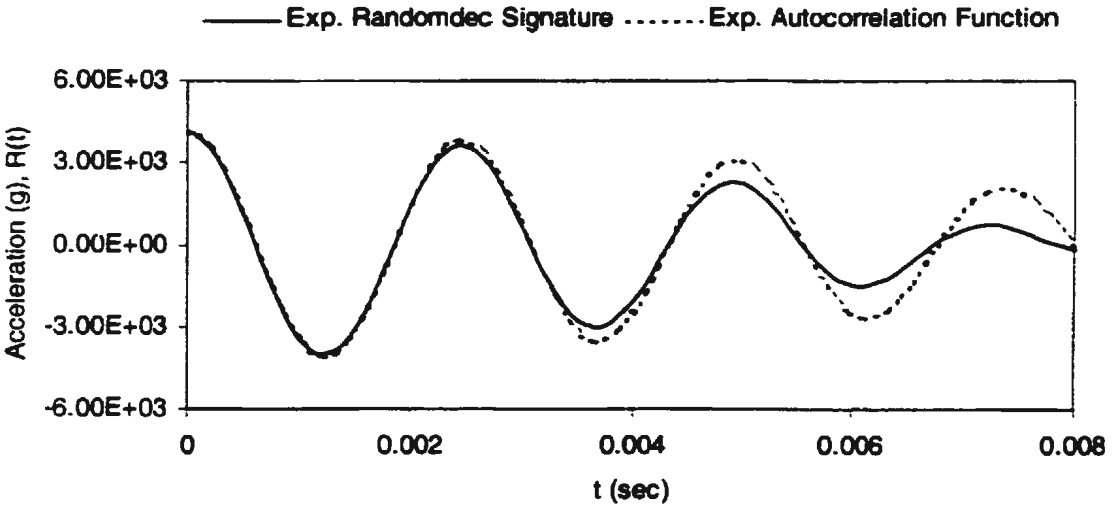

6.1.d: Crack length = 1.20 inch

Figure 6.1: Comparison between Experimental Randomdec Signatures and Autocorrelation Functions

Table 6.1: Comparison of Experimental Randomdec Signature and Autocorrelation Function Frequency (Hz)

No	Undamaged		Crack length of					
			0.40 inch		0.80 inch		1.20 inch	
	RS	ACT	RS	ACT	RS	ACT	RS	ACT
1	412.73	412.96	411.59	411.11	408.66	407.79	404.66	404.98

Note: RS = Randomdec Signature, ACT = Autocorrelation Function

A study of the sensitivity of the autocorrelation function to the crack length has also been carried out. The experimental autocorrelation functions obtained for the undamaged condition and for the crack conditions shown in Figures 6.1 are plotted again in Figure 6.2. It can be seen from Figure 6.2 that the autocorrelation functions have a similar behavior for the undamaged and damaged conditions. However, the crest and the trough of the first two cycles steadily shift to the right side when the crack becomes longer. This shifting causes the frequency to decrease as the crack length increases.

The above results indicate that the experimental autocorrelation functions can be used to represent the randomdec signatures and characterize the undamaged and the damaged responses of Model #1. This means that the experimental autocorrelation functions can also be used to represent the free vibration response. Hence, it can be used for verifying the numerical autocorrelation functions.

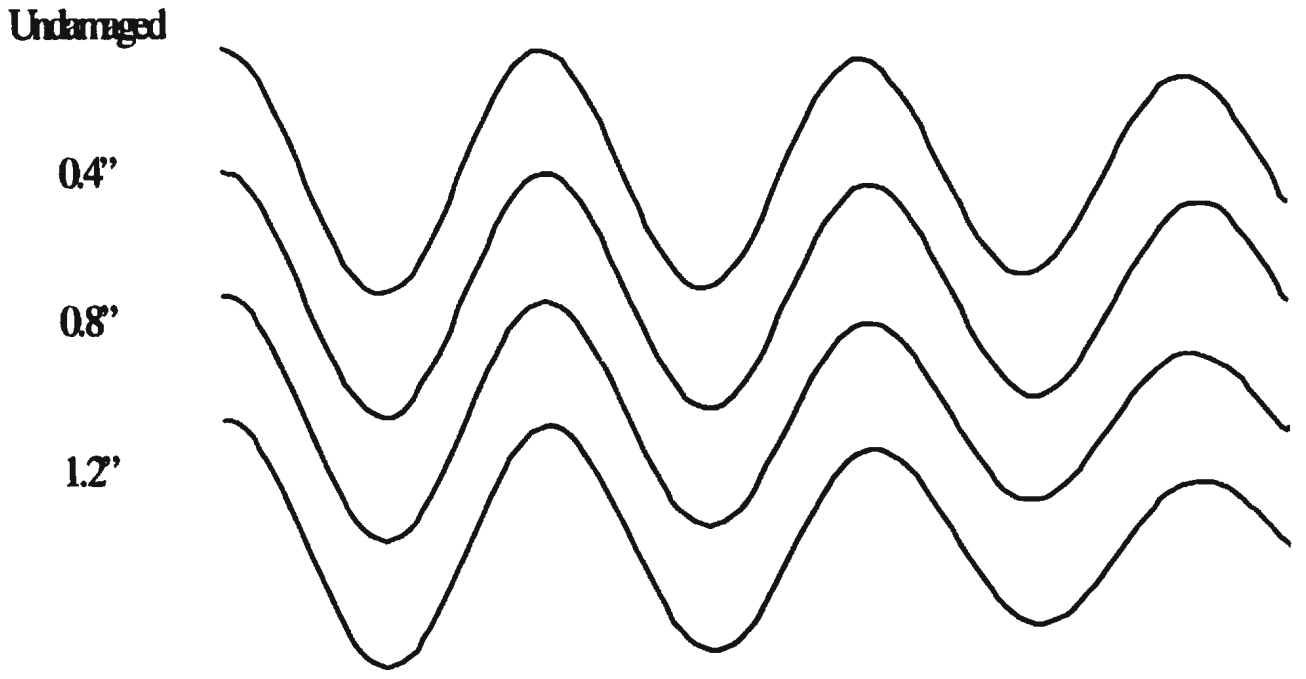

Figure 6.2: Comparison of the Experimental Autocorrelation Functions

6.2.2 Numerically Generated Data

Figure 6.3.a shows the comparison of experimental and numerical autocorrelation functions for the undamaged condition. Figures 6.3.b – 6.3.d show the comparison for the damaged conditions with crack lengths of 0.40 inch, 0.80 inch, and 1.20 inch, respectively. The frequencies for the fourth mode of the undamaged model along with the damaged model are shown in Table 5.6.

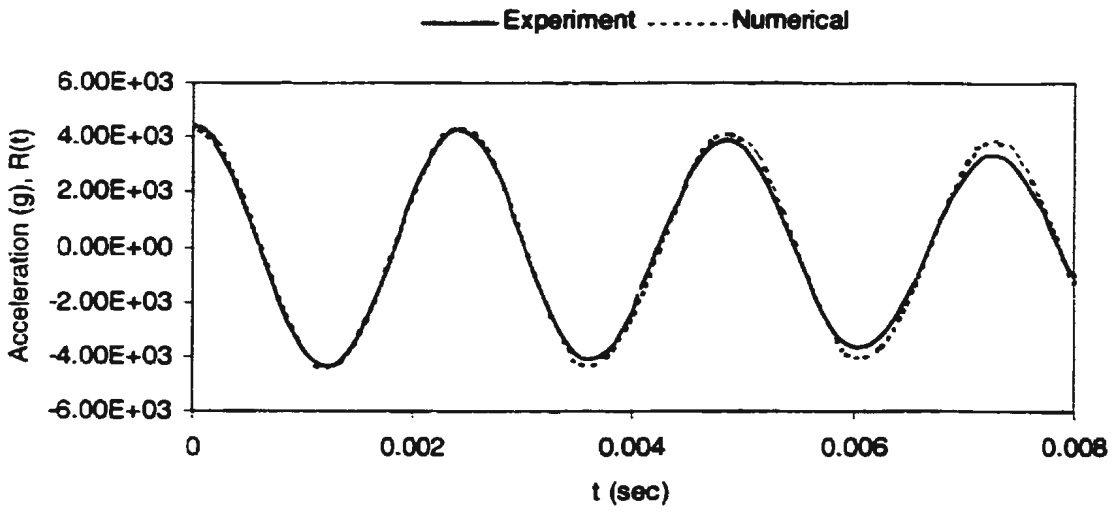

6.3.a: Undamaged

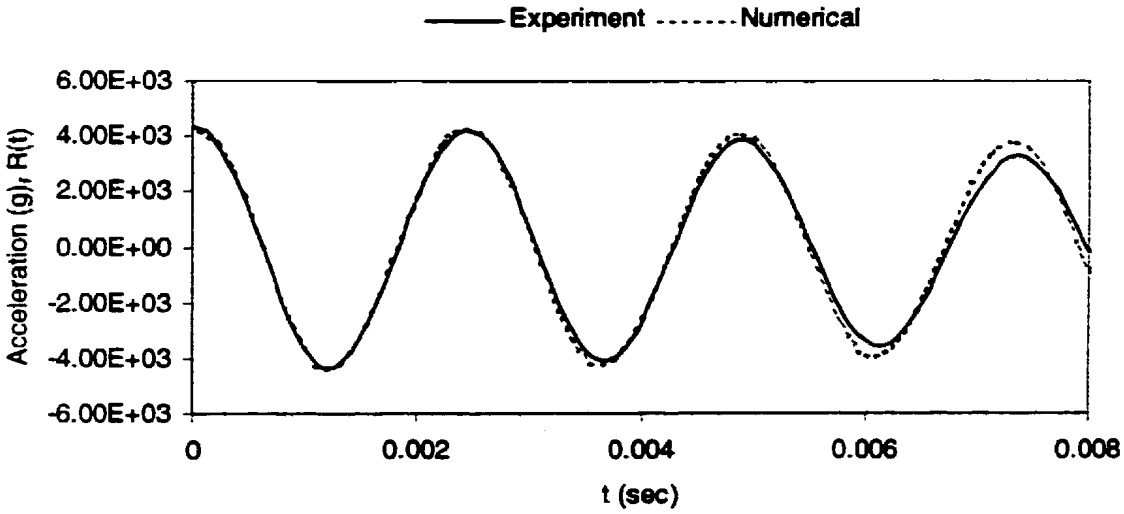

6.3.b: Crack length = 0.40 inch

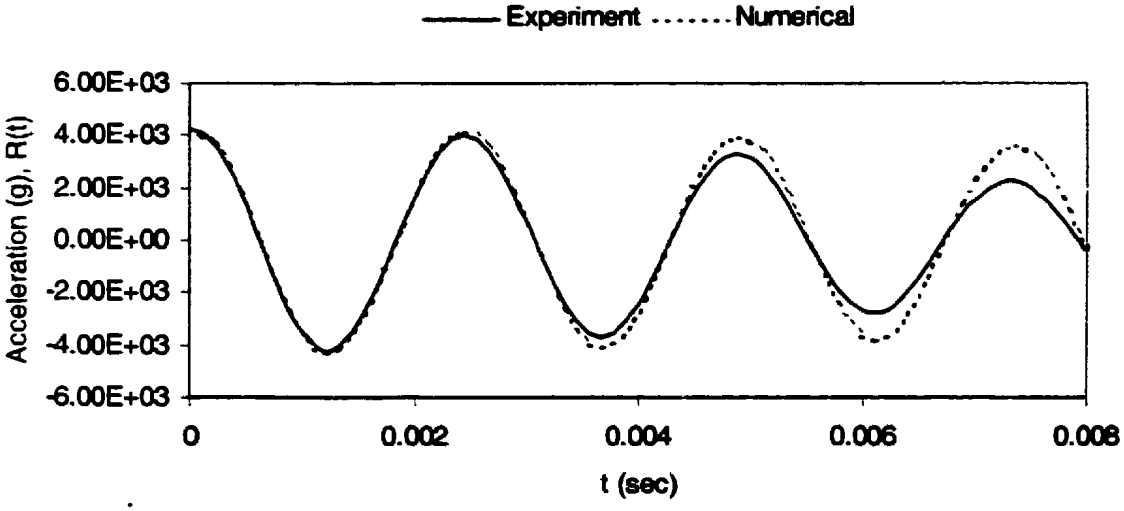

6.3.c: Crack length = 0.80 inch

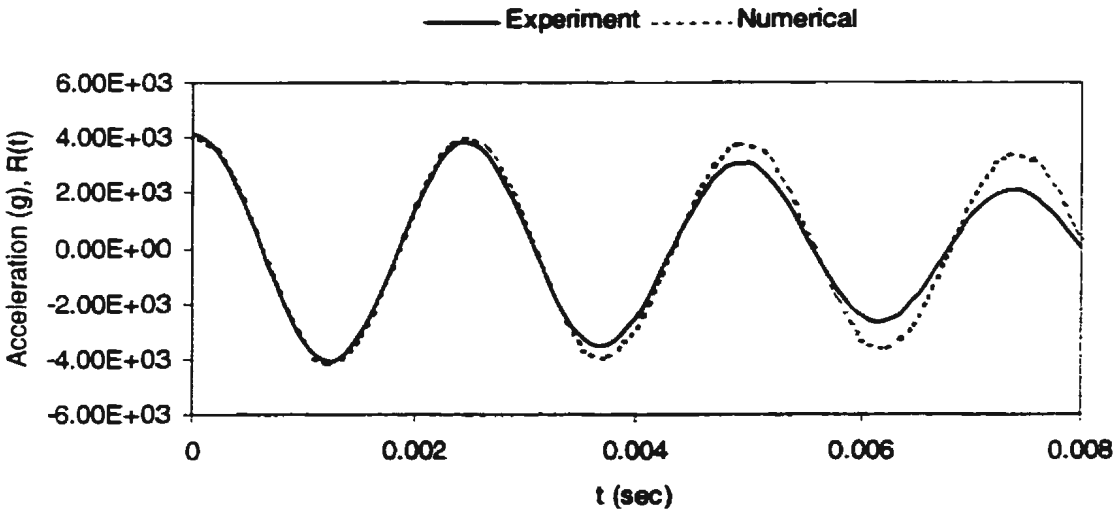

6.3.d: Crack length = 1.20 inch

Figure 6.3: Comparison of Experimental and Numerical Autocorrelation Functions

Table 6.2: Comparison of Experimental and Numerical Autocorrelation Functions
Frequency (Hz)

No	Undamaged		Crack length of					
			0.40 inch		0.80 inch		1.20 inch	
	Exp.	An.	Exp.	An.	Exp.	An.	Exp.	An.
1	412.96	412.86	411.11	411.08	407.79	408.25	404.98	404.84

Note: Exp. = Experiment; An. = Analysis

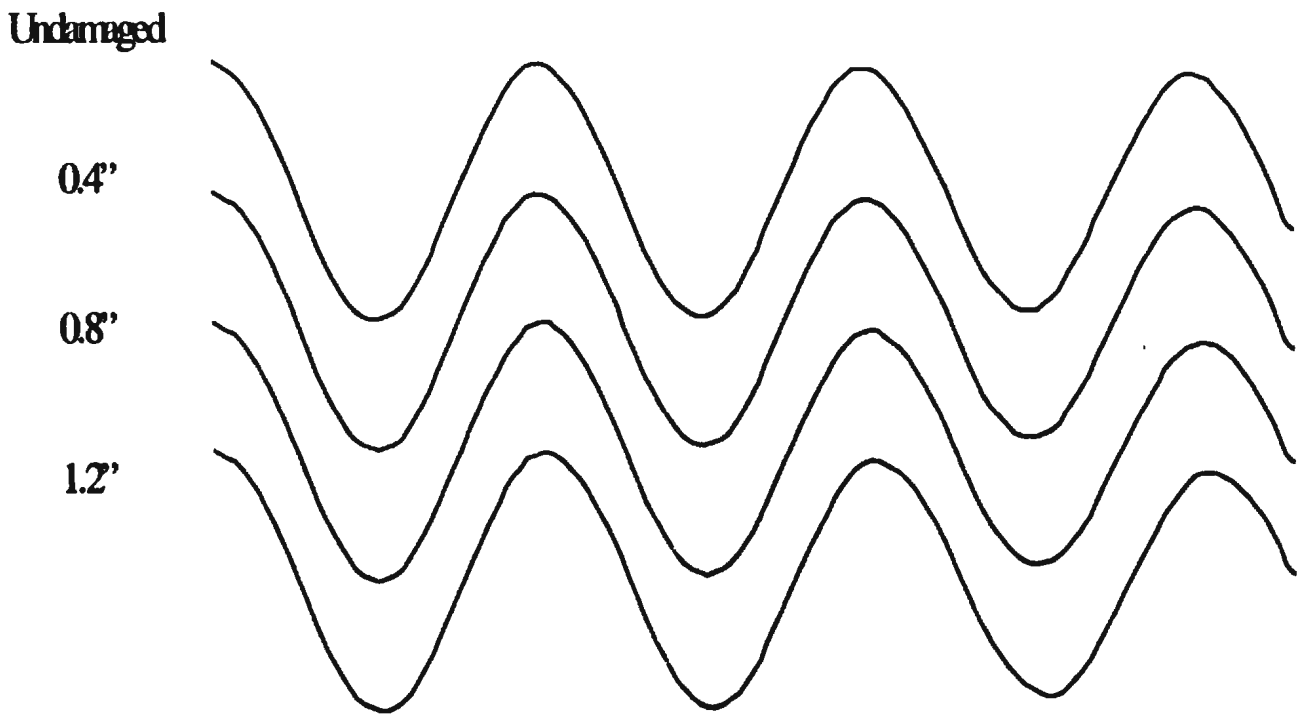

Figure 6.4: Comparison of the Numerical Autocorrelation Functions

It can be observed from Figures 6.3 and Table 6.2 that the agreement between the numerical autocorrelation functions and the experimental ones are also good for both the signatures and the frequencies. The numerical autocorrelation functions corresponding to various crack lengths are shown in Figure 6.4. Like the experimental ones, the numerical autocorrelation functions shown in Figure 6.4 also have a similar behavior for undamaged and damaged conditions. The crest and the trough of the first two cycles also steadily shift to the right side as the crack length increases. Moreover, Figure 6.4 shows that, at a saw cut length of 0.40 inch, the numerical autocorrelation function is similar to the undamaged ones. Changes in the magnitude become increasingly obvious when the crack increases.

6.3 Crosscorrelation Functions

It has been shown in the two previous sections that the experimental and numerical autocorrelation functions can be used to identify the dynamic behavior of the undamaged stiffened plate model and the model with several crack lengths. However, it is also noticed that the change in the frequency is small as a result of the occurrence of the crack. It can not be used as a practical method for crack identification, until the crack length becomes very large.

Based on these considerations, the use of the crosscorrelation functions to detect crack occurrence was investigated. The crosscorrelation function was calculated using the random responses obtained from two different locations, i.e., accelerometers #1 and #2. In

addition, their autocorrelation functions are also analyzed. Figures 6.5.a - 6.5.b show the autocorrelation functions for the undamaged condition obtained from accelerometers #1 and #2, respectively, whereas Figure 6.5.c shows their crosscorrelation functions.

As shown in Figures 6.5.a - 6.5.b, the autocorrelation functions obtained from two different locations have similar shapes. However, the magnitude of the autocorrelation function obtained from accelerometer #1 is slightly higher than that obtained from accelerometer #2. The difference in magnitude may be caused by the fact that Model #1 was asymmetric. Furthermore, the crosscorrelation function shown in Figure 6.5.c is also similar to the autocorrelation functions. However, the magnitude is completely different.

The autocorrelation functions for the damaged model with the crack lengths of 0.40 inch, 0.80 inch, and 1.20 inch are drawn in Figures 6.6.a - 6.6.b, 6.7.a - 6.7.b, and 6.8. a - 6.8.b, respectively. Their crosscorrelation functions are shown in Figures 6.6.d, 6.7.d, and 6.8.d, respectively. Similar to the undamaged condition, it can also be observed from Figures 6.6.a - 6.6.b that the autocorrelation functions also have similar shapes when the crack is 0.40 inch. The presence of damage caused the magnitude of autocorrelation function obtained from accelerometer #2 to be lower than that obtained from accelerometer #1.

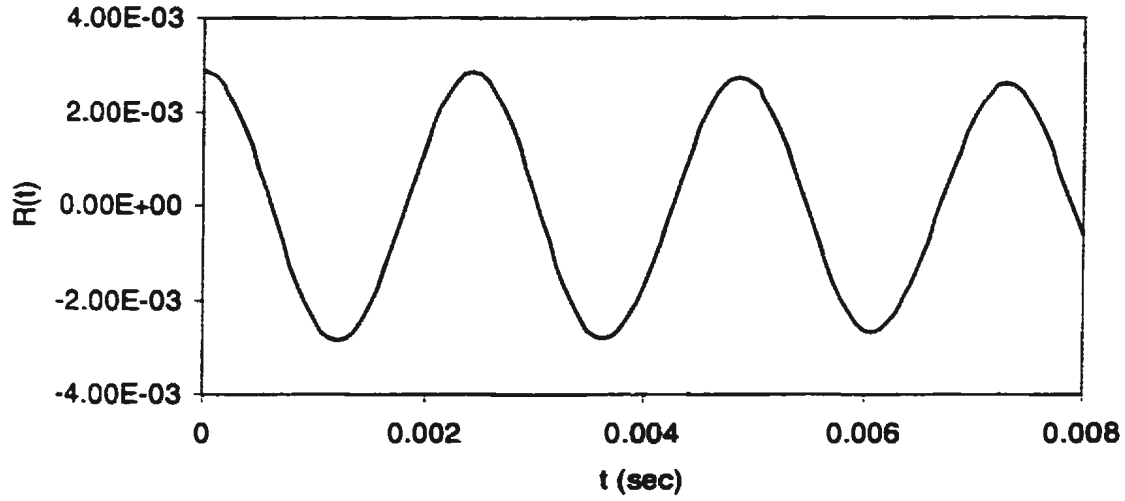

6.5.a: Autocorrelation Function at the Accelerometer #1

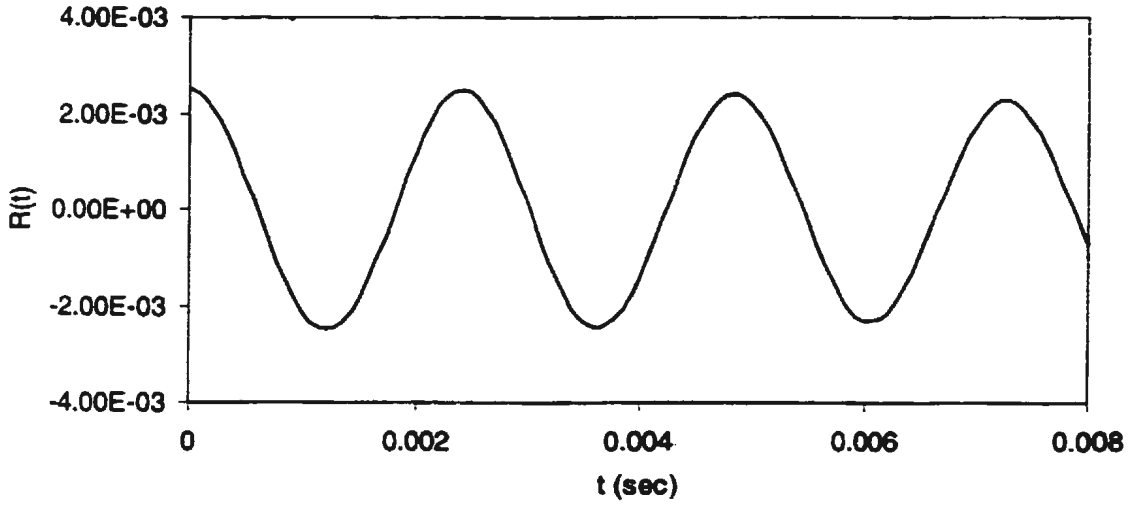

6.5.b: Autocorrelation Function at the Accelerometer #2

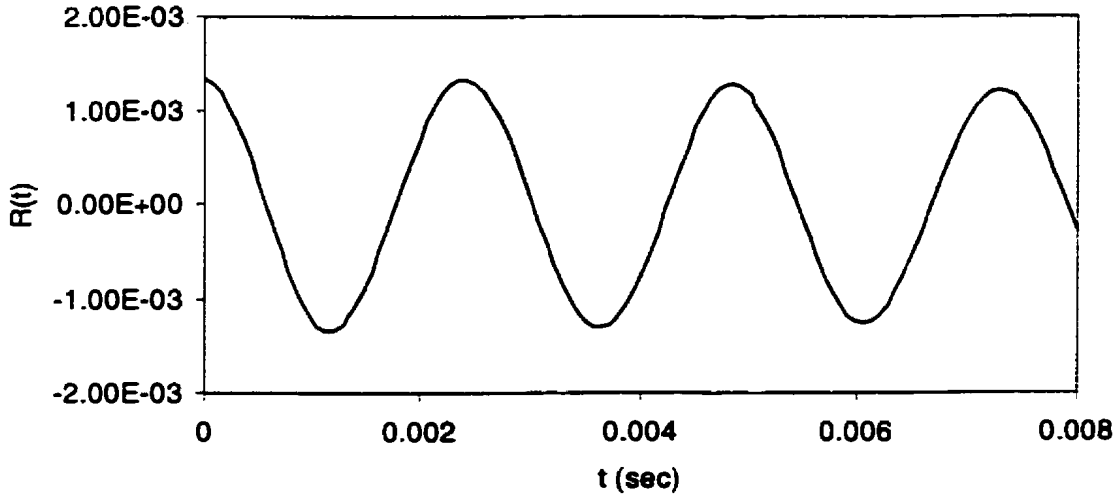

6.5.c: Crosscorrelation Function

Figure 6.5: Auto- and Cross-correlation Functions (Undamaged)

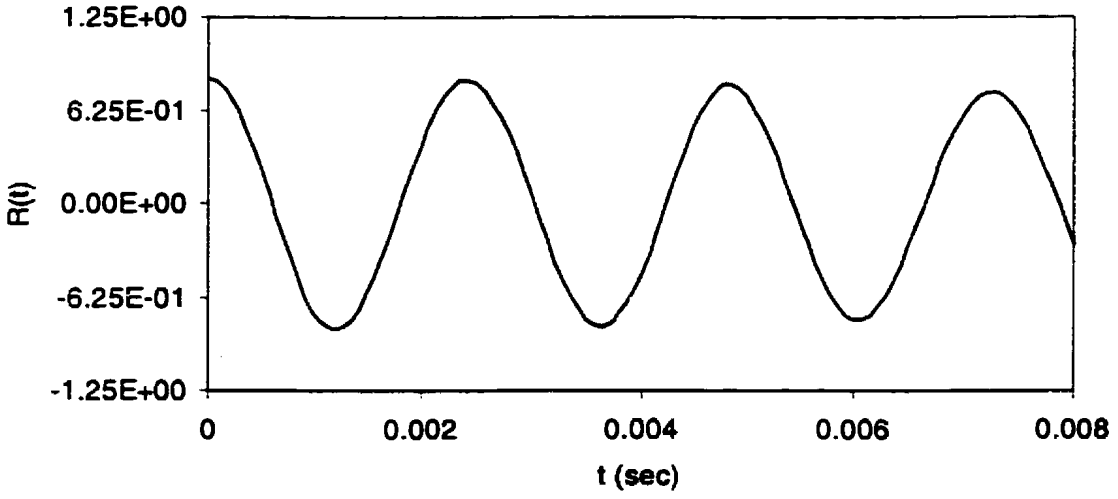

6.6.a: Autocorrelation Function at accelerometer #1

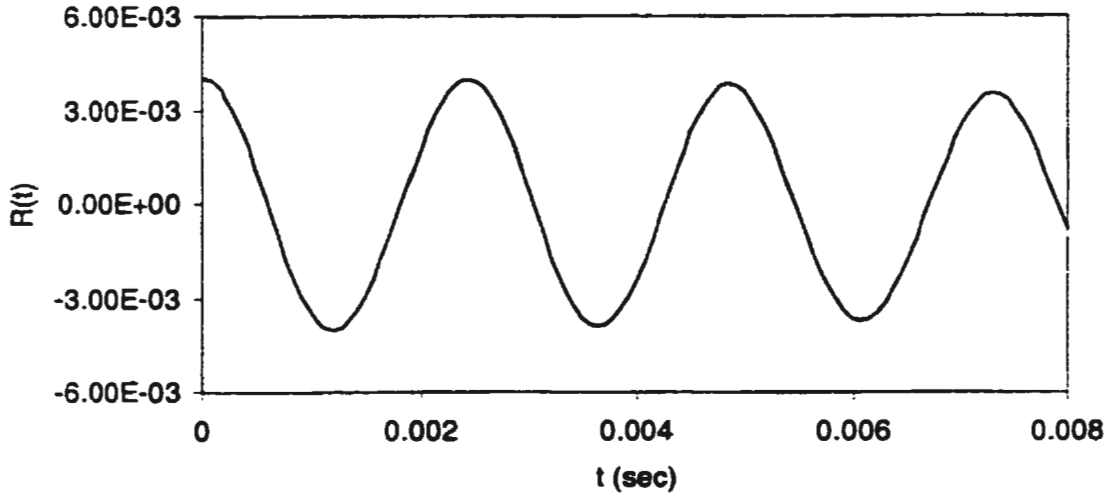

6.6.b: Autocorrelation Function at accelerometer #2

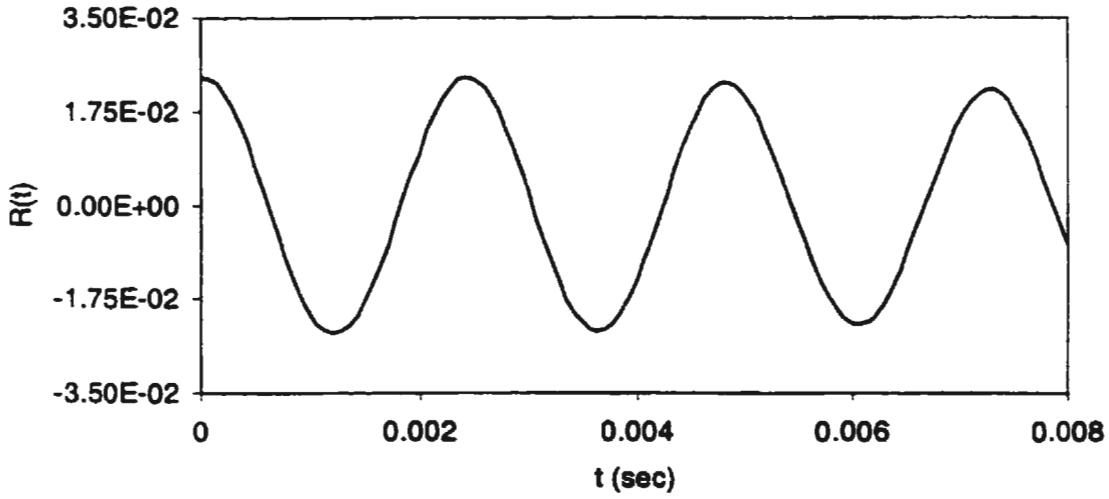

6.6.c: Crosscorrelation Function

Figure 6.6: Auto- and Cross-correlation Functions (Crack length = 0.40 inch)

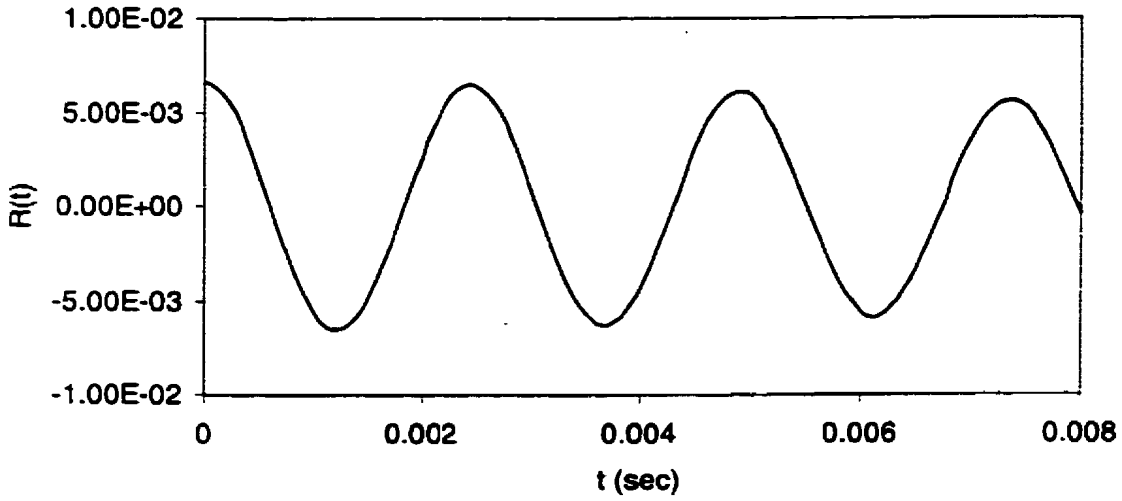

6.7.a: Autocorrelation Function at accelerometer #1

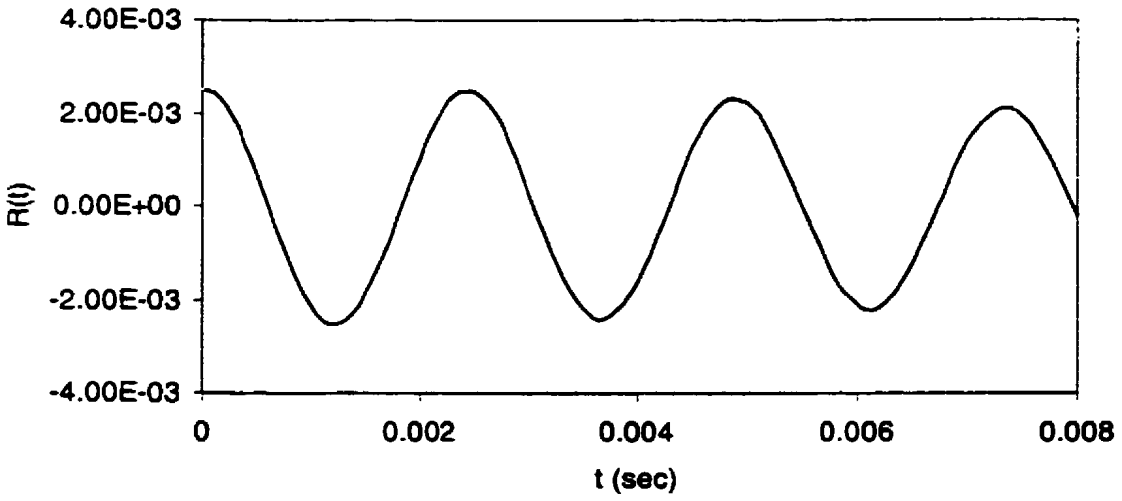

6.7.b: Autocorrelation Function at accelerometer Acc #2

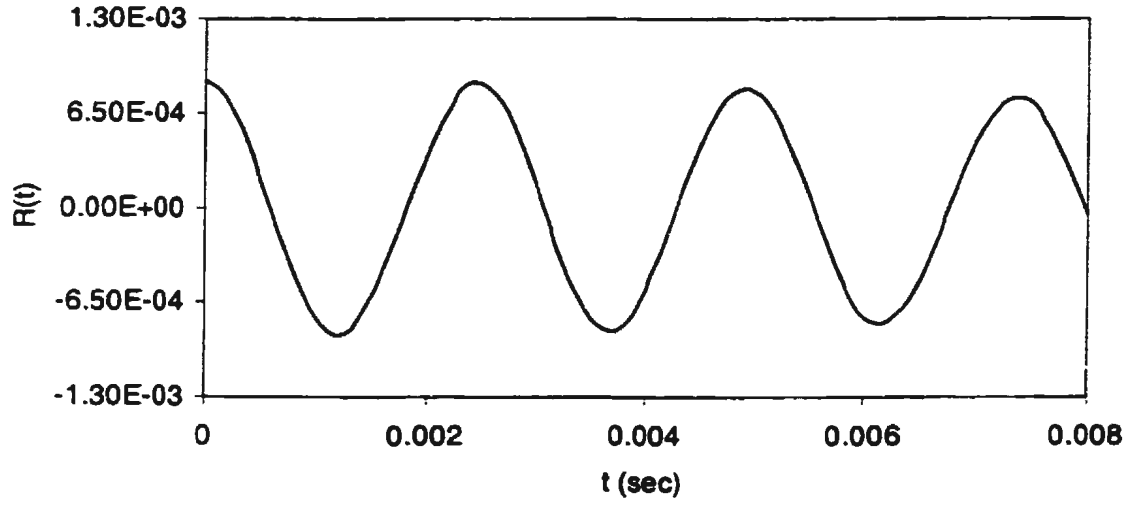

6.7.c: Crosscorrelation Function

Figure 6.7: Auto- and Cross-correlation Functions (Crack length = 0.80 inch)

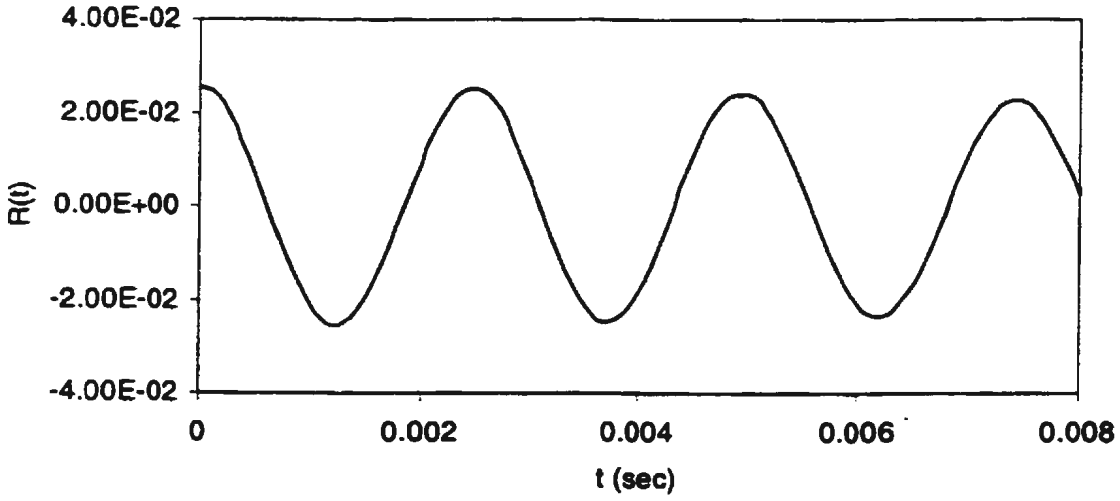

6.8.a: Autocorrelation Function at accelerometer Acc #1

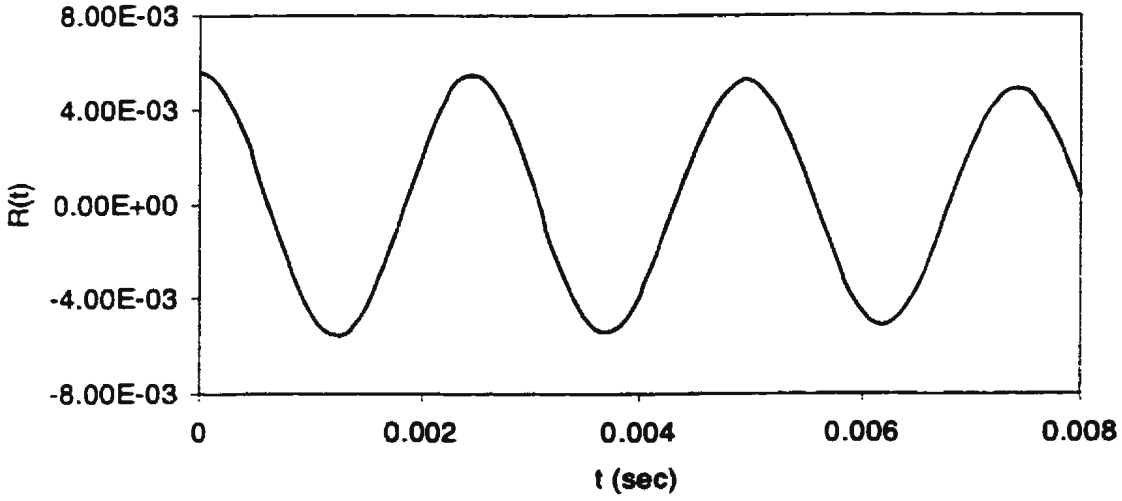

6.8.b: Autocorrelation Function at accelerometer #2

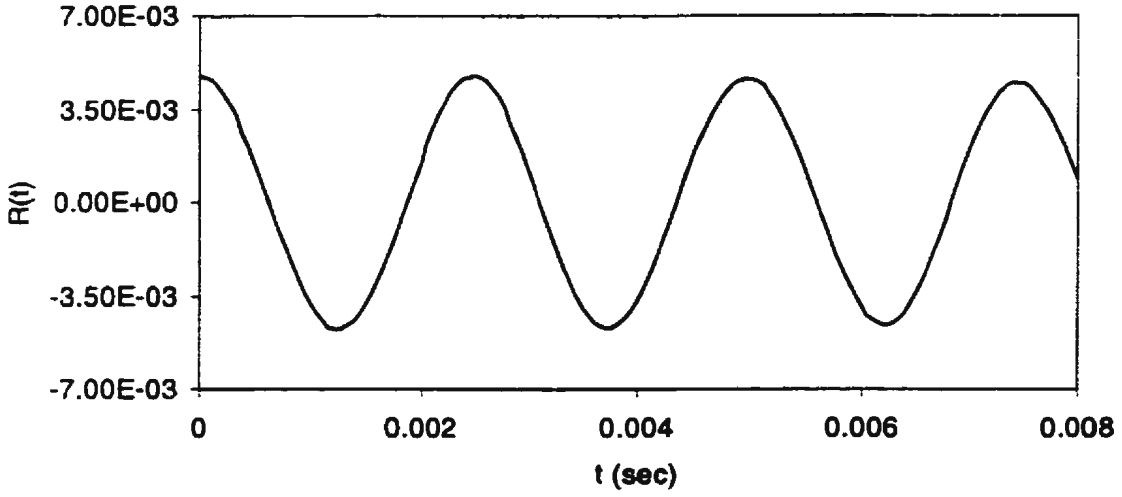

6.8.c: Crosscorrelation Function

Figure 6.8: Auto- and Cross-correlation Functions (Crack length = 1.20 inch)

This may be caused by the fact that the crack was nearer to accelerometer #2. The same condition is also found from the autocorrelation functions of Model #1 with different crack lengths as shown in Figures 6.7.a - 6.7.b and 6.8.a - 6.8.b. Furthermore, the crosscorrelation functions are also similar to their autocorrelation functions for all damage cases, see Figures 6.6.c, 6.7.c, and 6.8.c.

Based on the above, it can be seen that it is difficult to use the crosscorrelation functions as a tool for the identification of the occurrence of a damage in the structure.

6.4 Summary

Application of the auto and cross-correlation functions in the identification of damage for the stiffened plate model has been discussed. The relationship between the experimental autocorrelation function and the random decrement signature has been established. Using the autocorrelation functions, the frequency of the most predominant mode could be determined. However, the decrease in frequency as a result of damage occurrence was very small. There was a good agreement between the experimental and numerical autocorrelation functions. The crosscorrelation functions exhibited the same characteristic as the autocorrelation functions.

Chapter 7

The Identification of Damage in Stiffened Plates using Neural Network Techniques

7.1 Introduction

A neural network technique that has been used for identifying the occurrence of damage in the stiffened plate model will be presented in this chapter. The technique identified not only the occurrence of damage at several locations in the faceplate of the longitudinal of the model, but also the location and the extent of damage. The technique was applied to both experimentally measured and numerically generated autocorrelation function data. The experimental as well as the numerical autocorrelation functions for Model #1 were used as inputs to the network. Unlike the experimental study that only analyzed the autocorrelation functions of the damaged model at one location, the numerical study also investigated the autocorrelation functions of the damaged model at several locations.

A function $F(x,\dot{x})$ was used as the identification criterion. In the following sections,

the underlying theory and the results obtained are explained.

7.2 Theory

The random decrement equation for the structure has been derived in Chapter 3 as:

$$\ddot{x}_r(t) + 2\zeta_r\omega_{n,r}\dot{x}_r(t) + \omega_{n,r}^2 x_r(t) = 0 \tag{7.1}$$

Since $\omega_d^2 = \omega_n^2(1 - \zeta^2)$, Equation (7.1) can be rewritten as:

$$\ddot{x}_r(t) + \omega_{d,r}^2 x_r(t) + F_r(x_r,\dot{x}_r) = 0 \tag{7.2}$$

where

$$F_r(x_r,\dot{x}_r) = \omega_{n,r}^2 \zeta_r^2 x_r + 2\zeta_r \omega_{n,r} \dot{x}_r \tag{7.3}$$

The identification technique proposed uses a neural network algorithm to identify the function $F_r(x_r,\dot{x}_r)$. The displacement x_r and the velocity $\dot{x}_r$ are utilized in generating the autocorrelation function and its first derivative. The procedure for the identification of $F_r(x_r,\dot{x}_r)$ is detailed in section 3.5.

7.3 Results and Discussion

7.3.1 Experimental Data

Using the random response, one can easily calculate the autocorrelation function. Since both the autocorrelation function and its first derivative are used as inputs to the neural network. the first derivative was obtained using numerical differentiation. The frequencies ω_d could be easily calculated from the first cycle of the autocorrelation function curves. Only the first two cycles of the autocorrelation functions were needed for training the neural network. In order to minimize the round-off errors, the autocorrelation functions were normalized by dividing by its highest value.

Figures 7.1.a - 7.1.d show a comparison between the original autocorrelation function curves used in the training of the neural network and their predicted curves obtained using the neural network technique for the undamaged and the damaged cases. The input and output weights for the four cases, obtained when the neural network was iterated more than 8000 times and the error between the original and predicted curve was minimum, are tabulated in Table E.1 in Appendix E. It could be observed from Figures 7.1.a - 7.1.d that the agreement between the actual autocorrelation functions input and the predicted autocorrelation functions record is excellent in all conditions. This means that the neural network technique has predicted the experimental autocorrelation functions very well.

The values of the function $F(x,\dot{x})$ are tabulated in Table E.2 and drawn together in

Figure 7.2. Similar to the input and output weights, Table E.2 and Figure 7.2 also show that the various values of the function $F(x,\dot{x})$ as a function of time for the undamaged and the damaged conditions could be clearly identified. There is a consistent and appreciable change in the values of the function $F(x,\dot{x})$, as a crack is introduced and as its length grows from 0.40 inch to 1.20 inch.

A correlation between the peak values of the function $F(x,\dot{x})$ and the length of the crack, for a crack location of 0.90 inch from the heavy transverse member, is shown in Figure 7.3.

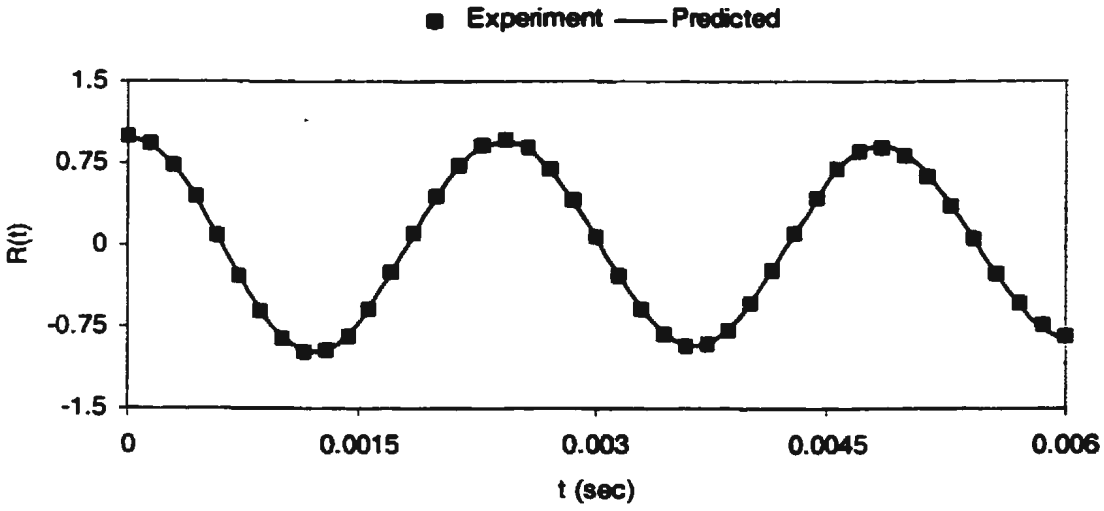

7.1.a: Undamaged

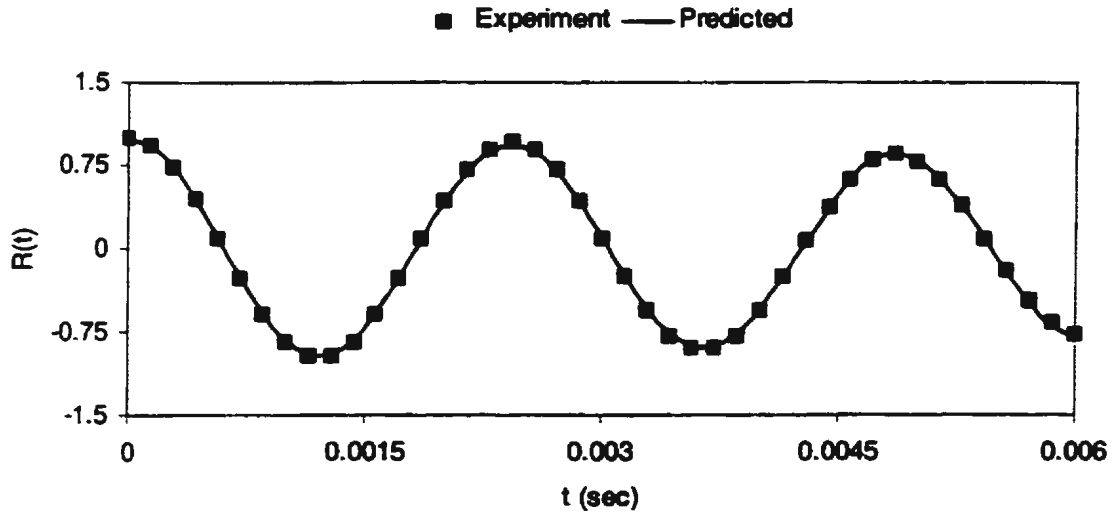

7.1.b: Crack length = 0.40 inch

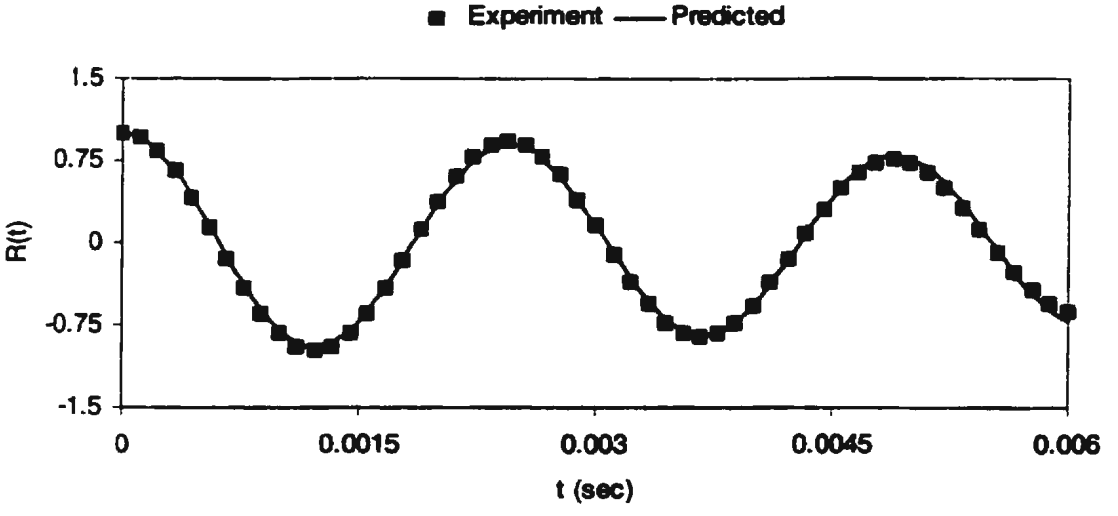

7.1.c: Crack length = 0.80 inch

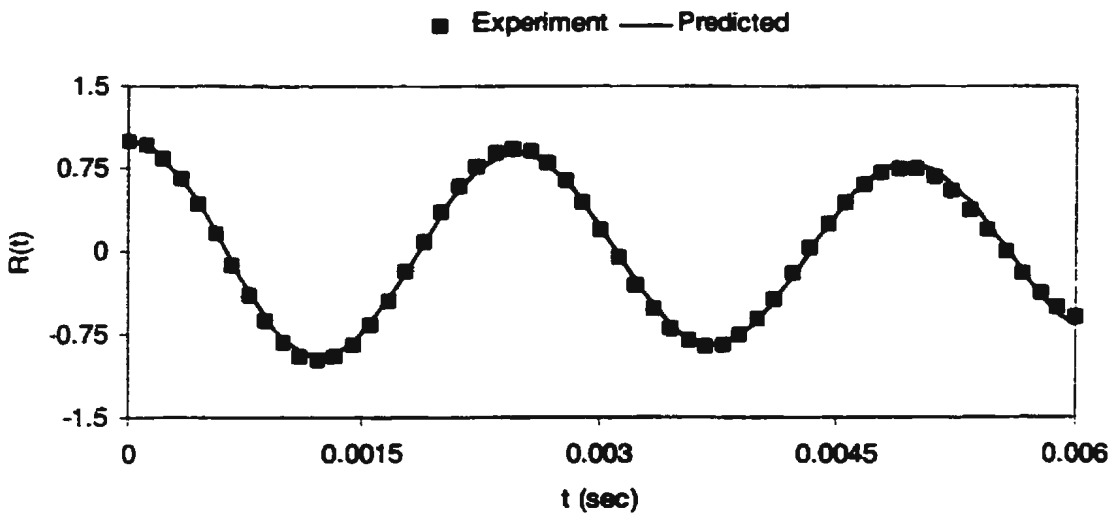

7.1.d: Crack length = 1.20 inch

Figure 7.1 : Comparison between the Autocorrelation Functions and Predicted Curves obtained using the Neural Network for Model #1 (Experiment, Crack at 0.90 inch away from center)

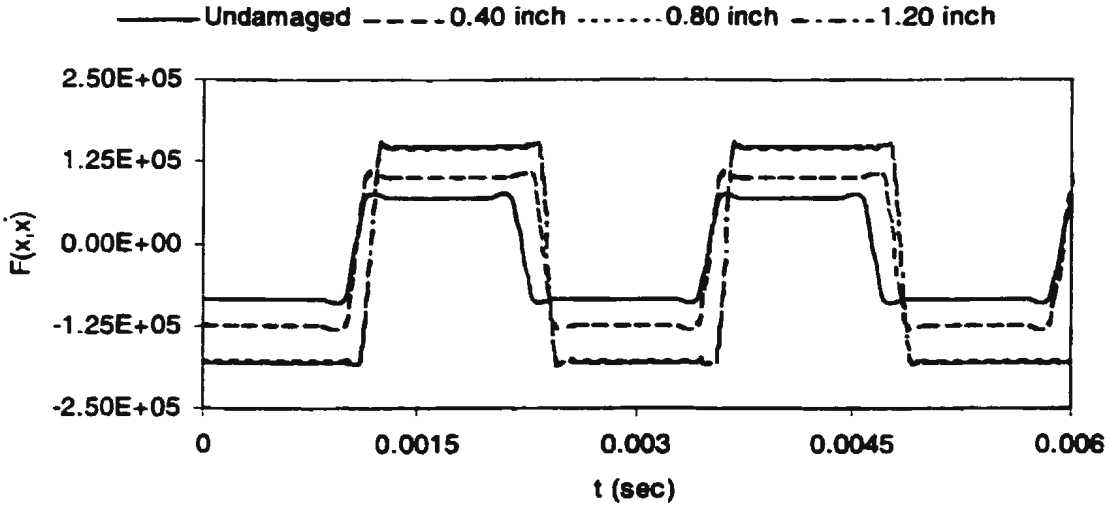

Figure 7.2. : Comparison of the Function $F(x,\dot{x})$ for the Undamaged and Damaged Conditions (Experiment, Crack at 0.90 inch away from center)

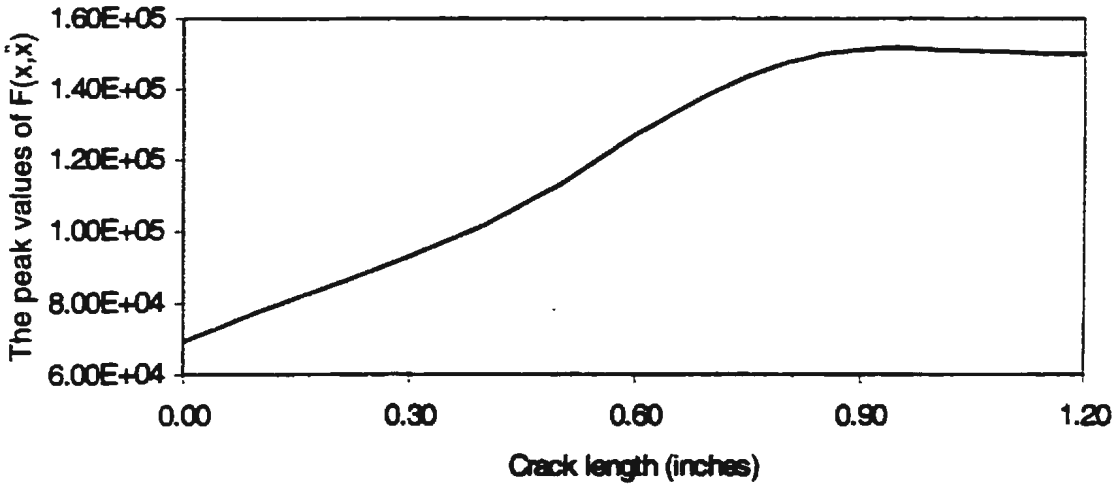

Figure 7.3: The Peak Values of Function $F(x,\dot{x})$ for each Crack Length (Experiment, Crack at 0.90 inch away from center)

It can be observed from Figure 7.3 that the minimum value of the function $F(x,\dot{x})$ corresponds to the undamaged condition. The presence of damage is indicated by an increase in the value of $F(x,\dot{x})$. The value of $F(x,\dot{x})$ increases as the crack length increases. Then it tapers off to a constant value as the length of the crack reaches a value of 0.85 inch. After reaching the maximum value, the value of function $F(x,\dot{x})$ decreases slightly. This phenomena has been used as a basis for identifying the presence of damages with small crack lengths ($\leq$ 1.20 inch) in Model #1.

This method can also be used to detect the occurrence of damage in similar structures. The function $F(x,\dot{x})$ is calculated for the undamaged structure and is used as a reference value. The structure is monitored and the value of the function $F(x,\dot{x})$ is calculated at specific

intervals of time and the history of the function $F(x,\dot{x})$ is monitored. Changes in the value of the function $F(x,\dot{x})$ indicates the occurrence of cracks.

7.3.2 Numerically Generated Data

This section deals with the use of the FE model for identifying the extent and the location of damage in the stiffened plate model. A FE model for Model #1 was developed so that it could be used for calculating the autocorrelation functions of the undamaged model and the damaged model with various damage lengths at several different locations. Three crack lengths of 0.40 inch, 0.80 inch and 1.20 inch were introduced in the model at ten different locations of the faceplate of the longitudinal.

The distance between each crack was 0.45 inch, and the locations were 0.00 inch, 0.45 inch, 0.90 inch,....., 3.60 inch, and 4.05 inch from the heavy transverse member, respectively. Similar to the experimental autocorrelation functions, the numerical autocorrelation functions were also normalized. The neural network was also trained using the first two cycles of the autocorrelation functions.

Figure 7.4 shows the results of the undamaged condition by comparing the original autocorrelation function and the predicted curve obtained using the neural network technique. Excellent matching is obtained between them. This indicates that the neural network technique also has a capability to predict the numerical autocorrelation function. Hence, the technique is used to calculate the predicted autocorrelation functions and the

values of function $F(x,\dot{x})$ for the damaged cases at different lengths and locations of the crack. The value of the function $F(x,\dot{x})$ of the undamaged model would be used as the starting point for all analyses.

A comparison between the numerical autocorrelation functions and their predicted curves for the model with the crack length of 0.40 inch, 0.80 inch, and 1.20 inch for the location of crack at the heavy transverse member, called "center" hereafter, is shown in Figures 7.5.a - 7.5.c. The input and output weights are tabulated in Table E.3. Figures 7.5 show that the predicted curves match closely with the original autocorrelation functions for all crack lengths. Moreover, Table E.3 also shows the difference in values between the undamaged and damaged cases.

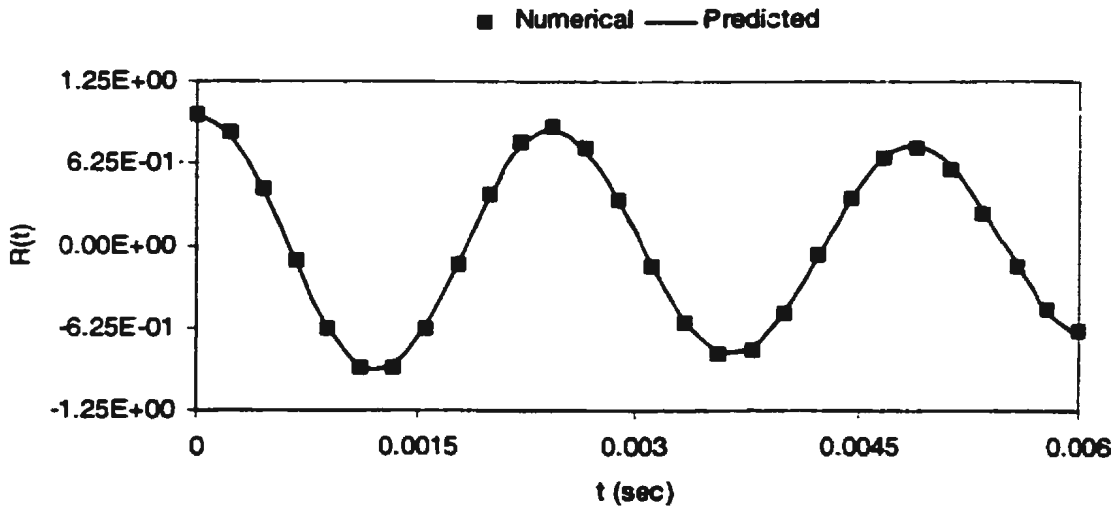

Figure 7.4: Comparison between the Autocorrelation Function and Predicted Curve obtained using the Neural Network (Numerical, Undamaged)

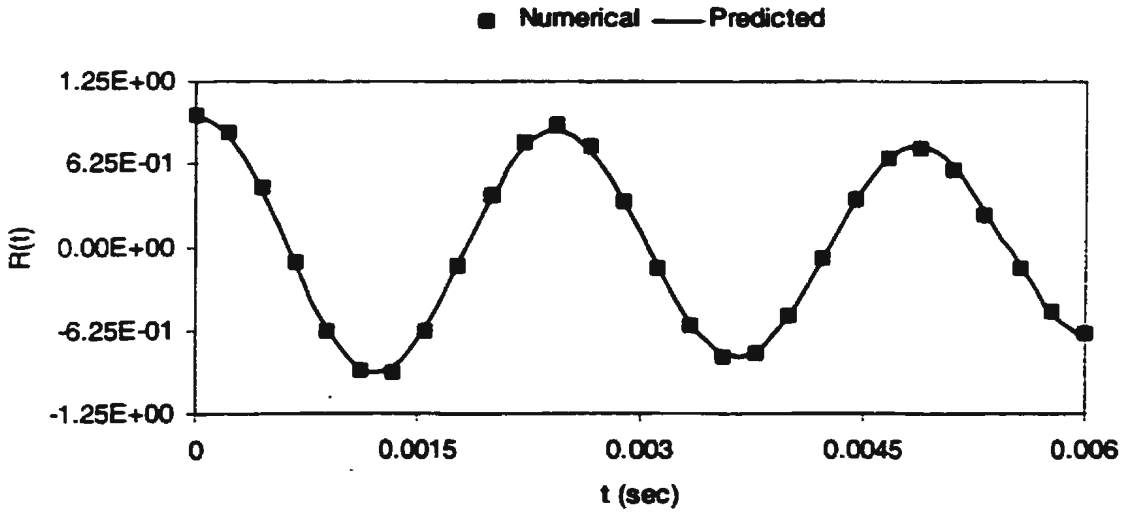

7.5.a: Crack length = 0.40 inch

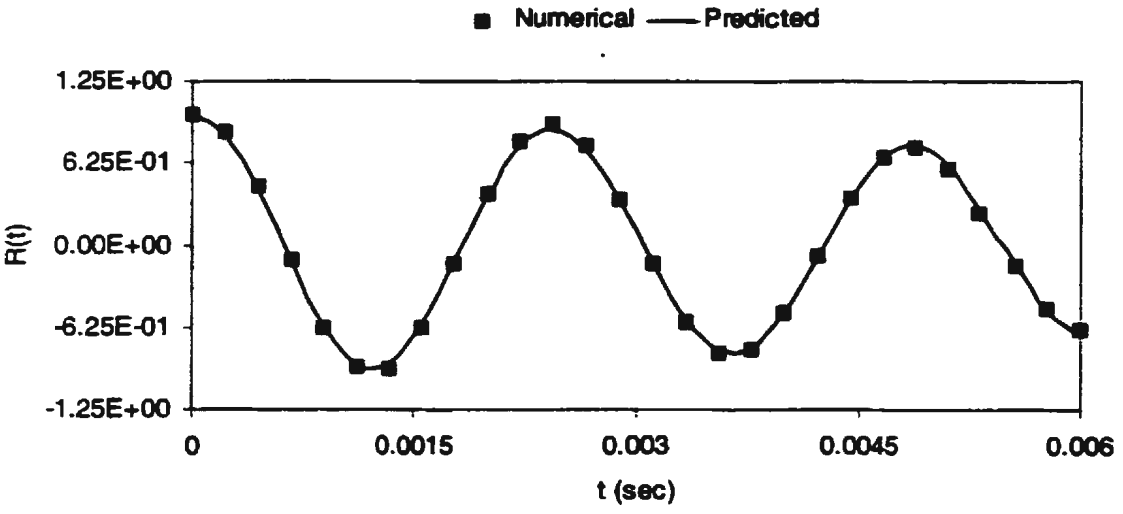

7.5.b: Crack length = 0.80 inch

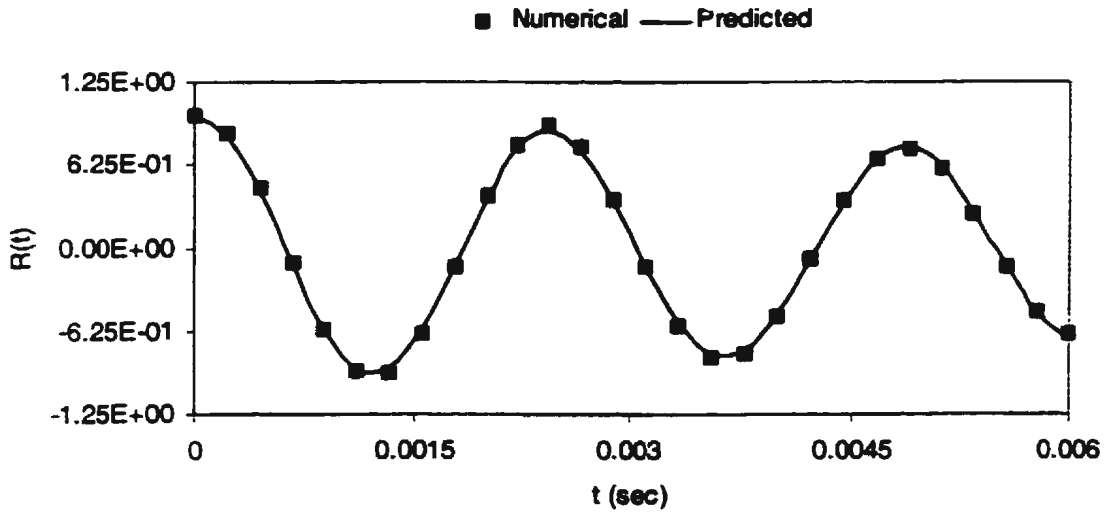

7.5.c: Crack length = 1.20 inch

Figure 7.5: Comparison between the Autocorrelation Functions and Predicted Curves obtained using the Neural Network (Numerical, Crack at Center)

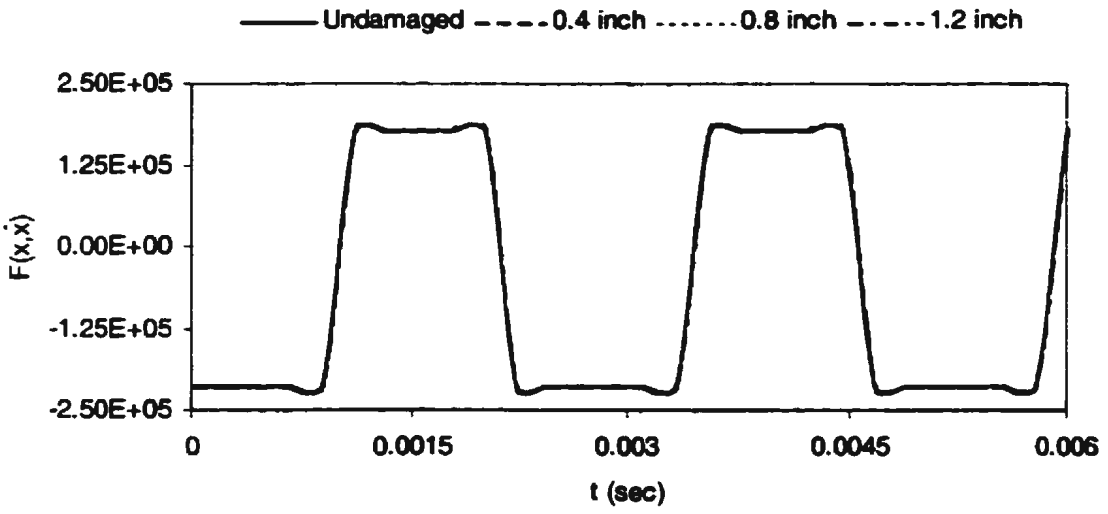

Figure 7.6: Comparison of the Function $F(x,\dot{x})$ for the Undamaged and Damaged Conditions (Numerical, Damaged, Crack at Center)

A comparison between the values of the functions $F(x,\dot{x})$ for all cases is plotted in Figure 7.6 as a function of time. Comparing with Figures 7.4 and 7.5, Figure 7.6 is completely different; even the values of the function $F(x,\dot{x})$ depend on the values of x and $\dot{x}$ as shown in Equation (7.3). The reason for this difference is that the input (W_I) and output (W_O) weights have similar, large, and negative values, see Table E.3. Furthermore, the function $F(x,\dot{x})$ has different amplitudes for the undamaged and damaged cases. However, the amplitude difference involved is not evident from looking at these graphs due to the magnitude of $F(x,\dot{x})$ and its variation. The difference involved becomes clear from Figure 7.7, wherein the maximum positive values of the function are plotted for various crack lengths.

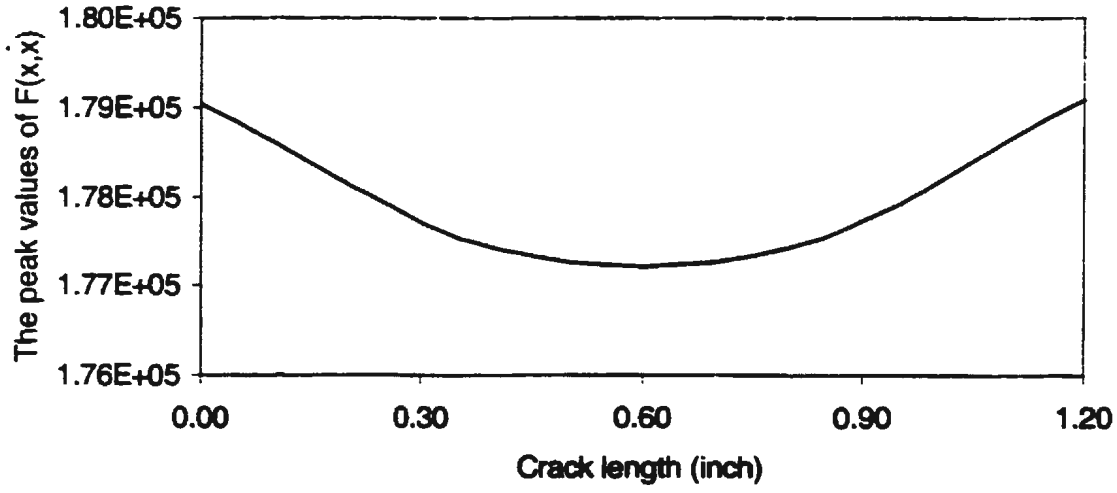

Figure 7.7: The Peak Values of Function $F(x,\dot{x})$ for each Crack Length (Numerical, Crack at Center)

Figure 7.7 shows the variation of the peak value of the function $F(x,\dot{x})$ as a function of crack length for the crack located at the center. It can be observed from this plot that the function $F(x,\dot{x})$ has a maximum value for the undamaged condition. The value decreases when the crack is introduced. It reaches a minimum value when the crack length is around 0.60 inch. The value of $F(x,\dot{x})$ gets increased as the crack length increases. However, comparing Figures 7.3 and 7.7, we notice a change in the values of the function $F(x,\dot{x})$ and also a change in the trend. This is mainly due to the fact that the values of the experimental and numerical autocorrelation functions used for the training the network are different, and the neural network technique is sensitive to small variations in the input. In addition, Figure 7.3 is for a crack located at 0.90 inch from the center, whereas Figure 7.7 is for a crack located at the center.

Based on the above results, the neural network technique is applied for calculating the predicted numerical autocorrelation functions and the values of the function $F(x,\dot{x})$ for the damaged model with different location of the crack. The crack locations are at distances of 0.45 inch, 0.90 inch, 1.35 inch,....., 3.60 inch, and 4.05 inch from the center of the heavy transverse member, respectively. They are denoted as the 0.45 inch, the 0.90 inch, the 1.35 inch, ..., the 3.60 inch, and the 4.05 inch "away from the center crack", hereafter. Figures 7.8.a - 7.8.c and 7.9.a - 7.9.c show a comparison between them for the 0.45 inch and the 4.05 inch 'away from the center crack" location.

From these Figures, it could be observed that the original autocorrelation functions

have similar shapes, even though the location of cracks are at or faraway from center of the heavy transverse member, and the crack lengths are 0.40 inch, 0.80 inch, or 1.20 inch, respectively. The agreement between the autocorrelation functions and their predicted curves is excellent for all conditions. An excellent agreement between the predicted and the original curves is also obtained for the 0.90 inch, 1.35 inch,....., the 3.15 inch, and the 3.60 inch "away from the center crack". The results are presented in Appendix E.

The input and output weights used for obtaining the predicted autocorrelation functions and the function $F(x,\dot{x})$ for each crack location are tabulated in Tables E.4 to E.13. For three different crack lengths at nine different locations, it could be observed from Tables E.4 - E.13 that the magnitudes of the undamaged and damaged cases are all different.

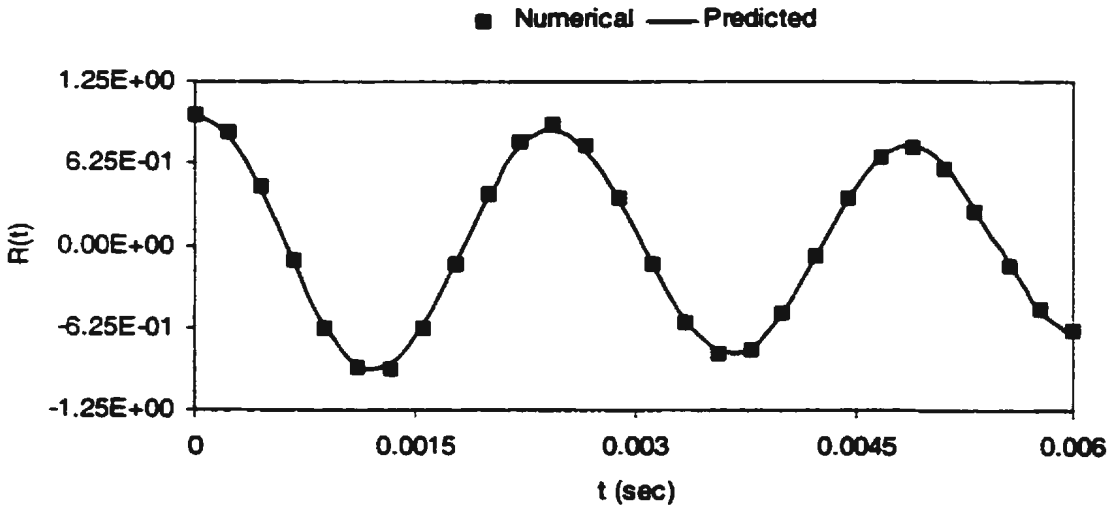

7.8.a: Crack length = 0.40 inch

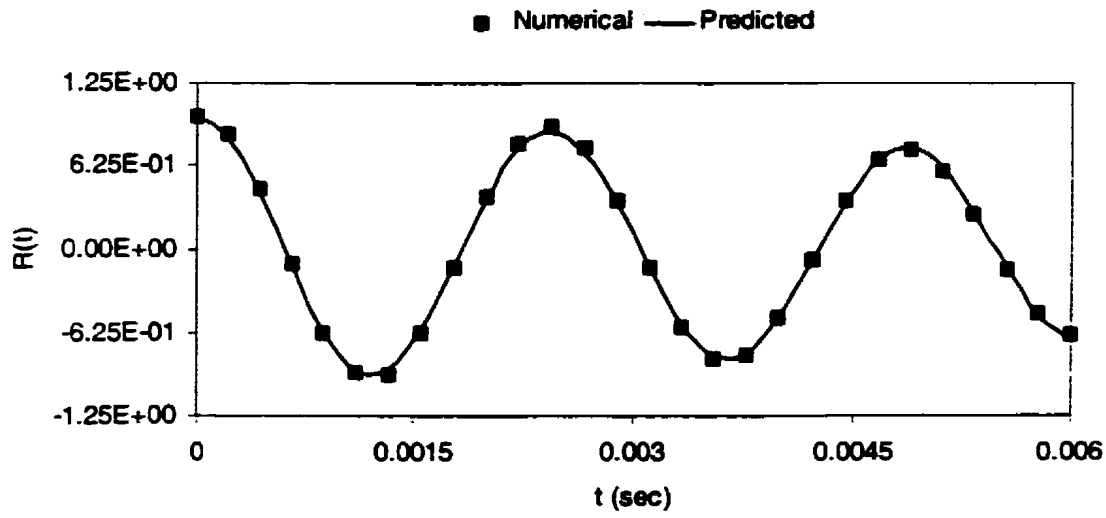

7.8.b: Crack length = 0.80 inch

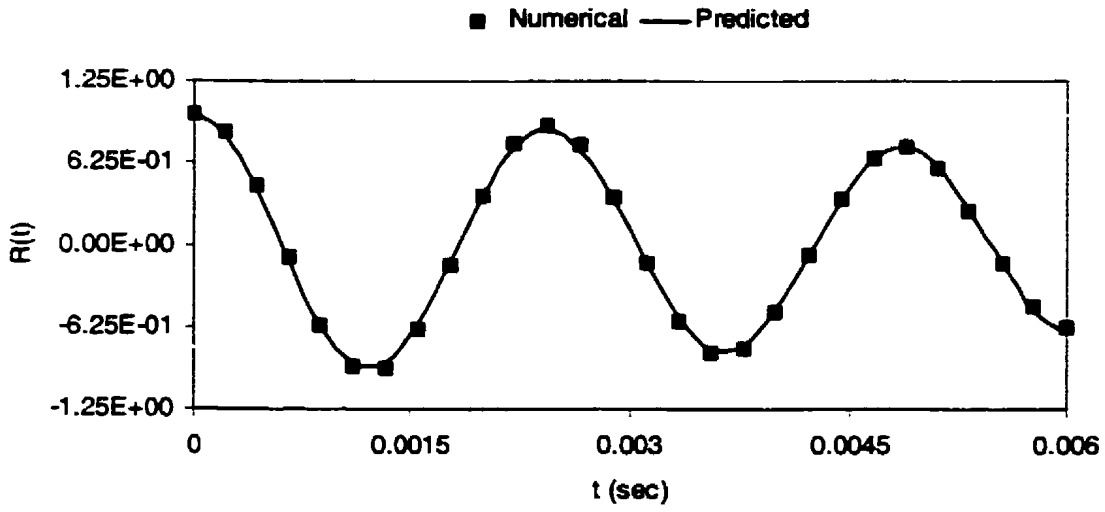

7.8.c: Crack length = 1.20 inch

Figure 7.8: Comparison between the Autocorrelation Functions and Predicted Curves obtained using the Neural Network (Numerical, Damaged, Crack at 0.45 inch away from the center)

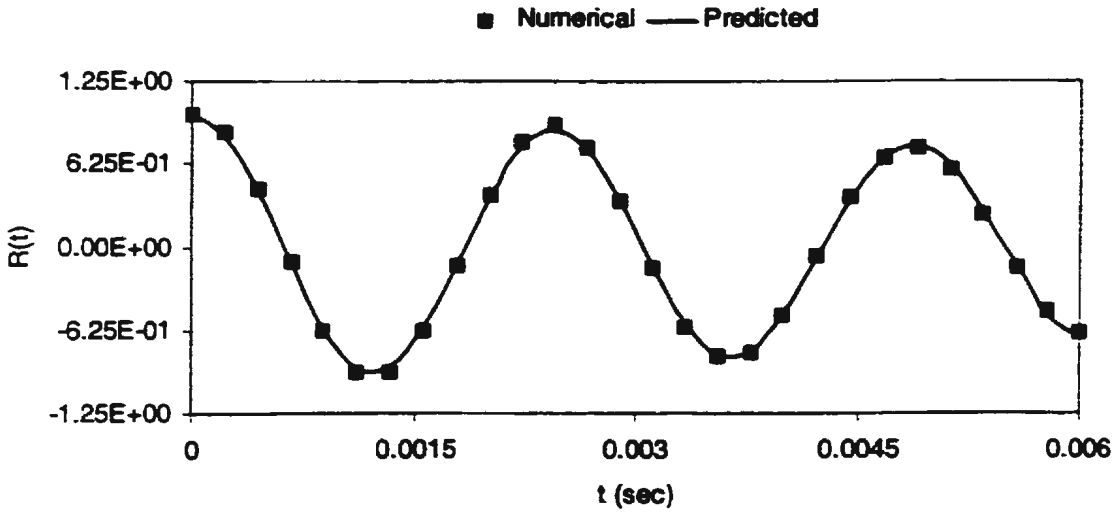

7.9.a: Crack length = 0.40 inch

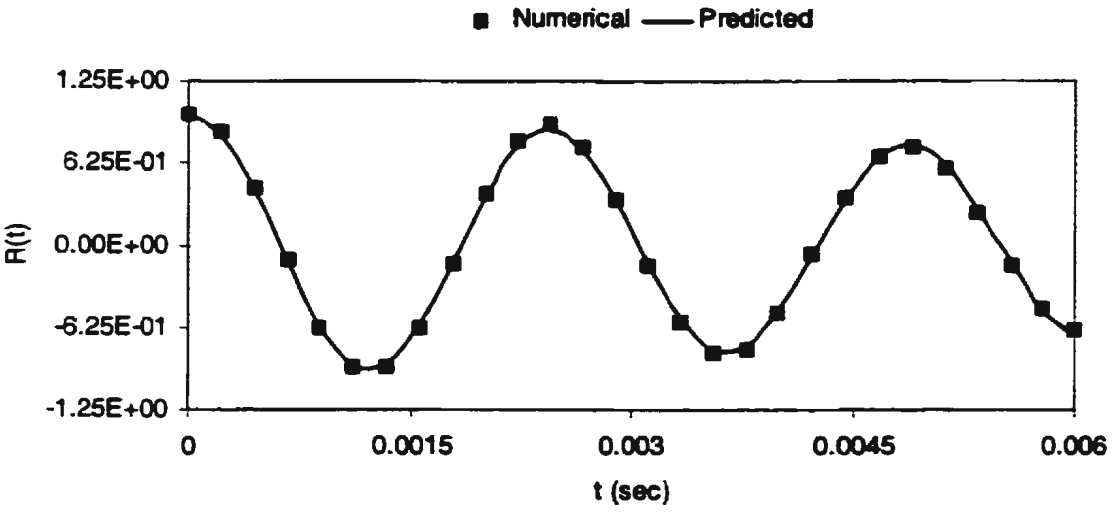

7.9.b: Crack length = 0.80 inch

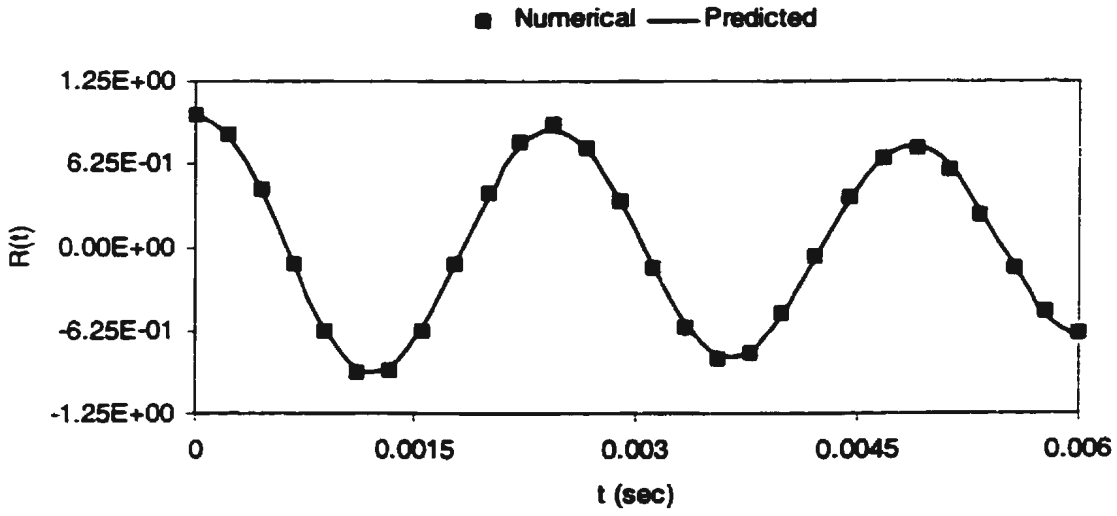

7.9.c: Crack length = 1.20 inch

Figure 7.9: Comparison between the Autocorrelation Functions and Predicted Curves obtained using the Neural Network (Numerical, Damaged, Crack at 4.05 inch away from the center)

Next, the correlation functions $F(x,\dot{x})$, for various crack locations, are plotted (as function of time) in Figures 7.10.a - 7.10.i, respectively. Similar to the center case, the functions $F(x,\dot{x})$ also have different values for all damaged cases. The difference involved is not evident from looking at these graphs because of the plotting scale. However, the difference involved becomes clear from Figures 7.11.a - 7.11.i.

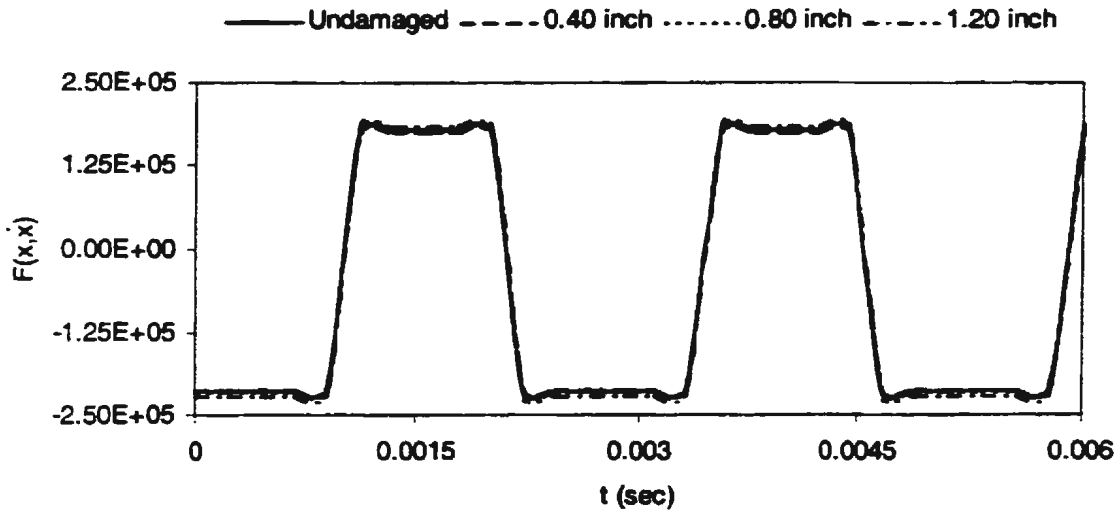

7.10.a: Numerical, Crack at 0.45 inch away from the center

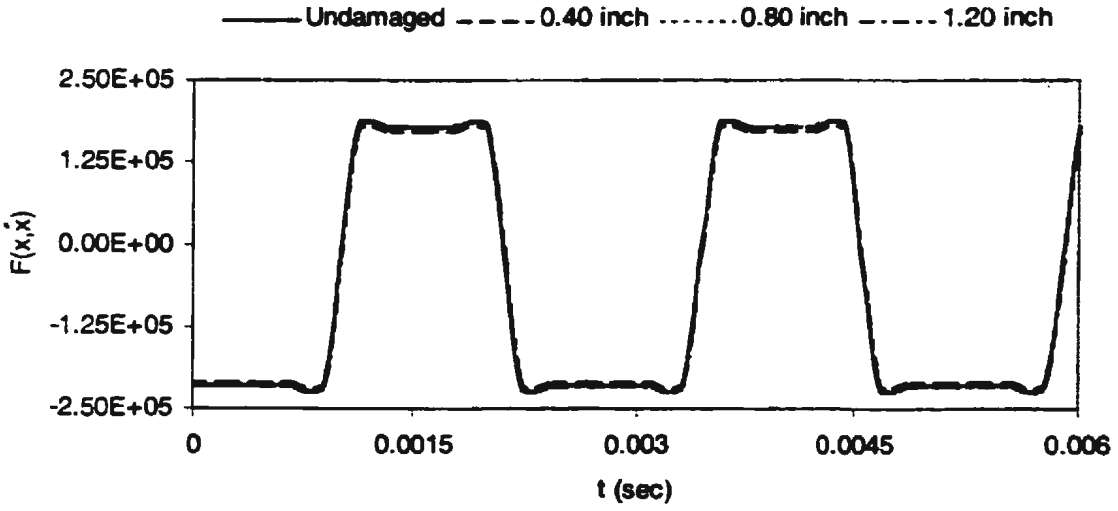

7.10.b: Numerical, Crack at 0.90 inch away from the center

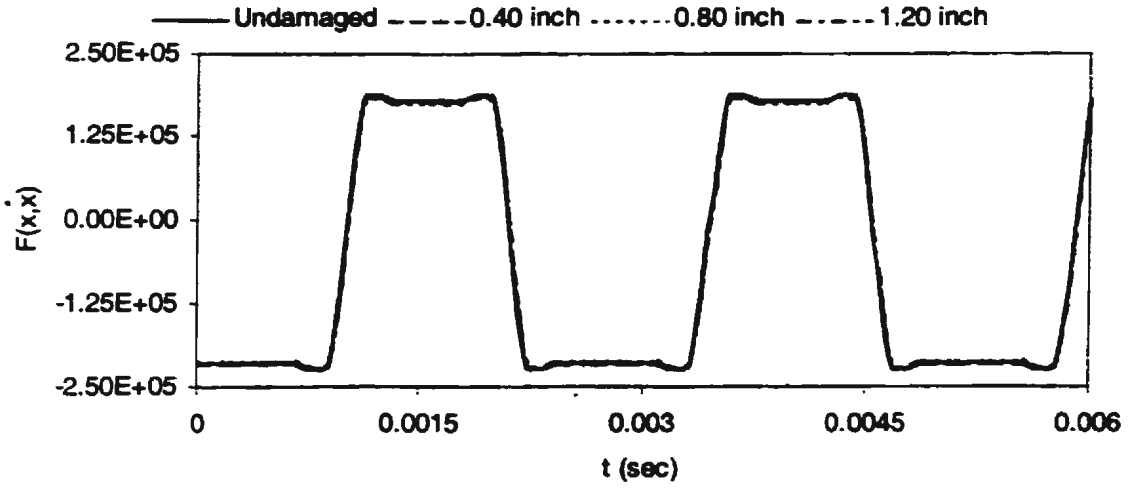

7.10.c: Numerical, Crack at 1.35 inch away from the center

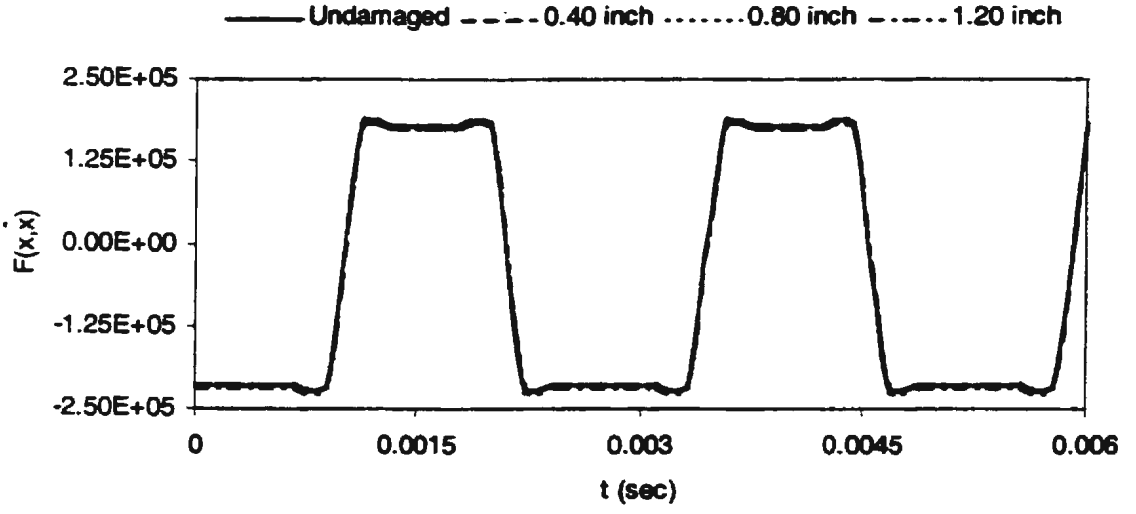

7.10.d: Numerical, Crack at 1.80 inch away from the center

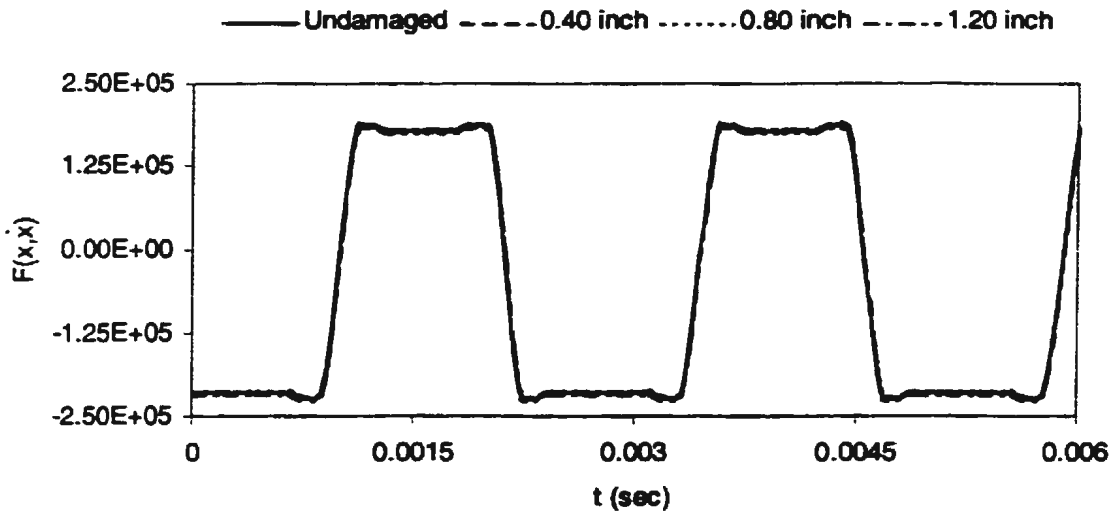

7.10.e: Numerical, Crack at 2.25 inch away from the center

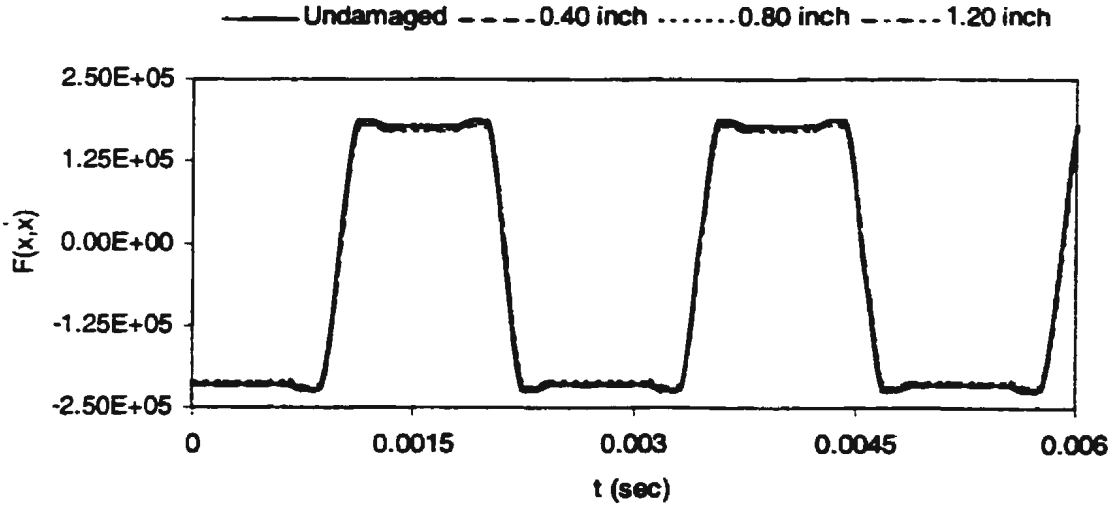

7.10.f: Numerical, Crack at 2.70 inch away from the center

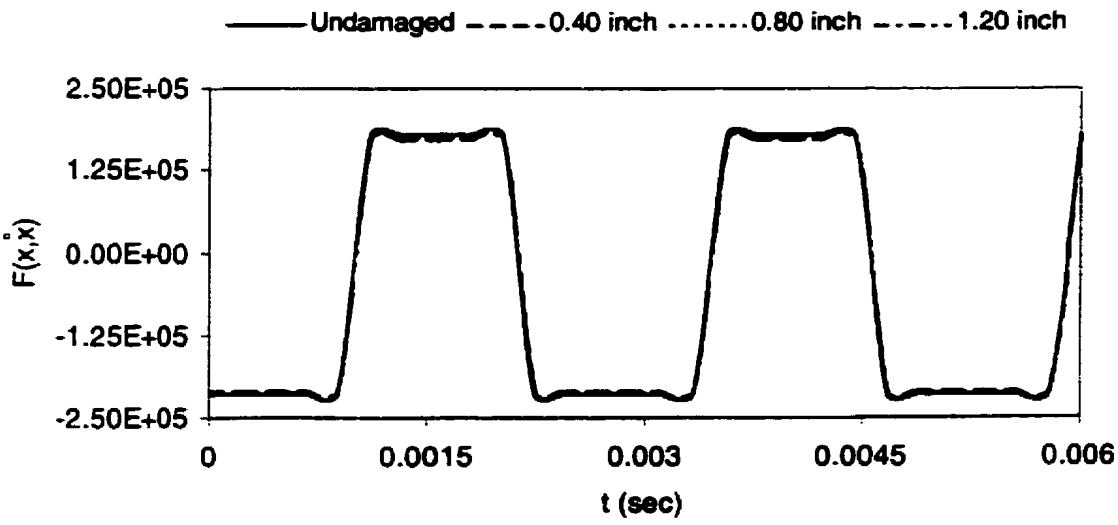

7.10.g: Numerical, Crack at 3.15 inch away from the center

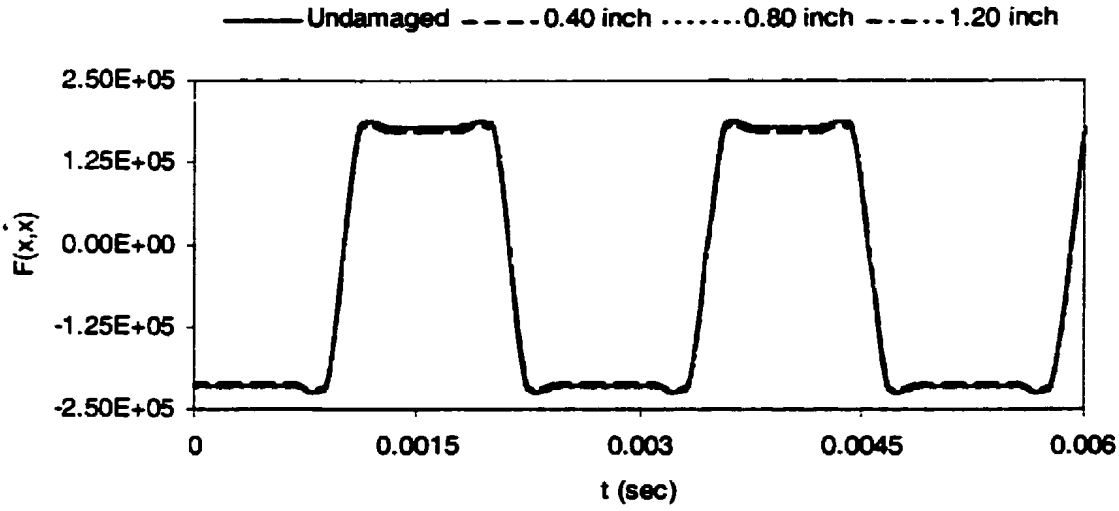

7.10.h: Numerical, Crack at 3.60 inch away from the center

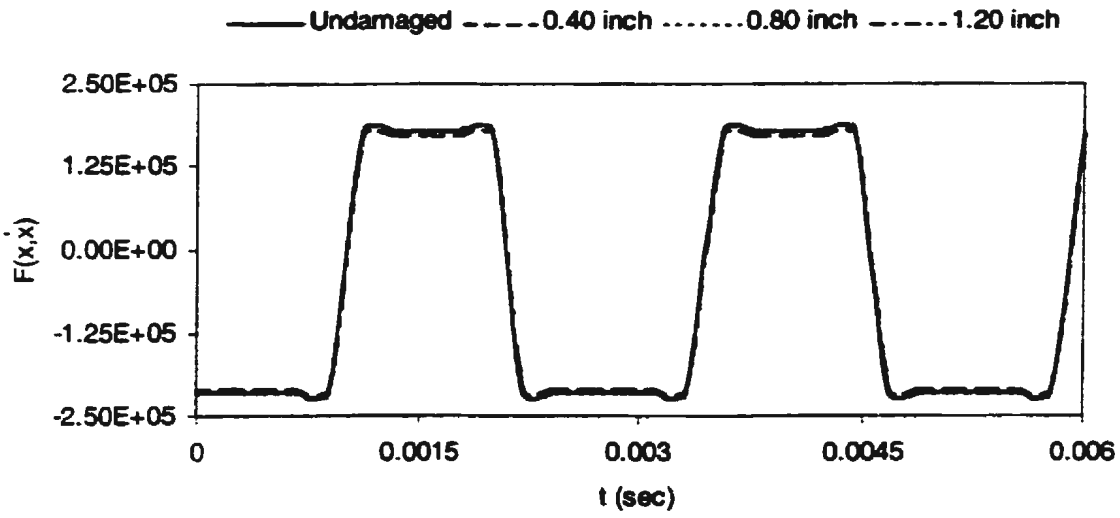

7.10.i: Numerical, Crack at 4.05 inch away from the center

Figure 7.10: Comparison of the Function $F(x,\dot{x})$ for the Undamaged and Damaged Conditions

For the 0.45 inch "away from the center crack" result shown in Figure 7.11.a, the function $F(x,\dot{x})$ has a similar shape as that of the center crack (see Figure 7.7). However, the value of the function $F(x,\dot{x})$ has increased slightly for the crack length of 1.20 inch. The value of the function $F(x,\dot{x})$ gets decreased and the location of its minimum moves from the crack length of 0.60 inch (Figure 7.11.a) to that of 0.40 inch for the 0.90 inch "away from the center crack" as shown in Figure 7.11. B. Nevertheless, the shape is still similar to that of the 0.45 inch "away from the center crack".

The similarity of shape is also obtained in Figure 7.11.c, i.e., for the 1.35 inch "away from the center crack". However, the function $F(x,\dot{x})$ has its minimum value, when the crack

length is 0.80 inch. Figure 7.11.d shows that the trend of the function $F(x,\dot{x})$ for the 1.80 inch "away from the center crack" is similar to that for the 1.35 inch "away from the center crack" shown in Figure 7.11.c. However, the minimum value of the function $F(x,\dot{x})$ occurs when the crack length is 0.75 inch. Similar shape for the function $F(x,\dot{x})$ is also obtained for the 2.25 inch "away from the center crack" as shown in Figure 7.11.e.

The shape of the function $F(x,\dot{x})$ for the 2.70 inch "away from the center crack" is shown in Figure 7.11.f. Comparing with Figures 7.11.a - 7.11.e, Figure 7.11.f is completely different. The maximum value of the function $F(x,\dot{x})$ is not at the undamaged condition or at the crack length of 1.20 inch, but at the crack length of approximately 0.30 inch. The minimum value of the function $F(x,\dot{x})$ is at a crack length of 0.80 inch. Similar shapes for functions $F(x,\dot{x})$ can be seen from Figures 7.11.g, h, and i, respectively. This means that the 2.70 inch "away from the center crack" is the starting point for the change of the shape of the function $F(x,\dot{x})$.

From all these figures of correlation between the values of the function $F(x,\dot{x})$ and crack lengths, at ten different crack locations, it can be seen that the function $F(x,\dot{x})$ has two different shapes. The function $F(x,\dot{x})$ has similar shapes when the location of the crack is between center and the 2.70 inch "away from the center crack". The slight difference between them, especially for the 0.90 inch and the 1.35 inch "away from the center crack", might be due to the fact that the model and its supports are unsymmetric, see Chapter 5. The function $F(x,\dot{x})$ starts to change its shape when the location of the crack is at 2.70 inch "away

from the center crack. Thereafter, the function $F(x,\dot{x})$ has a similar shape until the 4.05 inch "away from the center crack" location is reached.

In order to use the function $F(x,\dot{x})$ for damage identification, the values of function $F(x,\dot{x})$ for six different locations, shown in Figures 7.7 and 7.11.a - 7.11.e, are drawn together and plotted in Figure 7.12. To complement Figures 7.7, 7.11, and 7.12, Figures 7.13.a - 7.13.d and 7.14 show a plot of the maximum values of the function $F(x,\dot{x})$ as the function of the location of crack. The reason for using the values of the function $F(x,\dot{x})$ at six different locations of the crack only is that only for these values the crack appears and grows at the faceplate of the longitudinal around the heavy transverse member. The procedure for using Figures 7.12 and 7.14 for damage identification is as follows:

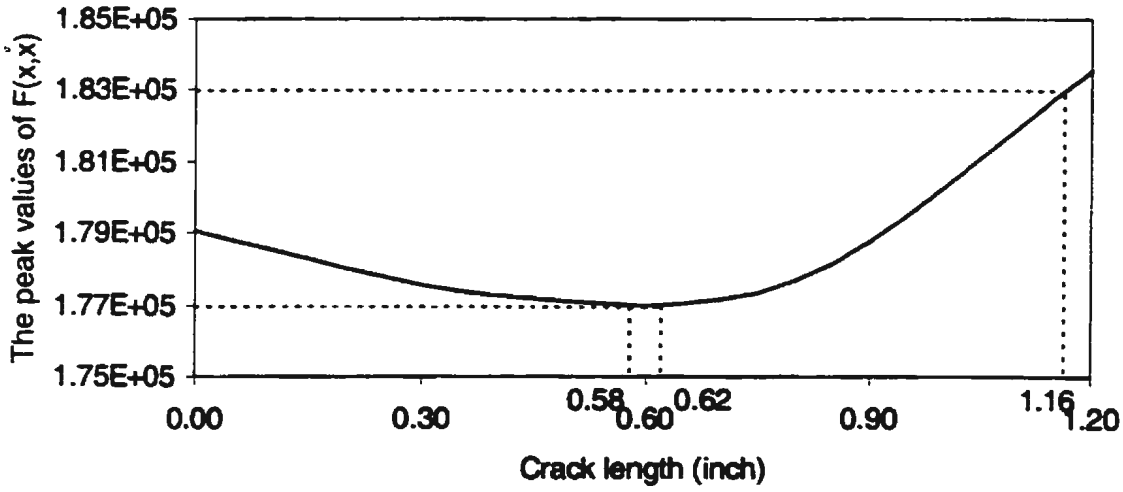

7.11.a: Numerical, Crack at 0.45 inch away from the center

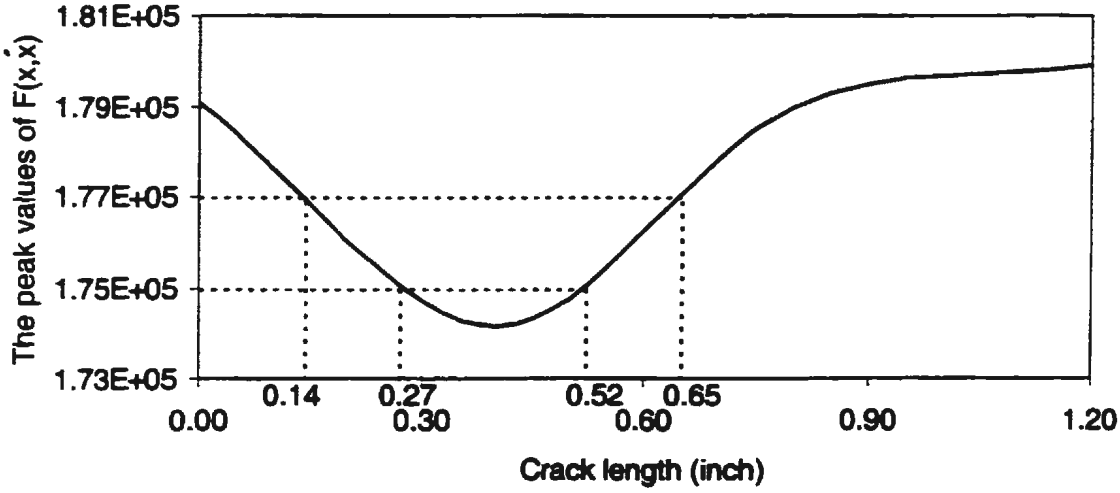

7.11.b: Numerical, Crack at 0.90 inch away from the center

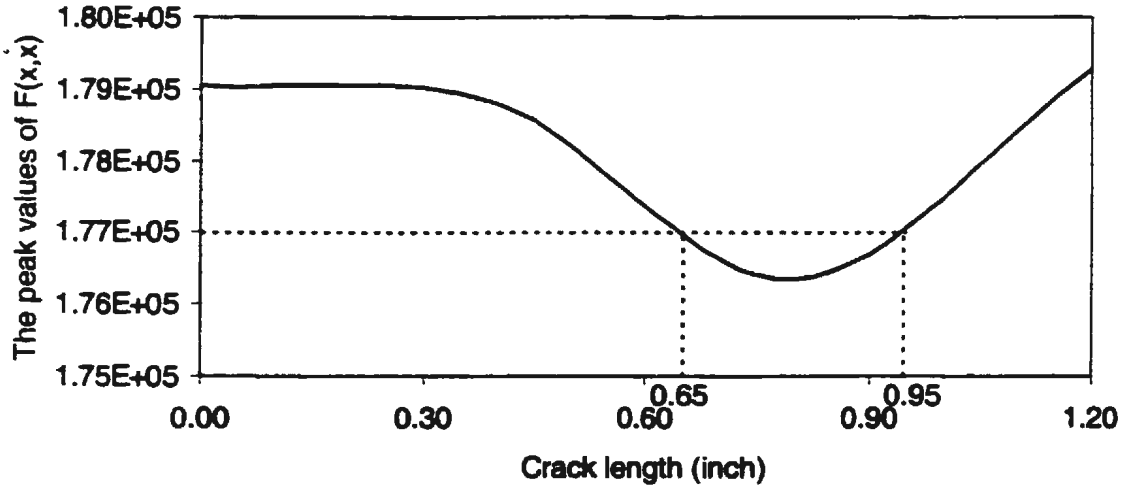

7.11.c: Numerical, Crack at 1.35 inch away from the center

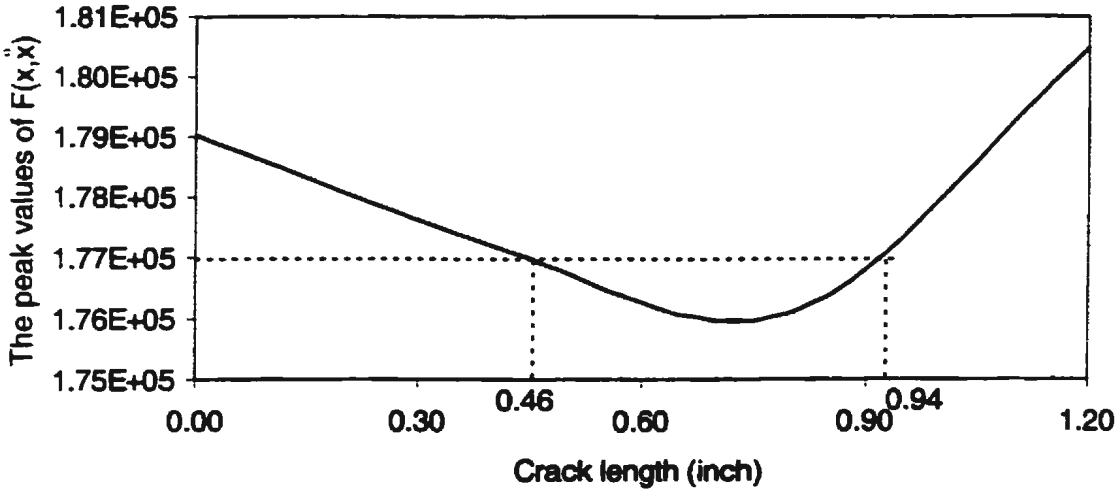

7.11.d: Numerical, Crack at 1.80 inch away from the center

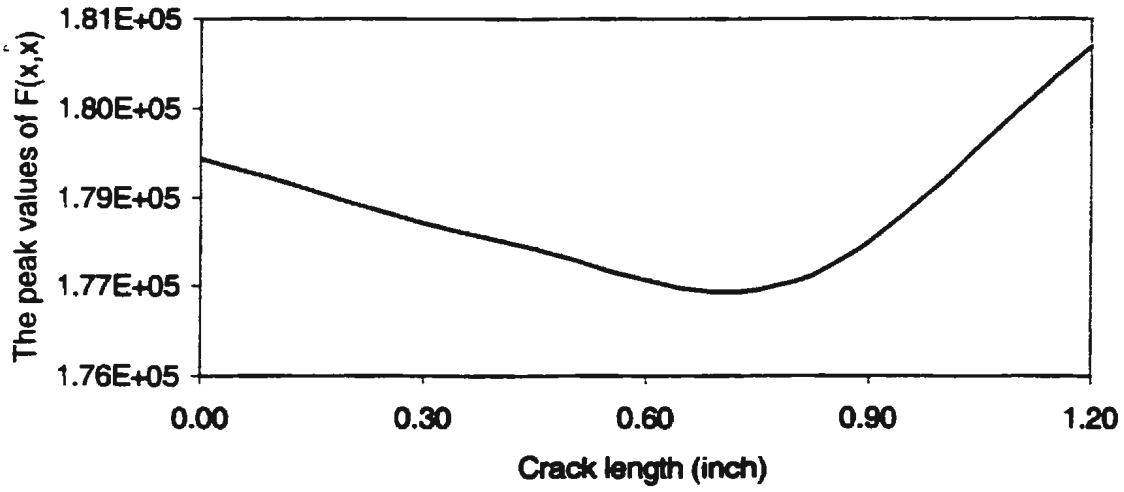

7.11.e: Numerical, Crack at 2.25 inch away from the center

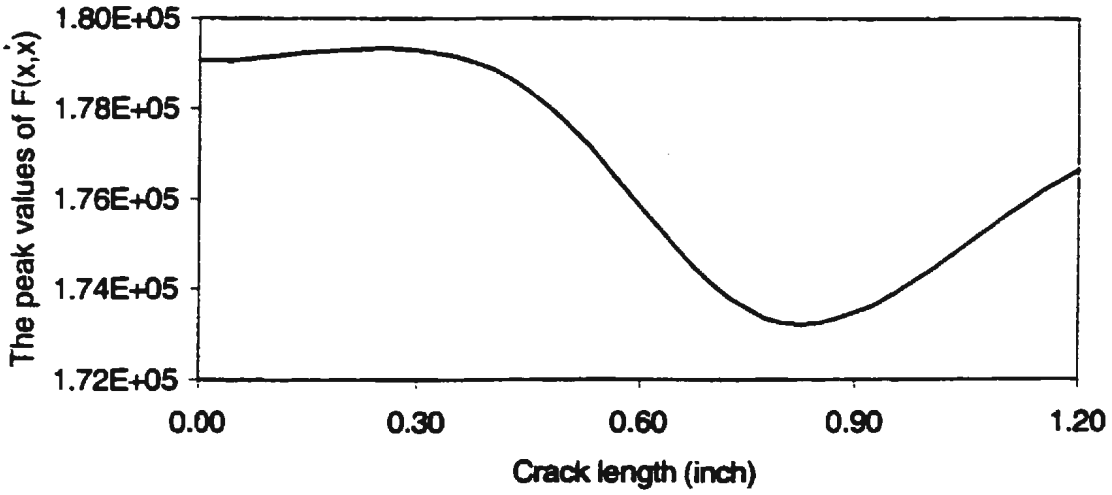

7.11.f: Numerical, Crack at 2.70 inch away from the center

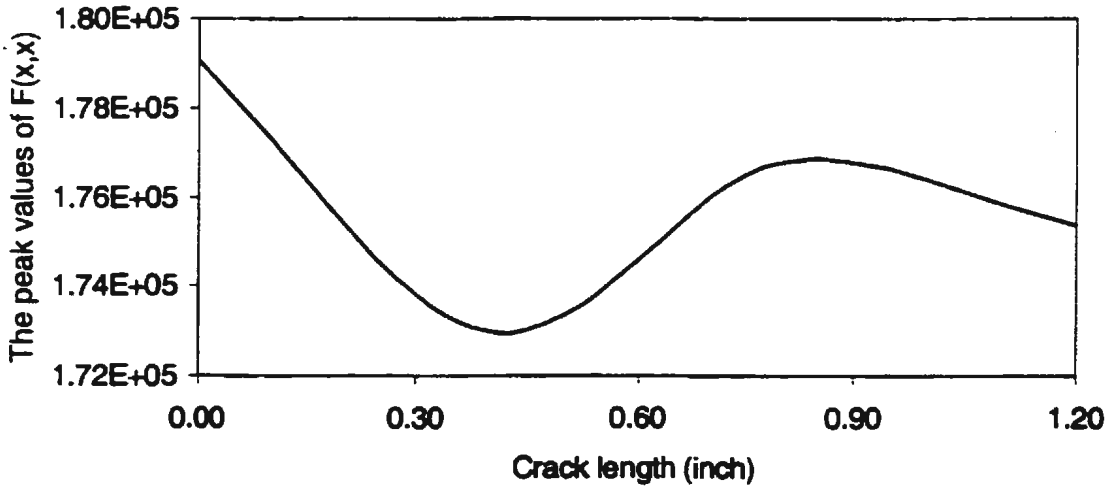

7.11.g: Numerical, Crack at 3.15 inch away from the center

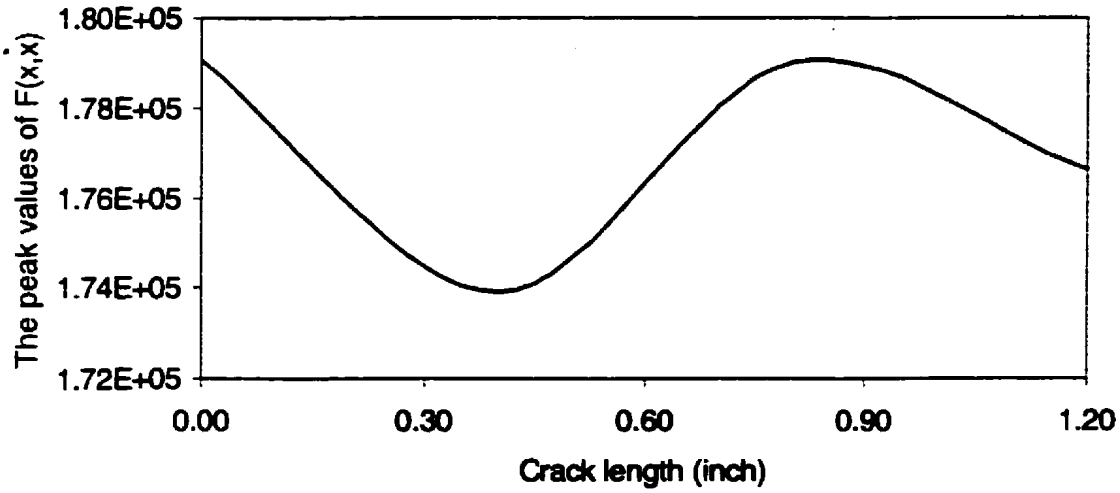

7.11.h: Numerical, Crack at 3.60 inch away from the center

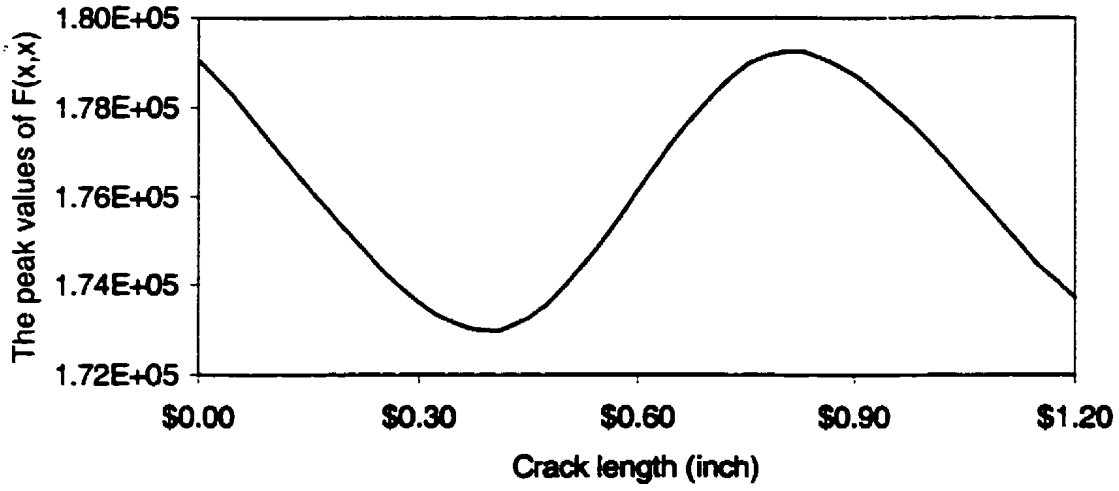

7.11.i: Numerical, Crack at 4.05 inch away from the center

Figure 7.11: The Peak Values of Function $F(x,\dot{x})$ for each Crack Length

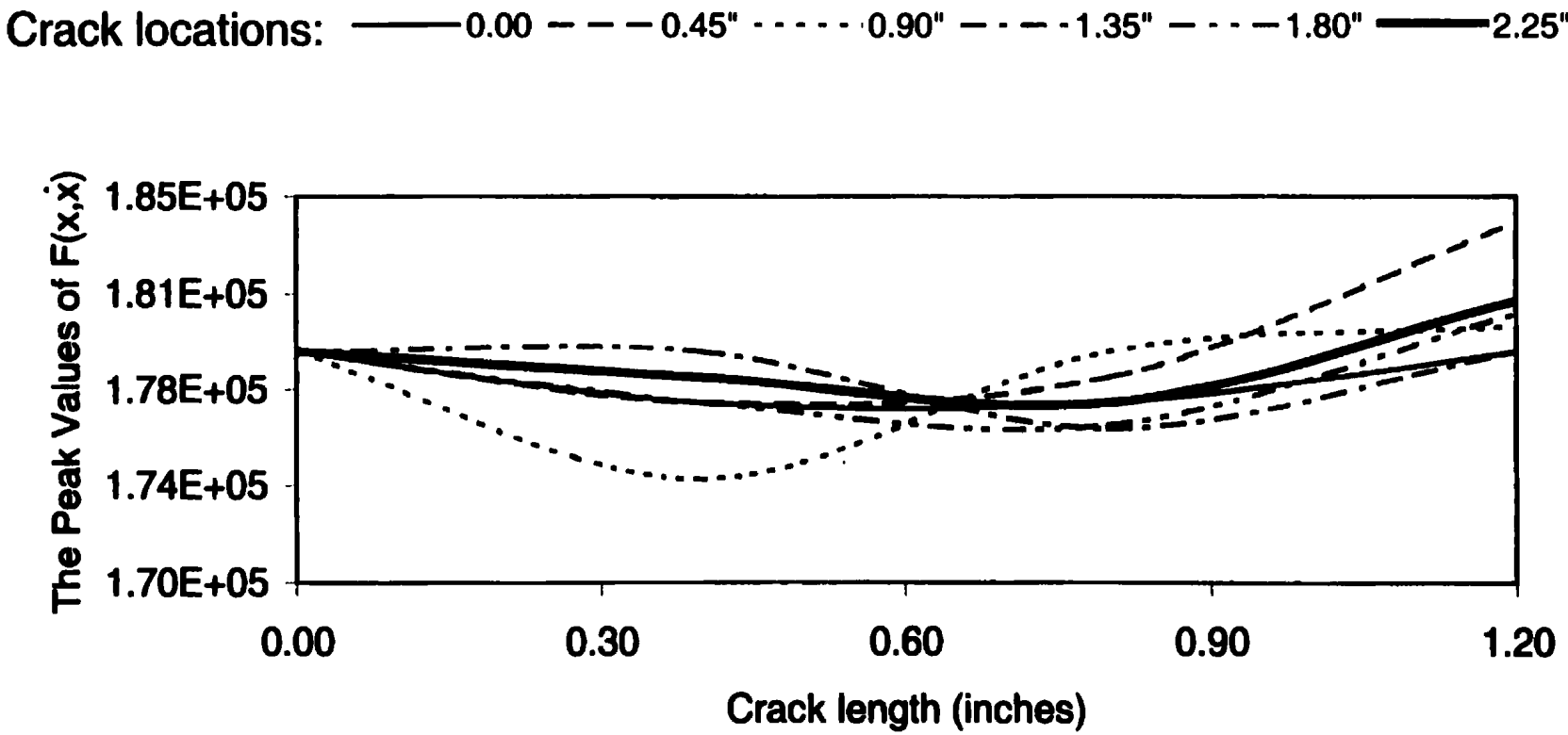

Figure 7.12: The Peak Values of Function $F(x, \dot{x})$ vs. the Crack Length (Numerical)

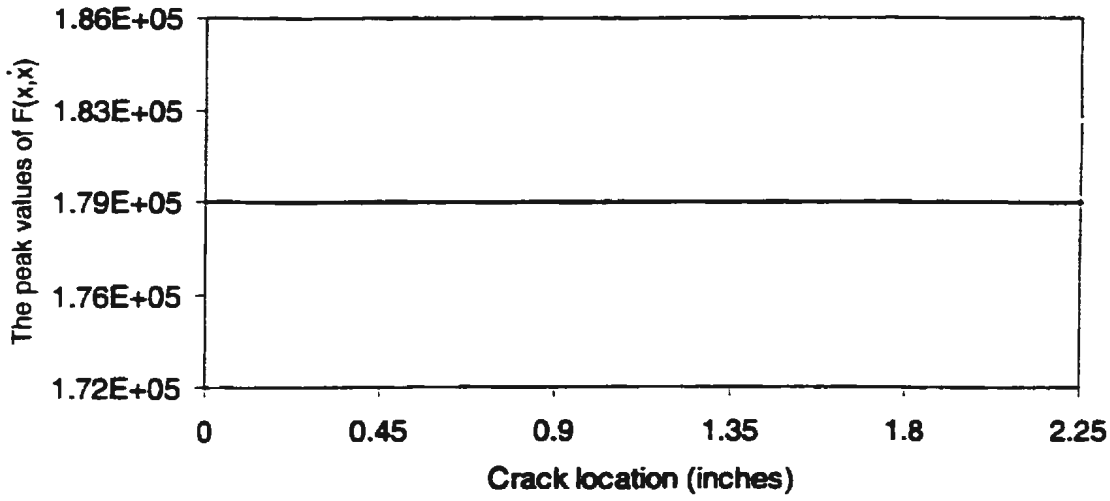

7.13.a: Numerical, Undamaged

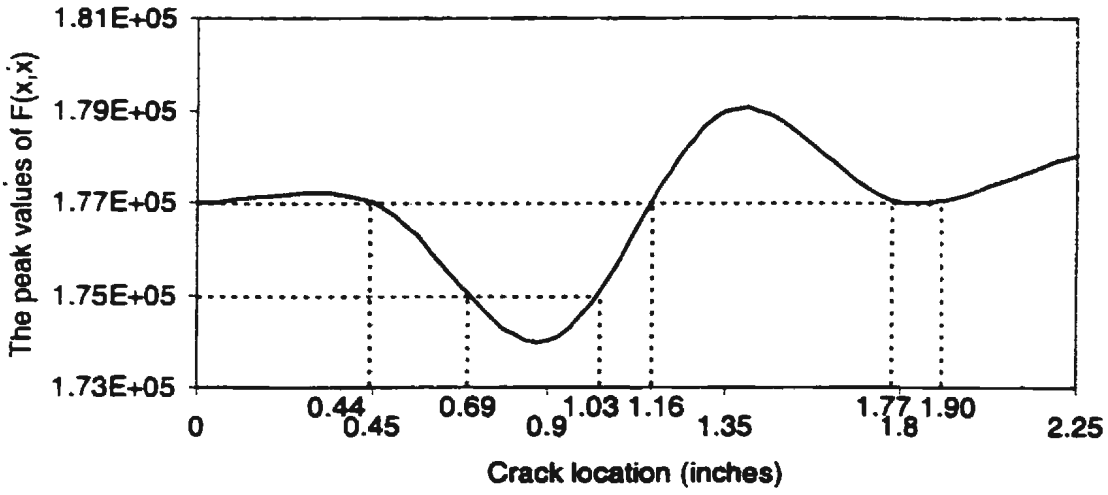

7.13.b: Numerical, Crack length = 0.40 inch

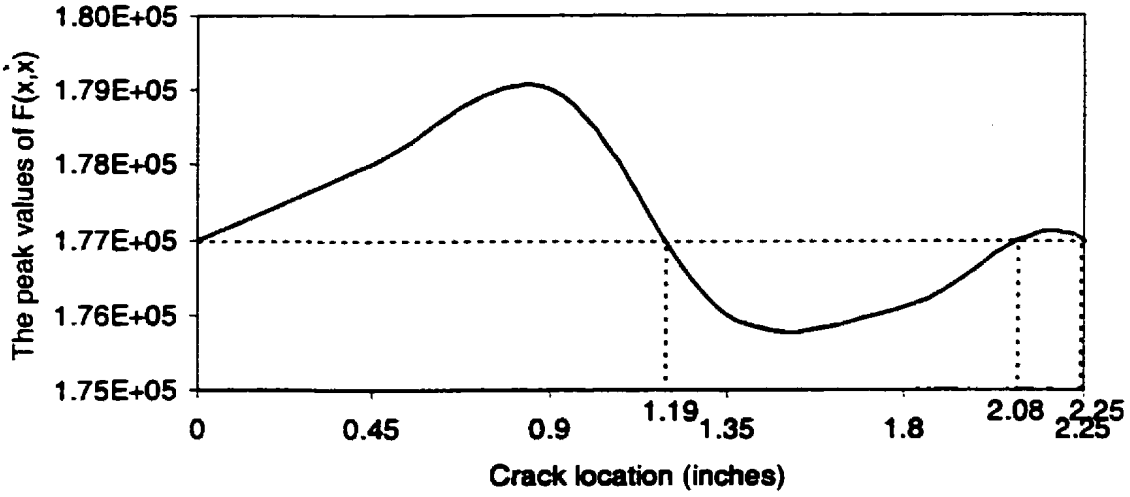

7.13.c: Numerical, Crack length = 0.80 inch

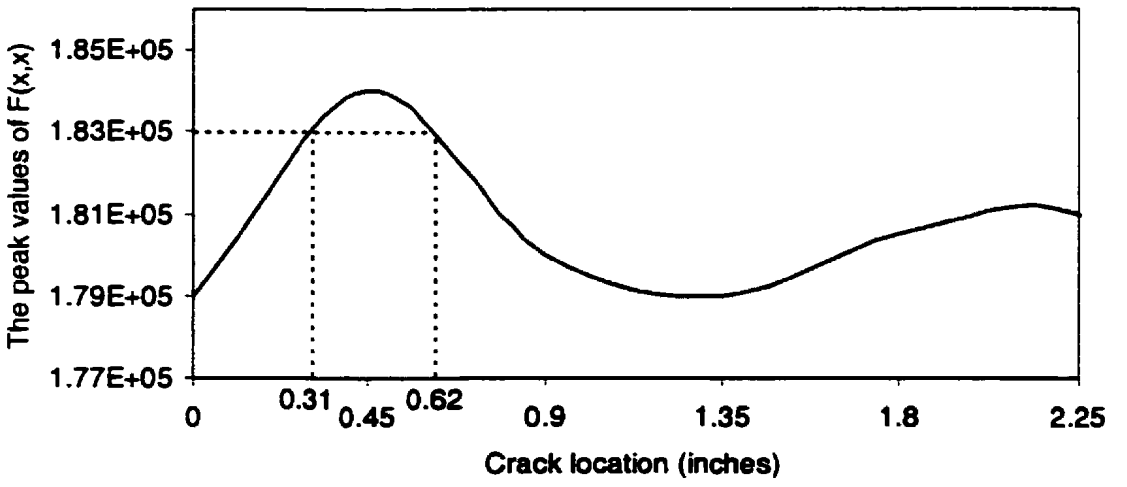

7.13.d: Numerical, Crack length = 1.20 inch

Figure 7.13: The Peak Values of Function $F(x,\dot{x})$ for each Crack Location

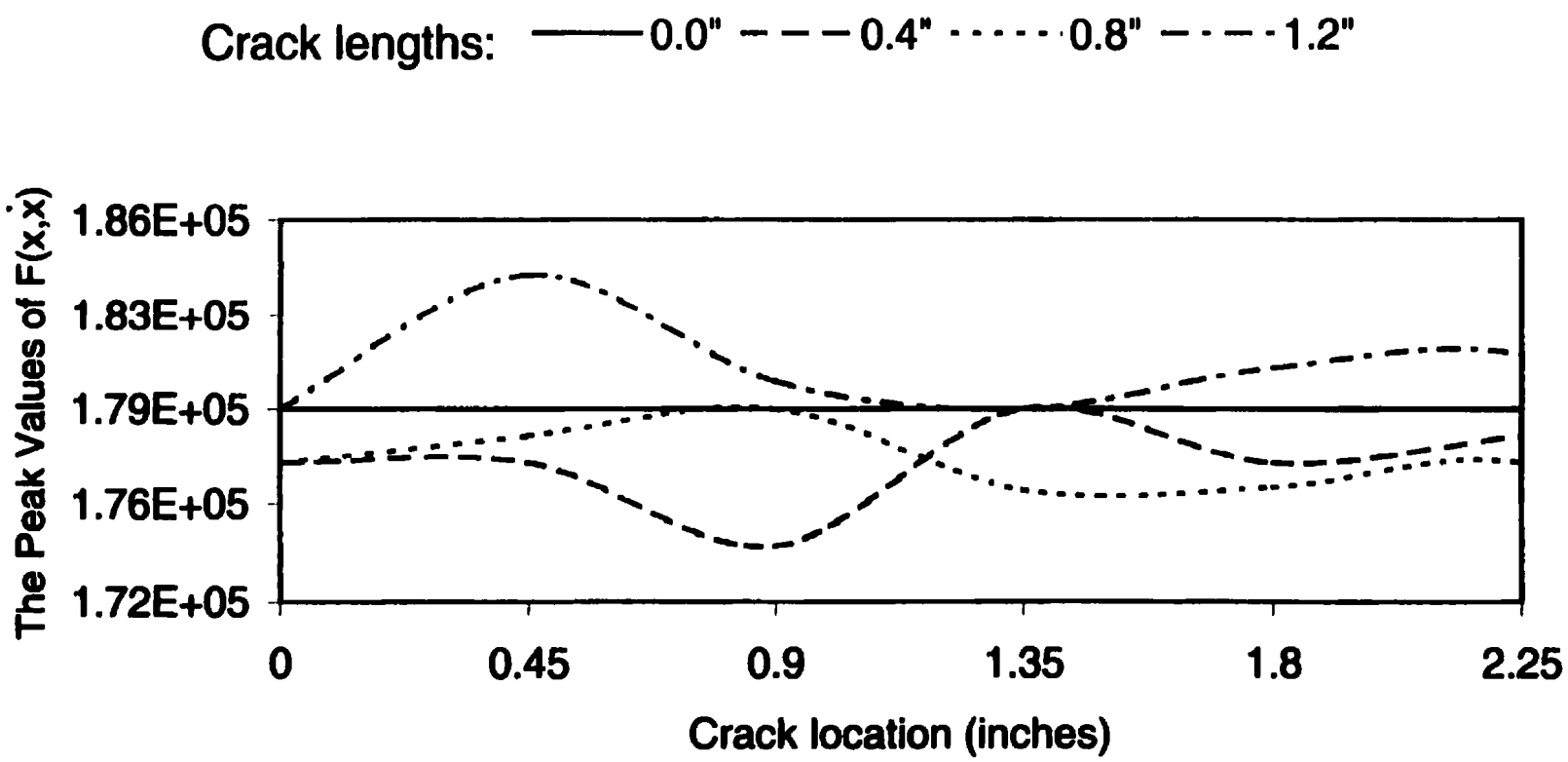

Figure 7.14: The Peak Values of Function $F(x, \dot{x})$ vs. the Crack Location (Numerical)

The damage is assumed to be present at a certain location of the longitudinal faceplate of the model. At periodic instants of time, the random response of the model is acquired, and the autocorrelation function is calculated. The autocorrelation function, its first derivative, and the frequency are used to train the neural network for predicting the value of the function $F(x,\dot{x})$. The value is then compared with that of the 'healthy" model for indicating the presence of damage. A change in the value of the function $F(x,\dot{x})$ indicates the occurrence of damage. In addition to this method, the change in the form of the crosscorrelation functions as stated in Chapter 6 can also be used for detecting damage.

In order to identify the extent and the location of crack, the value of the function $F(x,\dot{x})$ is compared with the values in Figures 7.12 and/ or 7.14. Three methods can be used to identify the extent and the location of the damage using Figures 7.12 or/ and 7.14.

The first method is that if the value of the function $F(x,\dot{x})$ crosses one curve in Figures 7.12 or 7.14 at one location only. For example: let us say that the value of the function $F(x,\dot{x})$ obtained is 1.83E+05. In Figures 7.12 or 7.11.a, this value crosses the curve of the 0.45 inch "away from the center crack". From this curve a crack length of approximately 1.16 inch (=1.20 inch) is obtained.

The second method is used if the value of the function $F(x,\dot{x})$ crosses one curve in Figures 7.12 or 7.14 at two locations or more. For example: let us say that 1.75E+05 is the value of the function $F(x,\dot{x})$ obtained from measurement. The curve of the 0.90 inch "away from the center crack" in Figures 7.12 of 7.11.b is crossed by the value 1.75E+05 at the crack

lengths of 0.27 inch and 0.52 inch. By averaging these two values, the crack length of approximately 0.40 inch is obtained. Similar results can also be obtained by feeding the value of the function $F(x,\dot{x})$ to Figure 7.14 or 7.13.b. In Figures 7.14 or 7.13.b, the value of 1.75E+05 crosses the curve of the 0.40 inch crack at the crack locations of 0.69 inch and 1.03 inch, respectively. By averaging these two values, the crack location of 0.85 inch (= 0.90 inch) is obtained. This result is similar to that obtained using Figures 7.12 or 7.11.b.

In order to verify that the second method can give the correct result, the value of the function $F(x,\dot{x})$ of 1.83E+05 used in an earlier part of the study is used again to obtain the extent and the location of crack using Figure 7.14 or 7.13.d. In Figures 7.14 or 7.13.d, the value of the function $F(x,\dot{x})$ crosses the curve of 1.20 inch at the location of 0.31 inch and 0.62 inch. The crack location of approximately 0.46 inch (= 0.45 inch) is obtained by averaging the two results. The result is similar to that obtained using Figure 7.12 or 7.11.a.

The third method is for cases where the value of the function $F(x,\dot{x})$ crosses more than one curve in Figures 7.12 and 7.14, at one or more locations. Supposing the value of 1.77E+05 is the output of the network. The value crosses four curves in Figures 7.12 or 7.11.a, b, c, d, and two curves in Figures 7.14 or 7.13.b, c. The results are tabulated in Tables 7.1 and 7.2. In order to obtain the extent and the location of the crack, the results in Tables 7.1 and 7.2 are compared. Similar results are obtained from two tables, i.e., a crack length of 0.70 inch (=0.8 inch) at the 1.80 inch is obtained from Table 7.1, and from Table 7.2 a the crack length of 0.80 inch at the 1.84 inch (=1.80 inch) is obtained.

The slight difference between the results obtained using the three methods is mainly due to the fact that the number of data used for creating curves in Figures 7.7. 7.11, 7.12, 7.13 and 7.14 are limited. However, this difference can be accepted. The damage identification method explored in the present study can also be used to identify the damage occurrence in similar structures. For a different structure, results from a FE model of the structure is needed to estimate the value of the function $F(x,\dot{x})$ for the undamaged and the damaged conditions.

Table 7.1: The Length and the Location of Crack obtained from Figures 7.11.a, b, c, d, or 7.12 for an output of 1.77E+05 from the function $F(x,\dot{x})$

Identification No	Crack Location (inches)	Crack Length (inches)		
		1	2	Average
1	0.45 (Fig. 7.11.a)	0.58	0.62	0.55
2	0.90 (Fig.7.11.b)	0.14	0.65	0.40
3	1.35 (Fig7.11.c)	0.65	0.95	0.80
4	**1.80** (Fig. 7.11.d)	0.46	0.94	**0.70**

Table 7.2: The Length and the Location of Crack obtained from Figures 7.13.b, c, or 7.14 for an output of 1.77E+05 from the function $F(x,\dot{x})$

Identification No	Crack Length (inches)	Crack Location (inches)				
		1	2	3	4	Average
1	0.40 (Fig. 7.13.b)	0.44	1.16	1.77	1.90	1.32
2	**0.80** (Fig. 7.13.c)	1.19	2.08	2.25	-	**1.84**

7.4 Summary

The neural network technique was used for identifying the crack location and size utilizing autocorrelation functions of the model; experimental and numerically generated data of Model #1 were used in the study. Experimentally, the technique was used to identify the presence and the extent of damage in Model #1 at a location 0.90 inch from center of the heavy transverse member. The output showed that the technique was able to discriminate between cracks of different lengths.

In order to identify the presence and the extent of damage at other locations, a FE model of Model #1 was developed for ten different locations of cracks. It was observed from the results that the analytical autocorrelation functions were in excellent agreement with their predicted curves obtained using the technique. As the output from the neural network, values of the function $F(x,\dot{x})$ for various crack lengths and locations were obtained. Two curves,

i.e., the function $F(x,\dot{x})$ vs. the crack length and the function $F(x,\dot{x})$ vs. the crack location, were plotted.

These curves were used to identify the extent and the location of the damage at the faceplate of the longitudinal when the value of the function $F(x,\dot{x})$ at a certain time was known. The results indicated that the technique was successful in identifying not only the presence of the damage but also its extent and location.

Chapter 8

Conclusions, Contributions, and Recommendations

8.1 Conclusions

The main objective of the present study is to develop a technique that can be used for identifying the occurrence of damage, the location of damage and its extent in the side shell of a ship's structure. Four different methods were tested. These methods are based on the use of the frequency response function, the randomdec signature, the auto- and cross-correlation functions, and the neural network technique. Based on the systematic study of the dynamic behavior of the undamaged and the damaged structure using four stiffened plate models, the following conclusions have been made:

1. The randomdec technique can be used to determine the free vibration response of the structure from its stationary random response.
2. The autocorrelation function can be use to represent the free vibration response of the

structure.

3. The presence of water can be modeled as a lumped added mass factor. It results in the decrease of the natural frequency. However, the shape of the random signatures or free vibration response remained the same as those in air. The increase of water depth also caused a decrease in the natural frequency.

4. Damage produces a shift in the natural frequencies that can be detected from the frequency response function. However, this shift is usually small and does not appear in all modes. From the models used in the present study, the significant shift only took place in connection with the fourth mode. This is the bending mode of the longitudinal.

5. It is very difficult to detect the changes in the natural frequencies due to damage occurrence using the randomdec signatures, the autocorrelation or the cross correlation functions.

6. Damage occurrence can be detected by monitoring the qualitative changes in the form of the crosscorrelation function.

7. The technique developed in the present study which uses a function $F(x,\dot{x})$ as a criterion for damage occurrence is successful. The use of the neural networks technique to determine the magnitude of the function $F(x,\dot{x})$ provides a tool which is consistent, robust, and unambiguous for detecting damage occurrence and its extent.

8. The technique also shows potential for the identifying the location of the damage.

However, more work needs to be done in this area.

8.2 Contributions

The main contribution of the present study is the development of a robust method for identifying damage occurrence as well as its extent and location. The use of neural network technique along with the randomdec signature and autocorrelation function produces an ambiguous method for the identification of damage.

8.3 Recommendations

The present study has demonstrated the capability of the neural network technique for identifying the damage occurrence in the stiffened plate model. In order to get the best results, the following suggestions are recommended for future studies:

(a) In order to ensure that the method developed in the present study can be generalized, models with different configurations should be tested.

(b) In order to ensure that the dynamic response of a ship's structure due to wave excitation can be analyzed using the developed approach, a full scale model testing should be conducted in a towing tank using wave excitations from the sea.

(c) Identification of critical points on a ship's structure and the feasibility of using the

developed technique as a part of a general response monitoring system should be investigated.

(d) A neural network technique which can identify the map from the autocorrelation function or the function $F(x,\dot{x})$ as input to the crack length or the crack location as output should be developed. The output is used to identify the extent or the location of the crack using Figures 7.12 or 7.14.

References and Bibliography

[01] Allemang, R. J., and Brown, D. L., "Modal Analysis and Testing", Shock and Vibration Handbook, Fourth Edition, McGraw-Hill Inc, pp. 21.1-21.74, 1996.

[02] Barai, S. V., and Pandey, P. C., "Vibration Signature Analysis Using Artificial Neural Networks", Journal of Computing in Civil Engineering, Vol. 9, No. 4, pp. 259-265, 1995.

[03] Barai, S. V., and Pandey, P. C., "Time-Delay Neural Networks in Damage Detection of Railway Bridges", Advances in Engineering Software, Vol. 28, No. 1, pp. 1-10, 1997.

[04] Bruel & Kjaer Inc., "Instruction manual of B & K 2034 dual channel signal analyzer", Vol. 1, 2, and 3, 1987.

[05] Caudill, M., and Butler, C., "Understanding Neural Networks: Computer Explorations", Vol 1, The MIT Press, Cambridge, USA, 1994.

[06] Ceravalo, R., and Stevano, A. D., "Damage Location in Structures Through a Connectivistic Use of FEM Modal Analyses", Modal Analysis: The International Journal of Analytical and Experimental Modal Analysis, Vol. 10, no. 3, pp.176, 1995.

[07] Chen, Y., and Swamidas, A. S. J., "Change of Modal Parameters due to Crack Growth in a Tripod Tower Platform", Canadian Journal of Civil Engineering, Vol. 20, 1993.

[08] Chen, Y., "Crack Detection in Plated T-joints Through Vibration Techniques", Ph.D. Dissertation, Faculty of Engineering and Applied Science, Memorial University of Newfoundland, St. John's, Canada, 1996.

[09] Cole, H. A., "On-line Failure Detection and Damping Measurement of Aerospace Structures by Random Decrement Signatures", NASA CR-2205, 1973.

[10] Cramer, E. H., Loseth, R., and Bitner-Gregersen, E., "Fatigue in Side Shell Longitudinals due to External Wave Pressure", Safety and Reliability Proceedings of the International Conference on Offshore Mechanics and Arctic Engineering (OMAE), Vol. 2, pp. 267-272, 1993.

[11] Curtis, A. J, and Lust, S. D., "Concepts in Vibration Data Analysis", Shock and Vibration Handbook, Fourth Edition, McGraw-Hill Inc, 1996.

[12] De Kat, J. O., Lemmen, P., Moore, C. S., and Vredeveldt, A. W., "Dynamic Loading and Strength of a Stranded Double Hull Tanker in Waves", Proceeding of the 5th International Offshore and Polar Engineering Conference, Vol. IV, pp.465-470, 1995.

[13] Doebling, S. W., Farrar, C. R., Prime, B. M., and Shevitz, D. W., "Damage Identification and Health Monitoring of Structural and Mechanical Systems from Changes in Their Vibration Characteristics: A Literature Review", Los Alamos National Laboratory, New Mexico, 1996.

[14] Elkordy, M. F., Chang, K. C.,and Lee, G. C., "Neural Networks Trained by Analytically Simulated Damage States", Journal of Computing in Civil Engineering, Vol. 7, No. 2, pp. 130-145, 1993.

[15] Ewins, D. J., "Modal Testing: Theory and Practice", Research Studies Press Ltd, England, 1996.

[16] Ghoneim, G. A., and Tadros, G., "Finite Element Analysis of Damaged Ship Hull Structures", Offshore Technology Proceedings of the International Conference on Offshore Mechanics and Arctic Engineering (OMAE), Vol. I-B, pp. 611-620, 1992.

[17] Haddara, M. R., "On the Random Decrement for Nonlinear Rolling Motion", Proceedings of the Eleventh International Conference on Offshore Mechanics and Arctic Engineering, Vol. II, Safety and Reliability, pp. 321-324, 1992.

[18] Haddara, M. R., Wishahy, M., and Wu, X., "Assessment of Ship's Transverse Stability at Sea", Ocean Engineering, Vol. 21, No. 8, pp. 781-800, 1994.

[19] Haddara, M. R., "On the Use of Neural Network Techniques for the Identification of Ship Stability Parameters at Sea", Proceedings of the Fourteenth International Conference on Offshore Mechanics and Arctic Engineering, Vol. II, Safety and Reliability, pp. 127-135, 1995.

[20] Haddara, M. R., and Hinchey, M., "On the Use of Neural Network Techniques in the Analysis of Free Roll Decay Curves", International Shipbuilding Progress, Vol. 42, No. 430, pp. 166-178, 1995.

[21] Haddara, M. R., and Sabin, G., " Parametric Identification of Hydrodynamic

Characteristic from Ship Maneuvering Trails using Neural Networks", Presented to the 24th American Towing Tank Conference, Texas A&M University, USA, 1995.

[22] Haddara, M. R., and Wang, Y., " Parametric Identification of Coupled Sway and Yaw Motions",Proceedings of the fifteenth International Conference on Offshore Mechanics and Arctic Engineering, Vol. I, Offshore Technology, pp. 267-273, 1996.

[23] Haddara, M. R., and Cao, S., " A Study of the Dynamic Response of Submerged Rectangular Flat Plates", Marine Structures, Vol. 9, pp. 913-933, 1996.

[24] Haddara, M. R., and Xu, J., "On the Use of Random Decrements in the Identification of Two Degrees of Freedom Systems", Proceedings the Canadian Society for Mechanical Engineering Forum1998, Vol. 4, pp. 499-507, Toronto, Canada, 1998.

[25] Haddara, M. R., and Xu, J., " On the Identification of Ship Coupled Heave-pitch Motions Using Neural Networks", Ocean Engineering, Vol. 26, No. 5, pp.381-400, 1999.

[26] Hansen, P. F., and Winterstein, S. R., " Fatigue Damage in the Side Shells of Ships", Marine Structures, Vol. 8, No. 8, pp. 631-655, 1995.

[27] Ibrahim, S. R., " Random Decrement Technique for Modal Identification of Structures", The AIAA Journal of Space Craft and Rockets, Vol. 14, no. 11, pp. 696-700, 1977.

[28] Ito, H., Hayashi, K., and Kitano, K., "A Comparative Study of Simplified Methods to Analyze the Strength of Double-Hulled Tankers in Collision", Proceeding of the 4th International Offshore and Polar Engineering Conference, Vol. IV, pp.563-569,

1994.

[29] Klenke, S. E., and Paez, T. L., "Damage Identification with Probabilistic Neural Networks", Proceedings of the 14th International Modal Analysis Conference, pp. 99-104, 1996.

[30] Kudva, J. N., Munir, N., and Tan, P., "Damage Detection in Smart Structures using Neural Networks and Finite Element Analysis", Paper presented at the ADPA/AIAA/ASME/SPIE Conference on Active Materials and Adaptive Structure, Session 30, pp. 559-562, 1992.

[31] Kuroiwa, T., Nakamura, T., Kawamoto, Y., Kondo, M., and Kusuba, S., "Study on Structural Damage of Ships due to Collision and Grounding", Proceeding of the 4th International Offshore and Polar Engineering Conference, Vol. IV, pp. 416-420, 1994.

[32] Krishnamoorthy, C. S., "Finite Element Analysis, Theory and Programming", Tata McGraw-Hill Publishing Company Limited, New Delhi, 1987.

[33] Lawry, M. H.," I-DEAS Master Series, Student Guide", Structural Dynamics Research Cooperation, USA, 1996.

[34] Leath, W. J., and Zimmerman, D. C., "Analysis of Neural Network Supervised Training with Application to Structural Damage Detection", Damage and Control of Large Structures, Proceeding of the 9th VPI & SU Symposium, pp. 583-594, 1993.

[35] Lim, T. W., Cabell, R. H., and Silcox, R. J., "On-Line Identification of Modal Parameters Using Artificial Neural Networks", Journal of Vibration and Acoustics,

Vol. 118, pp. 649-656, 1996.

[36] Mangal, L., Idichandy, V. G., and Ganapathy, C., "ART-based Multiple Neural Networks for Monitoring Offshore Platforms", Applied Ocean Research, Vol. 18, No. 2-3, pp. 137-143, 1996.

[37] Marshall, M. A., "Structural Integrity Monitoring of a Hydro-Elastic Model of a Jacket Platform", Ph.D. Dissertation, Faculty of Engineering and Applied Science, Memorial University of Newfoundland, St. John's, Canada, 1990.

[38] Masri, S. F., Nakamura, M., Chassiakos, A. G., and Caughey, T. K., "Neural Network Approach to Detection of Change in Structural Parameters", Journal of Engineering Mechanics, Vol. 122, No. 4, pp. 350-360, 1996.

[39] Osegueda, R. A., and D'Souza, P. D., "Damage Evaluation of an Offshore Structure Model using Vibration Measurements", Proceeding of the 2nd International Offshore and Polar Engineering Conference, Vol. IV, pp.550-557, 1992.

[40] Paik, J. K., and Lee, T. K., "Damage and Residual Strength of Double-Hull Tankers in Grounding", International Journal of Offshore and Polar Engineering, Vol. 5, No. 4, pp. 286-293, 1995.

[41] Rhim, J., and Lee, S. W., "A Neural Network Approach for Damage Detection and Identification of Structures", Computational Mechanics, Vol. 16, No. 6, pp. 437-443, 1995.

[42] Rodd, J. L., and Sikora, J. P., " Double Hull Grounding Experiments", Proceeding of the 5th International Offshore and Polar Engineering Conference, Vol. IV, pp. 446-

456, 1995.

[43] Roitman, N., Batista, R. C., Magluta, C., Viero, P. F., and Sarquis, F. M., "Identification of Structural Damages in Fixed Offshore Platforms", Proceeding of the 1st International Offshore and Polar Engineering Conference, Vol. IV, pp. 77-83, 1991.

[44] Roskilly, A. P., and Mesbahi, E., "Marine System Modelling using Artificial Neural Networks: An Introduction to the Theory and Practice", Transaction of Marine Engineering, Vol. 108, part 3, pp. 185-201, 1996.

[45] Satsangi, S. K., and Ray, C., "Structural Analysis of Ships' Stiffened Plate Panels in Bending", International Shipbuilding Progress, Vol. 45, No. 442, pp. 181-195, 1998.

[46] Seed, G. M., and Murphy, G. S., "The Applicability of Neural Networks in Modeling the Growth of Short Fatigue Cracks", Fatigue & Fracture of Engineering Material & Structures, Vol. 21 No. 2, pp. 183-190, 1998.

[47] Shahrivar, F., and Bouwkamp, J. G., " Damage Detection in Offshore Platform Using Vibration Information", Journal of Energy Resources Technology, Transaction of the ASME, Vol. 108, pp. 97-106, 1986.

[48] Spectral Dynamics, Inc., STAR System Reference Manual", 1994.

[49] Strathaus, R. S., and Bea, R., " Fatigue Database Development and Analysis", Technical Report SMP 1-1, Department of Naval Architecture & Offshore Engineering, University of California at Berkeley, 1992.

[50] Strathaus, R. S., and Bea, R., "SSIIS-The Ship Structural Integrity Information

System". Marine Technology, Vol. 33, No. 4, pp.299-308, 1996.

[51] Sucharski, D., "Crude Oil Tanker Hull Structure Fracturing: An Operator's Perspective", Paper presented at Prevention of Fracture in Ship Structure in Washington D. C., pp 87-124, 1995.

[52] Szewczyk, Z. P., and Hajela, P., "Damage Detection in Structures Based on Feature-Sensitive Neural Networks", Journal of Computing in Civil Engineering, Vol. 8, No. 2, pp. 163-178, 1994.

[53] The Math Works, Inc, "Matlab: Reference Guide", 1992.

[54] Vandiver, J. K., Dunwoody, A. B., and Campbell, R. B., "A Mathematical Basis for the Random Decrement Vibration Signature Analysis Technique", Journal of Mechanical Design, Vol. 104, pp. 307-313, 1982.

[55] Viero, P. F., and Roitman, N., "Application of Some Damage Identification Methods in Offshore Platforms", Marine Structures, Vol. 12, pp.107-126, 1999.

[56] Williams, L., "Artificial Neural Network Applications to Naval and Commercial Ships", Newport News Shipbuilding, The Society of Naval Architects and Marine Engineers (Hampton Roads Section), pp. 1-25, 1993.

[57] Worden, K., Ball, A. D., and Tomlinson G. R., "Neural Networks for Fault Location", Proceedings of the 11th International Modal Analysis Conference, Vol. 2, pp. 809-813, 1993.

[58] Wu, X., Ghaboussi, J., and Garrett, J. H., "Use of Neural Networks in Detection of Structural Damage", Computers and Structures, Vol. 42, No. 4, pp. 649-659, 1992.

[59] Xue, J., Pittaluga, A., and Cervetto, D., "Fatigue Damage Calculation for Oil Tanker and Container Ship Structures", Marine Structures, Vol. 7, No. 6, 1994.

[60] Yang, J. C. S., Dagalakis, N. G., and Hirt, M., "Application of the Random Decrement Technique in the Detection of an Induced Crack on an Offshore Platform Model", Computational Methods for Offshore Structures, ASME Publication, AMD Vol. 37, pp. 55-67, 1980.

[61] Yang, J. C. S., Aggour, M. S., Dagalakis, N. G., and Miller, R., "Damping of an Offshore Platform Model by Randomdec Method", Dynamic Response of Structures: Experimentation , Observation, Prediction and Control, Proceedings of the Second Specialty Conference, ASCE, New York, 1981.

[62] Yang, J. C. S., Chen, J., and Dagalakis, N. G., "Damage Detection in Offshore Structures by the Random Decrement Technique", Journal of Energy Resources Technology, Vol. 106, pp. 38-42, 1984.

[63] Yang, S. M., and Lee, G. S., "Vibration Control of Smart Structures by Using Neural Networks", The Journal of Dynamic Systems, Measurement, and Control, Vol. 119, pp. 34-39, 1997.

[64] Zubaydi, A., Haddara, M. R., and Swamidas, A. S. J., " On the Use of the Autocorrelation Function to Identify the Damage in the Side Shell of a Ship's Hull", Marine Structures, Vol. 13, pp. 537-551, 2000.

Appendix A

Finite Element (FE) Analysis

A.1 Introduction

The finite element analysis is a numerical method for solving problems of the engineering and mathematical physics problems. The basic idea behind the finite element analysis is to divide the structure, body, or region being analyzed into a large number of finite elements, or simple elements, and then these elements are connected together by nodes. These elements may be one, two, or three dimensional. FE analysis has been applied to the solution of plane stress problems, also to analysis of axisymmetric solids, plate bending, axisymmetric shell, and thin shell problems. In the following section, the equilibrium equation for dynamic analysis is introduced, and its application for the thin shell element is also discussed.

A.2 General Equation for Dynamic Analysis

The FE analysis dynamic equilibrium equation is derived using Hamilton principle (Krishnamoorthy, 1987) . The Lagrangian L is defined as:

$$L = T - \Pi \tag{A.1}$$

where L and Π are the kinetic and potential energy, respectively.

The kinetic energy of an element of volume, dV is given as:

$$dT = \frac{1}{2} \rho \{\dot{u}\}^T \{\dot{u}\}\, dV \tag{A.2}$$

where the overdot denotes the derivative with respect to time.

The total potential energy is defined as the sum of the internal work (the strain energy due to internal stresses) and the potential of the body forces and the surface tractions. It is expressed as:

$$\Pi = \iiint_V dU(u,v,w) - \iiint_V (\bar{X}u + \bar{Y}v + \bar{Z}w)\, dV - \iint_{S_1} (\bar{T}_x u + \bar{T}_y v + \bar{T}_z w)\, dS_1 \tag{A.3}$$

where S_1 is the surface of the body on which surface tractions are prescribed. $dU(u, v, w)$ denotes the strain energy per unit volume. The last two integrals represent the work done by the constant external forces, that is the body forces, $\bar{X}, \bar{Y}, \bar{Z}$, and surface tractions, $\bar{T}_x, \bar{T}_y, \bar{T}_z$.

If the strain energy in Equation (A.3) is defined as:

$$dU = \frac{1}{2}\{\epsilon\}^T\{\sigma\}\,dV = \frac{1}{2}\{\epsilon\}^T[\overline{C}]\{\epsilon\}\,dV \tag{A.4}$$

hence the total potential becomes:

$$\Pi = \frac{1}{2}\iiint_V (\,\{\epsilon\}^T[\overline{C}]\{\epsilon\} - 2\{u\}^T\{\overline{X}\}\,)\,dV - \iint_{S_1}\{u\}^T\{\overline{T}\}\,dS_1 \tag{A.5}$$

where:

$$\{u\}^T = [u\ \ v\ \ w]$$

$$\{\overline{X}\}^T = [\overline{X}\ \ \overline{Y}\ \ \overline{Z}]$$

$$\{\overline{T}\}^T = [\overline{T_x}\ \ \overline{T_y}\ \ \overline{T_z}]$$

Therefore, the energy functional in Equation (A.1) can be expressed in a matrix form for a linear elastic body as:

$$L = \frac{1}{2}\iiint_V (\,\rho\{\dot{u}\}^T\{\dot{u}\} - \{\epsilon\}^T[\overline{C}]\{\epsilon\} + 2\{u\}^T\{\overline{X}\}\,)\,dV + \iint_{S_1}\{u\}^T\{\overline{T}\}\,dS_1 \tag{A.6}$$

If the displacement model is defined as:

$$\{u\} = [N]\{y\} \tag{A.7}$$

and the strain displacement relation is:

$$\{\varepsilon\} = [B]\{y\} \tag{A.8}$$

Equation (A.6) can be expressed in the form:

$$L = \frac{1}{2}\iiint_V (\{y\}^T[B]^T[C][B]\{y\} - \rho\{\dot{y}\}^T[N]^T[N]\{\dot{y}\} - 2\{y\}^T[N]^T\{\bar{X}\})\,dV$$

$$- \iint_{S_1} \{y\}^T[N]^T\{\bar{T}\}\,dS_1 \tag{A.9}$$

Hamilton's principle states that the variation of the Lagrangian during any time interval t_1 and t_2 must be equal to zero, i.e.:

$$\delta\int_{t_1}^{t_2} L\,dt = 0 \tag{A.10}$$

Substituting Equation (A.9) and applying the variational principle to Equation (A.10), results in the following:

$$\int_{t_1}^{t_2} (\{\delta y\}^T \iiint_V ([B]^T[C][B]\,dV\,\{y\} - \{\delta\dot{y}\}^T \iiint_V \rho[N]^T[N]\,dV\,\{\dot{y}\}$$

$$- \{\delta y\}^T \iiint_V [N]^T\{\bar{X}\}\,dV - \{\delta y\}^T \iint_{S_1} [N]^T\{\bar{T}\}\,dS_1)\,dt = 0 \tag{A.11}$$

Integration of the second term of Equation (A.11) by parts with respect to time gives:

$$\int_{t_1}^{t_2} \{\delta \dot{y}\}^T \iiint_V \rho[N]^T[N]\, dV\, \{\ddot{y}\}\, dt = \left[\{\delta y\}^T \iiint_V \rho[N]^T[N]\, dV\, \{\dot{y}\}\right]_{t_1}^{t_2}$$

$$- \int_{t_1}^{t_2} \{\delta y\}^T \iiint_V \rho[N]^T[N] dV \{\ddot{y}\}\, dt \qquad \text{(A.12)}$$

According to Hamilton's principle, the tentative displacement configuration must satisfy given conditions at times t_1 and t_2, i.e., $\{\delta y(t_1)\} = \{\delta y(t_2)\} = \{0\}$. Therefore, the first term on the right-hand side of Equation (A.12) vanishes. Substituting the remaining term into Equation (A.11), yields:

$$\int_{t_1}^{t_2} \{\delta y\}^T \iiint_V \rho[N]^T[N]\, dV\, \{\ddot{y}\} + \iiint_V [B]^T[C][B]\, dV\, \{y\}$$

$$- \iiint_V [N]^T[\bar{X}]\, dV - \iint_{S_1} [N]^T[\bar{T}]\, dS_1)\, dt = 0 \qquad \text{(A.13)}$$

Since the variation of the modal displacements, $\{\delta y\}$, are arbitrary, the expression in parentheses mush vanish. Therefore, the equation of motion for the element is:

$$[m]\{\ddot{y}\} + [k]\{y\} = \{Q\} \qquad \text{(A.14)}$$

where:

$$[m] = \iiint_V \rho [N]^T [N] \, dV \tag{A.15}$$

$$[k] = \iiint_V [B]^T [C][B] \, dV \tag{A.16}$$

$$[Q] = \iiint_V [N]^T [\bar{X}] \, dV + \iint_{S_1} [N]^T \{\bar{T}\} \, dS_1 \tag{A.17}$$

In practice, the system has a mechanism for energy dissipation through the form of viscous damping assumed proportional to the velocity. Hence, the dynamic equilibrium equation for damped system can be expressed as:

$$[m]\{\ddot{y}\} + [c]\{\dot{y}\} + [k]\{y\} = \{Q\} \tag{A.18}$$

Equation (A.18) is the same as that given in Equation (3.1).

Determination of the finite element damping matrix is quite difficult, if not impossible. In most cases, the damping is assumed to be proportional to the mass and the stiffness of the system as shown in Equation (3.1). The damping matrix is constructed using the mass matrix and the stiffness matrix, together with experimental results.

A.3 Thin Shell Theory

A thin shell is a three dimensional continuous medium for which one dimension, the thickness, is small with respect to the two others. It can be derived from a thin plate by

initially forming the midsurface to a singly or doubly curved surface; therefore, thin shell theory can be derived based on Love-Kirchhoff plate theory. This theory assumes that as the shell deforms and the midsurface stretches and bends, the fibres of the shell initially straight and normal to the midsurface, remain straight and normal to the surface. It also assumes that the stress perpendicular to the midsurface through the thickness is zero.

A.4 Eight Noded Shell Element

The eight noded shell element is used for modeling the stiffened plate. The element which is based on the degeneration concept and numerical integration technique is adopted for evaluation of the integral across the thickness. Figure A.1 shows atypical curved shell element with eight nodes on the midsurface and an additional node at the center of the midsurface. The basic expressions to define the shell characteristics and necessary Equations leading to formulation of the stiffness matrix as shown in Equations (A.18) is explained in this section.

A.4.1 Shape Functions

The shape functions of the eight noded shell elements are treated as a two dimensional isoparametric element in (r, s) coordinates, and are given below:

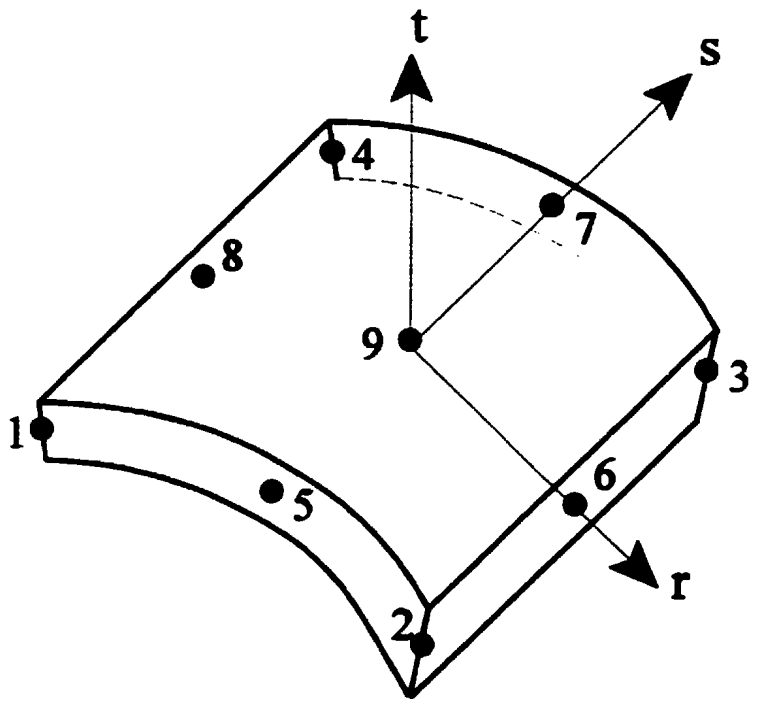

Figure A.1: The Eight Noded Shell Element

For nodes 1, 2, 3, and 4:

$$N_i = \frac{1}{2}[(1 + rr_i)(1 + ss_i)(rr_i + ss_i - 1)] \tag{A.19}$$

For nodes 5 and 7:

$$N_i = \frac{1}{2}(1 - r^2)(1 + ss_i) \tag{A.20}$$

For nodes 6 and 8:

$$N_i = \frac{1}{2}(1 - s^2)(1 + rr_i) \tag{A.21}$$

For node 9:

$$N_i = \frac{1}{2}(1 - r^2)(1 - s^2) \tag{A.22}$$

Assuming the line joining the top and bottom nodes to be straight, the shape of element is defined by the eight nodal values:

$$\begin{Bmatrix} x \\ y \\ z \end{Bmatrix} = \sum_{i=1}^{8} N_i \left\{ \begin{Bmatrix} x_i \\ y_i \\ z_i \end{Bmatrix} + t \begin{Bmatrix} x_i^* \\ y_i^* \\ z_i^* \end{Bmatrix} \right\} \tag{A.23}$$

In Equation (A.23), x_i, y_i, z_i are the global coordinates of the midsurface node i that are computed by taking the average of the top and bottom node coordinates. Also, x_i^*, y_i^*, z_i^* are the global coordinates of the point $(r_i, s_i, 1)$ with respect to the nodes $(r_i, s_i, 0)$ as shown in Figure A.2. They are obtained by dividing the differences between the top and bottom node coordinates by 2.

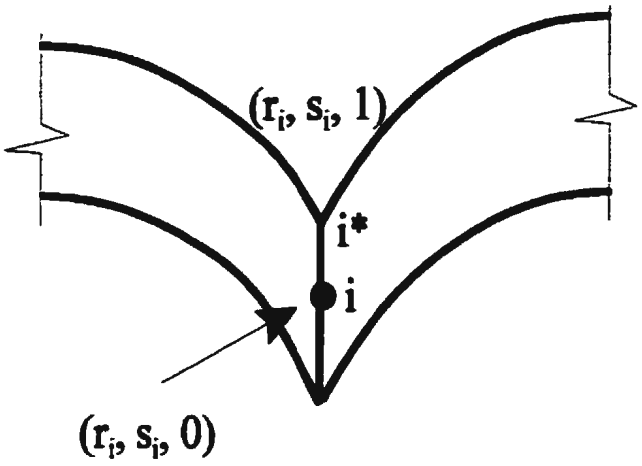

Figure A.2: Local Coordinates of Top and Midsurface

A.4.2 Displacement Field

Using the shape functions obtained in the previous section, the displacement field within the element is given by:

$$\begin{Bmatrix} u \\ v \\ w \end{Bmatrix} = \sum_{i=1}^{8} N_i \left\{ \begin{Bmatrix} u_i \\ v_i \\ w_i \end{Bmatrix} + t \begin{Bmatrix} u_i^* \\ v_i^* \\ w_i^* \end{Bmatrix} \right\} \tag{A.24}$$

where u_1, v_1, w_i are the displacements of the node i in the x, y, z directions respectively, and u_1^*, y_1^*, w_i^* are the relative global displacements at point i caused by the rotation of the normal. As N_9 vanishes at r, $s = +1$, inter element compatibility is unaffected.

In order to specify the displacements in terms of the nodal displacements and rotations, the relative displacements u_1^* , y_1^* and w_i^* are expressed in terms of the rotations α_i and β_i at the node i . If α_i and β_i are defined as the rotations of the normal about the axes $\bar{a}$ and $\bar{b}$, which lie in the midsurface as shown in Figure A.3, the two vectors $\bar{a}$ and $\bar{b}$ are obtained as follows:

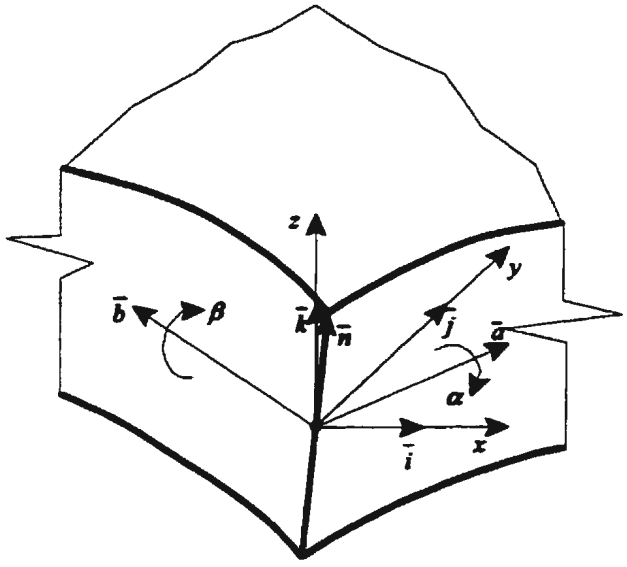

Figure A.3: Global and Rotational Axis

Let $\bar{i}$, $\bar{j}$, $\bar{k}$ be the unit vector in the x , y and z directions, respectively, as shown in Figure A.3. Vector $\bar{n}$ is defined by the input data so that this vector is normal to the midsurface, i.e. the top and bottom nodes, and x^*, y^*, z^* are the coordinates of a vector

along $\bar{n}$, i.e.:

$$\bar{n} = x^{*}\bar{i}, y^{*}\bar{j}, z^{*}\bar{k} \tag{A.25}$$

Therefore, $\bar{a}$ is defined as a vector perpendicular to $\bar{n}$ and also to vertical $\bar{k}$, i.e.:

$$\begin{aligned} \bar{a} &= \bar{k} \times \bar{n} \\ &= \bar{k} \times (x^{*}\bar{i} + y^{*}\bar{j} + z^{*}\bar{k}) \\ &= -y^{*}\bar{i} + x^{*}\bar{j} \end{aligned} \tag{A.26}$$

and $\bar{b}$ is defined as a vector perpendicular to both $\bar{n}$ and $\bar{a}$, i.e.:

$$\begin{aligned} \bar{b} &= \bar{n} \times \bar{a} \\ &= (x^{*}\bar{i} + y^{*}\bar{j} + z^{*}\bar{k}) \times (-y^{*}\bar{i} + x^{*}\bar{j}) \\ &= -x^{*}z^{*}\bar{i} - y^{*}x^{*}\bar{j} + (y^{*}y^{*} + x^{*}x^{*})\bar{k} \end{aligned} \tag{A.27}$$

It can be seen from Equations (A.26) and (A.27) that when $\bar{k}$ and $\bar{n}$ coincide, the vectors $\bar{a}$ and $\bar{b}$ are not specific. In this case they are defined as:

$$\bar{a} = \bar{j} \quad \text{and} \quad \bar{b} = \bar{i} \tag{A.28}$$

By normalizing the vectors $\bar{a}$ and $\bar{b}$, the direction cosines of these vectors with

respect to x, y, and z directions can be obtained.

Furthermore, let a_1, a_2, a_3 be the direction cosines of $\bar{a}$ with respect to x, y, and z axis, respectively, and b_1, b_2, b_3 be the direction cosines of $\bar{b}$ with respect to x, y, and z axis, respectively. Since α and β rotate with respect to $\bar{a}$ and $\bar{b}$, respectively, the displacement at $t = 1$ is $\frac{h}{2}(\bar{b}\alpha + \bar{a}\beta)$, where h is the thickness at the point. Therefore, the relative displacements at i in the global directions are given by:

$$\begin{bmatrix} u_i^* & v_i^* & w_i^* \end{bmatrix} = -\frac{1}{2} h_i \alpha_i \begin{bmatrix} b_1 & b_2 & b_3 \end{bmatrix}_i + \frac{1}{2} h_i \beta_i \begin{bmatrix} a_1 & a_2 & a_3 \end{bmatrix}_i \qquad \text{(A.29)}$$

Substituting Equation (A.29) into Equation (A.24), the following equation is obtained:

$$\begin{Bmatrix} u \\ v \\ w \end{Bmatrix} = \sum_{i=1}^{9} N_i \left\{ \begin{Bmatrix} u_i \\ v_i \\ w_i \end{Bmatrix} - \frac{th_i\alpha_i}{2} \begin{Bmatrix} b_1 \\ b_2 \\ b_3 \end{Bmatrix} + \frac{th_i\beta_i}{2} \begin{Bmatrix} a_1 \\ a_2 \\ a_3 \end{Bmatrix} \right\} \qquad \text{(A.30)}$$

A.4.3 Jacobian Matrix

It can be seen from section 3.3.3.1 that the shape functions are functions of r and s alone;

therefore, the Jacobian matrix may be computed as:

$$[J] = \begin{bmatrix} \sum_{i=1}^{8}(x_i + tx_i^*) & \frac{\partial N_i}{\partial r} & \sum_{i=1}^{8}(y_i + ty_i^*) & \frac{\partial N_i}{\partial r} & \sum_{i=1}^{8}(z_i + tz_i^*) & \frac{\partial N_i}{\partial r} \\ \sum_{i=1}^{8}(x_i + tx_i^*) & \frac{\partial N_i}{\partial s} & \sum_{i=1}^{8}(y_i + ty_i^*) & \frac{\partial N_i}{\partial s} & \sum_{i=1}^{8}(z_i + tz_i^*) & \frac{\partial N_i}{\partial s} \\ \sum_{i=1}^{8} N_i x_i^* & & \sum_{i=1}^{8} N_i y_i^* & & \sum_{i=1}^{8} N_i z_i^* & \end{bmatrix} \quad \text{(A.31)}$$

By inverting the matrix $[J]$, the derivatives with respect to global coordinate can be obtained.

A.4.4 Strain Displacement Matrix

If ϵ is the vector of strains at any point inside element, the element strains and the nodal displacement are related as given by Equation (A.8):

$$\{\epsilon\} = [B]\{y\}$$

where:

$$\{\epsilon\} = \begin{Bmatrix} \epsilon_x \\ \epsilon_y \\ \epsilon_z \\ \gamma_{xy} \\ \gamma_{yz} \\ \gamma_{zx} \end{Bmatrix} = \begin{Bmatrix} \dfrac{\partial u}{\partial x} \\ \dfrac{\partial v}{\partial y} \\ \dfrac{\partial w}{\partial z} \\ \dfrac{\partial u}{\partial y} + \dfrac{\partial v}{\partial x} \\ \dfrac{\partial v}{\partial z} + \dfrac{\partial w}{\partial y} \\ \dfrac{\partial u}{\partial z} + \dfrac{\partial w}{\partial x} \end{Bmatrix}, \quad \{y\}^T = [\, u_1 v_1 w_1 \;\; \alpha_1 \beta_1 \;\; u_2 v_2 w_2 \;\; \alpha_2 \beta_2 \;\; \ldots\ldots \;\; u_9 v_9 w_9 \;\; \alpha_9 \beta_9 \,],$$

and

$[B]$ is the strain-displacement matrix and will be function of the derivative of shape function $[N]$.

In order to establish the strain-displacement relation, first, the derivatives of displacements with respect to local coordinates must be obtained by differentiating Equation (A.30) with respect to r, s and t. Hence:

$$\begin{bmatrix} \dfrac{\partial u}{\partial r} & \dfrac{\partial v}{\partial r} & \dfrac{\partial w}{\partial r} \\ \dfrac{\partial u}{\partial s} & \dfrac{\partial v}{\partial s} & \dfrac{\partial w}{\partial s} \\ \dfrac{\partial u}{\partial t} & \dfrac{\partial v}{\partial t} & \dfrac{\partial w}{\partial t} \end{bmatrix} = \sum_{i=1}^{9} \begin{Bmatrix} \dfrac{\partial N_i}{\partial r} \\ \dfrac{\partial N_i}{\partial s} \\ 0 \end{Bmatrix} [\, u_i \;\; v_i \;\; w_i \,] - \frac{1}{2} \sum_{i=1}^{9} \begin{Bmatrix} t\, h_i \dfrac{\partial N_i}{\partial r} \\ t\, h_i \dfrac{\partial N_i}{\partial s} \\ h_i N_i \end{Bmatrix} \alpha_i [\, b_i \;\; b_2 \;\; b_3 \,]_i$$

$$+\frac{1}{2}\sum_{i=1}^{9}\begin{Bmatrix} t\,h_i\dfrac{\partial N_i}{\partial r} \\ t\,h_i\dfrac{\partial N_i}{\partial s} \\ h_i N_i \end{Bmatrix}\beta_i\,[\,a_1\;\;a_2\;\;a_3\,]_i \tag{A.32}$$

By using the Jacobian inverse and Equation (A.33) . . .

$$\begin{bmatrix} \dfrac{\partial u}{\partial x} & \dfrac{\partial v}{\partial x} & \dfrac{\partial w}{\partial x} \\ \dfrac{\partial u}{\partial y} & \dfrac{\partial v}{\partial y} & \dfrac{\partial w}{\partial y} \\ \dfrac{\partial u}{\partial z} & \dfrac{\partial v}{\partial z} & \dfrac{\partial w}{\partial z} \end{bmatrix} = \begin{bmatrix} J_{11}^{*} & J_{12}^{*} & J_{13}^{*} \\ J_{21}^{*} & J_{22}^{*} & J_{23}^{*} \\ J_{31}^{*} & J_{32}^{*} & J_{33}^{*} \end{bmatrix} \begin{bmatrix} \dfrac{\partial u}{\partial r} & \dfrac{\partial v}{\partial r} & \dfrac{\partial w}{\partial r} \\ \dfrac{\partial u}{\partial s} & \dfrac{\partial v}{\partial s} & \dfrac{\partial w}{\partial s} \\ \dfrac{\partial u}{\partial t} & \dfrac{\partial v}{\partial t} & \dfrac{\partial w}{\partial t} \end{bmatrix} \tag{A.33}$$

the derivatives with respect to the global coordinates are found, and the strain displacement matrix $[B]$ can be obtained.

A.4.5 Stress Displacement Matrix

In order to obtain stress displacement matrix $[\overline{C}]$, it is necessary to know the relation between the vector of the stress $\{\sigma\}$ to that of the strain $\{\epsilon\}$. For linear elastic material, which obeys Hooke's law, the relation is given by:

$$\{\sigma\} = [\overline{C}]\,\{\epsilon\} \tag{A.34}$$

For linear elastic isotropic material of which every plane is a plane of symmetry of the material's behavior, only two constants, (i.e. Young's Modulus E and Poisson's Ratio μ), are required to describe the constitutive relation. Therefore, the following relation is obtained for stress-strain relation in x', y', z' coordinates:

$$\{\sigma'\} = [\bar{C}]\,\{\epsilon'\} \tag{A.35}$$

or:

$$\begin{Bmatrix} \sigma_{x'} \\ \sigma_{y'} \\ \sigma_{z'} \\ \tau_{x'y'} \\ \tau_{y'z'} \\ \tau_{z'x'} \end{Bmatrix} = \frac{E}{1-\mu^2} \begin{bmatrix} 1 & \mu & 0 & 0 & 0 & 0 \\ \mu & 1 & 0 & 0 & 0 & 0 \\ 0 & 0 & 0 & 0 & 0 & 0 \\ 0 & 0 & 0 & \dfrac{1-\mu}{2} & 0 & 0 \\ 0 & 0 & 0 & 0 & \dfrac{\alpha(1-\mu)}{2} & 0 \\ 0 & 0 & 0 & 0 & 0 & \dfrac{\alpha(1-\mu)}{2} \end{bmatrix} \begin{Bmatrix} \epsilon_{x'} \\ \epsilon_{y'} \\ \epsilon_{z'} \\ \gamma_{x'y'} \\ \gamma_{y'z'} \\ \gamma_{z'x'} \end{Bmatrix} \tag{A.36}$$

where α is a factor used to account for a better representation of shear deformation when a constant strain is assumed across the thickness, rather than the correct quadratic. $[\bar{C}]$ obtained using Equation (A.36) along with $[B]$ is then used to obtain element stiffness $[k]$ in Equation (A.18).

Appendix B

Modal Analysis

B.1 Theory

Theory of modal analysis refers to that portion of the classical vibration theory that explains the existence of natural frequencies, damping factors, and mode shapes for linear systems. It starts with a description of the structure's physical characteristics, usually in terms of its mass, stiffness, and damping properties. Theory of modal analysis is then applied, and the structure's behaviors such as the natural frequencies and the mode shapes are determined. Finally, the frequency response functions and the impulse responses are obtained.

By applying Laplace transform to Equation (3.1):

$$\mathcal{L}([M]\{\ddot{y}(t)\} + [C]\{\dot{y}(t)\} + [K]\{y(t)\}) = \mathcal{L}(\{f(t)\}) \qquad \text{(B.1)}$$

one obtains:

$$[B(s)]\{y(s)\} = \{f(s)\} + ([M]s + [C])\{y(0)\} + [M]\{\dot{y}(0)\} \qquad \text{(B.2)}$$

where:

$$[B(s)] = [M]s^2 + [C]s + [K] \qquad \text{(B.3)}$$

Rearrangement of the above equation leads to:

$$\{y(s)\} = [H(s)](\{f(s)\} + ([M]s + [C])\{y(0)\} + [M]\{\dot{y}(0)\}) \qquad \text{(B.4)}$$

where:

$[H(s)] = [B(s)]^{-1}$.

Assuming Equation (B.4) has zero initial conditions, then:

$$\{y(s)\} = [H(s)]\{f(s)\} \qquad \text{(B.5)}$$

Let the Fourier variable be $s = j\omega$, then:

$$[H(j\omega)] = [B(j\omega)]^{-1} = \frac{adj[B(j\omega)]}{\det[B(j\omega)]} \qquad \text{(B.6)}$$

In Equation (B.6), $[H(j\omega)]$ is Frequency Response Function, called FRF hereafter, $[B(j\omega)] = [M]\omega^2 + j\omega[C] + [K]$, $adj[B(j\omega)]$ is the adjoint matrix of $[B(j\omega)]$, and

$\det[B(j\omega)]$ is the determinant of $[B(j\omega)]$.

Since both the adjoint matrix of $[B(j\omega)]$ and the determinant of $[B(j\omega)]$ are polynomial in $j\omega$, the element of $[H(j\omega)]$ is a rational fraction in $j\omega$; therefore, it is possible to represent any element of the $[H(j\omega)]$ in a partial fraction form:

$$[H(j\omega)] = \sum_{r=1}^{n} \left[\frac{[A_r]}{j\omega - \omega_r} + \frac{[A_r^*]}{j\omega - \omega_r^*}\right] \tag{B.7}$$

where $[A_r]$ that reflects the corresponding mode shape; ω_r is the r^{th} complex frequency, whose imaginary part gives the damped natural frequency and whose real part give the damping coefficient. And A^* designates the corresponding complex conjugate.

For a homogeneous solution, Equation (B.2) leads to:

$$[B(j\omega)]\{y(j\omega)\} = \{0\} \tag{B.8}$$

and the characteristic polynomial equation is obtained from:

$$\det[B(j\omega)] = 0 \tag{B.9}$$

The roots ω_i of the characteristic equation are called eigenvalues or complex frequencies. Substituting the eigenvalues into the Equation (B.8), solving for $\{y(j\omega)\}$, and normalizing $\{y(j\omega)\}$ to unity yields the eigenvector U_i corresponding to the eigenvalue ω_i.

The FRF has many forms in terms of input (excitation) and output (response). The most common forms of FRF are:

a. Receptance, in the form of displacement/force, where displacement is the output.

b. Mobility, in the form of velocity/force, where velocity is the output.

c. Inertance, in the form of acceleration/force, where the acceleration is the output.

The output from the experimental and numerical study were accelerations; therefore, the present study utilized the inertance FRF.

B.2 Experiment

Experimental modal analysis is carried out to verify or correct the results of the analytical approach and to obtain information on the systems, which cannot be numerically modeled. It is started with the measurement of FRF to describe the response properties of the structure. Theory of modal analysis described in the above section is then performed, and the structure's behaviors such as natural frequencies and mode shapes are determined in term of a modal model. Finally, the structural model is obtained.

Equation (B.7) is the general matrix form that is used in experimental modal analysis. Since the continuous systems have an infinite number of degree-of-freedoms, a finite number of modes must be chosen so that they can be used to represent the dynamic behavior of the

system. In the frequency range of interest, Equation (B.7) can be written as:

$$H_{ik}(j\omega) = P_{ik}(j\omega) + \sum_{r=1}^{n} \left[\frac{A_{ikr}}{j\omega - \omega_r} + \frac{A_{ikr}^{*}}{j\omega - \omega_r^{*}}\right] + Q_{ik}(j\omega) \qquad \text{(B.10)}$$

In Equation (B.10), the lower residual $Q_{ik}(j\omega)$ is the residual inertia that represents the inertia of the lower modes and is an inverse function of the frequency squared; and the upper residual $P_{ik}(j\omega)$ is the residual flexibility, which represents the flexibility of the upper modes and is constant with frequency.

The experimental modal analysis comprises of two phases. the measurement of FRFs and the estimation of modal parameters. The measurement of the FRFs is the most important phase, since it is used as inputs to estimate modal parameters of the system such as natural frequencies, damping ratios, and mode shapes.

In order to measure FRFs, there are four different configurations of modal testing that can be considered. Those are:

- Single input/ single output (SISO)
- Single input/ multiple outputs (SIMO)
- Multiple input/ single output (MISO)
- Multiple inputs/ multiple outputs (MIMO)

These different testing conditions are largely a function of the number of acquisition channels or excitation sources. The present study used a single input/ single output (SISO) functions to measure the acceleration FRF of the stiffened plate models at six different locations.

The FRFs are estimated using the least squares or the total least squares techniques, the auto-power spectra, and the cross power spectra. Least squares methods minimize the square of the magnitude error and thus compute the best estimate of the magnitude of the FRFs. Three algorithms, referred to as H_1, H_2 and H_v algorithms, are available for estimating the FRFs.

H_1 assumes that noise exists in the output and the input is free of noise. Hence:

$$[H_1]\{X\} = \{Y\} - \{\eta\} \tag{B.11}$$

H_2 algorithm considers the noise to be present in the input and to be absent in the output:

$$[H_2]\{\{X\} - \{v\} = \{Y\} \tag{B.12}$$

H_v assumes the noise to exists both in the input and output signals, consequently:

$$[H_v]\{\{X\} - \{v\} = \{Y\} - \{\eta\} \tag{B.13}$$

While the excitation could be single or multiple, the equation derived for single excitation is given as:

$$H_1 = \frac{G_{xy}}{G_{xx}} \tag{B.14}$$

$$H_2 = \frac{G_{yy}}{G_{yx}} \tag{B.15}$$

where:

$$G_{xx} = \sum_{i=1}^{n} X_i X_i^*$$

$$G_{yy} = \sum_{i=1}^{n} Y_i Y_i^*$$

$$G_{xy} = G_{yx} = \sum_{i=1}^{n} X_i Y_i^* = \sum_{i=1}^{n} Y_i X_i^*$$

In any actual measurement situation, the noise occurs both in output and input; therefore, the above numerical model can be represented in block diagram form as shown in Figure B.1.

In Figure B.1, an apostrophe denotes the true measured input/output; therefore, H_1 and H_2 are defined as:

$$H_1 = \frac{H}{(1 + \varepsilon_1)} \tag{B.16}$$

$$H_2 = H(1 + \varepsilon_2) \tag{B.17}$$

where:

$$\varepsilon_1 = \frac{G_{vv}}{G_{xx}}$$

$$v = v_1 + v_2$$

$$\varepsilon_2 = \frac{G_{\eta\eta}}{G_{yy}}$$

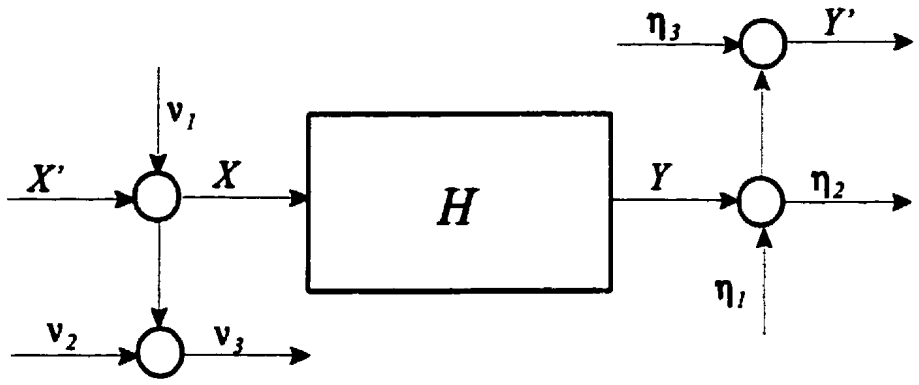

Figure B.1: System with Noise

From the above equations, it can be observed that H_1 is the lower bound and H_2 is the upper bound of H.

In addition to the attractiveness of H_1, H_2 and H_v in terms of the minimization of the error, the availability of auto- and cross-power spectra allows the determination of another important function, called the ordinary coherence function. It is frequency dependent and computed as follows:

$$\gamma^2 = \frac{|G_{yx}|^2}{G_{xx} G_{yy}} = \frac{G_{xy} G_{yx}}{G_{xx} G_{yy}} \tag{B.18}$$

γ^2 is real valued and varies from 0 to 1. The coherence function is used to measure the degree of noise in measurement. Zero value of coherence function means that the response is generated by the noise or a source other than the measured input. When the coherence is equal to 1 at any specific frequency, the measurement is perfect, i.e., the output is caused totally by the measured input. Error such as leakage can cause the coherent function to be less than one. By increasing the number of averages, the variance of the coherence will be less.

There are a number of features of digital Fourier analysis that will give rise to erroneous results of FRFs, if they are not properly treated. These are the results of the discretization approximation and of the need to limit the length of the time history. The specific features of aliassing, leakage, windowing, zooming and averaging will be discussed in the subsequent sections.

B.2.1 Aliasing

Aliasing is an effect introduced by the sampling of the time signal, whereby, after sampling, high frequencies appear as lower ones. Aliasing occurs when the sample rate is less than twice the highest frequency in the data. The frequencies above half the sampling frequency will be folded back into the frequencies below half the sampling frequency, producing erroneous results. Hence, aliasing error may be avoided by using sampling rate which is at least twice that of the highest significant frequency component in the signal.

B.2.2 Leakage and Windowing

The need to take only a finite length of time history coupled with the assumption of periodically causes leakage that is discontinuous in magnitude and slope at the ends of the sample analyzed. The discontinuity in magnitude and slope will cause additional frequency components to be calculated in order to account for the signal discontinuity that occurs at its ends. The use of a weighting function or of data windows can solve the problem.

Windowing involves the imposition of a prescribed profile on the time signal prior to performing the Fourier Transform. There are many forms of windowing such as Rectangular, Transient, Exponential, Hanning, Flat Top and Kaiser Bessel. For stationary signals, the use of the Hanning window is suggested by Allemang (1996).

B.2.3 Averaging

Averaging is the process involving several individual time records, or samples, before a result is obtained which can be used with confidence. The number of averaging required are determined by two major considerations: the desired accuracy and statistical reliability, and the noise level in signals. There are two types of averaging: sequential and overlap. The overlap process in intended to enhance the measured data by including consecutive history data before the previous data are complete.

There are several time averaging methods, such as Linear, Exponential, and Peak Averaging. These can be performed with or without the overlapping of the time record. The analyzer used in the present study provides 50%, 75%, and 85% degree of overlap.

B.2.4 Zoom

Zoom means the reduction in the frequency span of measurement, which automatically requires a longer time history record. When the frequency response function peak in the frequency narrower than the resolution then error occurs. One way to increase the frequency resolution while maintaining baseband frequency range is to increase the data window length by an integer factor while using the same sample frequency. In addition, increase of the frequency resolution minimizes the leakage error.

Appendix C

Instrumentation and Calibrations

C.1 Signal Generators

There are many different signals which can be used to excite the structure for modal testing, and several of these are in widespread use. Basically, they can be divided into two types: transient and continuous signals. The transient signal is basically a discontinuous signal such as an impact test, which is generated using a hammer. It is a relatively simple means of exciting the model to generate vibration motion. However, the transient signal is limited in its usefulness for performing tests, which require high precision and accuracy.

On the other hand, the continuous signal can provide sufficient power into the system to excite as many frequencies as required. It has a good signal to noise ratio, since the exciter is fixed at a certain point and has a good repeatability. For the excitation forcing function, normally two type of continuous signals are used: a random and a fast sine sweep. In the present study, both signals were used. The fast sine sweep signal was used to obtain the

acceleration responses in which the combination of them will produce the acceleration FRFs. The random signal was used to produce the acceleration random responses.

There are three types of the random signals: a true random, a pseudo random, and a periodic random signals in which the samples are shown in Figure C.1. The advantages of the random signals are that the signals cover a wide range of natural frequencies, and represent the realistic service environment. The random signals used in the present study were the pseudo random signals with unknown magnitude.

The pseudo random signals were generated by a Wavetex model 132 noise generator. This generator is a source of analog and digital noise, as well as precision source of sine, triangle, and square waveforms. Noise outputs, or waveforms can be used individually, or combined to provide selectable, calibrated signal-to-noise and noise-to-signal ratios to +60dB. Waveforms can be varied over a frequency range of 0.2 Hz to 2.0 MHz in 6 decade ranges.

The fast sine sweep signal, for which the sample is shown in Figure C.2, is a sinusoidal signal with a constant amplitude, which continuously increases in frequency from a small value to the specified maximum value. The advantages of this signal include: reduced noise, high signal to noise ratio, and minimized signal leakage. However, this signal does not represent the realistic service environment.

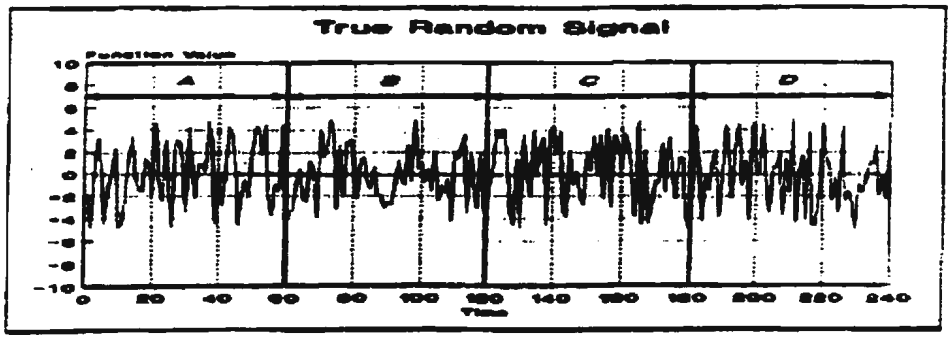

a. True random signal

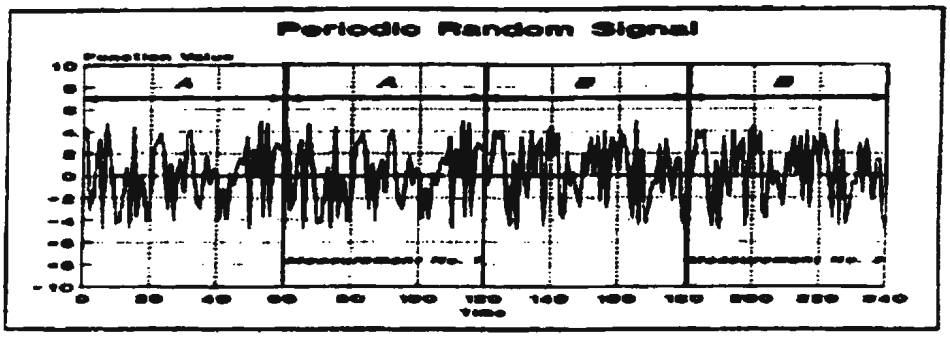

b. Periodic random signal

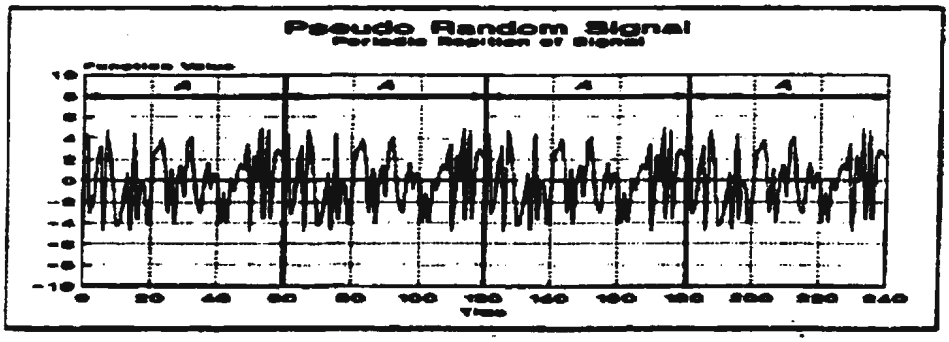

c. Pseudo random signal

Figure C.1: Samples of Random Signal

In the present study, the fast sine sweep signal was generated by a HP 3314A function generator. This generator was a multi-mode HP-IB programmable function generator featuring sine, square, and triangular functions ranges from 0.001 Hz to 19.99 MHz. It had sophisticated implementation of the operating modes plus precision control of the trigger signal.

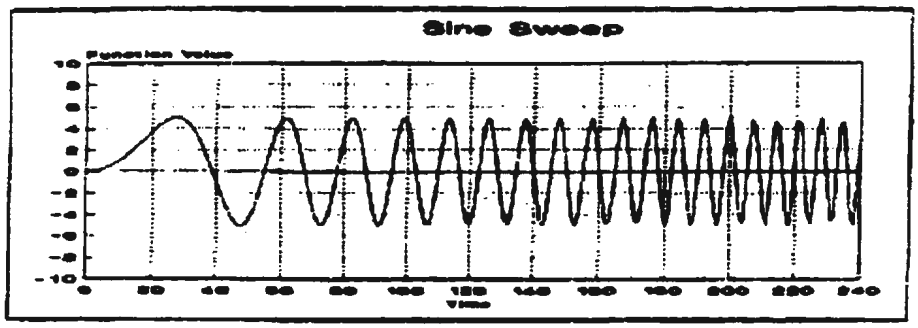

Figure C.2: Sample of Fast Sine Sweep Signal

C.2 Exciter

There are three types of exciter, or vibrator, or shaker: mechanical (out-of-balance rotating masses), electromagnetic (moving coil in magnetic field), and electrohydraulic [Ewins, 1996]. The most common type of exciter used for the modal testing is the electromagnetic or electrodynamic, in which the supplied input signal is converted to an alternating magnetic field in which a coil is placed which is attached to the drive part of the device, and to the structure.

A B&K type 4801 exciter body along with a type 4812 exciter head were used in the

present study to excite the stiffened plate models. The exciter is strong enough to handle a variety of sizes and weights of test objects and fixtures, even in the horizontal position. The maximum force rating was 445 Newtons (100 lbs) for vibrating specimens at frequencies ranging from 10 Hz up to 20 kHz.

C.3 Transducer

Transducer is device for measuring the excitation forces and the various responses of interest. The most popular and widely-used means of measuring the parameters of interest in modal testing is the piezoelectric type of transducer. There are three types of piezoelectric transducer available for mobility measurement: force gauges, accelerometers and impedance heads. The basic principle of operation makes use of the fact that an element of piezoelectric material generates an electrical charge across its end faces when subjected to a mechanical stress.

In the present study, STRUCTCEL model no. 330A accelerometers were used for measuring the acceleration FRFs and the acceleration random responses. Each accelerometer has 2.0 grams of weight. These accelerometers were encased in a plastic cup and have measuring device with a 3-pin transistor-header configuration. The specifications of these accelerometers are listed in Table C.1.

The accelerometers could be used measuring the responses in air and in water. When the experiment in water was carried out, the accelerometers and all their submerged wire

connections were made water-tight using petroleum-jelly.

Table C.1: Specification of STRUCTCEL Accelerometers

Sensitivity (mV/g)	200
Range (± 10V) (g)	10
Resolution (g)	0.001
Frequency range (± 5% sens. dev.) (Hz)	1 - 1000
Resonant frequency (Hz)	3000
Excitation (± VDC)	15
Temperature range (°F)	0 - 130
Shock (max) (g)	5000
Weight (gm)	2
Connector (pin)	3

C.4 Load Cell

A load cell or a force transducer is the simplest type of piezoelectric transducer. A Kistler model 912 S/N 2010 quart dynamic load cell was used in the present study. It measured compression forces from less than 1 lb. to 5000 lbs and tension forces from 0 lb. to 100 lbs. This load cell model was rigid and had a very high sensitivity, near infinite resolution and fast response. It was attached to the exciter through a connecting rod, to transmit the force signal to the stiffened plate models. The load cell was screwed directly onto the side shell of

the stiffened plate models and the connecting rod from the exciter.

C.5 Analyzer

An analyzer is used to measure the specific parameters of interest: force and response levels. In principle, each analyzer is a form of voltmeter. Although, the signal processing required to extract the necessary information concerning magnitude and phase of each parameter requires some very complex, and sophisticated devices.

There are three of these in current use: tracking filters, frequency responses analyzers, and spectrum analyzers. In the present study, two analyzers were used for data acquisition. One was a B & K 2034 dual channel signal analyzer, and the other was Keithley 570 data acquisition system.

A B&K dual channel signal analyzer type 2034 can be used for measuring FRFs, coherence, for both auto- and cross-spectra, for both auto- and cross-correlation, impulse response, signal-to-noise ratio, sound intensity, orbits, and probability density/ distribution functions. In the present study, this device was used to measure the acceleration FRFs and the coherence. This analyzer was a flexible, easy-to-use, and fully self-contained two channel FFT analysis system with 801 lines of resolution. It had a built-in digital zoom to 25.6 kHz.

A Keithly 570 is a 12 bit data acquisition system that can acquire up to 32 channels. It takes only several nano-seconds to switch between channels. The digital interval between each sample in each channel in the experimental measurement was 10 milliseconds; hence

the data acquired by these channels are assumed to be independent, simultaneous, and continuous. In the present study, this device was used to digitize the measured random responses so that the random response could be analyzed using other software packages.

C.6 STAR Software

The STAR System is a series of software products for testing and analyzing the dynamics of mechanical structures. STAR is an acronym for Structural Testing, Analysis and Reporting which described the general capabilities of the system (Spectral Dynamics, Inc., 1994). The STAR System can be used for three related types of dynamic analyses such as time domain analysis, operating deflection shapes analysis, and modal analysis. The STAR System has four various products such as STAR Base®, STAR View®, STAR Modal® , and STAR Struct®, which are able to share the same data base.

In the present study, the STAR Struct®, which contains all the capabilities of STAR View® and STAR Modal® plus extended analysis capabilities, was used to acquire the measurements from a B&K analyzer through the General Purpose Interface Board (GPIB) interface. This software uses the acceleration FRFs to identify the modal parameters of the stiffened plate models such as natural frequencies and damping ratios.

C.7 Connecting Rod

In addition to the instruments explained in the previous subsection, there were also an important components that influenced the process of the experiment. These were the connecting rods, which transmitted the signal from the exciter to the load cell. There were two types of the connecting rods, made of mild steels, used in the present study. The type 1 was used to connect the exciter to the long steel rod part. The type 2 was designed to connect the long steel rod part to the load cell, and to protect the instruments from overloading in which it would be yielding when the exciting force became large.

C.8 Calibration

In order for measured experimental data has accurate results, all the transducers used in the experiments were carefully calibrated. The calibration was carried out in two steps. The first step involved the calibration of the excitation channel that includes the force transducer and the dual mode amplifier. The second step involved the calibration of the response channel that includes the accelerometers, the differential amplifier and the oscilloscope. The details of the calibration are as follows:

C.8.1 Load Cell

The calibration of the model 912 S/N 2010 load cell was done using the standard weight,

dual mode amplifier, and an oscilloscope. The setup for the load cell's calibration is shown in Figure C.3. The standard weight excited the load cell, and the response was amplified by the dual mode amplifier, which was properly set so that the expected channel sensitivity of 1V/lb was obtained. An oscilloscope was used to measure the response.

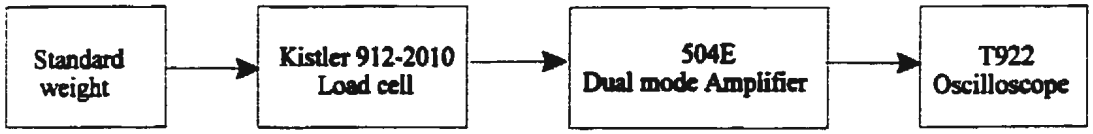

Figure C.3: Calibration Setup for Load Cell

C.8.2 Accelerometers

The calibration of six accelerometers model PCB 330A were done using the hand-held calibrator model PCB 394B05 and an oscilloscope. The setup for the accelerometer's calibration is shown in Figure C.4.

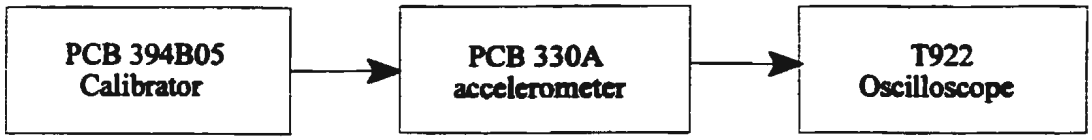

Figure C.4. Calibration Setup for Accelerometer

Each accelerometer to be calibrated was attached to the socket of the calibrator, which was then vibrated. The output of the calibrator was a constant level of 1g (RMS). The output was sent to an oscilloscope to calculate the calibration factor of each accelerometer. Each accelerometer was calibrated one by one. The results are tabulated in Table C.2.

Table C.2: Calibration Factors of Accelerometers

Channel No.	1	2	3	4	5	6
Accelerometer series (S/N)	20093	20403	20505	20502	20397	19944
Calibration Factor (V/g)	1.3	1.5	1.5	1.4	1.6	1.6

Appendix D

Dynamic Response of Models #2, #3, and #4

D.1 Model #2

Model #2 was investigated for each 0.20 inch of crack length. This crack length was shorter than the crack length that was investigated in Model #1, i.e., 0.40 inch. However, the maximum crack length to be identified was remained same, i.e., 1.20 inch. Also, the location of the crack for both models was the same, i.e., at the faceplate of longitudinal (at a distance of 0.90 inch from the heavy transverse member). The reason to change the crack length was to check the sensitivity of the techniques on the crack length. Moreover, in addition to in air, the experiment of Model #2 was also conducted in water for identifying the effect of the presence of water on the dynamic responses of the model.

Since Models #1 and #2 have similar dimensions and characteristics, their experimental and numerical acceleration FRFs also have similar shape for both undamaged and damaged conditions. The difference between them is for the values of frequencies only.

Based on this consideration, only a comparison between the numerical free vibration responses and the experimental randomdec signatures along with their frequencies is presented and discussed in the following sections.

D.1.1 In air

Figure D.1.a shows a comparison between the numerical free vibration response and the experimental randomdec signature for the undamaged model, whereas Figures D.1 .b - D.1.g show a comparison for the damaged model with crack lengths of 0.20 inch, 0.40 inch, 0.60 inch, 0.80 inch, 1.00 inch, and 1.20 inch, respectively. A comparison of their frequencies is tabulated together in Table D.1.

It can be observed from Figures D.1.a - D.1.g and Table D.1 that the experimental randomdec signatures and the numerical free vibration responses are in good agreement for both the undamaged and the damaged conditions. For crack length of 0.20 inch, the results are similar to the undamaged ones for both the frequency and the responses. The difference in the results appeared when the crack length increased. Similar to Model #1, Figures D.1 also show the difference in magnitudes between experimental and numerical results.

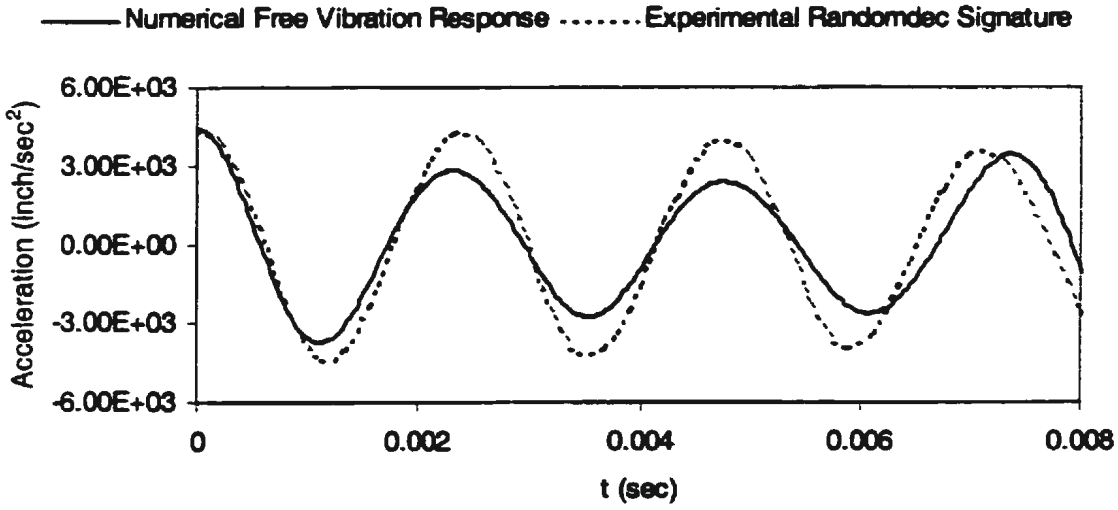

D.1.a: Undamaged

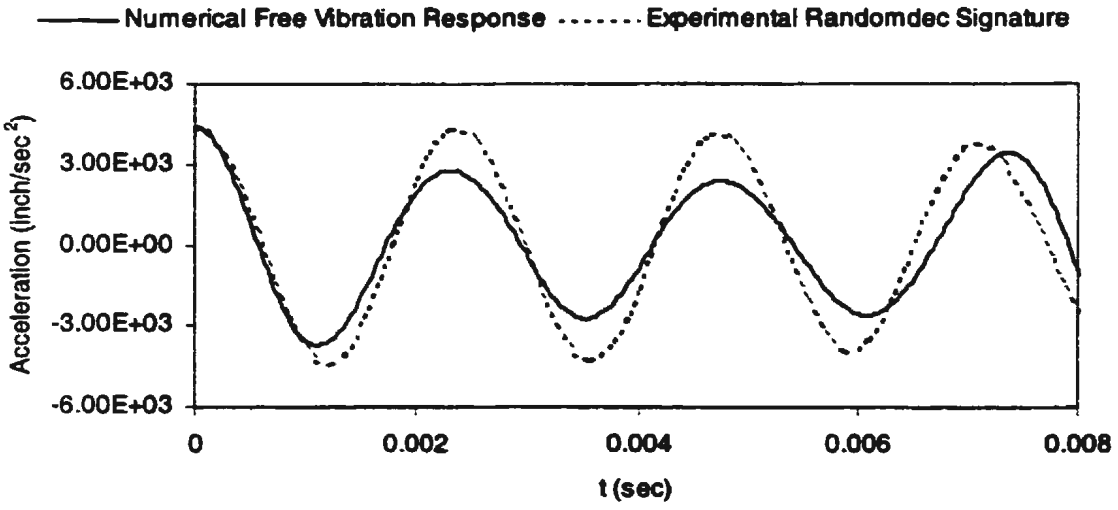

D.1.b: Crack length = 0.20 inch

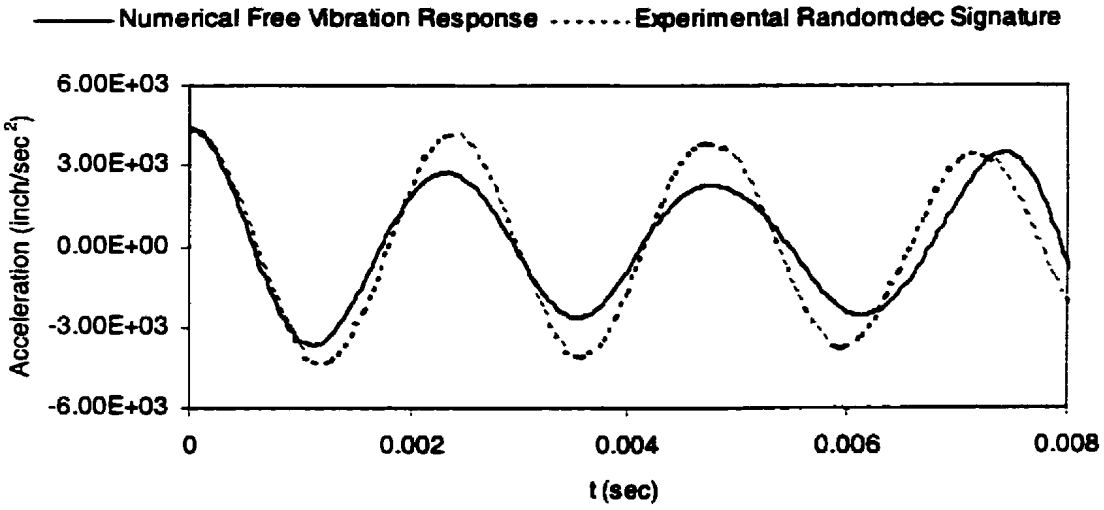

D.1.c: Crack length = 0.40 inch

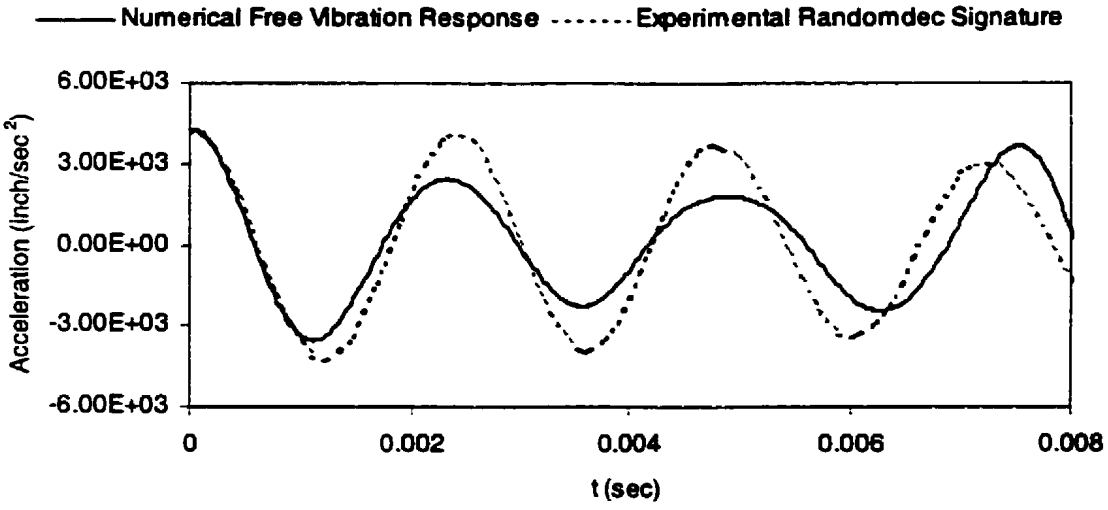

D.1.d: Crack length = 0.60 inch

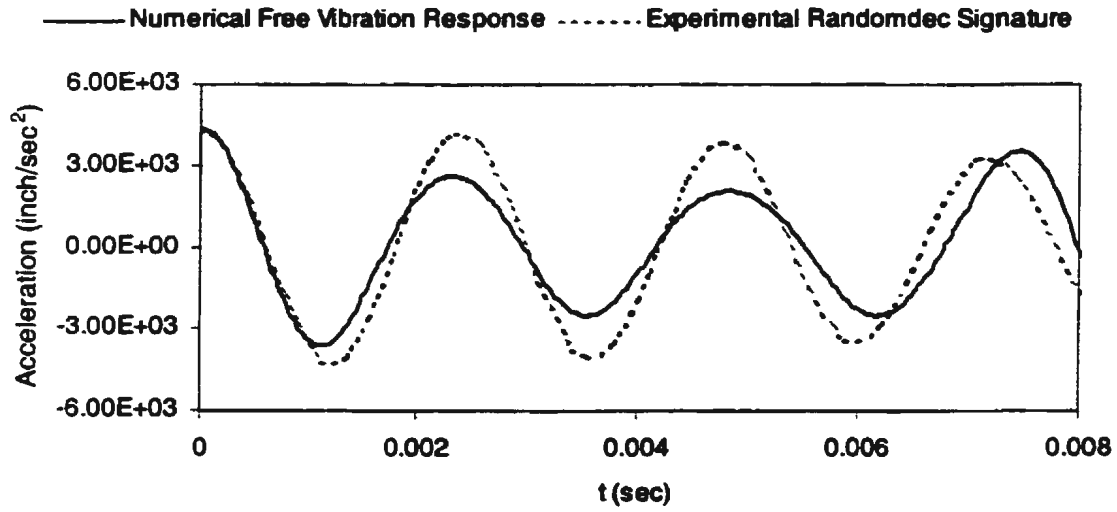

D.1.e: Crack length = 0.80 inch

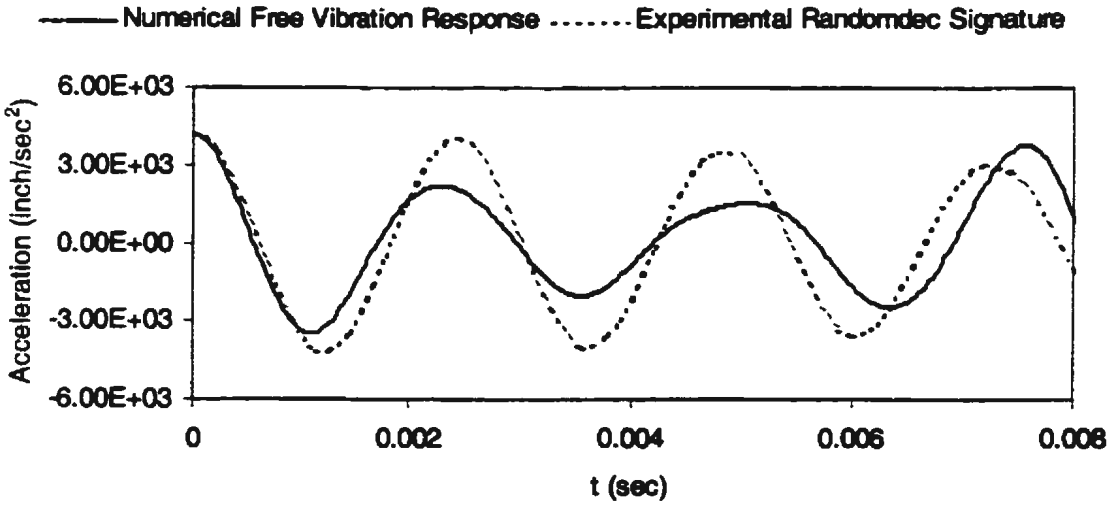

D.1.f: Crack length = 1.00 inch

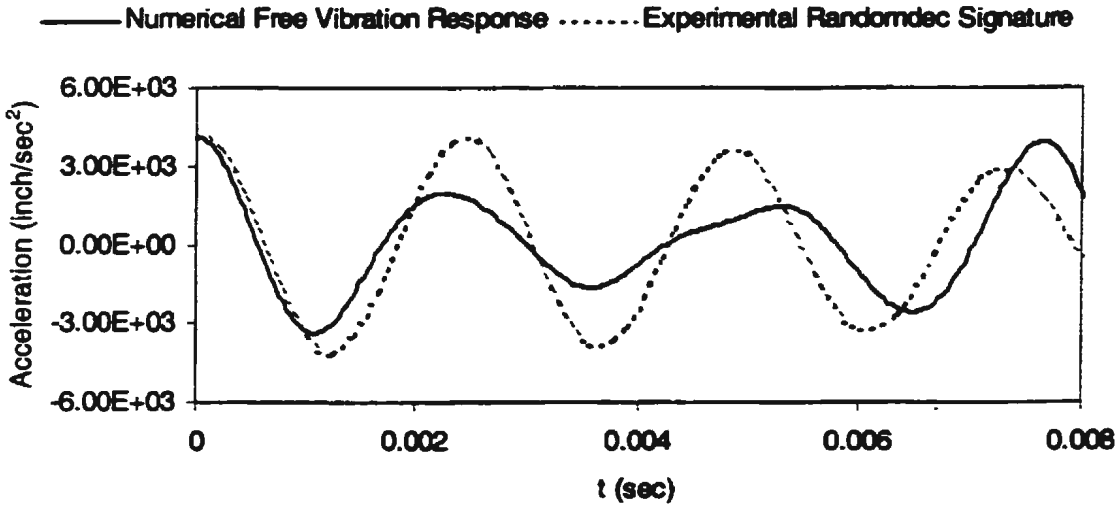

D.1.g: Crack length = 1.20 inch

Figure D.1: Comparison between Experimental Randomdec Signatures and Numerical Free Vibration Responses of Model #2 in Air

Table D.1: Comparison of Experimental Randomdec Signature and Numerical Free Vibration Response Frequencies of Model #2 in Air (Hz)

No	Crack length (Inches)	Exp. Randomdec Signature	Num. Free Vibration Response
1	0.00	421.59	421.74
2	0.20	421.20	421.20
3	0.40	420.67	420.17
4	0.60	417.94	417.99
5	0.80	415.66	415.56
6	1.00	413.44	412.67
7	1.20	410.87	410.50

However, the results in Table D.1 indicate that the frequencies of Model #2 are slightly higher than those of Model #1, see Table 5.4 for comparison. The cause is that the thicknesses of each model were slightly different as discussed in Chapter 4. Also, in order to carry out the experiment in water, Model #2 was submerged in water for both the undamaged and the damaged conditions.

The experiment in air was conducted after the experiment in water was carried out. Moreover, due to the difficulty in installing, the load on the bolts for clamping Model #2 might be slightly different from that for Model #1. Therefore, the boundary conditions for both models might also be slightly different.

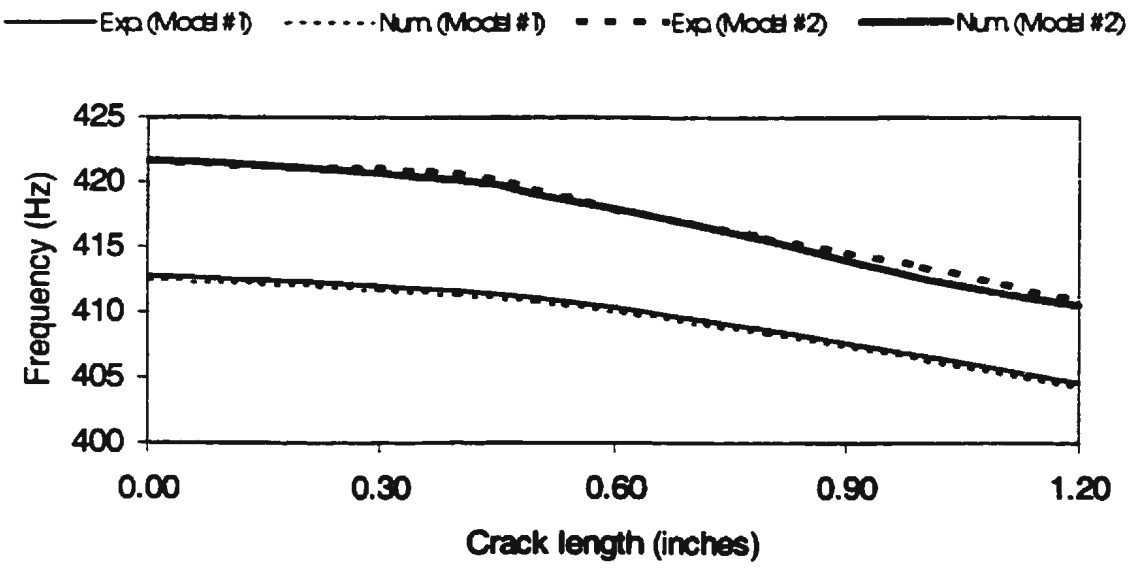

Figure D.2: Comparison between Frequencies of Models #1 and #2 in Air

Nevertheless, Figure D.2 indicates that the frequencies for both Models #1 and #2 decreased with a similar trend when the crack length is appeared and increased. Based on the above results, it is evident that the randomdec technique as well as the FE model could be applied for identifying the dynamic behavior of the undamaged Model #2 and Model #2 with several damaged lengths; hence they would be used to identify the dynamic behavior of the undamaged and damaged of Model #2 in water.

D.1.2 In Water

In order to carry out the experiment in water, Model #2 was submerged in two different conditions. One was in partial submergence, and the other was in full submergence. The reason is that, in the present study, the stiffened plate model represents the inner side shell of double hull tankers in which one of its function is to separate a cargo hold and a side wall tank. The partial submergence condition represents the cargo hold is full loaded, and the side wall tank is an empty. The full submergence condition represents the cargo hold and the side wall tank are full loaded.

D.1.2.1 Partial Submergence

Experimentally, the partial submergence means that the longitudinal and the heavy transverse member are full submerged in water, and the side shell is submerged at one side only, i.e., the side with the longitudinal and the heavy transverse member. Numerically, the partial

submergence means that the mass of Model #2 is added with the mass of water surround Model #2 using Equation 3.16. A comparison between the numerical free vibration responses and the experimental randomdec signatures for the undamaged and the damaged conditions is presented separately in Figure D.3.a - D.3.g. For comparison, their frequencies for the fourth mode are given in Table D.2.

It is found from Figures D.3 and Table D.2 that the numerical free vibration responses and the experimental randomdec signatures have a relatively good agreement for the undamaged model and the model with several crack lengths. Comparing with the undamaged results, the results for the crack with the length of 0.20 inch are almost the same. Similar to the results for Models #1 and #2 in air, Figures D.3 also show the difference in the magnitude between the numerical free vibration responses and the experimental randomdec signatures.

However, Figures D.3 do not show discernible change in the shapes, when they are compared with those of Figures D.1. This means that the presence of water did not influence the dynamic behavior of Model #2. Also, for t = 0.008 seconds, the number of cycles obtained from Figures D.3 is slightly less than those obtained from Figures D.1 for both the undamaged and the damaged conditions. The following comments may explain the causes.

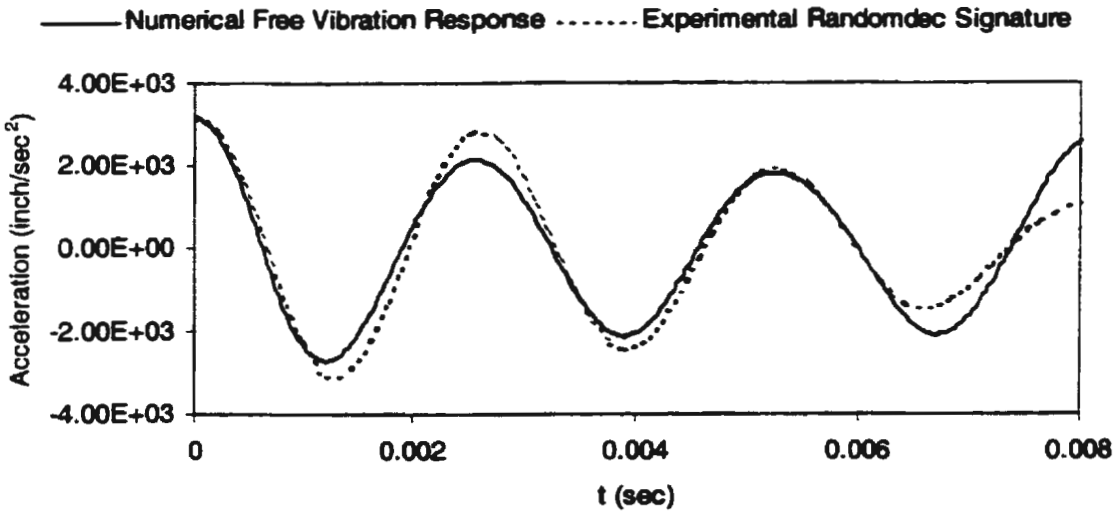

D.3.a: Undamaged

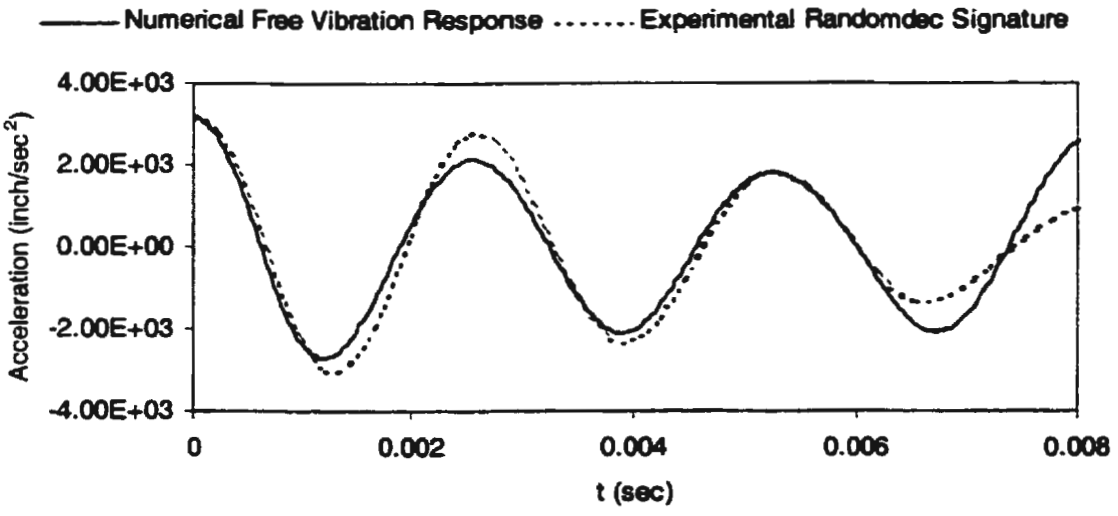

D.3.b: Crack length = 0.20 inch

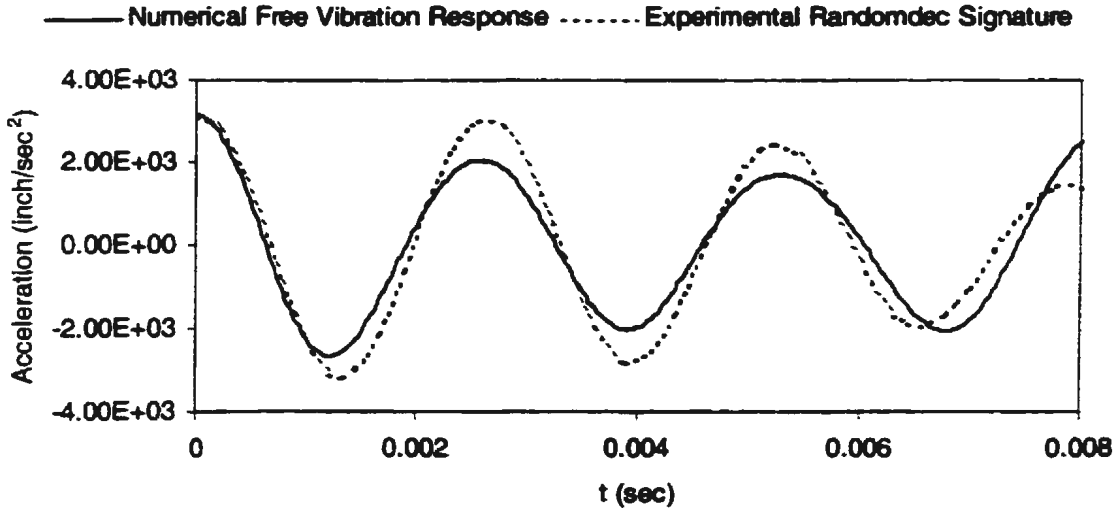

D.3.c: Crack length = 0.40 inch

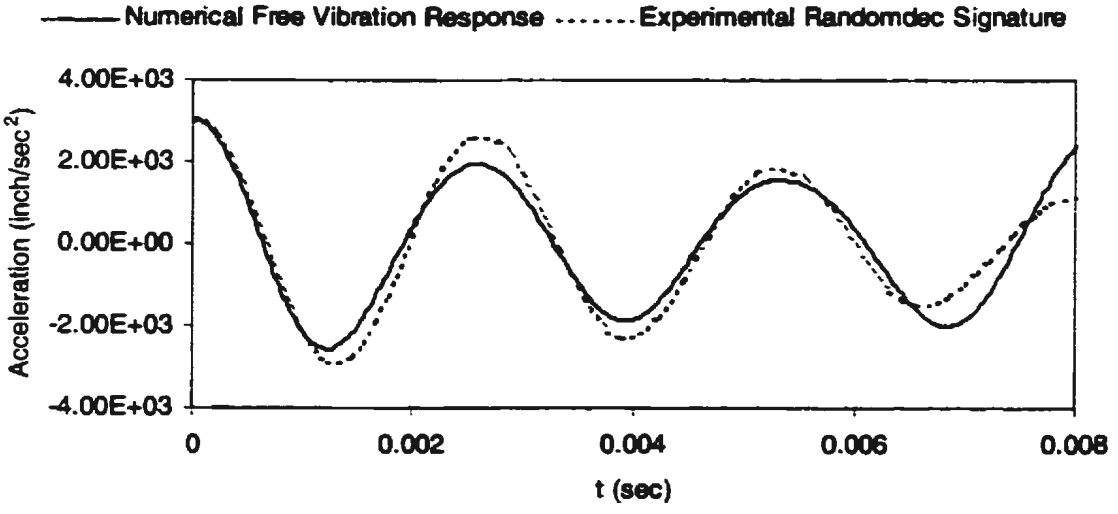

D.3.d: Crack length = 0.60 inch

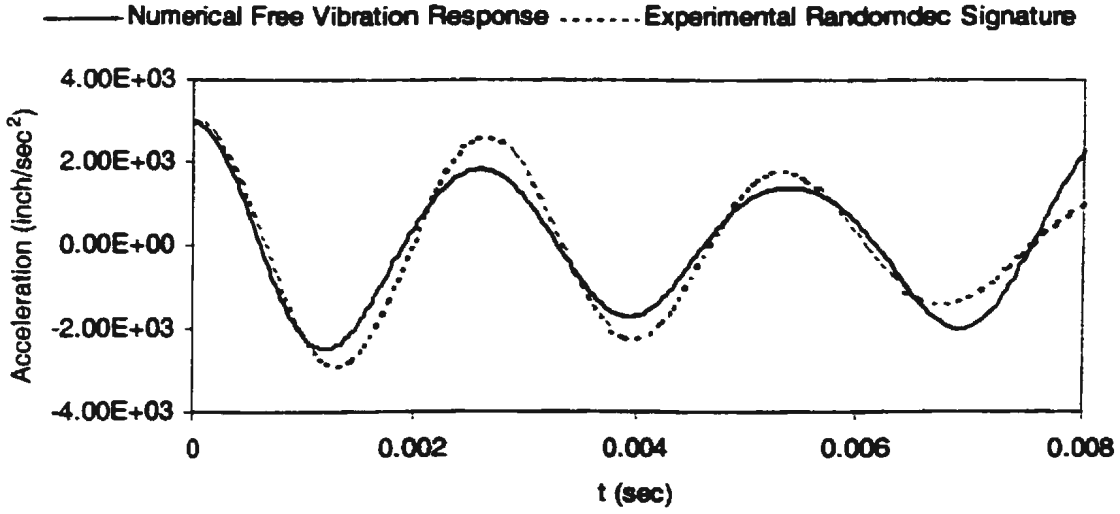

D.3.e: Crack length = 0.80 inch

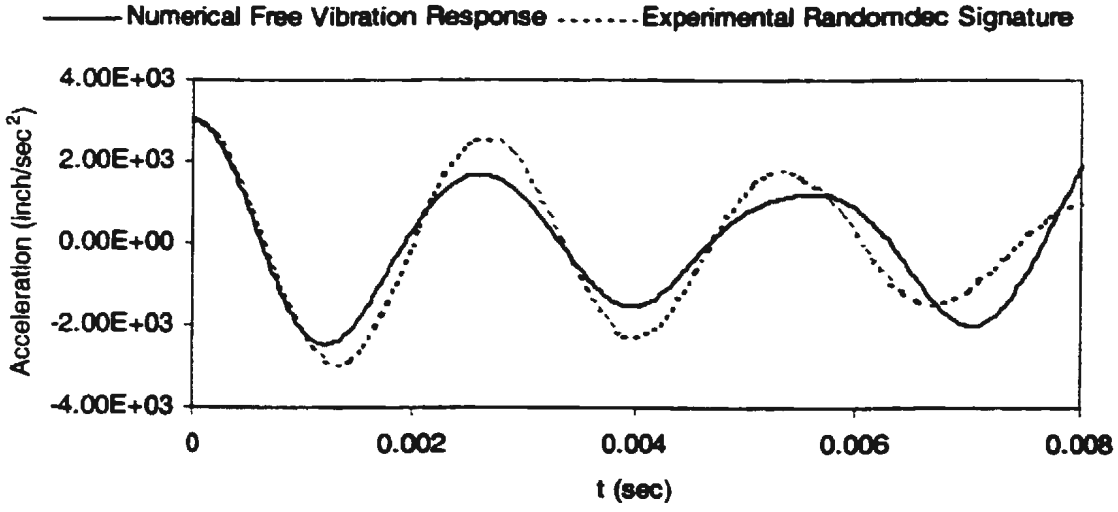

D.3.f: Crack length = 1.00 inch

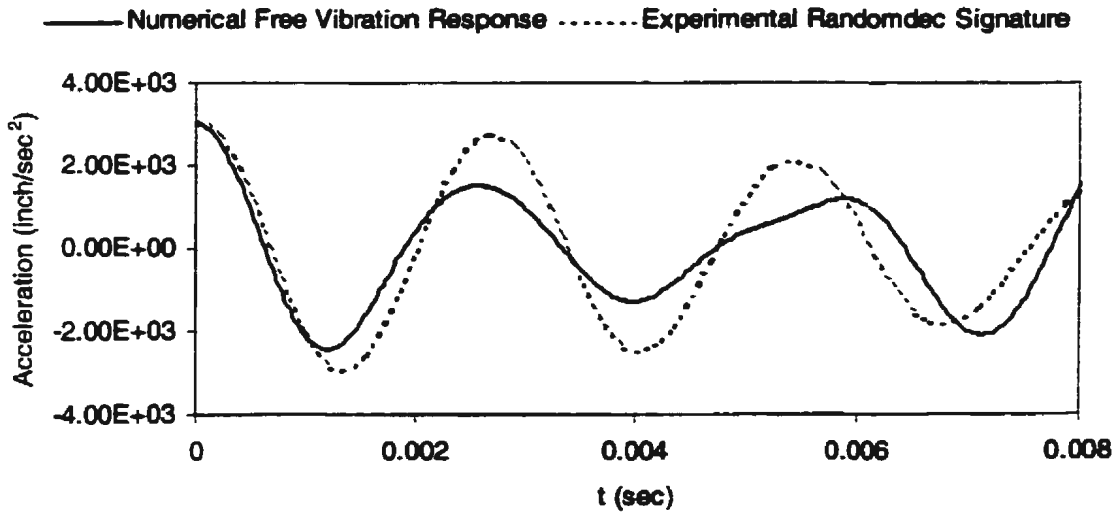

D.3.g: Crack length = 1.20 inch

Figure D.3: Comparison between Experimental Randomdec Signatures and Numerical Free Vibration Responses of Model #2 in Water (Partial Submergence)

Table D.2: Comparison of Experimental Randomdec Signature and Numerical Free Vibration Response Frequencies of Model #2 in Water (Partial Submergence) (Hz)

No	Crack length (Inches)	Exp. Randomdec Signature	Num. Free Vibration Response
1	0.00	381.45	381.48
2	0.20	381.10	381.09
3	0.40	380.34	380.16
4	0.60	378.64	378.58
5	0.80	376.64	376.60
6	1.00	373.56	373.51
7	1.20	370.17	370.11

In the experiments, the stiffened plate model was placed symmetrically in the tank for both in the x and y directions. Therefore, the presence of water did not change the symmetry of the system, it only increased the density and damping ratios of the model. In the numerical study, the water effect was modeled as an added mass and the increase in damping ratios; however, the stiffness remain the same as that in air. Because of this, it could be observed from Table D.2 that, the presence of water caused the frequencies of vibrating undamaged and damaged stiffened plate model decreased. In Figures D.3, this was represented by shifting the crest and the trough of signatures and responses to the right side.

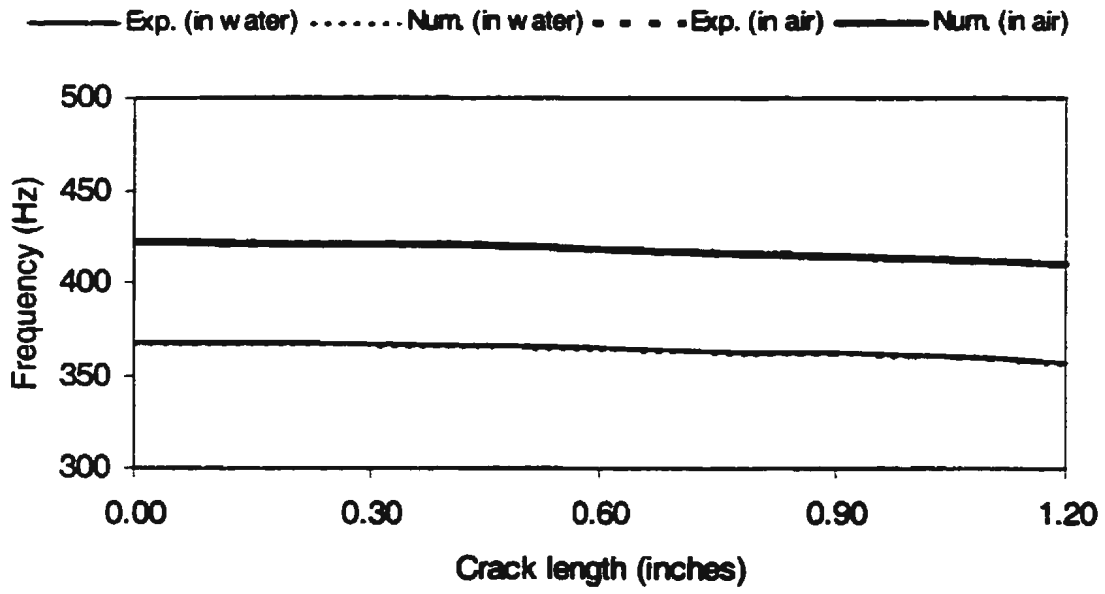

Figure D.4. : Comparison of the Frequencies of Model #2 in Air and Water (Partial Submregence)

In order to ensure that the effect of water only caused the decrease of frequencies, the frequencies in water were compared with those in air, and the results are plotted together in Figure D.4. It can be seen from Figure D.4 that the frequencies in water also decrease when the crack length increased. Moreover, the decrease of frequencies in water has a similar pattern with those in air for both the numerical free vibration responses and the experimental randomdec signatures.

Based on the above results, the randomdec technique and the FE model could also be used to identify the dynamic behavior of Model #2 in water/ partial; therefore, they were applied to identify the dynamic behavior of the undamaged and the damaged Model #2 , which was full submerged in water.

D.1.2.2 Full Submergence

The full submergence means that all members of Model #2, i.e., the longitudinal, the heavy transverse member, and the side shell, are full submerged in water. Therefore, for analyzing using the FE analysis, the mass of water was added to Model #2 in this condition was heavier than that was added to Model #2 in the partial submergence. The depth of water above the side shell was 4.00 inch. This was due to in the fact that the height of the tank was limited. In fact, the increase of the depth of submergence causes the increase of an added mass and damping ratio of the model as proven by Haddara and Cao (1996). However, they have also proven that the added mass and damping ratio approached to limiting values with the increase in the depth of submergence.

The experimental randomdec signatures were compared with the numerical free vibration responses, and the results are drawn together in Figure D.5.a - D.5.g for both the undamaged and the damaged conditions. Table D.3 shows a comparison between their frequencies at the fourth mode. As observed from Figures D.5, the agreement between the experimental randomdec signatures and the numerical free vibration responses are in a good condition for both the undamaged and the damaged ones. Table D.3 also shows the good agreement between their frequencies, and the decrease in frequencies with the increase of the damage length. However, when compared with the results shown in Figures D.3, Figures D.5 did not show the significant change in signatures and responses for both the undamaged and the damaged conditions. Similar to the partial submergence, this means that an additional water above the side shell also did not influence the behavior of Model #2.

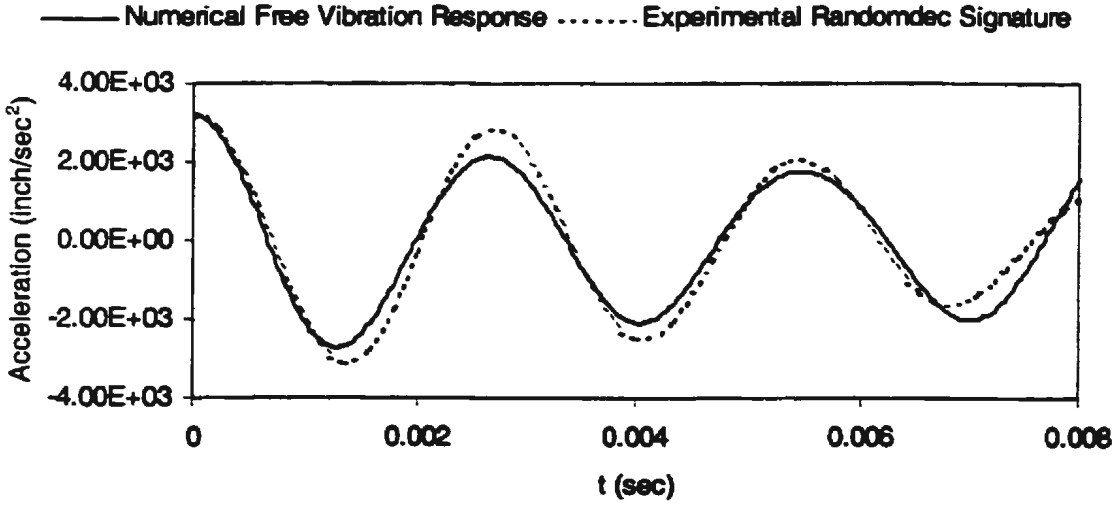

D.5.a: Undamaged

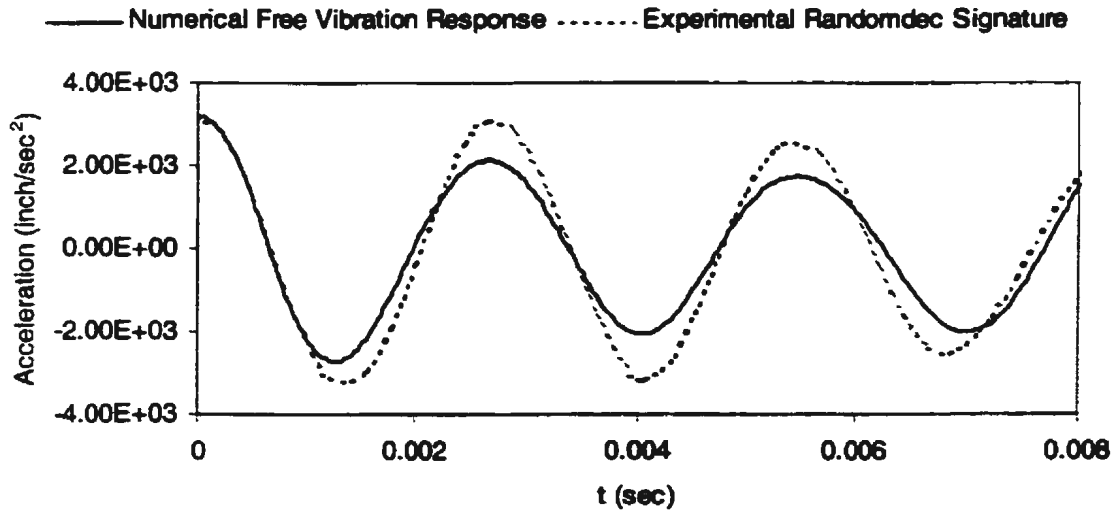

D.5.b: Crack length = 0.20 inch

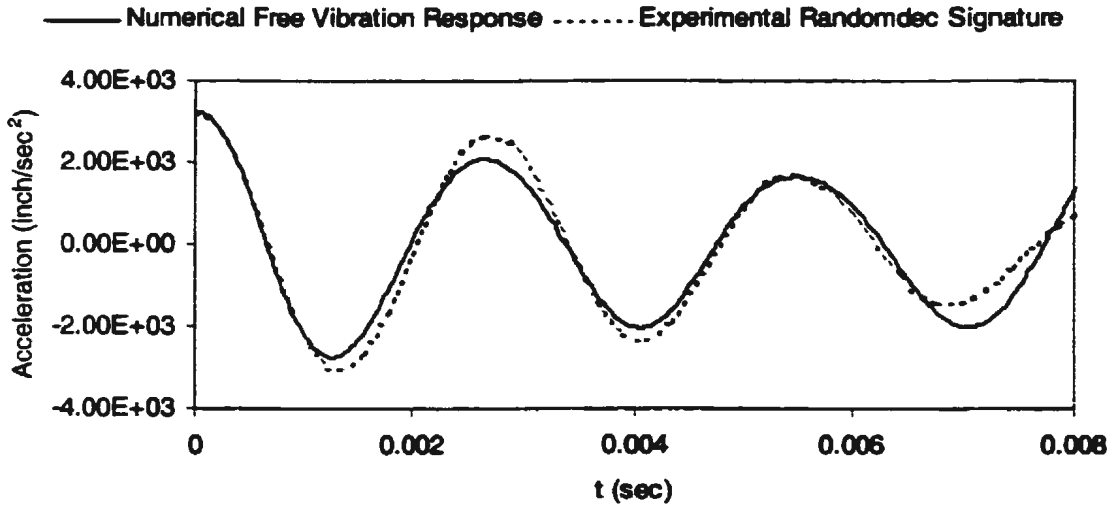

D.5.c: Crack length = 0.40 inch

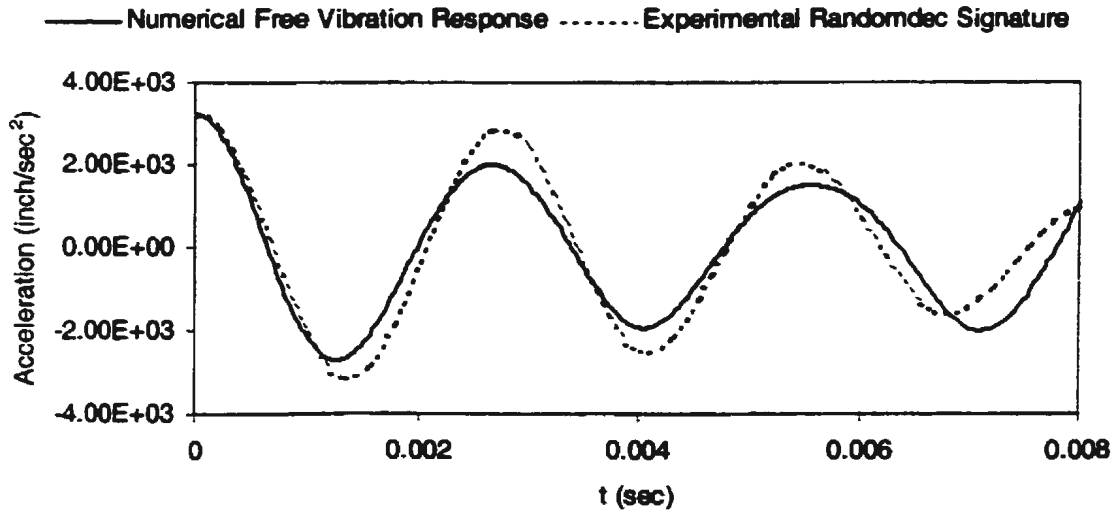

D.5.d: Crack length = 0.60 inch

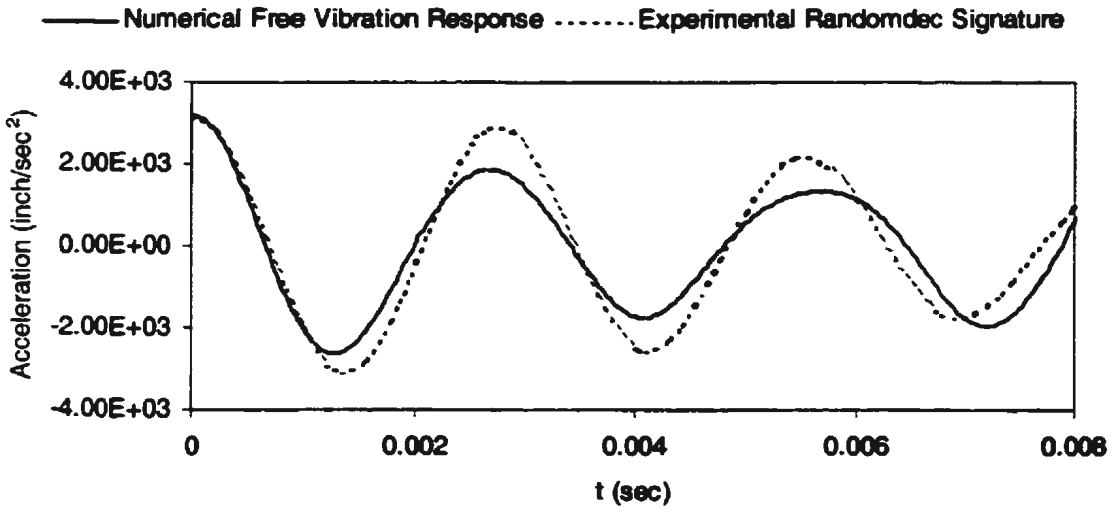

D.5.e: Crack length = 0.80 inch

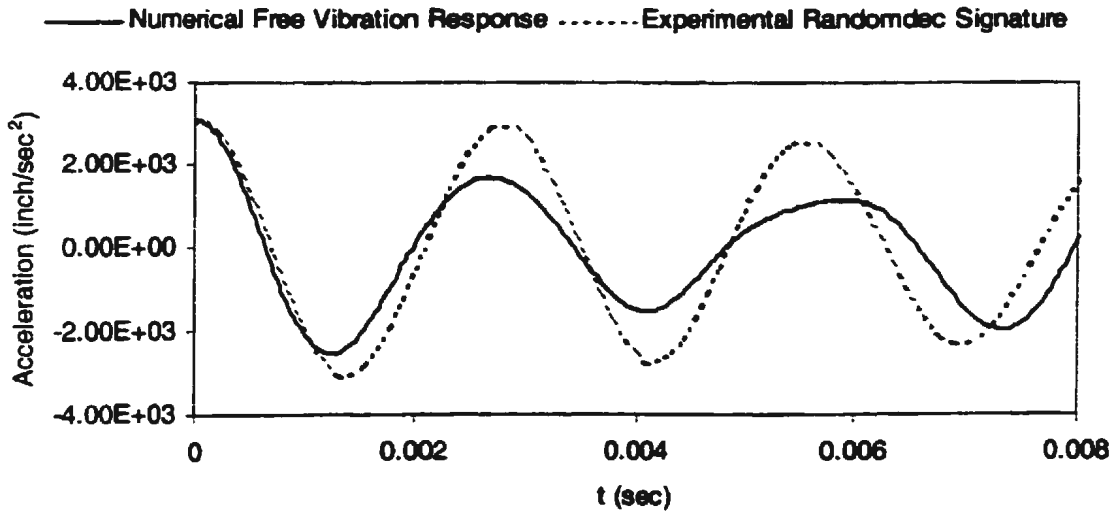

D.5.f: Crack length = 1.00 inch

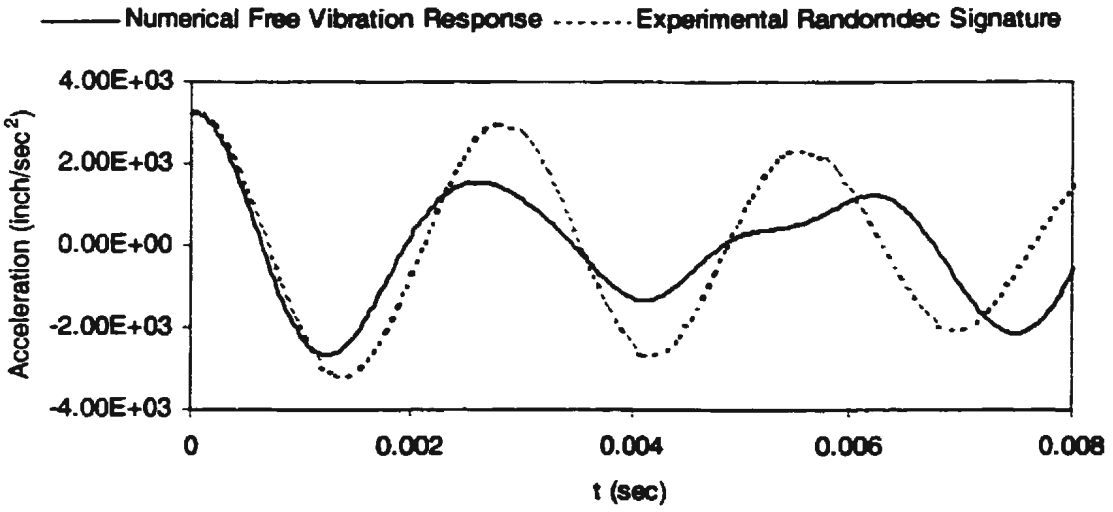

D.5.g: Crack length = 1.20 inch

Figure D.5: Comparison between Experimental Randomdec Signatures and Numerical Free Vibration Responses of Model #2 in Water (Full Submergence)

Table D.3: Comparison of Experimental Randomdec Signature and Numerical Free Vibration Response Frequencies of Model #2 in Water (Full Submergence) (Hz)

No	Crack length (Inches)	Exp. Randomdec Signature	Num. Free Vibration Response
1	0.00	367.42	367.59
2	0.20	367.17	367.23
3	0.40	366.13	366.21
4	0.60	364.80	364.80
5	0.80	362.15	362.68
6	1.00	360.52	360.43
7	1.20	356.78	356.92

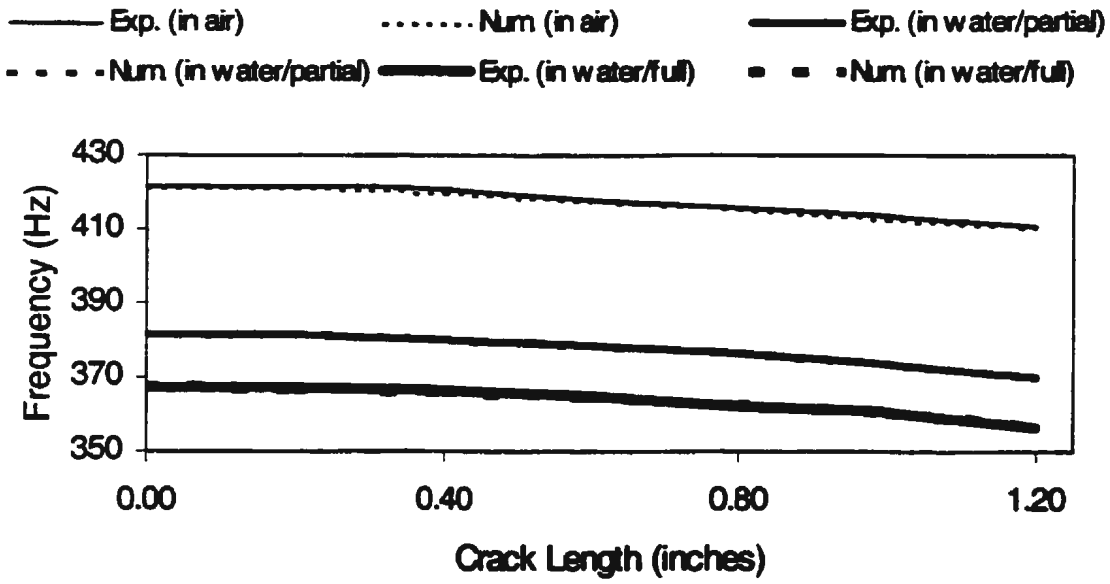

Figure D.6: Comparison of Frequencies of Model #2 in Air and Water (Partial and Full Submergence Conditions)

The differences between them could only be shown from the comparison of their frequencies as shown in Figure D.6. It can be seen from Figure D.6 that the increase of the water depth above the side shell causes the decrease of frequencies. However, Figure D.6 indicates that the decrease in frequencies from the partial submergence to the full submergence is smaller than from in air to the partial submergence for both the undamaged and the damaged conditions. This is due to in fact that the partial submergence condition needed water with the depth of 15.00 inch for submerging the longitudinal, the heavy transverse member, and one side of the side shell of Model #2.

The full submergence condition only needed an additional water with the depth of 4.00 inch above the side shell from the partial submergence condition for submerging the whole model. The added mass of water, in the term of mass density, was then distributed to the whole parts of Model #2. From Figure 5.5, It could be seen that the mode shape for the fourth mode was the vertical vibration in which the bending mode of the side shell and the longitudinal was dominant. This also caused the change in frequencies from in air to the partial submergence was more dominant than that from the partial submergence to the full submergence. Nevertheless, the most important thing that could be observed from Figure D.6 is that the presence of water for both partial and full submergence conditions, did not influence the behavior of Model #2, it only decreased the frequencies. Therefore, the decrease in frequency in air and water has similarly trends for both the undamaged and the damaged conditions.

From the results obtained from Models #1 and #2, it could be concluded that the

randomdec technique as well as the FE model has accurately identified the dynamic behavior of the undamaged model and the model with several damaged lengths in air and water. Hence, they were applied to investigate the other models, i.e., Models #3 and #4, in air and water. The crack location of Model #3 and #4 was different from that of Model #1 and #2. The effect of the crack location on the experimental randomdec signatures, the numerical free vibration responses, and their frequencies are studied.

D.2 Model #3

In order to verify the capability of the randomdec technique and the FE model for identifying the effect of the crack location on the dynamics behavior of the stiffened plate model, Model #3, which also had similar dimensions and characteristics to Models #1 and #2, was investigated. The crack was also made at the face of the longitudinal; however, the location of the crack was 1.35 inch from the heavy transverse member or 0.45 inch far away from the location of the crack of Models #1 and #2. As in the case of Model #2, the analysis was also investigated for each 0.20 crack length in air and water, partial and full submergences.

D.2.1 In air

The numerical free vibration responses along with the experimental randomdec signatures for the undamaged and the damaged model were compared, and the results were presented together in Figures D.7 .a - D.7.g. Their frequencies for the fourth mode were calculated

from Figures D.7, and the results were tabulated together in Table D.4.

It can be analyzed from Figures D.7 and Table D.4 that the experimental randomdec signatures match closely to the numerical free vibration responses, especially for the first cycle and their frequencies. However, the results shown in Figures D.7 and Table D.4 are different from those shown in Figures D.1 and Table D.2, i.e., the frequencies of Model #3 were higher than those of Model #2. This might be also be due to the similar problems that were faced by Model #2.

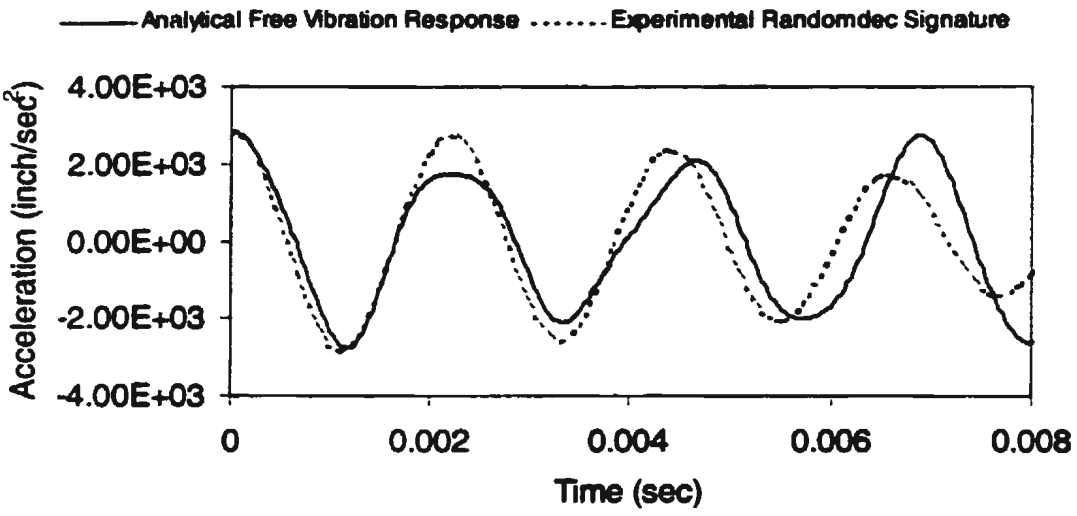

D.7.a: Undamaged

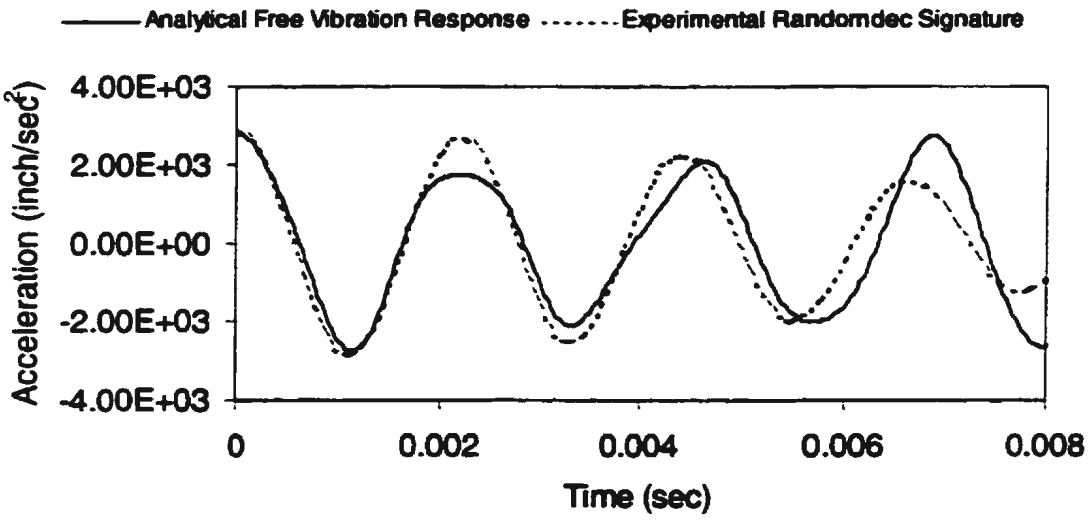

D.7.b: Crack length = 0.20 inch

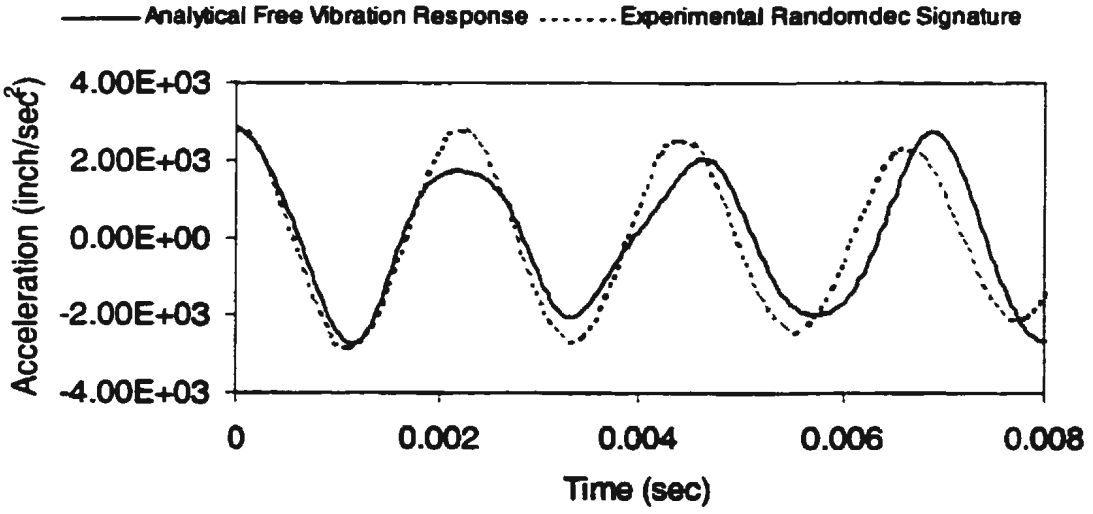

D.7.c: Crack length = 0.40 inch

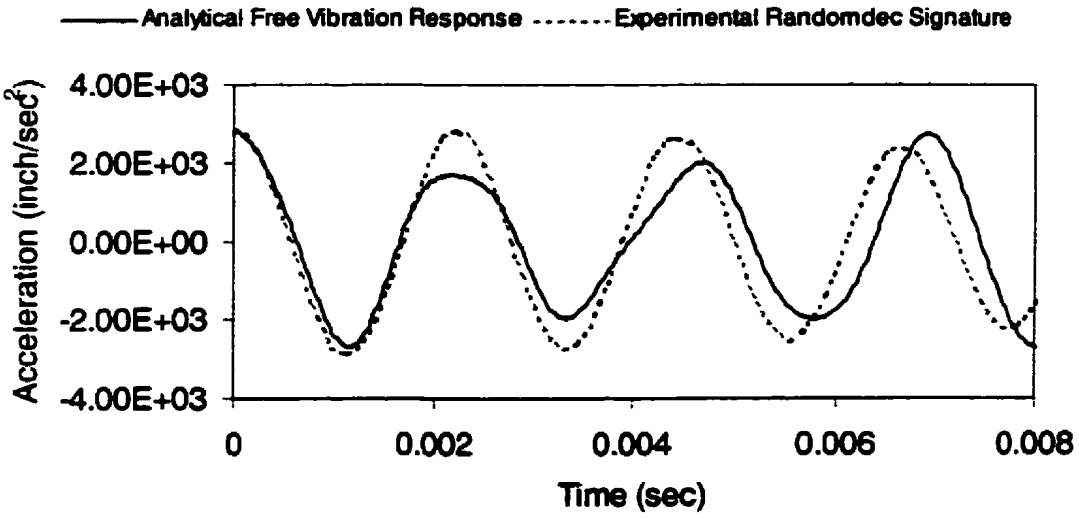

D.7.d: Crack length = 0.60 inch

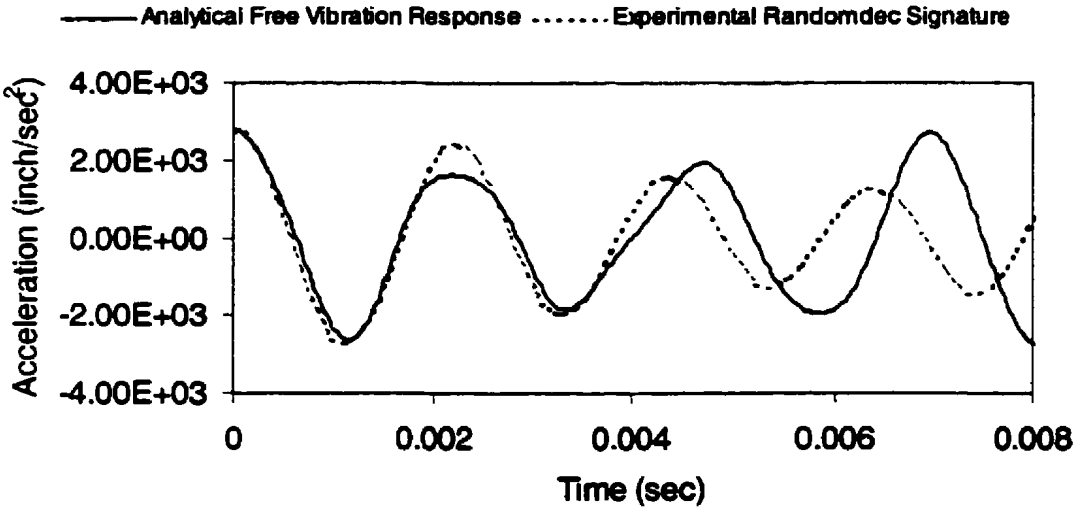

D.7.e: Crack length = 0.80 inch

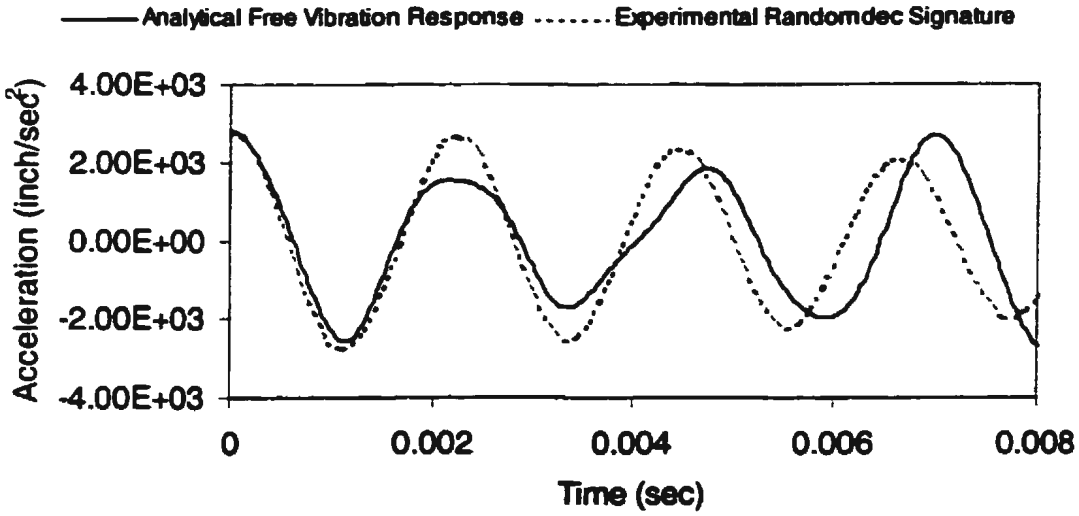

D.7.f: Crack length = 1.00 inch

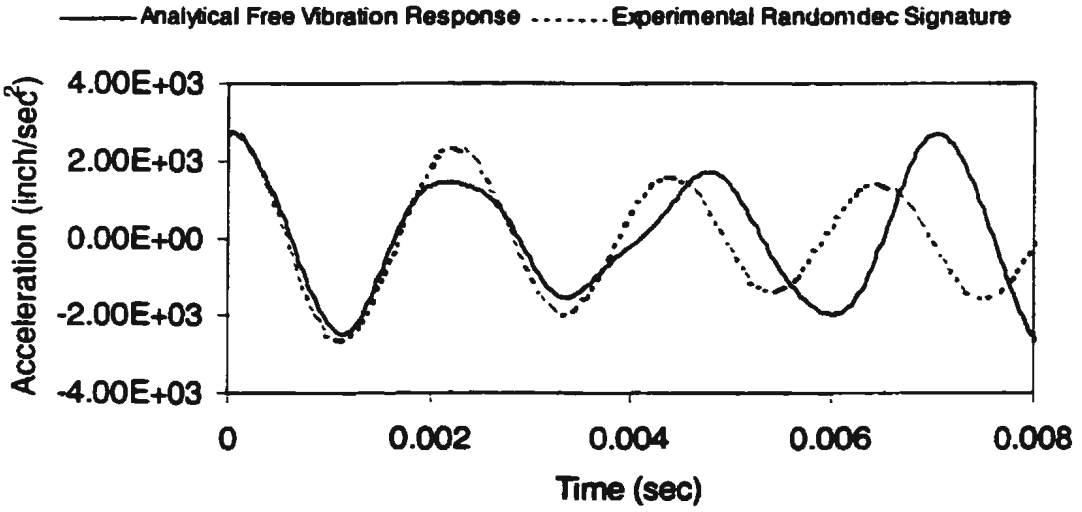

D.7.g: Crack length = 1.20 inch

Figure D.7: Comparison between Experimental Randomdec Signatures and Numerical Free Vibration Responses of Model #3 in Air

Table D.4: Comparison of Experimental Randomdec Signature and Numerical Free Vibration Response Frequencies of Model #3 in Air (Hz)

No	Crack length (Inches)	Exp. Randomdec Signature	Num. Free Vibration Response
1	0.00	453.34	453.13
2	0.20	452.40	452.49
3	0.40	451.66	451.88
4	0.60	450.77	450.90
5	0.80	449.24	449.35
6	1.00	446.97	447.11
7	1.20	444.86	444.84

The original thicknesses of Model #3 were slightly different from Models #1 and #2. Model #3 was also submerged in water for identifying its dynamic responses due to the presence of water. However, the experimental studies of Models #2 and #3 in air and water were conducted in different seasons, in which the temperature of water was different. The experiment of Model #2 was carried out in the Fall 1999 (November - December 1999), whereas Model #3 was in the Winter 2000 (January - February 2000). These might be caused the thicknesses of Models #2 and #3 were different.

Because of this reason, the results obtained from Models #2 and #3 could not be compared each others for analyzing the effect of the crack location on the frequencies. The only solution could be used for solving this problem is that by comparing the trend of the decrease in their frequencies and the percentages. Figure D.8 shows a comparison between

the experimental and numerical frequencies of Models #2 and #3 in air for both the undamaged and the damaged conditions. For convenience, the percentage decrease in frequencies is also tabulated together in Table D.5.

From Figure D.8, it can be seen that the decrease in frequencies of Models #2 and #3 is almost the same for the small cracks ($\leq$ 0.40 inch). When the crack length becomes longer, the decrease in frequency of Model #3 is slightly lower than that of Model #2. However, the percentage difference in the results for each crack lengths are very small, i.e., the maximum difference is less than 2.00 % for the crack length of 1.20 inch as shown in Table D.5. The cause is that the crack location of Model #3 was only 0.45 inch from that of Model #2, and the length of Models #2 and #3 was 22.00 inch. This means that the difference distance between the two crack locations was only 2.05 % of the total length.

The reason for choosing this distance is that the crack always appears at the location which has the high stress concentration such as the location near the heavy transverse member, as discussed in Chapter 2. Also, it can be observed from the mode shape of the fourth mode in Figure 5.8.d that the location of the maximum deflection of the longitudinal was at the center near the heavy transverse member. This means that the maximum bending moment that caused the crack was also at the center. Therefore, the more far the crack location from the center, the change in frequency is decreased.

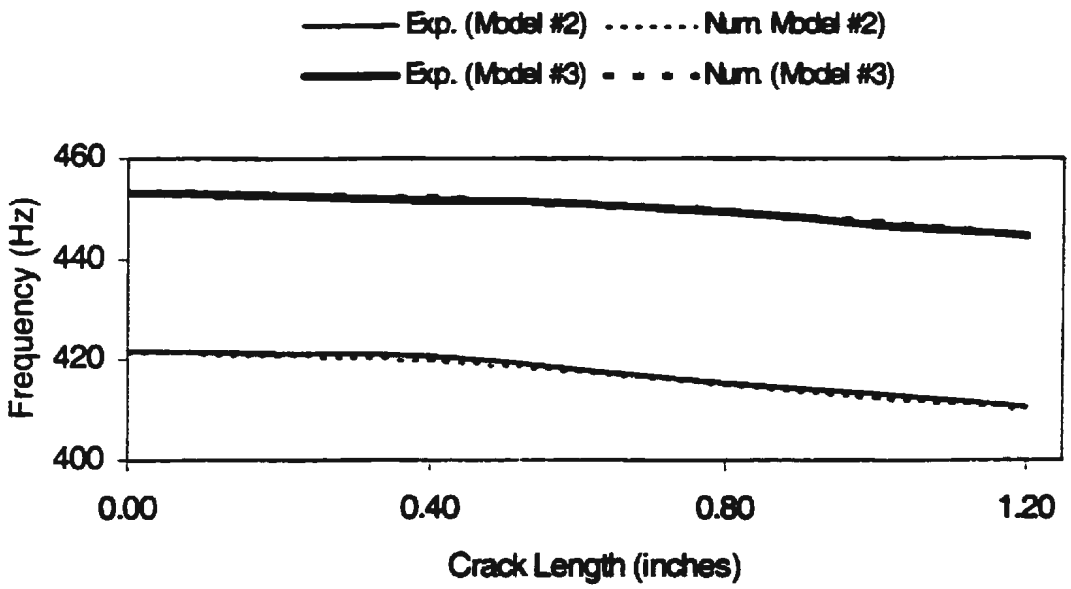

Figure D.8: Comparison of the Decrease in Frequencies of Models #2 and #3 in Air

Table D.5: Percentage Decrease in Frequencies of Models #2 and #3 in Air

Crack length (inches)	Numerical Free Vibration Response				Experimental Randomdec Signature			
	Model #2		Model #3		Model #2		Model #3	
	Freq. (Hz)	%	Freq. (Hz)	%	Freq. (Hz)	%	Freq. (Hz)	%
0.00	421.74	100	453.13	100	421.59	100	453.34	100
0.20	421.20	99.872	452.49	99.859	421.20	99.907	452.40	99.792
0.40	420.17	99.628	451.98	99.746	420.67	99.781	451.66	99.629
0.60	417.99	99.111	450.90	99.508	417.94	99.134	450.77	99.431
0.80	415.56	98.535	449.35	99.166	415.66	98.593	449.24	99.095
1.00	412.67	97.849	447.11	98.671	413.44	98.067	446.97	98.594
1.20	410.50	97.335	444.84	98.171	410.87	97.457	444.86	98.129

Based on the above results, it can be concluded that the randomdec technique as well as the FE model could be used to analyze the effect of the crack location on the dynamics behavior of the stiffened plate model in air. In order to ensure that the methods could be also used to observe the model submerged in water, they were used again to identify the dynamic behavior of Model #3 in water for both in partial and full submergence conditions.

D.2.2 In Water

D.2.2.1 Partial Submergence

Figures D.9.a -D.9.g show the comparison between the experimental randomdec signatures and the free vibration responses for the undamaged and the damaged conditions. Table D.6 tabulates the comparison between their frequencies obtained from Figures D.9. It can be observed from Figures D.9 that the experimental randomdec signatures and the numerical free vibration responses are in a good agreement, especially for the first cycle and their frequencies. Furthermore, Table D.6 also indicates that the comparison between the experimental and numerical frequencies are an excellent.

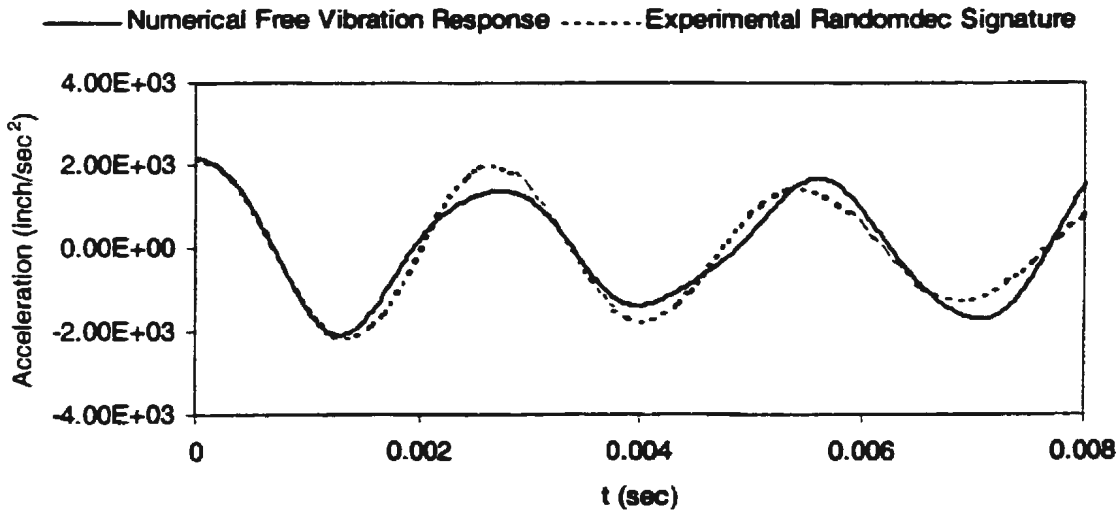

D.9.a: Undamaged

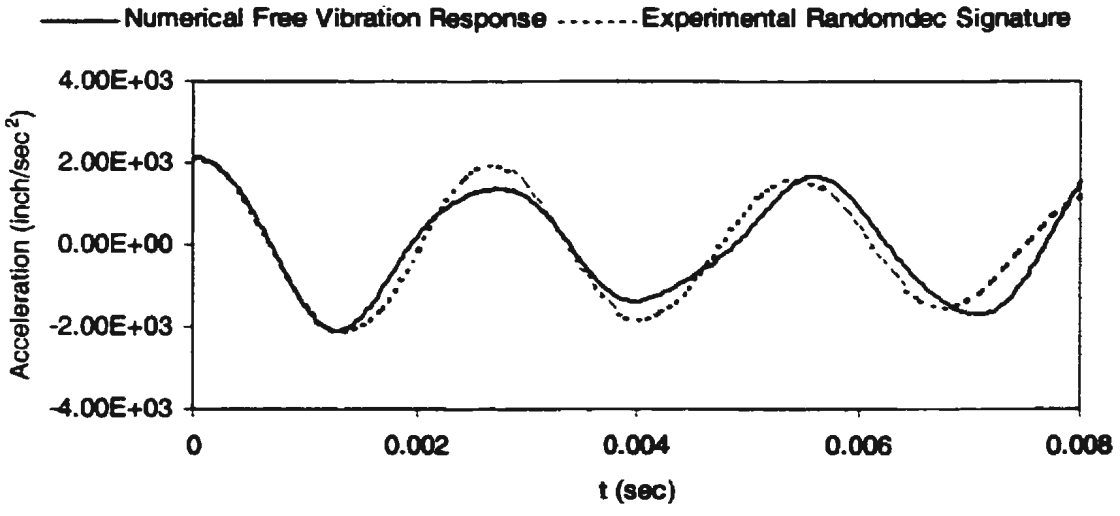

D.9.b: Crack length = 0.20 inch

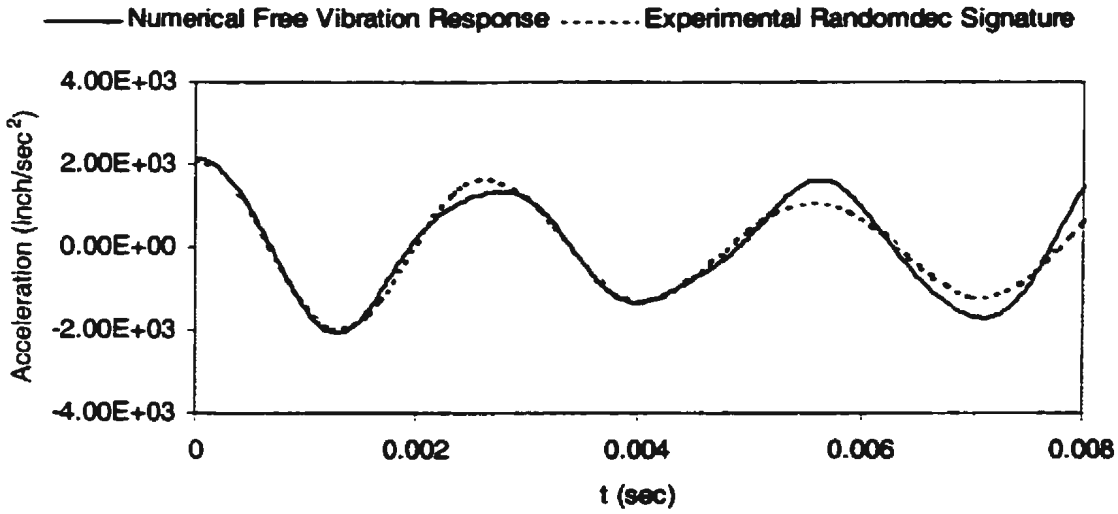

D.9.c: Crack length = 0.40 inch

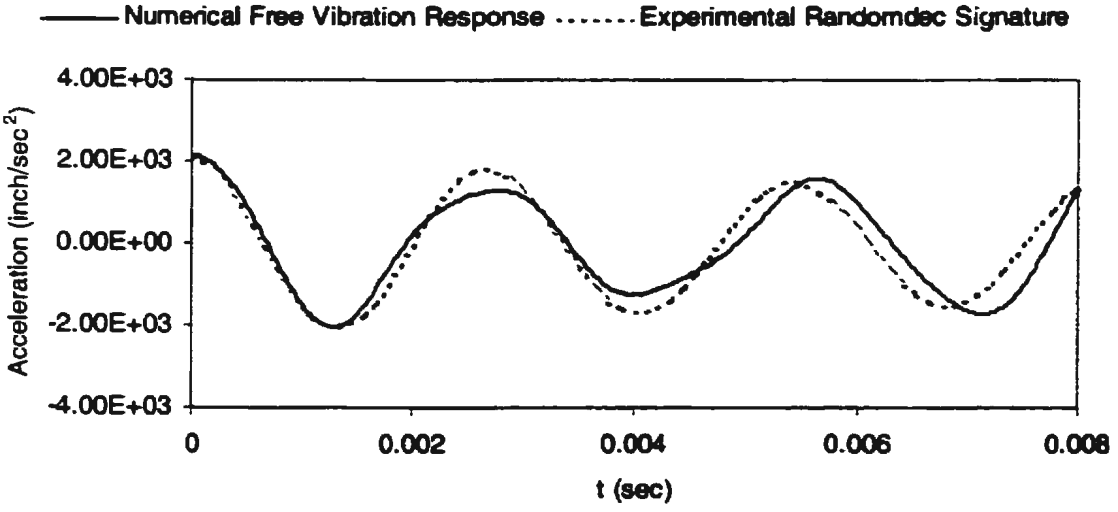

D.9.d: Crack length = 0.60 inch

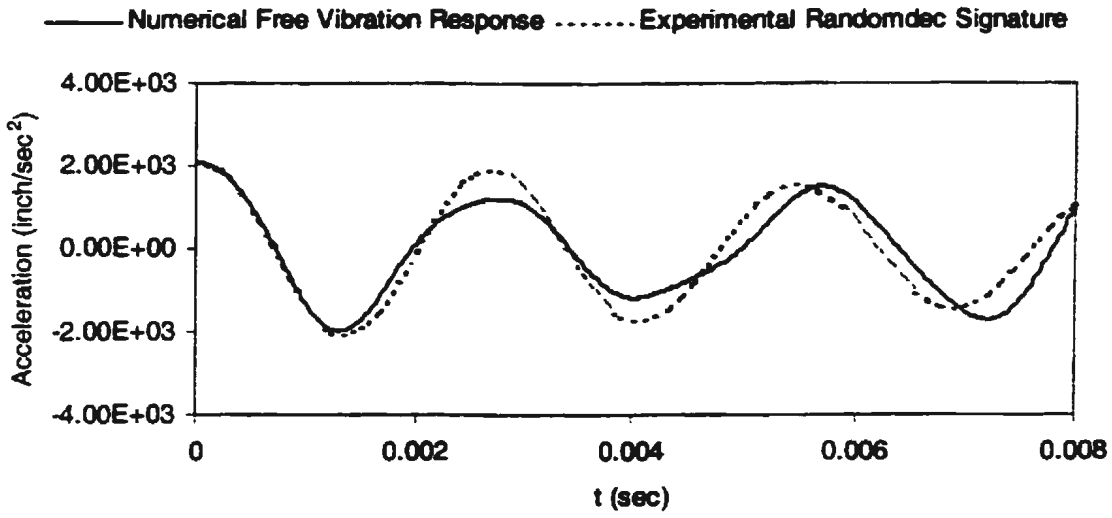

D.9.e: Crack length = 0.80 inch

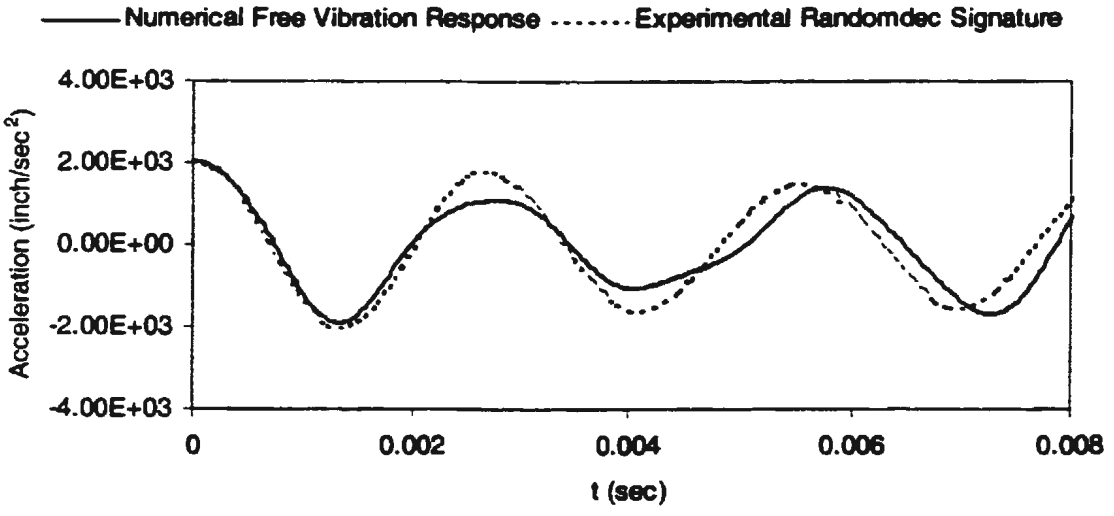

D.9.f: Crack length = 1.00 inch

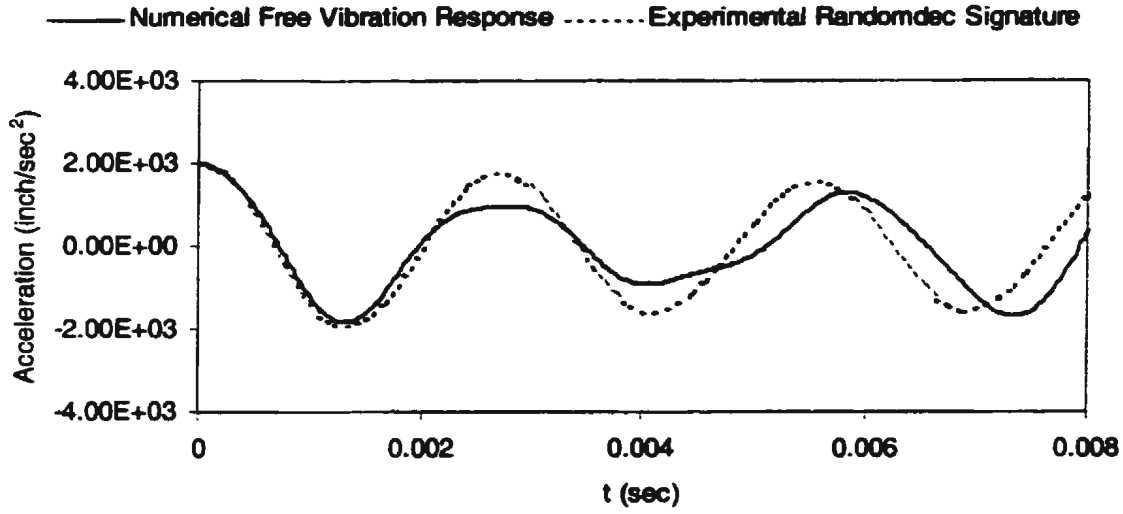

D.9.g: Crack length = 1.20 inch

Figure D.9: Comparison between Experimental Randomdec Signatures and Numerical Free Vibration Responses of Model #3 in Water (Partial Submergence)

Table D.6: Comparison of Experimental Randomdec Signature and Numerical Free Vibration Response Frequencies of Model #3 in Water (Partial Submergence) (Hz)

No	Crack length (Inches)	Exp. Randomdec Signature	Num. Free Vibration Response
1	0.00	371.60	371.61
2	0.20	371.42	371.01
3	0.40	370.86	370.61
4	0.60	370.02	369.76
5	0.80	368.31	368.09
6	1.00	366.53	366.46
7	1.20	364.89	364.70

Unlike the frequencies in air in which the frequencies of Model #3 were higher than those of Model #2, the frequencies of Model #3 in water, partial submergence, tabulated in Table D.6 were lower than those tabulated in Table D.2. Moreover, the decrease percentage in frequencies between Models #2 and #3 due to the presence of water was also different. The frequencies of Model # 2 were decreased approximately by 13.00 %, whereas those of Model #3 were decreased approximately by 19.00 %. This might also be caused by the difference between the temperature of water.

In order to check the effect of the crack location in water on the decrease in frequencies, the percentage decrease in frequencies of Models #2 and #3 due to the presence of water were drawn and tabulated together in Figure D.10 and Table D.7, respectively.

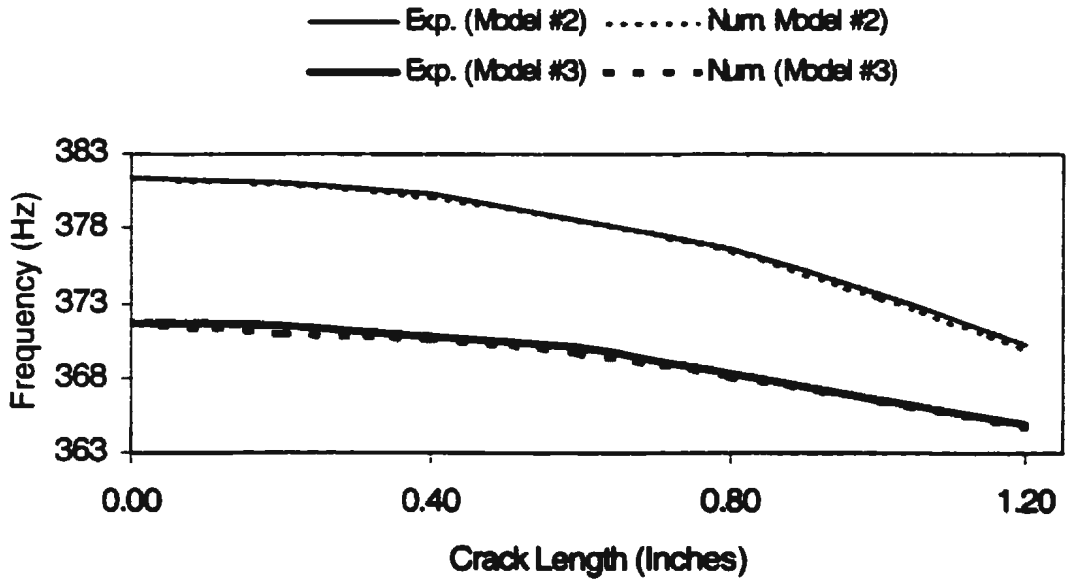

Figure D.10: Comparison of Frequencies of Models #2 and #3 in Water (Partial Submergence)

Table D.7: Percentage Decrease in Frequencies of Models #2 and #3 in Water (Partial Submergence)

Crack length (inches)	Numerical Free Vibration Response				Experimental Randomdec Signature			
	Model #2		Model #3		Model #2		Model #3	
	Freq. (Hz)	%	Freq. (Hz)	%	Freq. (Hz)	%	Freq. (Hz)	%
0.00	381.48	100	371.61	100	381.45	100	371.60	100
0.20	381.09	99.898	371.01	99.838	381.10	99.908	371.42	99.951
0.40	380.16	99.654	370.61	99.731	380.34	99.709	370.86	99.801
0.60	378.58	99.240	369.76	99.502	378.64	99.263	370.02	99.575
0.80	376.60	98.721	368.09	99.053	376.64	98.739	368.31	99.115
1.00	373.51	97.911	366.46	98.614	373.56	97.931	366.53	98.636
1.20	370.11	97.020	364.70	98.141	370.17	97.043	364.89	98.194

From Figure D.10 and Table D.7, it could be determined that the frequencies of Models #2 and #3 in water decreased with the similar pattern for the small cracks ($\leq$ 0.60 inch). When the crack length increased, the decrease in frequencies of Model #3 was not as sharp as Model #2. Furthermore, the results in Table D.7 had similarity with the results in Table D.2, i.e., the decrease percentage for each crack lengths were very small and the maximum difference was less than 2.00 % for the crack of 1.20 inch. This similarity means that the presence of water only caused the decrease in frequencies only, not the signatures. Based on the above results, the randomdec technique and the FE model were used for identifying the dynamic behavior of Model #3 that was full submerged in water in the following section.

D.2.2.2 Full Submergence

The experimental randomdec signatures and the numerical free vibration responses in full submergence conditions for the undamaged and the damaged conditions were compared each others, and the results are drawn in Figures D.11.a - D.11.g. Table D.8 gives the comparison of their frequencies obtained from Figures D.11. It was found from Figures D.11 that the agreement between the numerical free vibration responses and the experimental randomdec signatures was seen to be good for both the undamaged and the damaged conditions. The signatures and responses shown in Figure D.11 were similar to Figures D.9. The comparison of their frequencies shown in Table D.9 was also excellent in all cases.

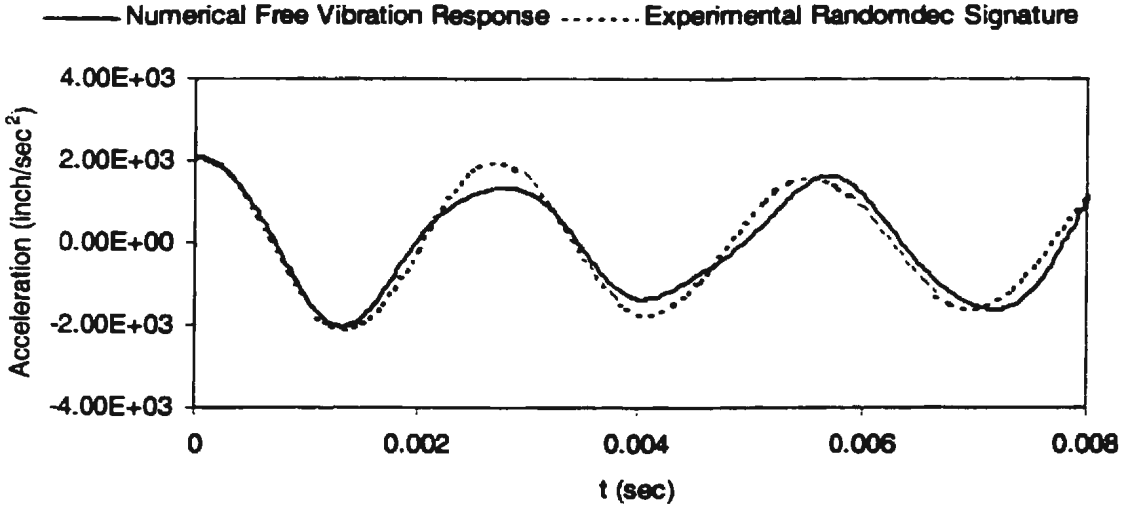

D.11.a: Undamaged

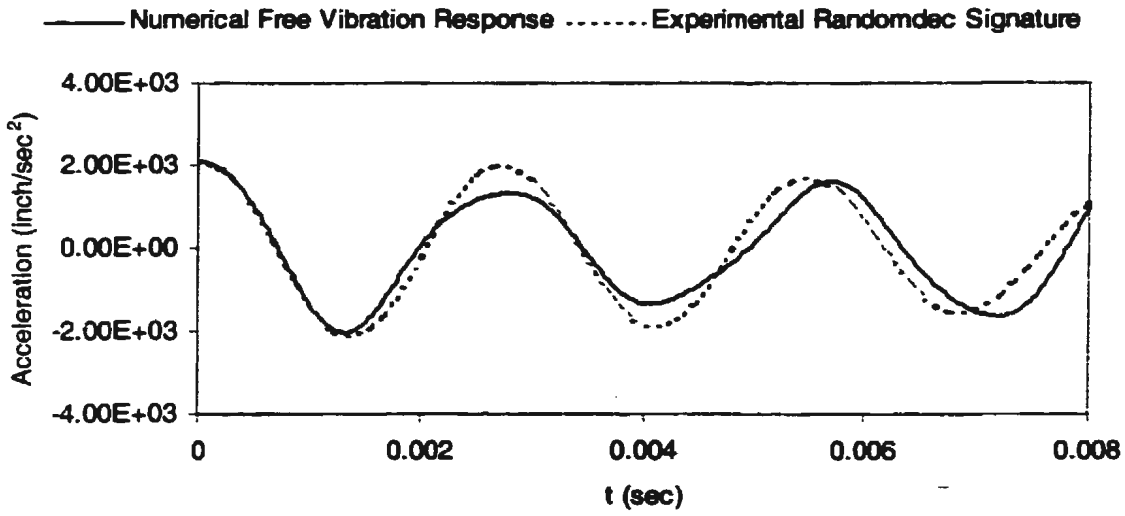

D.11.b: Crack length = 0.20 inch

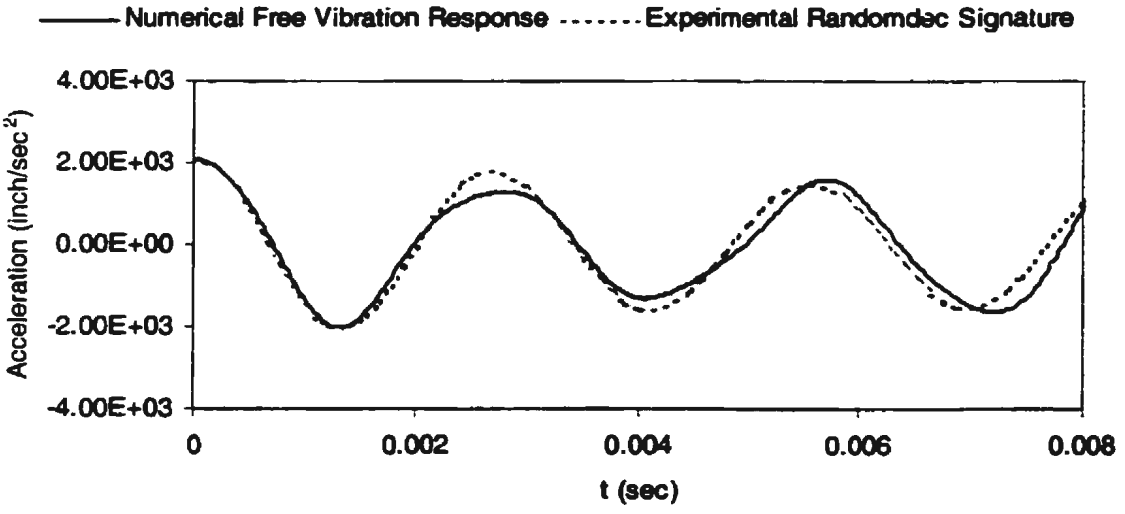

D.11.c: Crack length = 0.40 inch

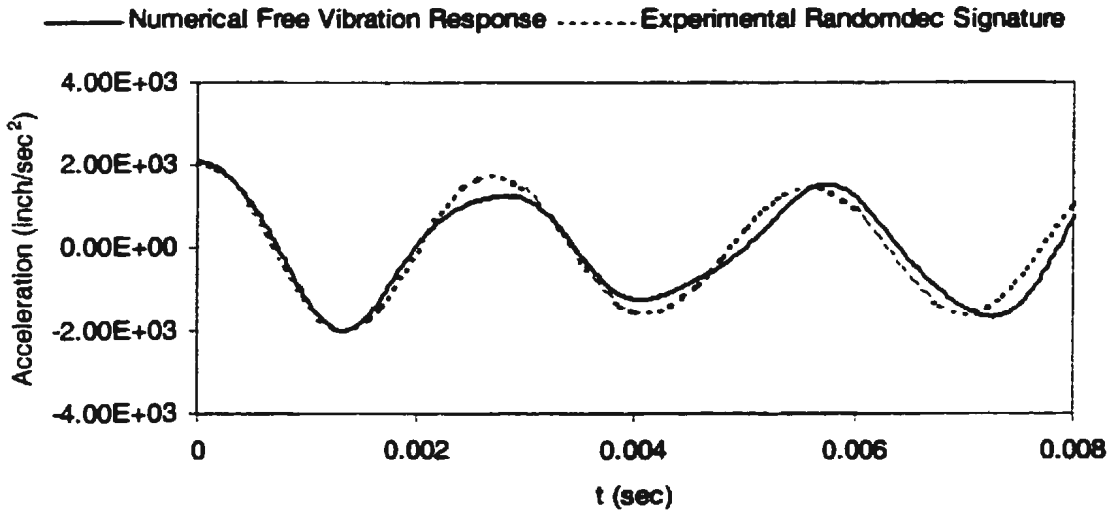

D.11.d: Crack length = 0.60 inch

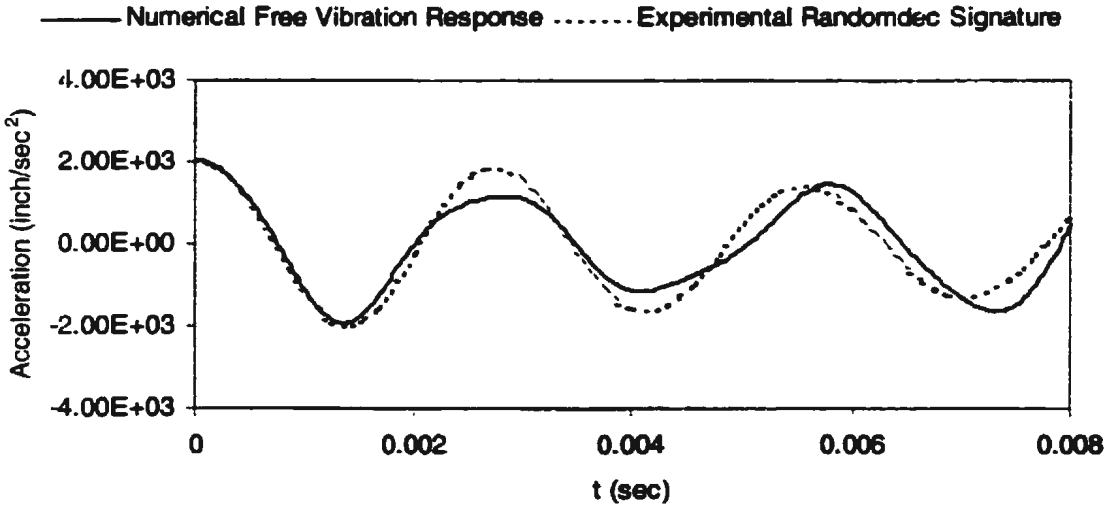

D.11.e: Crack length = 0.80 inch

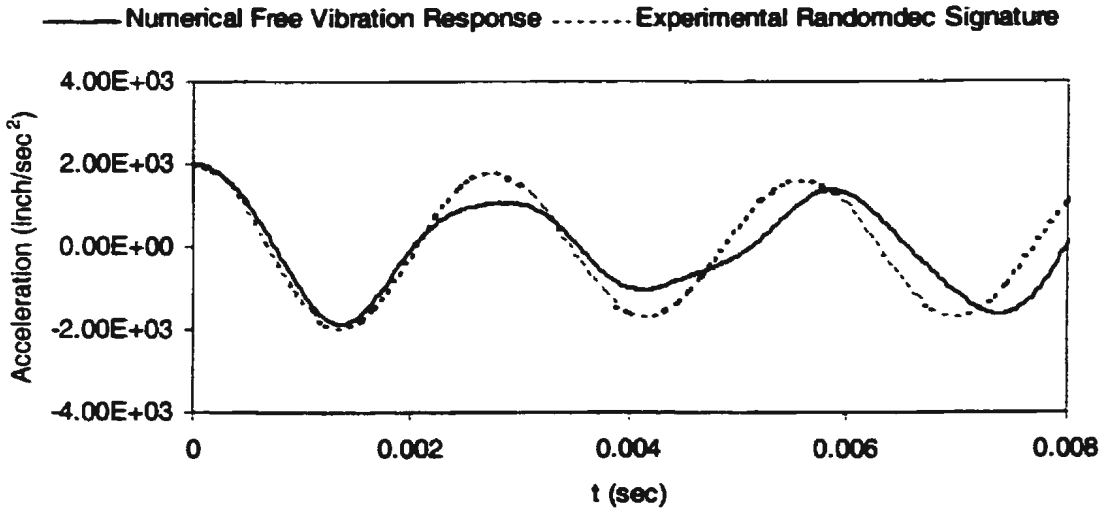

D.11.f: Crack length = 1.00 inch

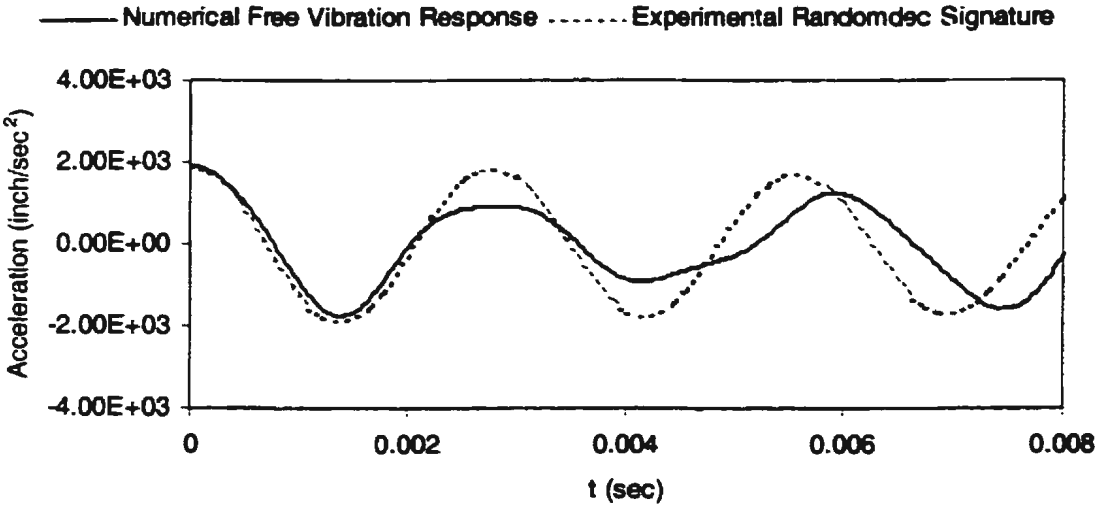

D.11.g: Crack length = 1.20 inch

Figure D.11: Comparison between Experimental Randomdec Signatures and Numerical Free Vibration Responses of Model #3 in Water (Full Submergence)

Table D.8: Comparison of Experimental Randomdec Signature and Numerical Free Vibration Response Frequencies of Model #3 in Water (Full Submergence) (Hz)

No	Crack length (Inches)	Exp. Randomdec Signature	Num. Free Vibration Response
1	0.00	366.83	366.71
2	0.20	366.37	366.58
3	0.40	365.68	365.92
4	0.60	364.78	364.93
5	0.80	363.48	363.52
6	1.00	361.60	361.46
7	1.20	359.83	359.84

However, the environmental condition, i.e., the temperature of water, is still the cause of the difference in the results. Figure D.12 and Table D.9 show the effect of the environmental condition on the change in frequencies. For the cracks with the length less than 0.60 inch, Figure D.12 and Table D.9 present that the frequencies of Models #2 and #3 decreased with the similar pattern. With the increase of the crack lengths, the decrease in frequencies of Model #3 was slightly lower than that of Model #2. The results shown in Figures D.12 and Table D.9 had similarity to those shown in Tables D.4 and D.7, i.e., the decrease percentage for each crack lengths were very small and the maximum difference was less than 2.00 % for the crack length of 1.20 inch.

Furthermore, Figure D.12 shows that the frequencies of Models #2 and #3 in full submergence are almost the same, whereas in partial submergence (see Figure D.6) they are

different. This might be also due to the difference of the environmental condition. Nevertheless, there is the similarity in the decrease percentage between the results in Figure D.6 and D.12. This means that the randomdec signature as well as the FE model accurately analyzed the dynamic responses of the stiffened plate model for both in air and water.

In order to get the large difference between frequencies due to the difference of the crack location, the randomdec technique and the FE model were then used for identifying Model #4 which has different location of the crack.

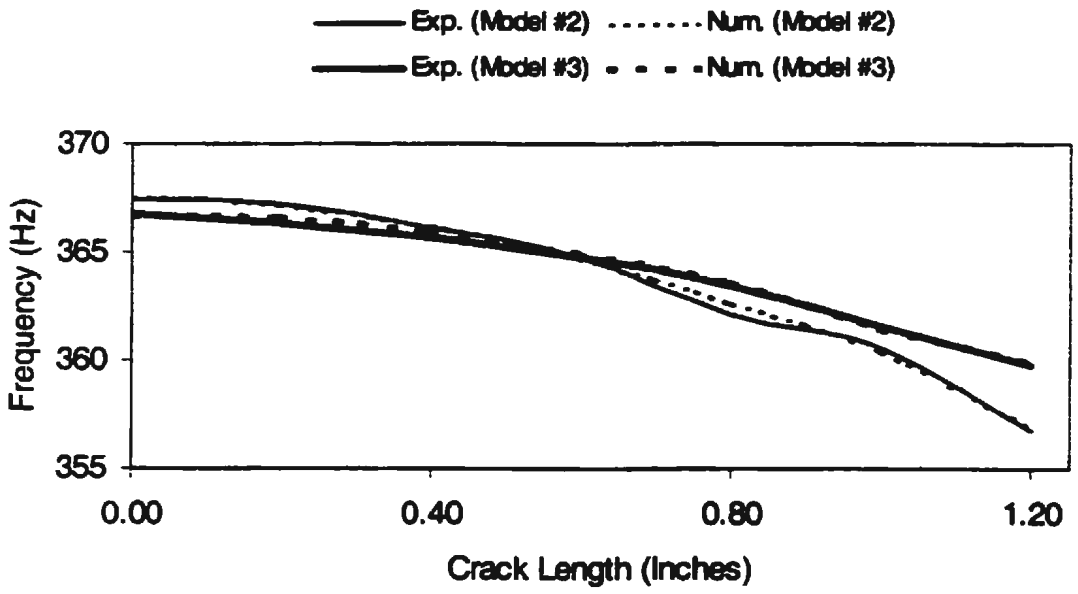

Figure D.12: Comparison of Frequencies of Models #2 and #3 in Water (Full Submergence)

Table D.9: Percentage Decrease in Frequencies of Models #2 and #3 in Water (Full Submergence)

Crack length (inches)	Numerical Free Vibration Response				Experimental Randomdec Signature			
	Model #2		Model #3		Model #2		Model #3	
	Freq. (Hz)	%	Freq. (Hz)	%	Freq. (Hz)	%	Freq. (Hz)	%
0.00	367.59	100	366.71	100	367.42	100	366.83	100
0.20	367.23	99.902	366.58	99.965	367.17	99.931	366.37	99.875
0.40	366.21	99.625	365.92	99.785	366.13	99.649	365.68	99.687
0.60	364.80	99.241	364.93	99.515	364.80	99.287	364.78	99.441
0.80	362.68	98.664	363.52	99.130	362.15	98.566	363.48	99.087
1.00	360.43	98.052	361.46	98.568	360.52	98.122	361.60	98.574
1.20	356.92	97.097	359.84	98.127	356.78	97.104	359.83	98.092

D.3 Model #4

The dimensions and characteristics of Model #4 were also slightly different to those of Models #1, #2, and #3. The crack was made at the distance of 1.80 inch from the heavy transverse member or 0.90 inch far away from the location of the crack of Models #1 and #2 or 0.45 inch far away from the crack location of Model #3. The reasons for choosing this distance are the same as that was explained for Model #3. Similar to Models #2 and #3, the investigation of the dynamic behavior of Model #4 was also carried out for each 0.20 crack length in air and water, partial and full submergences.

D.3.1 In air

The experimental randomdec signatures are compared with the numerical free vibration responses for both the undamaged and the damaged conditions, and the results are drawn together in Figures D.13.a - D.13.g. The frequencies obtained from these figures for the fourth mode are tabulated in Table D.10. Figures D.13 and Table D.10 indicate that the experimental and numerical results are closed each others for both signatures and frequencies. The change in signatures and the decrease in frequencies due to the occurrence of the damage could be also seen from Figures D.13 and Table D.10. The signatures shown in Figures D.13 are similar to those shown in Figure 5.11, D.1 and D.7; however, the frequencies shown in Table D.10 were different from those shown in Tables 5.4, D.1 and D.4, respectively.

In addition to the problem of thickness and model installation, the difference time for carrying out the experiment for Models #3 and #4 caused the results between them are also different. Like Model #3, the experiment of Model #4 was also carried out in the winter 2000. However, Model #4 was tested during March and April 2000 in which the temperature was lower than February and March 2000. Hence the results obtained from Model #4 could not be also compared with those obtained from Models #2 or #3 for checking the effect of the crack location on the signature and frequency.

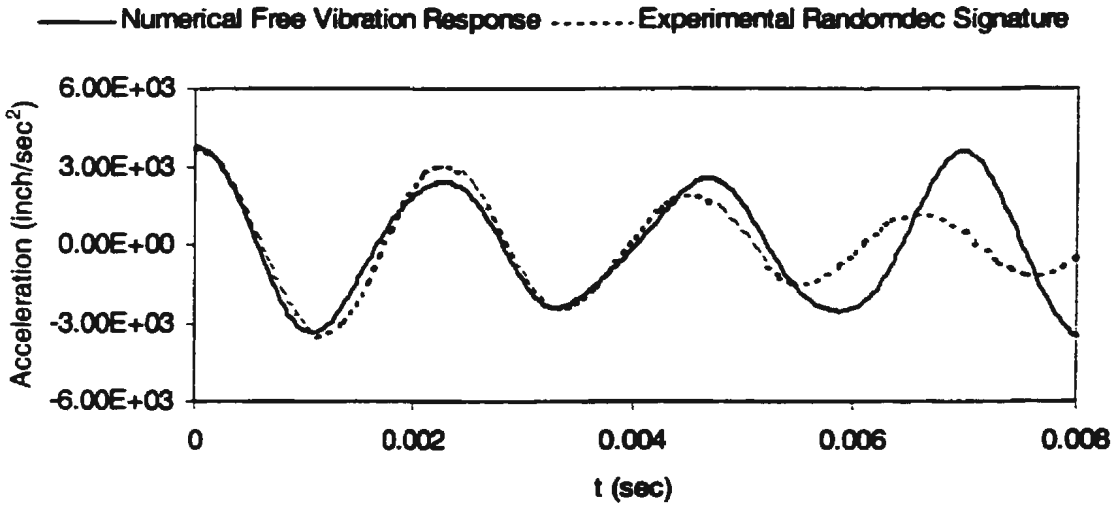

D.13.a: Undamaged

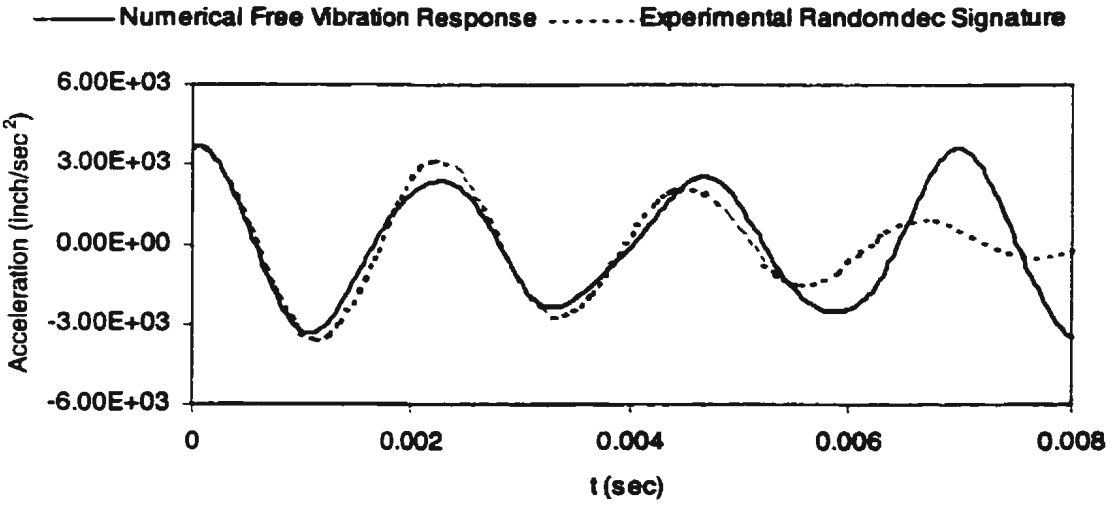

D.13.b: Crack length = 0.20 inch

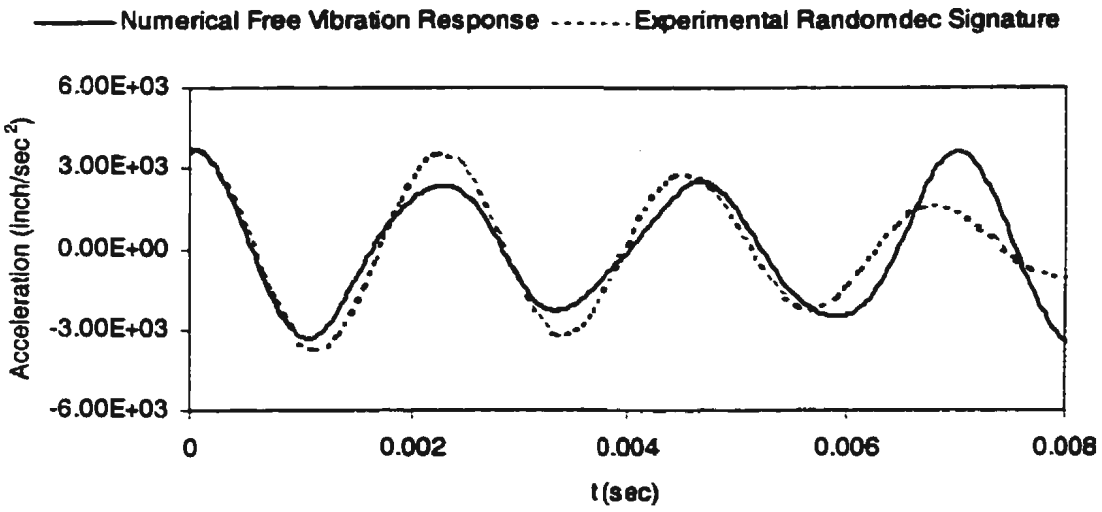

D.13.c: Crack length = 0.40 inch

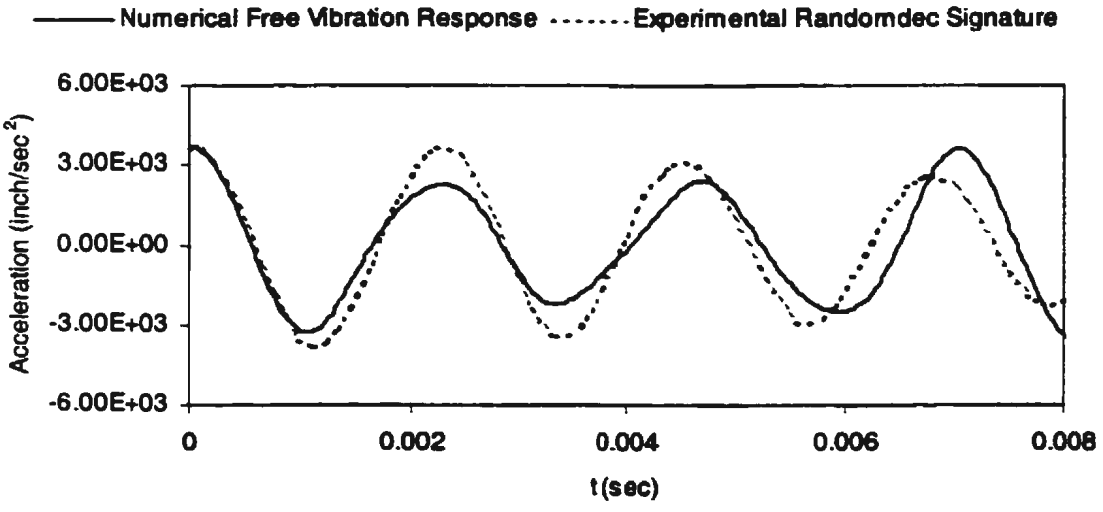

D.13.d: Crack length = 0.60 inch

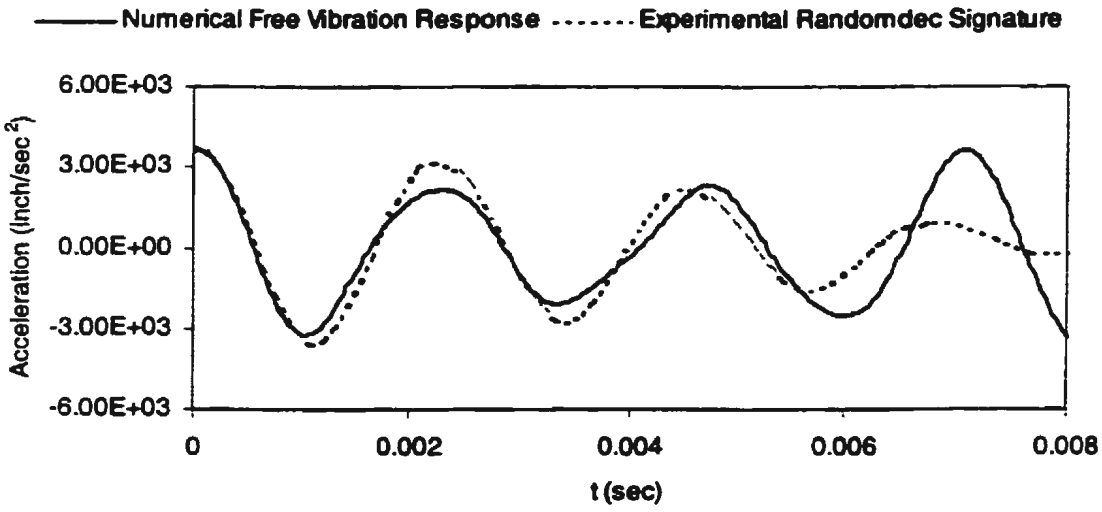

D.13.e: Crack length = 0.80 inch

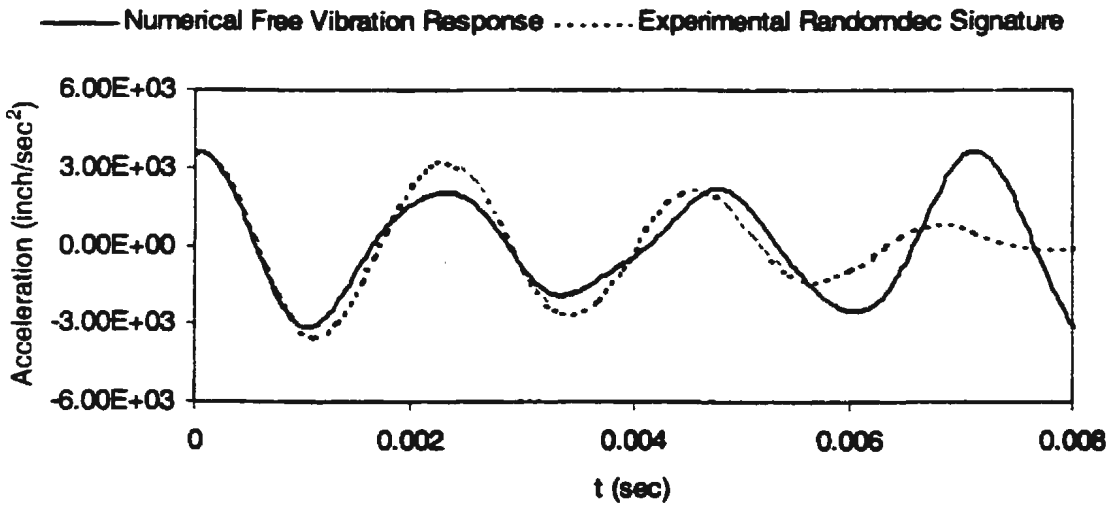

D.13.f: Crack length = 1.00 inch

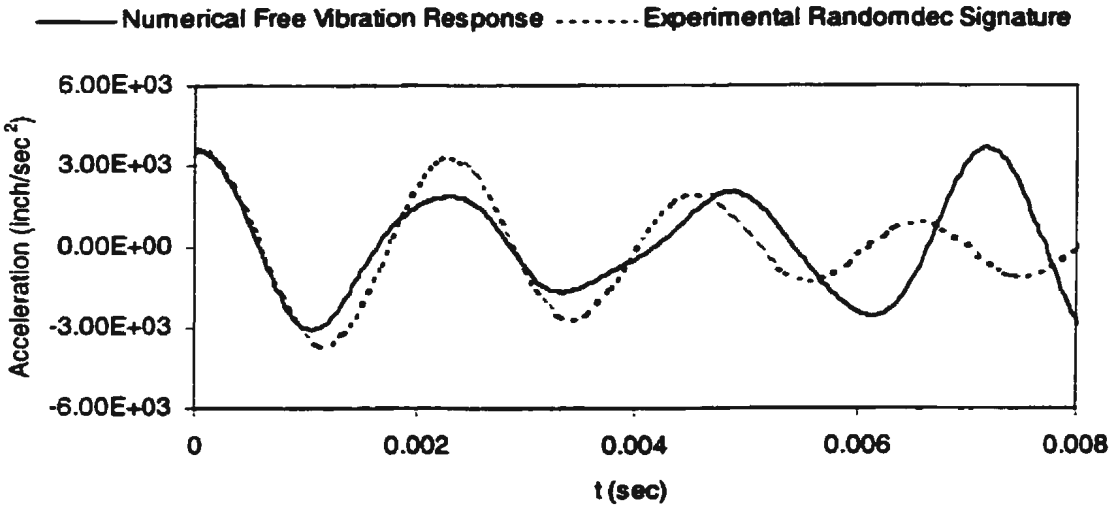

D.13.g: Crack length = 1.20 inch

Figure D.13: Comparison between Experimental Randomdec Signatures and Numerical Free Vibration Responses of Model #4 in Air

Table D.10: Comparison of Experimental Randomdec Signature and Numerical Free Vibration Response Frequencies for Model #4 in Air (Hz)

No	Crack length (Inches)	Exp. Randomdec Signature	Num. Free Vibration Response
1	0.00	442.22	441.90
2	0.20	442.19	441.59
3	0.40	441.03	440.82
4	0.60	440.07	439.88
5	0.80	438.17	438.66
6	1.00	436.55	436.76
7	1.20	434.08	434.40

In order to check the effect of the crack location to the frequencies, the trend of the decrease in the frequencies and the percentages for Models #2, #3, and #4 in air for both experimental and numerical results are compared, and the results are drawn together in Figure D.14, and tabulated in Table D.11. For the crack length less than 0.40 inch, Figure D.14 and Table D.11 show that the decrease in frequencies of Models #2, #3, and #4 is almost the same. The decrease in frequencies of Model #4 is slightly lower than those of Models #2 and #3 when the crack length became longer. These results indicated that, for the same crack length, the different in crack location caused the percentage of decrease in frequencies was also different.

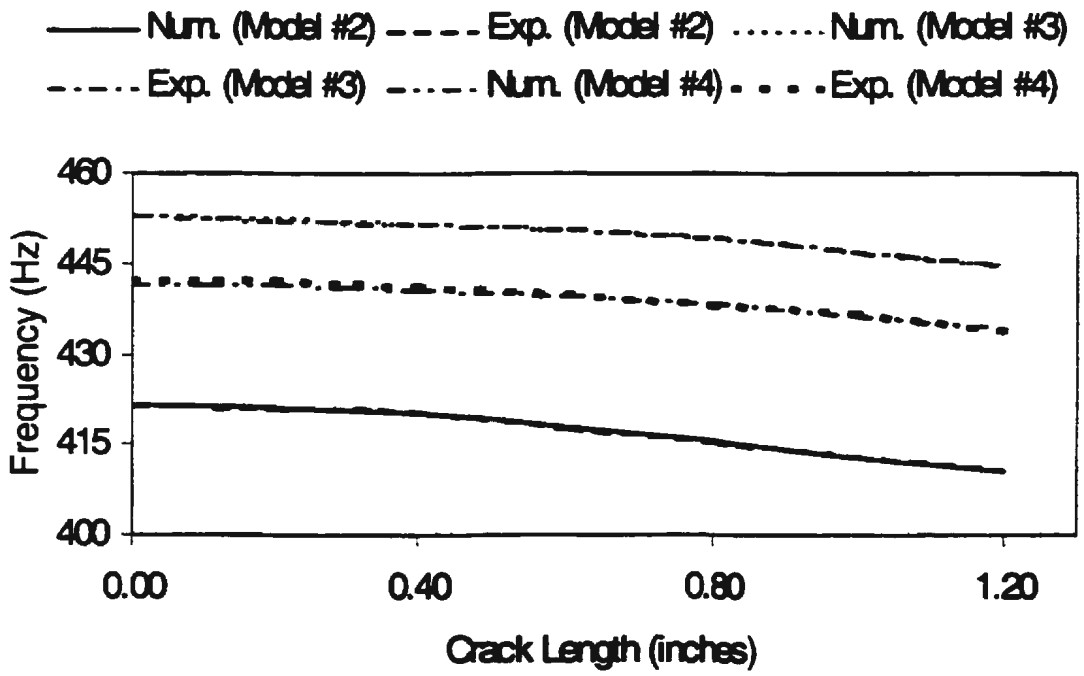

Figure D.14: Comparison of Frequencies of Models #2, #3, and #4 in Air

Table D.11: Percentage Decrease in Frequencies of Models #2, #3, and #4 in Air

Crack length (inches)	Numerical Free Vibration Response						Experimental Randomdec Signature					
	Model #2		Model #3		Model #4		Model #2		Model #3		Model #4	
	Freq. (Hz)	%	Freq. (Hz)	%	Freq (Hz)	%	Freq. (Hz)	%	Freq. (Hz)	%	Freq (Hz)	%
0.00	421.74	100	453.13	100	441.90	100	421.59	100	453.34	100	442.22	100
0.20	421.20	99.872	452.49	99.859	441.59	99.930	421.20	99.907	452.40	99.792	442.19	99.993
0.40	420.17	99.628	451.98	99.746	440.82	99.756	420.67	99.781	451.66	99.629	441.03	99.731
0.60	417.99	99.111	450.90	99.508	439.88	99.543	417.94	99.134	450.77	99.431	440.07	99.514
0.80	415.56	98.535	449.35	99.166	438.66	99.267	415.66	98.593	449.24	99.095	438.17	99.084
1.00	412.67	97.849	447.11	98.671	436.76	98.837	413.44	98.067	446.97	98.594	436.55	98.718
1.20	410.50	97.335	444.84	98.171	434.40	98.303	410.87	97.457	444.86	98.129	434.08	98.159

Similar to Models #2 and #3, Table D.11 also shows that the difference in the results for each crack lengths were also very small for the crack length of 1.20 inch, i.e., the maximum difference was less than 2.00 %. This was also due to in the fact that the distance of the crack of Model #4 was only 0.45 inch from Model #3 or 0.90 inch from Model #2, or 1.35 inch from the heavy transverse member.

It can be concluded from the results obtained from Models #2, #3, and #4 vibrated in air that the randomdec technique as well as the FE model could identify the effect of the crack location on the dynamics behavior of the stiffened plate model in air. In order to ensure that the methods could be also used to observe Model #4 submerged in water, they were used again to identify the dynamic behavior of Model #4 in water, partial and full submergence.

D.3.2 In Water

D.3.2.1 Partial Submergence

Figures D.15.a, b, c, d, e, f, and g show a comparison between the experimental randomdec signatures and the numerical free vibration responses for undamaged and damaged model with crack lengths 0.20 inch, 0.40 inch, 0.60 inch, 0.80 inch, 1.00 inch, and 1.20 inch, respectively. For comparison, the frequencies obtained from Figure D.15.a through D.15.g are tabulated in Table D.12.

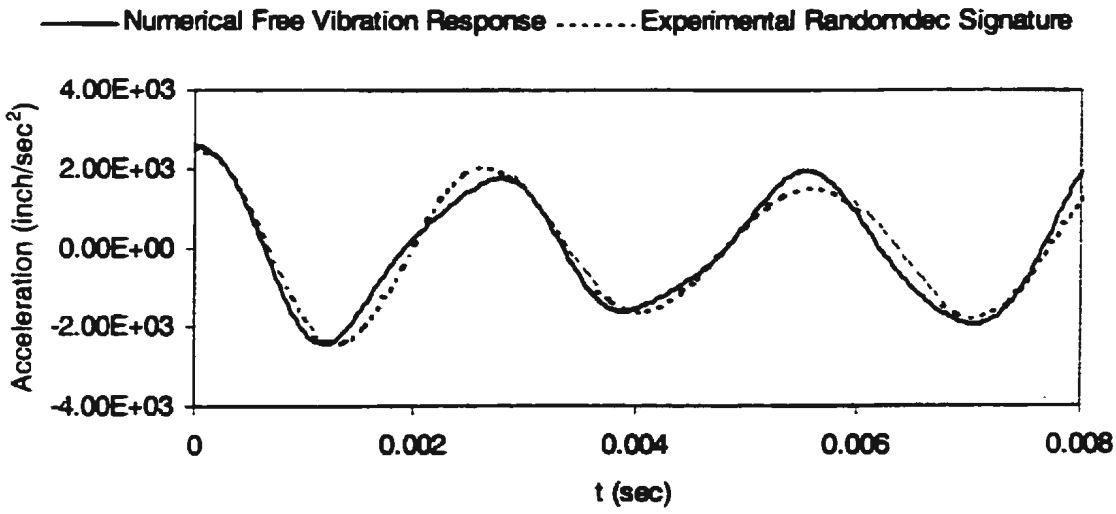

D.15.a: Undamaged

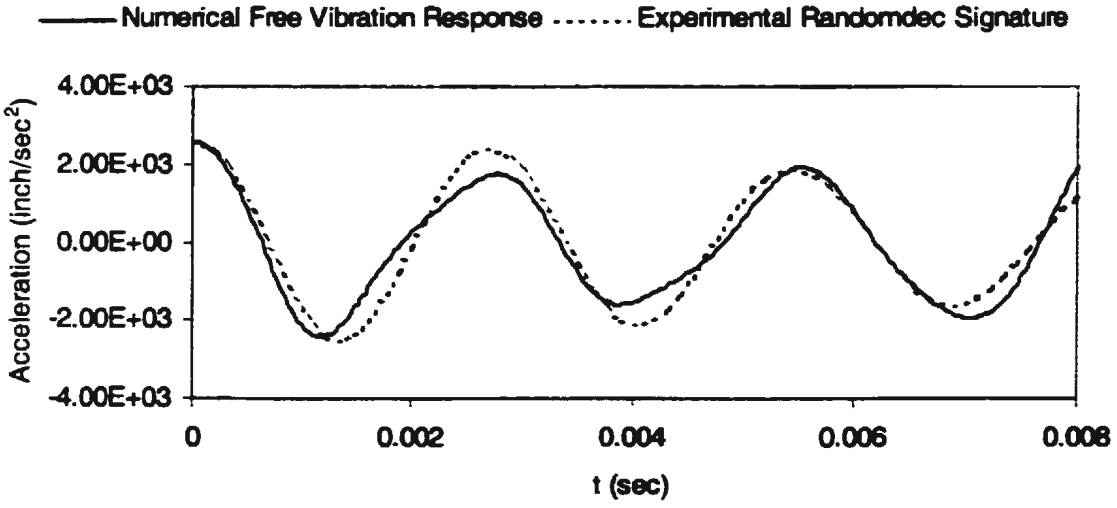

D.15.b: Crack length = 0.20 inch

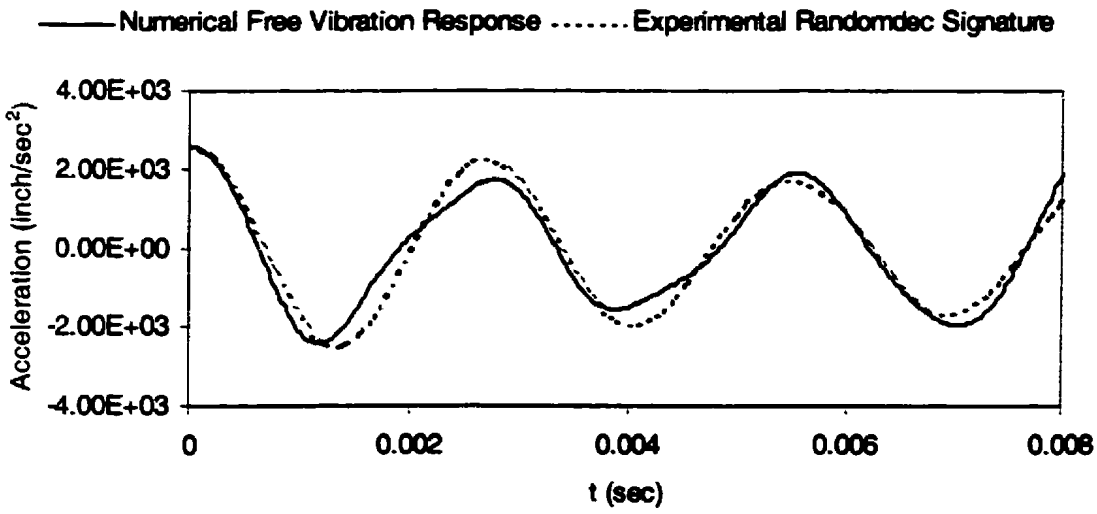

D.15.c: Crack length = 0.40 inch

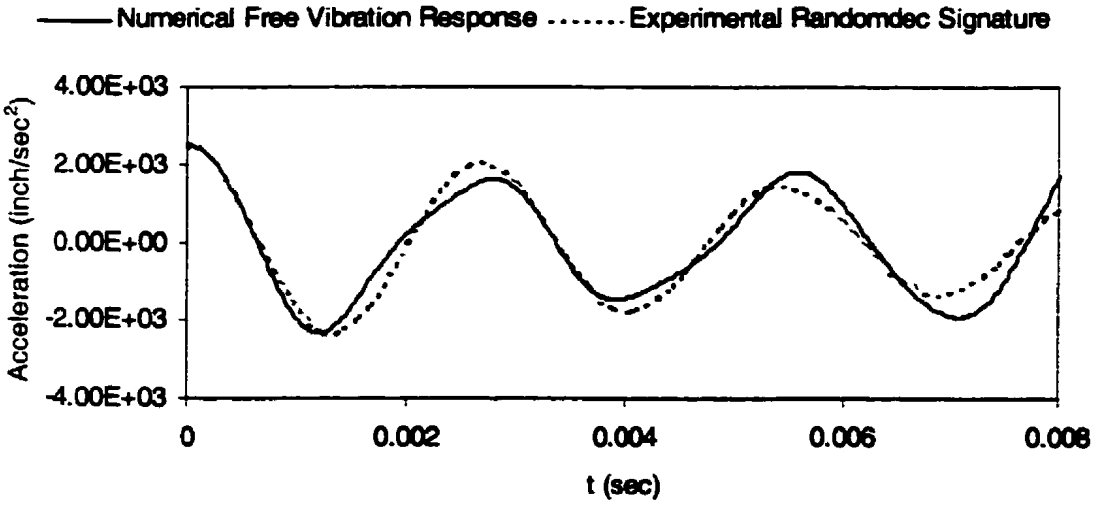

D.15.d: Crack length = 0.60 inch

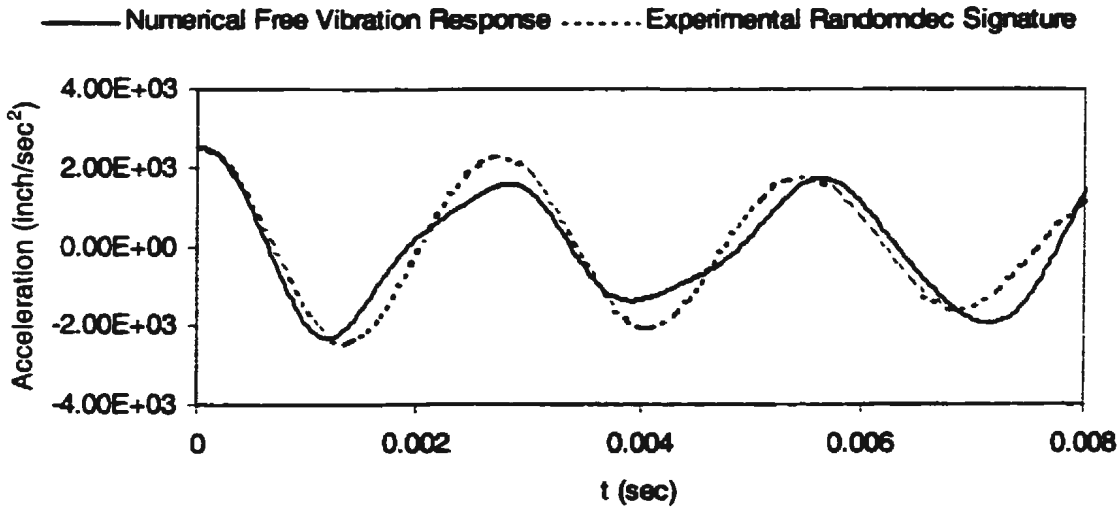

D.15.e: Crack length = 0.80 inch

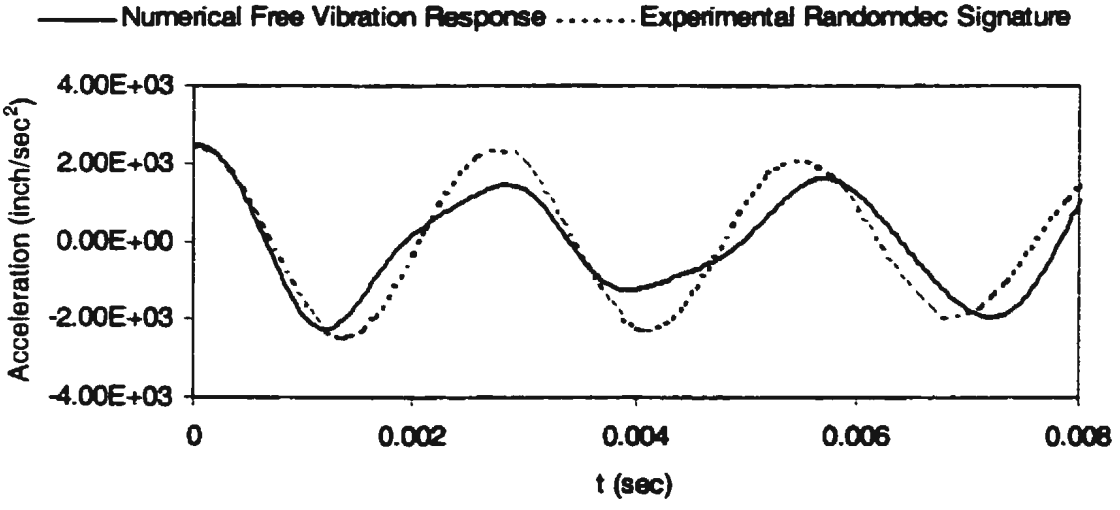

D.15.f: Crack length = 1.00 inch

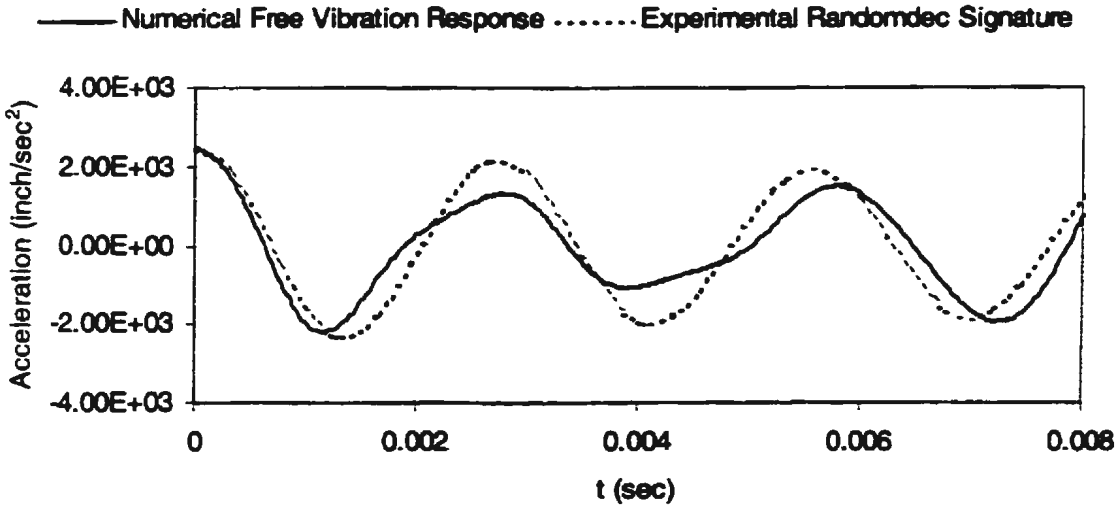

D.15.g: Crack length = 1.20 inch

Figure D.15: Comparison between Experimental Randomdec Signatures and Numerical Free Vibration Responses of Model #4 in Water (Partial Submergence)

Table D.12: Comparison of Experimental Randomdec Signature and Numerical Free Vibration Response Frequencies of Model #4 in Water (Partial Submergence) (Hz)

No	Crack length (Inches)	Exp. Randomdec Signature	Num. Free Vibration Response
1	0.00	370.31	370.34
2	0.20	370.08	370.14
3	0.40	369.61	369.58
4	0.60	368.51	368.40
5	0.80	367.09	367.12
6	1.00	365.24	365.12
7	1.20	363.23	363.25

Similar to the dynamic behavior of Model #4 in air, Figures D.15 and Table D.12 also show a good agreement between the experimental and the numerical results for both signatures and frequencies. Also, the decrease percentage in frequencies of Model #4 due to the presence of water was different from those of Models #2 and #3. The frequencies of Model # 4 were decreased approximately by 12.00 %, whereas those of Models #2 and #3 were decreased approximately by 13.00 % and 19.00 %, respectively. The difference between the temperature of water might cause this difference.

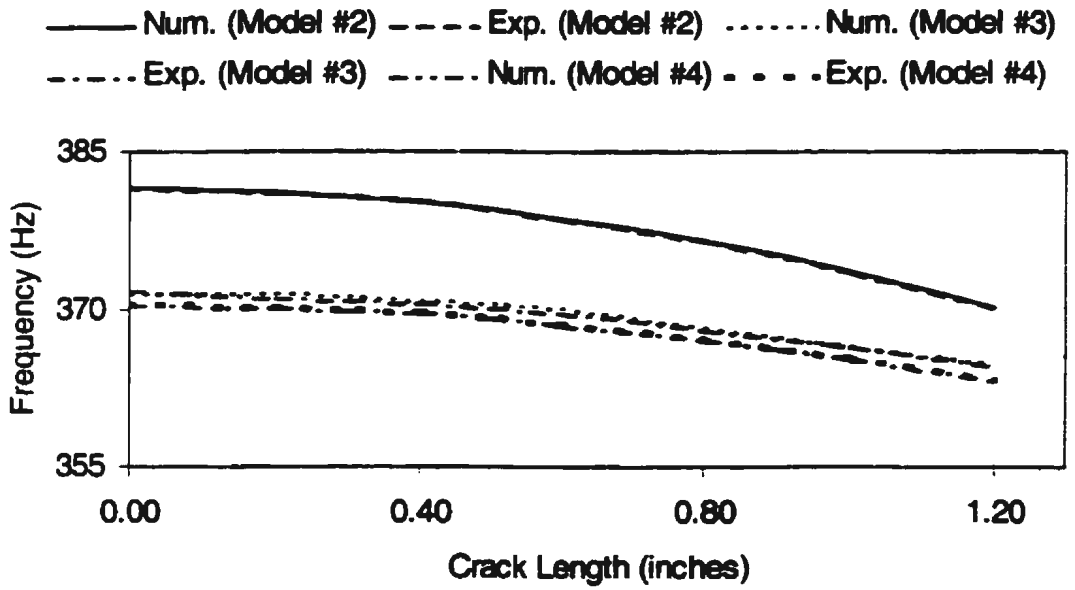

Figure D.16: Comparison of Frequencies of Models #2, #3, and #4 in Water (Partial Submergence)

Table D.13: Percentage Decrease in Frequencies of Models #2, #3, and #4 in Water (Partial Submergence)

Crack length (inches)	Numerical Free Vibration Response						Experimental Randomdec Signature					
	Model #2		Model #3		Model #4		Model #2		Model #3		Model #4	
	Freq. (Hz)	%	Freq. (Hz)	%	Freq. (Hz)	%	Freq. (Hz)	%	Freq. (Hz)	%	Freq. (Hz)	%
0.00	381.48	100	371.61	100	370.34	100	381.45	100	371.60	100	370.31	100
0.20	381.09	99.898	371.01	99.838	370.14	99.946	381.10	99.908	371.42	99.951	370.08	99.937
0.40	380.16	99.654	370.61	99.731	369.58	99.795	380.34	99.709	370.86	99.801	369.62	99.814
0.60	378.58	99.240	369.76	99.502	368.40	99.476	378.64	99.263	370.02	99.575	368.51	99.514
0.80	376.60	98.721	368.09	99.053	367.12	99.131	376.64	98.739	368.31	99.115	367.09	99.130
1.00	373.51	97.911	366.46	98.614	365.28	98.634	373.56	97.931	366.53	98.636	365.24	99.631
1.20	370.11	97.020	364.70	98.141	363.25	98.086	370.17	97.043	364.89	98.194	363.23	98.088

Furthermore, the effect of the crack location on the frequencies for Models #2, #3, and #4 are plotted and tabulated together in Figure D.16 and Table D.13, respectively. It can be seen from Figure D.16 and Table D.13 that the decrease in frequencies of Models #2, #3, and #4 is almost the same. When the crack length increases, the decrease in frequencies of Models #2 and #3 is slightly higher than those of Model #4. The maximum decrease percentage shown in Table D.13 is also very small, i.e., less than 2.00 % for the crack length of 1.20 inch.

Based on the above results, finally, the dynamic behavior of Model #4 full submerged in water' was also identified using the randomdec technique and the FE model.

D.3.2.2 Full Submergence

The experimental randomdec signatures and the numerical free vibration responses for both the undamaged and the damaged conditions are drawn together in Figure D.17.a - D.17.g. A comparison between their frequencies at the fourth mode is tabulated in Table D.14. As observed from Figures D.17, the experimental randomdec signatures and the numerical free vibration responses are in a good agreement. The good agreement between their frequencies was showed by Table D.14. Table D.14 also showed the decrease in frequencies when the damage length increased.

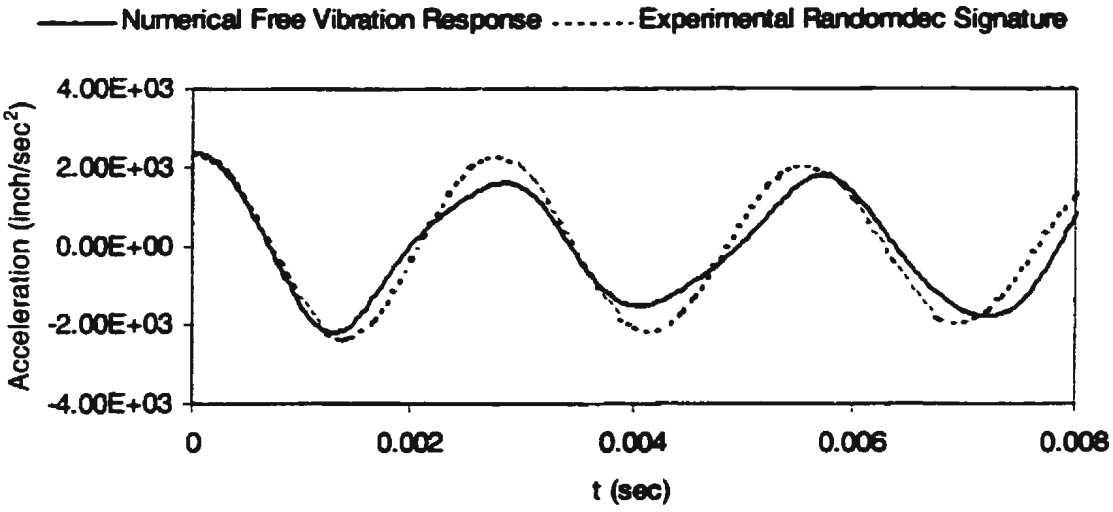

D.17.a: Undamaged

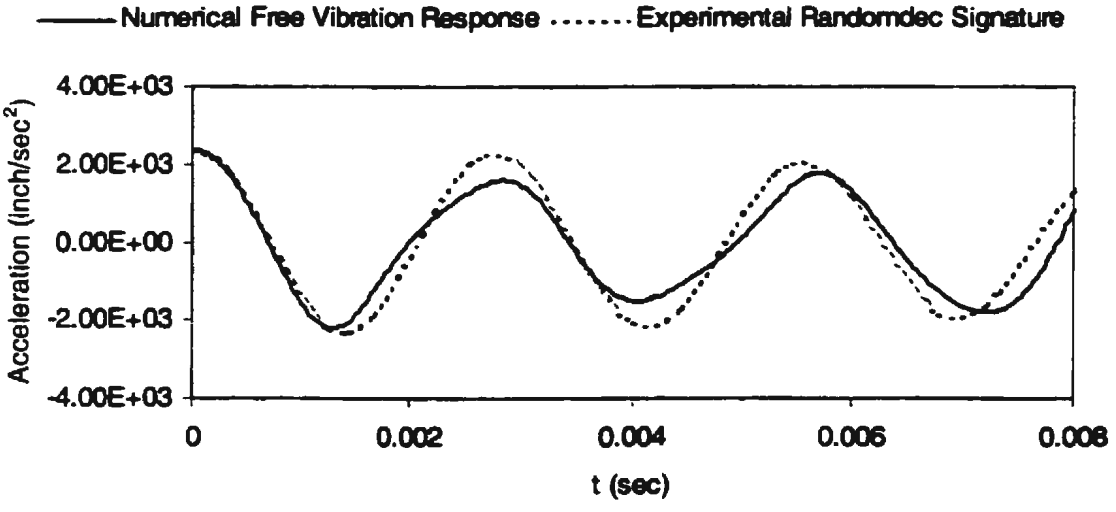

D.17.b: Crack length = 0.20 inch

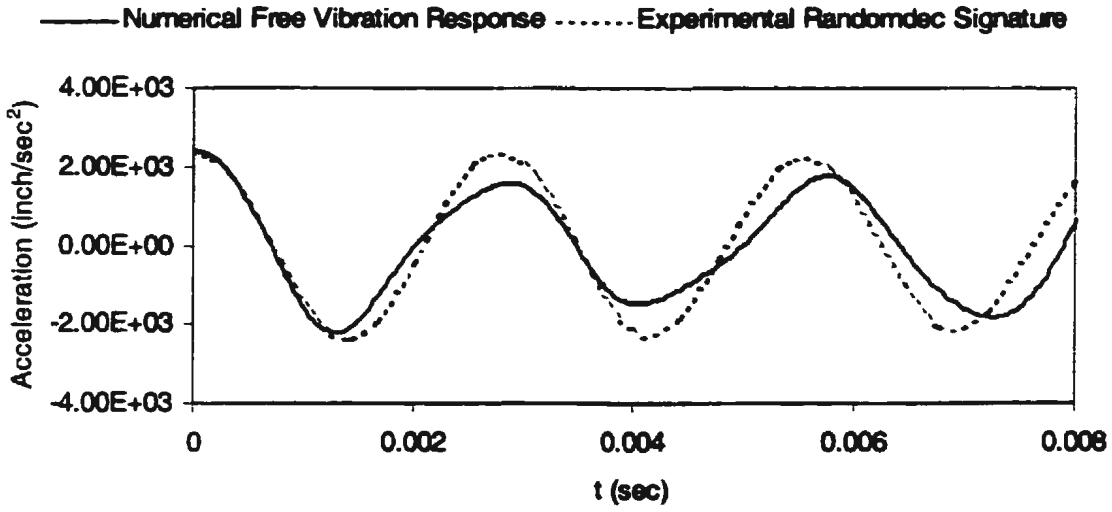

D.17.c: Crack length = 0.40 inch

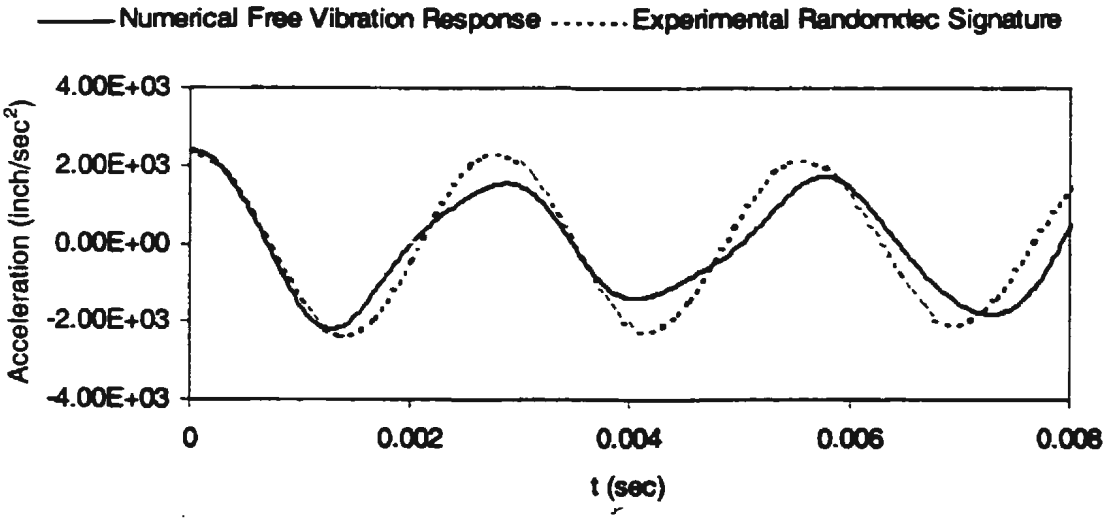

D.17.d: Crack length = 0.60 inch

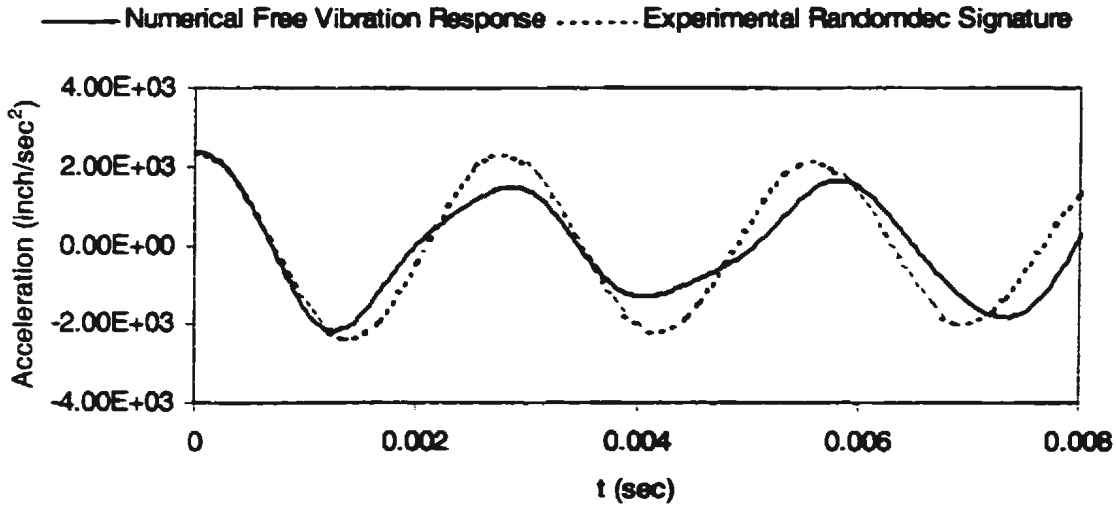

D.17.e: Crack length = 0.80 inch

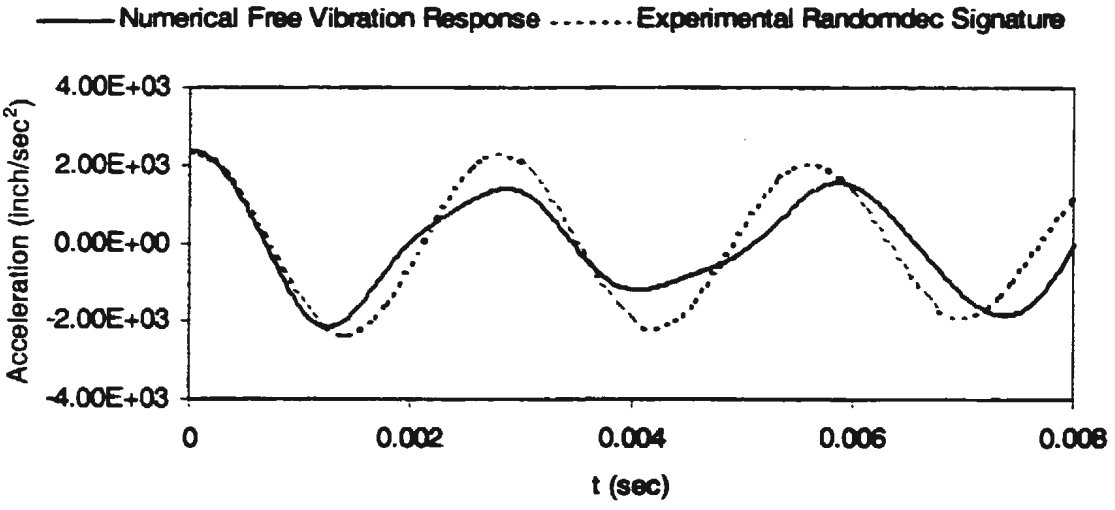

D.17.f: Crack length = 1.00 inch

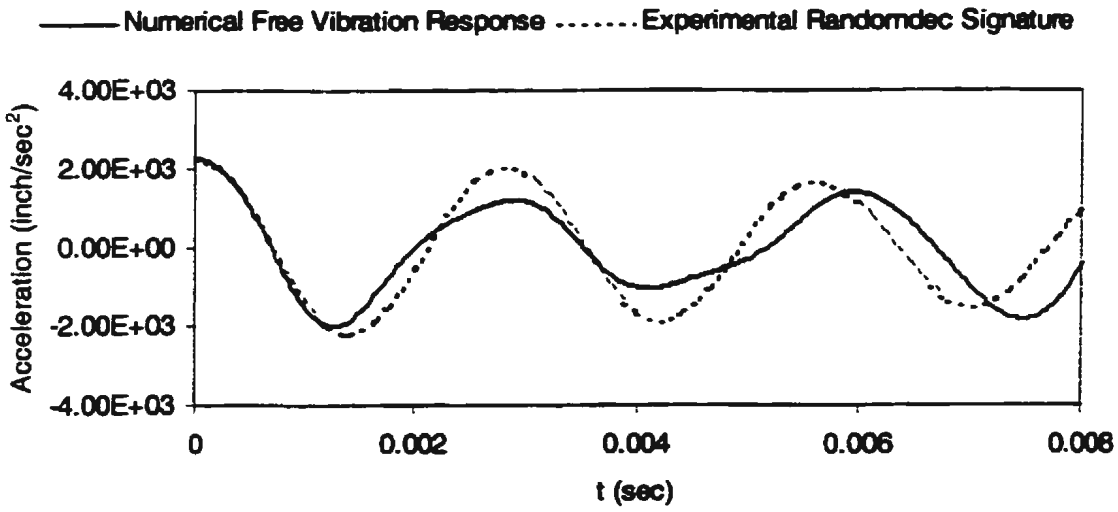

D.17.g: Crack length = 1.20 inch

Figure D.17: Comparison between Experimental Randomdec Signatures and Numerical Free Vibration Responses of Model #4 in Water (Full Submergence)

Table D.14: Comparison of Experimental Randomdec Signature and Numerical Free Vibration Response Frequencies of Model #4 in Water (Full Submergence) (Hz)

No	Crack length (Inches)	Exp. Randomdec Signature	Num. Free Vibration Response
1	0.00	361.57	361.56
2	0.20	361.37	361.37
3	0.40	360.76	360.76
4	0.60	359.71	359.74
5	0.80	358.42	358.43
6	1.00	356.86	356.90
7	1.20	354.50	354.50

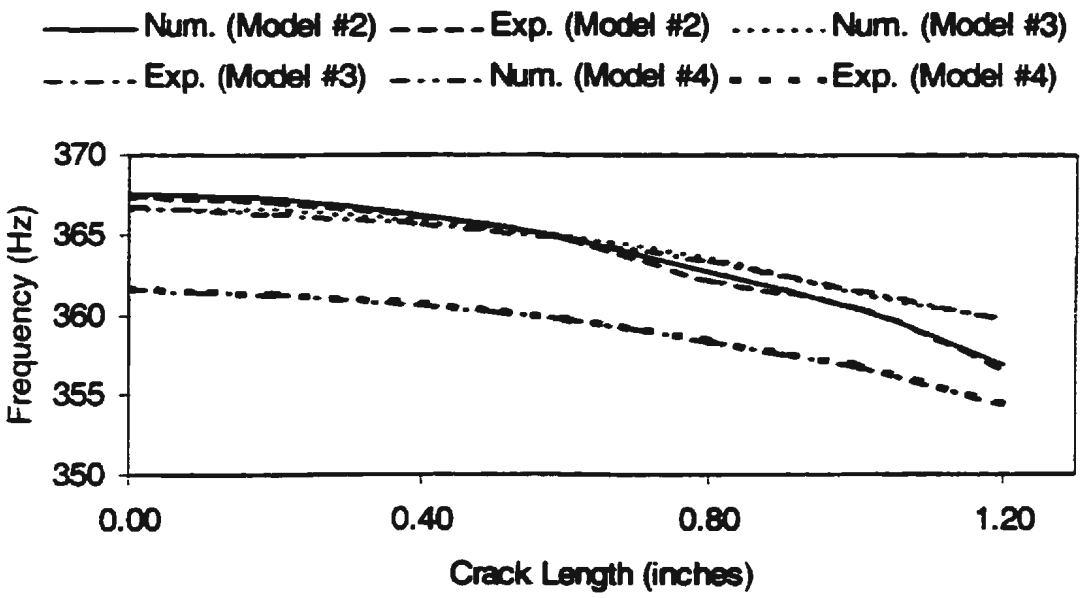

Figure D.18: Comparison of Frequencies of Models #2, #3, and #4 in Water (Full Submergence)

Figure D.18 shows a comparison between the experimental and numerical frequencies of Models #2, #3 and #4 for both the undamaged and the damaged conditions. For convenience, the percentage decrease in frequencies is also tabulated together in Table D.15. From Figure D.18, it can be seen that the decrease in frequencies of Models #2, #3, and #4 is almost the same for the small cracks ($\leq$ 0.4 inch). However, the increase of the crack length caused the decrease in frequency of Model #4 was slightly lower than that of Models #2 and #3. Moreover, Table D.15 indicated that the percentage difference in the results for each crack lengths were also very small.

Table D.15: Percentage Decrease in Frequencies of Models #2,#3, and #4 in Water (Full Submergence)

Crack length (Inches)	Numerical Free Vibration Response						Experimental Randomdec Signature					
	Model #2		Model #3		Model #4		Model #2		Model #3		Model #4	
	Freq. (Hz)	%	Freq. (Hz)	%	Freq. (Hz)	%	Freq. (Hz)	%	Freq. (Hz)	%	Freq. (Hz)	%
0.00	367.59	100	366.71	100	361.56	100	367.42	100	366.83	100	361.57	100
0.20	367.23	99.902	366.58	99.965	361.37	99.947	367.17	99.931	366.37	99.875	361.37	99.945
0.40	366.21	99.625	365.92	99.785	360.76	99.779	366.13	99.649	365.68	99.687	360.76	99.776
0.60	364.80	99.241	364.93	99.515	359.74	99.497	364.80	99.287	364.78	99.441	359.71	99.486
0.80	362.68	98.664	363.52	99.130	358.43	99.134	362.15	98.566	363.48	99.087	358.42	99.129
1.00	360.43	98.052	361.46	98.568	356.90	98.711	360.52	98.122	361.60	98.574	356.86	98.697
1.20	356.92	97.097	359.84	98.127	354.50	98.047	356.78	97.104	359.83	98.092	354.50	98.045

Appendix E

Tables and Figures (Chapter 7)

Table E.1: The Input (W_I) and Output (W_O) Weights of the Model #1 (Experiment)

W_I			
Undamaged	0.40 inch	0.80 inch	1.20 inch
-6930	-10220.4	-14763.6	-14983.2
-6930	-10220.4	-14763.6	-14983.2
-6930	-10220.4	-14763.6	-14983.2
-6930	-10220.4	-14763.6	-14983.2
-6930	-10220.4	-14763.6	-14983.2
-6930	-10220.4	-14763.6	-14983.2
-6930	-10220.4	-14763.6	-14983.2
-6930	-10220.4	-14763.6	-14983.2
-6930	-10220.4	-14763.6	-14983.2
-6930	-10220.4	-14763.6	-14983.2
-6930	-10220.4	-14763.6	-14983.2
-6930	-10220.4	-14763.6	-14983.2
-6930	-10220.4	-14763.6	-14983.2
-6930	-10220.4	-14763.6	-14983.2
-6930	-10220.4	-14763.6	-14983.2
-6930	-10220.4	-14763.6	-14983.2
-6930	-10220.4	-14763.6	-14983.2
-6930	-10220.4	-14763.6	-14983.2
-6930	-10220.4	-14763.6	-14983.2
-6930	-10220.4	-14763.6	-14983.2
-6930	-10220.4	-14763.6	-14983.2

Table E.1 (Continue)

W_I (Continue)			
Undamaged	0.40 inch	0.80 inch	1.20 inch
-6930	-10220.4	-14763.6	-14983.2
-6930	-10220.4	-14763.6	-14983.2
-6930	-10220.4	-14763.6	-14983.2
-6930	-10220.4	-14763.6	-14983.2
-6930	-10220.4	-14763.6	-14983.2
-6930	-10220.4	-14763.6	-14983.2
-6930	-10220.4	-14763.6	-14983.2
-6930	-10220.4	-14763.6	-14983.2
-6930	-10220.4	-14763.6	-14983.2
-6930	-10220.4	-14763.6	-14983.2
-6930	-10220.4	-14763.6	-14983.2
-6930	-10220.4	-14763.6	-14983.2
-6930	-10220.4	-14763.6	-14983.2

W_O			
Undamaged	0.40 inch	0.80 inch	1.20 inch
-6930	-10220.4	-14763.6	-14983.2
-6930	-10220.4	-14763.6	-14983.2
-6930	-10220.4	-14763.6	-14983.2
-6930	-10220.4	-14763.6	-14983.2
-6930	-10220.4	-14763.6	-14983.2
-6930	-10220.4	-14763.6	-14983.2
-6930	-10220.4	-14763.6	-14983.2
-6930	-10220.4	-14763.6	-14983.2
-6930	-10220.4	-14763.6	-14983.2
-6930	-10220.4	-14763.6	-14983.2
-6930	-10220.4	-14763.6	-14983.2
-6930	-10220.4	-14763.6	-14983.2

Table E.2: The Experimental Damping and Non Linear Part of the Restoring Force

t (sec)	Undamaged	0.40 inch	t (sec)	0.80 inch	1.20 inch
0.000000	-83138	-122623	0.000000	-177142	-179777
0.000143	-83138	-122623	0.000111	-177142	-179777
0.000286	-83138	-122623	0.000222	-177142	-179777
0.000429	-83138	-122623	0.000333	-177142	-179777
0.000571	-83138	-122623	0.000444	-177142	-179777
0.000714	-83138	-122623	0.000556	-177142	-179777
0.000857	-83138	-122623	0.000667	-177142	-179777
0.001000	-83138	-122623	0.000778	-177142	-179777
0.001143	69282	102186	0.000889	-177142	-179777
0.001286	69282	102186	0.001000	-177142	-179777
0.001429	69282	102186	0.001111	-177142	-179777
0.001571	69282	102186	0.001222	147618	149814
0.001714	69282	102186	0.001333	147618	149814
0.001857	69282	102186	0.001444	147618	149814
0.00200	69282	102186	0.001556	147618	149814
0.002143	69282	102186	0.001667	147618	149814
0.002286	-83138	102186	0.001778	147618	149814
0.002429	-83138	-122623	0.001889	147618	149814
0.002571	-83138	-122623	0.002000	147618	149814
0.002714	-83138	-122623	0.002111	147618	149814
0.002857	-83138	-122623	0.002222	147618	149814
0.00300	-83138	-122623	0.002333	147618	149814
0.003143	-83138	-122623	0.002444	-177142	-179777
0.003286	-83138	-122623	0.002556	-177142	-179777
0.003429	-83138	-122623	0.002667	-177142	-179777
0.003571	69282	102186	0.002778	-177142	-179777
0.003714	69282	102186	0.002889	-177142	-179777
0.003857	69282	102186	0.003000	-177142	-179777
0.004000	69282	102186	0.003111	-177142	-179777
0.004143	69282	102186	0.003222	-177142	-179777
0.004286	69282	102186	0.003333	-177142	-179777
0.004429	69282	102186	0.003444	-177142	-179777
0.004571	69282	102186	0.003556	-177142	-179777
0.004714	-83138	102186	0.003667	147618	149814
0.004857	-83138	-122623	0.003778	147618	149814
0.005000	-83138	-122623	0.003889	147618	149814

Table E.2 (Continue)

t (sec)	Undamaged	0.40 inch	t (sec)	0.80 inch	1.20 inch
			0.004000	147618	149814
			0.004111	147618	149814
			0.004222	147618	149814
			0.004333	147618	149814
			0.004444	147618	149814
			0.004556	147618	149814
			0.004667	147618	149814
			0.004778	147618	149814
			0.004889	-177142	-179777
			0.005000	-177142	-179777

Table E.3: The Input (W_I) and Output (W_O) Weights (Numerical, Center)

W_I			
Undamaged	0.40 inch	0.80 inch	1.20 inch
-17906.4	-17744.4	-17744.4	-17910
-17906.4	-17744.4	-17744.4	-17910
-17906.4	-17744.4	-17744.4	-17910
-17906.4	-17744.4	-17744.4	-17910
-17906.4	-17744.4	-17744.4	-17910
-17906.4	-17744.4	-17744.4	-17910
-17906.4	-17744.4	-17744.4	-17910
-17906.4	-17744.4	-17744.4	-17910
-17906.4	-17744.4	-17744.4	-17910
-17906.4	-17744.4	-17744.4	-17910
-17906.4	-17744.4	-17744.4	-17910
-17906.4	-17744.4	-17744.4	-17910
-17906.4	-17744.4	-17744.4	-17910
-17906.4	-17744.4	-17744.4	-17910
-17906.4	-17744.4	-17744.4	-17910
-17906.4	-17744.4	-17744.4	-17910
-17906.4	-17744.4	-17744.4	-17910
-17906.4	-17744.4	-17744.4	-17910
-17906.4	-17744.4	-17744.4	-17910
-17906.4	-17744.4	-17744.4	-17910
-17906.4	-17744.4	-17744.4	-17910
-17906.4	-17744.4	-17744.4	-17910
-17906.4	-17744.4	-17744.4	-17910
-17906.4	-17744.4	-17744.4	-17910
-17906.4	-17744.4	-17744.4	-17910
-17906.4	-17744.4	-17744.4	-17910
-17906.4	-17744.4	-17744.4	-17910
-17906.4	-17744.4	-17744.4	-17910
-17906.4	-17744.4	-17744.4	-17910
-17906.4	-17744.4	-17744.4	-17910
-17906.4	-17744.4	-17744.4	-17910
-17906.4	-17744.4	-17744.4	-17910
-17906.4	-17744.4	-17744.4	-17910
-17906.4	-17744.4	-17744.4	-17910
-17906.4	-17744.4	-17744.4	-17910
-17906.4	-17744.4	-17744.4	-17910

Table E.3 (Continue)

W_o			
Undamaged	0.40 inch	0.80 inch	1.20 inch
-17906.4	-17744.4	-17744.4	-17910
-17906.4	-17744.4	-17744.4	-17910
-17906.4	-17744.4	-17744.4	-17910
-17906.4	-17744.4	-17744.4	-17910
-17906.4	-17744.4	-17744.4	-17910
-17906.4	-17744.4	-17744.4	-17910
-17906.4	-17744.4	-17744.4	-17910
-17906.4	-17744.4	-17744.4	-17910
-17906.4	-17744.4	-17744.4	-17910
-17906.4	-17744.4	-17744.4	-17910
-17906.4	-17744.4	-17744.4	-17910
-17906.4	-17744.4	-17744.4	-17910

Table E.4: The Input (W_I) and Output (W_O) Weights (Numerical, 0.45 inch)

W_I			
Undamaged	0.40 inch	0.80 inch	1.20 inch
-17906.4	-17726.4	-17771.4	-18356.4
-17906.4	-17726.4	-17771.4	-18356.4
-17906.4	-17726.4	-17771.4	-18356.4
-17906.4	-17726.4	-17771.4	-18356.4
-17906.4	-17726.4	-17771.4	-18356.4
-17906.4	-17726.4	-17771.4	-18356.4
-17906.4	-17726.4	-17771.4	-18356.4
-17906.4	-17726.4	-17771.4	-18356.4
-17906.4	-17726.4	-17771.4	-18356.4
-17906.4	-17726.4	-17771.4	-18356.4
-17906.4	-17726.4	-17771.4	-18356.4
-17906.4	-17726.4	-17771.4	-18356.4
-17906.4	-17726.4	-17771.4	-18356.4
-17906.4	-17726.4	-17771.4	-18356.4
-17906.4	-17726.4	-17771.4	-18356.4
-17906.4	-17726.4	-17771.4	-18356.4
-17906.4	-17726.4	-17771.4	-18356.4
-17906.4	-17726.4	-17771.4	-18356.4
-17906.4	-17726.4	-17771.4	-18356.4
-17906.4	-17726.4	-17771.4	-18356.4
-17906.4	-17726.4	-17771.4	-18356.4
-17906.4	-17726.4	-17771.4	-18356.4
-17906.4	-17726.4	-17771.4	-18356.4
-17906.4	-17726.4	-17771.4	-18356.4
-17906.4	-17726.4	-17771.4	-18356.4
-17906.4	-17726.4	-17771.4	-18356.4
-17906.4	-17726.4	-17771.4	-18356.4
-17906.4	-17726.4	-17771.4	-18356.4
-17906.4	-17726.4	-17771.4	-18356.4
-17906.4	-17726.4	-17771.4	-18356.4
-17906.4	-17726.4	-17771.4	-18356.4
-17906.4	-17726.4	-17771.4	-18356.4
-17906.4	-17726.4	-17771.4	-18356.4
-17906.4	-17726.4	-17771.4	-18356.4
-17906.4	-17726.4	-17771.4	-18356.4
-17906.4	-17726.4	-17771.4	-18356.4
-17906.4	-17726.4	-17771.4	-18356.4
-17906.4	-17726.4	-17771.4	-18356.4
-17906.4	-17726.4	-17771.4	-18356.4
-17906.4	-17726.4	-17771.4	-18356.4
-17906.4	-17726.4	-17771.4	-18356.4
-17906.4	-17726.4	-17771.4	-18356.4
-17906.4	-17726.4	-17771.4	-18356.4
-17906.4	-17726.4	-17771.4	-18356.4
-17906.4	-17726.4	-17771.4	-18356.4

Table E.4 (Continue)

W_o			
Undamaged	0.40 inch	0.80 inch	1.20 inch
-17906.4	-17726.4	-17771.4	-18356.4
-17906.4	-17726.4	-17771.4	-18356.4
-17906.4	-17726.4	-17771.4	-18356.4
-17906.4	-17726.4	-17771.4	-18356.4
-17906.4	-17726.4	-17771.4	-18356.4
-17906.4	-17726.4	-17771.4	-18356.4
-17906.4	-17726.4	-17771.4	-18356.4
-17906.4	-17726.4	-17771.4	-18356.4
-17906.4	-17726.4	-17771.4	-18356.4
-17906.4	-17726.4	-17771.4	-18356.4
-17906.4	-17726.4	-17771.4	-18356.4
-17906.4	-17726.4	-17771.4	-18356.4

Table E.5: The Input (W_I) and Output (W_O) Weights (Numerical, 0.90 inch)

W_I			
Undamaged	0.40 inch	0.80 inch	1.20 inch
-17906.4	-17418.6	-17901	-17991
-17906.4	-17418.6	-17901	-17991
-17906.4	-17418.6	-17901	-17991
-17906.4	-17418.6	-17901	-17991
-17906.4	-17418.6	-17901	-17991
-17906.4	-17418.6	-17901	-17991
-17906.4	-17418.6	-17901	-17991
-17906.4	-17418.6	-17901	-17991
-17906.4	-17418.6	-17901	-17991
-17906.4	-17418.6	-17901	-17991
-17906.4	-17418.6	-17901	-17991
-17906.4	-17418.6	-17901	-17991
-17906.4	-17418.6	-17901	-17991
-17906.4	-17418.6	-17901	-17991
-17906.4	-17418.6	-17901	-17991
-17906.4	-17418.6	-17901	-17991
-17906.4	-17418.6	-17901	-17991
-17906.4	-17418.6	-17901	-17991
-17906.4	-17418.6	-17901	-17991
-17906.4	-17418.6	-17901	-17991
-17906.4	-17418.6	-17901	-17991
-17906.4	-17418.6	-17901	-17991
-17906.4	-17418.6	-17901	-17991
-17906.4	-17418.6	-17901	-17991
-17906.4	-17418.6	-17901	-17991
-17906.4	-17418.6	-17901	-17991
-17906.4	-17418.6	-17901	-17991
-17906.4	-17418.6	-17901	-17991
-17906.4	-17418.6	-17901	-17991
-17906.4	-17418.6	-17901	-17991
-17906.4	-17418.6	-17901	-17991
-17906.4	-17418.6	-17901	-17991
-17906.4	-17418.6	-17901	-17991

Table E.5 (Continue)

W_o			
Undamaged	0.40 inch	0.80 inch	1.20 inch
-17906.4	-17418.6	-17901	-17991
-17906.4	-17418.6	-17901	-17991
-17906.4	-17418.6	-17901	-17991
-17906.4	-17418.6	-17901	-17991
-17906.4	-17418.6	-17901	-17991
-17906.4	-17418.6	-17901	-17991
-17906.4	-17418.6	-17901	-17991
-17906.4	-17418.6	-17901	-17991
-17906.4	-17418.6	-17901	-17991
-17906.4	-17418.6	-17901	-17991
-17906.4	-17418.6	-17901	-17991
-17906.4	-17418.6	-17901	-17991

Table E.6: The Input (W_I) and Output (W_O) Weights (Numerical, 1.35 inch)

W_I			
Undamaged	0.40 inch	0.80 inch	1.20 inch
-17906.4	-17881.2	-17636.4	-17929.8
-17906.4	-17881.2	-17636.4	-17929.8
-17906.4	-17881.2	-17636.4	-17929.8
-17906.4	-17881.2	-17636.4	-17929.8
-17906.4	-17881.2	-17636.4	-17929.8
-17906.4	-17881.2	-17636.4	-17929.8
-17906.4	-17881.2	-17636.4	-17929.8
-17906.4	-17881.2	-17636.4	-17929.8
-17906.4	-17881.2	-17636.4	-17929.8
-17906.4	-17881.2	-17636.4	-17929.8
-17906.4	-17881.2	-17636.4	-17929.8
-17906.4	-17881.2	-17636.4	-17929.8
-17906.4	-17881.2	-17636.4	-17929.8
-17906.4	-17881.2	-17636.4	-17929.8
-17906.4	-17881.2	-17636.4	-17929.8
-17906.4	-17881.2	-17636.4	-17929.8
-17906.4	-17881.2	-17636.4	-17929.8
-17906.4	-17881.2	-17636.4	-17929.8
-17906.4	-17881.2	-17636.4	-17929.8
-17906.4	-17881.2	-17636.4	-17929.8
-17906.4	-17881.2	-17636.4	-17929.8
-17906.4	-17881.2	-17636.4	-17929.8
-17906.4	-17881.2	-17636.4	-17929.8
-17906.4	-17881.2	-17636.4	-17929.8
-17906.4	-17881.2	-17636.4	-17929.8
-17906.4	-17881.2	-17636.4	-17929.8
-17906.4	-17881.2	-17636.4	-17929.8
-17906.4	-17881.2	-17636.4	-17929.8
-17906.4	-17881.2	-17636.4	-17929.8
-17906.4	-17881.2	-17636.4	-17929.8
-17906.4	-17881.2	-17636.4	-17929.8
-17906.4	-17881.2	-17636.4	-17929.8
-17906.4	-17881.2	-17636.4	-17929.8
-17906.4	-17881.2	-17636.4	-17929.8
-17906.4	-17881.2	-17636.4	-17929.8
-17906.4	-17881.2	-17636.4	-17929.8
-17906.4	-17881.2	-17636.4	-17929.8
-17906.4	-17881.2	-17636.4	-17929.8
-17906.4	-17881.2	-17636.4	-17929.8
-17906.4	-17881.2	-17636.4	-17929.8
-17906.4	-17881.2	-17636.4	-17929.8
-17906.4	-17881.2	-17636.4	-17929.8
-17906.4	-17881.2	-17636.4	-17929.8
-17906.4	-17881.2	-17636.4	-17929.8
-17906.4	-17881.2	-17636.4	-17929.8
-17906.4	-17881.2	-17636.4	-17929.8
-17906.4	-17881.2	-17636.4	-17929.8
-17906.4	-17881.2	-17636.4	-17929.8
-17906.4	-17881.2	-17636.4	-17929.8

Table E.6 (Continue)

W_o			
Undamaged	0.40 inch	0.80 inch	1.20 inch
-17906.4	-17881.2	-17636.4	-17929.8
-17906.4	-17881.2	-17636.4	-17929.8
-17906.4	-17881.2	-17636.4	-17929.8
-17906.4	-17881.2	-17636.4	-17929.8
-17906.4	-17881.2	-17636.4	-17929.8
-17906.4	-17881.2	-17636.4	-17929.8
-17906.4	-17881.2	-17636.4	-17929.8
-17906.4	-17881.2	-17636.4	-17929.8
-17906.4	-17881.2	-17636.4	-17929.8
-17906.4	-17881.2	-17636.4	-17929.8
-17906.4	-17881.2	-17636.4	-17929.8
-17906.4	-17881.2	-17636.4	-17929.8

Table E.7: The Input (W_I) and Output (W_O) Weights (Numerical, 1.80 inch)

W_I			
Undamaged	0.40 inch	0.80 inch	1.20 inch
-17906.4	-17721	-17613	-17307
-17906.4	-17721	-17613	-17307
-17906.4	-17721	-17613	-17307
-17906.4	-17721	-17613	-17307
-17906.4	-17721	-17613	-17307
-17906.4	-17721	-17613	-17307
-17906.4	-17721	-17613	-17307
-17906.4	-17721	-17613	-17307
-17906.4	-17721	-17613	-17307
-17906.4	-17721	-17613	-17307
-17906.4	-17721	-17613	-17307
-17906.4	-17721	-17613	-17307
-17906.4	-17721	-17613	-17307
-17906.4	-17721	-17613	-17307
-17906.4	-17721	-17613	-17307
-17906.4	-17721	-17613	-17307
-17906.4	-17721	-17613	-17307
-17906.4	-17721	-17613	-17307
-17906.4	-17721	-17613	-17307
-17906.4	-17721	-17613	-17307
-17906.4	-17721	-17613	-17307
-17906.4	-17721	-17613	-17307
-17906.4	-17721	-17613	-17307
-17906.4	-17721	-17613	-17307
-17906.4	-17721	-17613	-17307
-17906.4	-17721	-17613	-17307
-17906.4	-17721	-17613	-17307
-17906.4	-17721	-17613	-17307
-17906.4	-17721	-17613	-17307
-17906.4	-17721	-17613	-17307
-17906.4	-17721	-17613	-17307
-17906.4	-17721	-17613	-17307
-17906.4	-17721	-17613	-17307
-17906.4	-17721	-17613	-17307
-17906.4	-17721	-17613	-17307
-17906.4	-17721	-17613	-17307
-17906.4	-17721	-17613	-17307

Table E.7 (Continue)

W_o			
Undamaged	0.40 inch	0.80 inch	1.20 inch
-17906.4	-17721	-17613	-17307
-17906.4	-17721	-17613	-17307
-17906.4	-17721	-17613	-17307
-17906.4	-17721	-17613	-17307
-17906.4	-17721	-17613	-17307
-17906.4	-17721	-17613	-17307
-17906.4	-17721	-17613	-17307
-17906.4	-17721	-17613	-17307
-17906.4	-17721	-17613	-17307
-17906.4	-17721	-17613	-17307
-17906.4	-17721	-17613	-17307
-17906.4	-17721	-17613	-17307

Table E.8: The Input (W_I) and Output (W_O) Weights (Numerical, 2.25 inch)

W_I			
Undamaged	0.40 inch	0.80 inch	1.20 inch
-17906.4	-17793	-17733.6	-18064.8
-17906.4	-17793	-17733.6	-18064.8
-17906.4	-17793	-17733.6	-18064.8
-17906.4	-17793	-17733.6	-18064.8
-17906.4	-17793	-17733.6	-18064.8
-17906.4	-17793	-17733.6	-18064.8
-17906.4	-17793	-17733.6	-18064.8
-17906.4	-17793	-17733.6	-18064.8
-17906.4	-17793	-17733.6	-18064.8
-17906.4	-17793	-17733.6	-18064.8
-17906.4	-17793	-17733.6	-18064.8
-17906.4	-17793	-17733.6	-18064.8
-17906.4	-17793	-17733.6	-18064.8
-17906.4	-17793	-17733.6	-18064.8
-17906.4	-17793	-17733.6	-18064.8
-17906.4	-17793	-17733.6	-18064.8
-17906.4	-17793	-17733.6	-18064.8
-17906.4	-17793	-17733.6	-18064.8
-17906.4	-17793	-17733.6	-18064.8
-17906.4	-17793	-17733.6	-18064.8
-17906.4	-17793	-17733.6	-18064.8
-17906.4	-17793	-17733.6	-18064.8
-17906.4	-17793	-17733.6	-18064.8
-17906.4	-17793	-17733.6	-18064.8
-17906.4	-17793	-17733.6	-18064.8
-17906.4	-17793	-17733.6	-18064.8
-17906.4	-17793	-17733.6	-18064.8
-17906.4	-17793	-17733.6	-18064.8
-17906.4	-17793	-17733.6	-18064.8
-17906.4	-17793	-17733.6	-18064.8
-17906.4	-17793	-17733.6	-18064.8
-17906.4	-17793	-17733.6	-18064.8
-17906.4	-17793	-17733.6	-18064.8
-17906.4	-17793	-17733.6	-18064.8

Table E.8 (Continue)

W_o			
Undamaged	0.40 inch	0.80 inch	1.20 inch
-17906.4	-17793	-17733.6	-18064.8
-17906.4	-17793	-17733.6	-18064.8
-17906.4	-17793	-17733.6	-18064.8
-17906.4	-17793	-17733.6	-18064.8
-17906.4	-17793	-17733.6	-18064.8
-17906.4	-17793	-17733.6	-18064.8
-17906.4	-17793	-17733.6	-18064.8
-17906.4	-17793	-17733.6	-18064.8
-17906.4	-17793	-17733.6	-18064.8
-17906.4	-17793	-17733.6	-18064.8
-17906.4	-17793	-17733.6	-18064.8
-17906.4	-17793	-17733.6	-18064.8

Table E.9: The Input (W_I) and Output (W_O) Weights (Numerical, 2.70 inch)

W_I			
Undamaged	0.40 inch	0.80 inch	1.20 inch
-17906.4	-17890.2	-17326.8	-17667
-17906.4	-17890.2	-17326.8	-17667
-17906.4	-17890.2	-17326.8	-17667
-17906.4	-17890.2	-17326.8	-17667
-17906.4	-17890.2	-17326.8	-17667
-17906.4	-17890.2	-17326.8	-17667
-17906.4	-17890.2	-17326.8	-17667
-17906.4	-17890.2	-17326.8	-17667
-17906.4	-17890.2	-17326.8	-17667
-17906.4	-17890.2	-17326.8	-17667
-17906.4	-17890.2	-17326.8	-17667
-17906.4	-17890.2	-17326.8	-17667
-17906.4	-17890.2	-17326.8	-17667
-17906.4	-17890.2	-17326.8	-17667
-17906.4	-17890.2	-17326.8	-17667
-17906.4	-17890.2	-17326.8	-17667
-17906.4	-17890.2	-17326.8	-17667
-17906.4	-17890.2	-17326.8	-17667
-17906.4	-17890.2	-17326.8	-17667
-17906.4	-17890.2	-17326.8	-17667
-17906.4	-17890.2	-17326.8	-17667
-17906.4	-17890.2	-17326.8	-17667
-17906.4	-17890.2	-17326.8	-17667
-17906.4	-17890.2	-17326.8	-17667
-17906.4	-17890.2	-17326.8	-17667
-17906.4	-17890.2	-17326.8	-17667
-17906.4	-17890.2	-17326.8	-17667
-17906.4	-17890.2	-17326.8	-17667
-17906.4	-17890.2	-17326.8	-17667
-17906.4	-17890.2	-17326.8	-17667
-17906.4	-17890.2	-17326.8	-17667
-17906.4	-17890.2	-17326.8	-17667
-17906.4	-17890.2	-17326.8	-17667
-17906.4	-17890.2	-17326.8	-17667
-17906.4	-17890.2	-17326.8	-17667

Table E.9 (Continue)

W_o			
Undamaged	0.40 inch	0.80 inch	1.20 inch
-17906.4	-17890.2	-17326.8	-17667
-17906.4	-17890.2	-17326.8	-17667
-17906.4	-17890.2	-17326.8	-17667
-17906.4	-17890.2	-17326.8	-17667
-17906.4	-17890.2	-17326.8	-17667
-17906.4	-17890.2	-17326.8	-17667
-17906.4	-17890.2	-17326.8	-17667
-17906.4	-17890.2	-17326.8	-17667
-17906.4	-17890.2	-17326.8	-17667
-17906.4	-17890.2	-17326.8	-17667
-17906.4	-17890.2	-17326.8	-17667
-17906.4	-17890.2	-17326.8	-17667

Table E.10: The Input (W_I) and Output (W_O) Weights (Numerical, 3.15 inch)

W_I			
Undamaged	0.40 inch	0.80 inch	1.20 inch
-17906.4	-17298	-17679.6	-17539.2
-17906.4	-17298	-17679.6	-17539.2
-17906.4	-17298	-17679.6	-17539.2
-17906.4	-17298	-17679.6	-17539.2
-17906.4	-17298	-17679.6	-17539.2
-17906.4	-17298	-17679.6	-17539.2
-17906.4	-17298	-17679.6	-17539.2
-17906.4	-17298	-17679.6	-17539.2
-17906.4	-17298	-17679.6	-17539.2
-17906.4	-17298	-17679.6	-17539.2
-17906.4	-17298	-17679.6	-17539.2
-17906.4	-17298	-17679.6	-17539.2
-17906.4	-17298	-17679.6	-17539.2
-17906.4	-17298	-17679.6	-17539.2
-17906.4	-17298	-17679.6	-17539.2
-17906.4	-17298	-17679.6	-17539.2
-17906.4	-17298	-17679.6	-17539.2
-17906.4	-17298	-17679.6	-17539.2
-17906.4	-17298	-17679.6	-17539.2
-17906.4	-17298	-17679.6	-17539.2
-17906.4	-17298	-17679.6	-17539.2
-17906.4	-17298	-17679.6	-17539.2
-17906.4	-17298	-17679.6	-17539.2
-17906.4	-17298	-17679.6	-17539.2
-17906.4	-17298	-17679.6	-17539.2
-17906.4	-17298	-17679.6	-17539.2
-17906.4	-17298	-17679.6	-17539.2
-17906.4	-17298	-17679.6	-17539.2
-17906.4	-17298	-17679.6	-17539.2
-17906.4	-17298	-17679.6	-17539.2
-17906.4	-17298	-17679.6	-17539.2
-17906.4	-17298	-17679.6	-17539.2
-17906.4	-17298	-17679.6	-17539.2
-17906.4	-17298	-17679.6	-17539.2
-17906.4	-17298	-17679.6	-17539.2
-17906.4	-17298	-17679.6	-17539.2

Table E.10 (Continue)

W_o			
Undamaged	0.40 inch	0.80 inch	1.20 inch
-17906.4	-17298	-17679.6	-17539.2
-17906.4	-17298	-17679.6	-17539.2
-17906.4	-17298	-17679.6	-17539.2
-17906.4	-17298	-17679.6	-17539.2
-17906.4	-17298	-17679.6	-17539.2
-17906.4	-17298	-17679.6	-17539.2
-17906.4	-17298	-17679.6	-17539.2
-17906.4	-17298	-17679.6	-17539.2
-17906.4	-17298	-17679.6	-17539.2
-17906.4	-17298	-17679.6	-17539.2
-17906.4	-17298	-17679.6	-17539.2
-17906.4	-17298	-17679.6	-17539.2

Table E.11: The Input (W_I) and Output (W_O) Weights (Numerical, 3.60 inch)

W_I			
Undamaged	0.40 inch	0.80 inch	1.20 inch
-17906.4	-17395.2	-17904.6	-17667
-17906.4	-17395.2	-17904.6	-17667
-17906.4	-17395.2	-17904.6	-17667
-17906.4	-17395.2	-17904.6	-17667
-17906.4	-17395.2	-17904.6	-17667
-17906.4	-17395.2	-17904.6	-17667
-17906.4	-17395.2	-17904.6	-17667
-17906.4	-17395.2	-17904.6	-17667
-17906.4	-17395.2	-17904.6	-17667
-17906.4	-17395.2	-17904.6	-17667
-17906.4	-17395.2	-17904.6	-17667
-17906.4	-17395.2	-17904.6	-17667
-17906.4	-17395.2	-17904.6	-17667
-17906.4	-17395.2	-17904.6	-17667
-17906.4	-17395.2	-17904.6	-17667
-17906.4	-17395.2	-17904.6	-17667
-17906.4	-17395.2	-17904.6	-17667
-17906.4	-17395.2	-17904.6	-17667
-17906.4	-17395.2	-17904.6	-17667
-17906.4	-17395.2	-17904.6	-17667
-17906.4	-17395.2	-17904.6	-17667
-17906.4	-17395.2	-17904.6	-17667
-17906.4	-17395.2	-17904.6	-17667
-17906.4	-17395.2	-17904.6	-17667
-17906.4	-17395.2	-17904.6	-17667
-17906.4	-17395.2	-17904.6	-17667
-17906.4	-17395.2	-17904.6	-17667
-17906.4	-17395.2	-17904.6	-17667
-17906.4	-17395.2	-17904.6	-17667
-17906.4	-17395.2	-17904.6	-17667
-17906.4	-17395.2	-17904.6	-17667
-17906.4	-17395.2	-17904.6	-17667
-17906.4	-17395.2	-17904.6	-17667
-17906.4	-17395.2	-17904.6	-17667
-17906.4	-17395.2	-17904.6	-17667
-17906.4	-17395.2	-17904.6	-17667
-17906.4	-17395.2	-17904.6	-17667

Table E.11 (Continue)

W_o			
Undamaged	0.40 inch	0.80 inch	1.20 inch
-17906.4	-17395.2	-17904.6	-17667
-17906.4	-17395.2	-17904.6	-17667
-17906.4	-17395.2	-17904.6	-17667
-17906.4	-17395.2	-17904.6	-17667
-17906.4	-17395.2	-17904.6	-17667
-17906.4	-17395.2	-17904.6	-17667
-17906.4	-17395.2	-17904.6	-17667
-17906.4	-17395.2	-17904.6	-17667
-17906.4	-17395.2	-17904.6	-17667
-17906.4	-17395.2	-17904.6	-17667
-17906.4	-17395.2	-17904.6	-17667
-17906.4	-17395.2	-17904.6	-17667

Table E.12: The Input (W_I) and Output (W_O) Weights (Numerical, 4.05 inch)

W_I			
Undamaged	0.40 inch	0.80 inch	1.20 inch
-17906.4	-17299.8	-17928	-17373.6
-17906.4	-17299.8	-17928	-17373.6
-17906.4	-17299.8	-17928	-17373.6
-17906.4	-17299.8	-17928	-17373.6
-17906.4	-17299.8	-17928	-17373.6
-17906.4	-17299.8	-17928	-17373.6
-17906.4	-17299.8	-17928	-17373.6
-17906.4	-17299.8	-17928	-17373.6
-17906.4	-17299.8	-17928	-17373.6
-17906.4	-17299.8	-17928	-17373.6
-17906.4	-17299.8	-17928	-17373.6
-17906.4	-17299.8	-17928	-17373.6
-17906.4	-17299.8	-17928	-17373.6
-17906.4	-17299.8	-17928	-17373.6
-17906.4	-17299.8	-17928	-17373.6
-17906.4	-17299.8	-17928	-17373.6
-17906.4	-17299.8	-17928	-17373.6
-17906.4	-17299.8	-17928	-17373.6
-17906.4	-17299.8	-17928	-17373.6
-17906.4	-17299.8	-17928	-17373.6
-17906.4	-17299.8	-17928	-17373.6
-17906.4	-17299.8	-17928	-17373.6
-17906.4	-17299.8	-17928	-17373.6
-17906.4	-17299.8	-17928	-17373.6
-17906.4	-17299.8	-17928	-17373.6
-17906.4	-17299.8	-17928	-17373.6
-17906.4	-17299.8	-17928	-17373.6
-17906.4	-17299.8	-17928	-17373.6
-17906.4	-17299.8	-17928	-17373.6
-17906.4	-17299.8	-17928	-17373.6
-17906.4	-17299.8	-17928	-17373.6
-17906.4	-17299.8	-17928	-17373.6
-17906.4	-17299.8	-17928	-17373.6
-17906.4	-17299.8	-17928	-17373.6
-17906.4	-17299.8	-17928	-17373.6
-17906.4	-17299.8	-17928	-17373.6
-17906.4	-17299.8	-17928	-17373.6

Table E.12 (Continue)

W_o			
Undamaged	0.40 inch	0.80 inch	1.20 inch
-17906.4	-17299.8	-17928	-17373.6
-17906.4	-17299.8	-17928	-17373.6
-17906.4	-17299.8	-17928	-17373.6
-17906.4	-17299.8	-17928	-17373.6
-17906.4	-17299.8	-17928	-17373.6
-17906.4	-17299.8	-17928	-17373.6
-17906.4	-17299.8	-17928	-17373.6
-17906.4	-17299.8	-17928	-17373.6
-17906.4	-17299.8	-17928	-17373.6
-17906.4	-17299.8	-17928	-17373.6
-17906.4	-17299.8	-17928	-17373.6
-17906.4	-17299.8	-17928	-17373.6

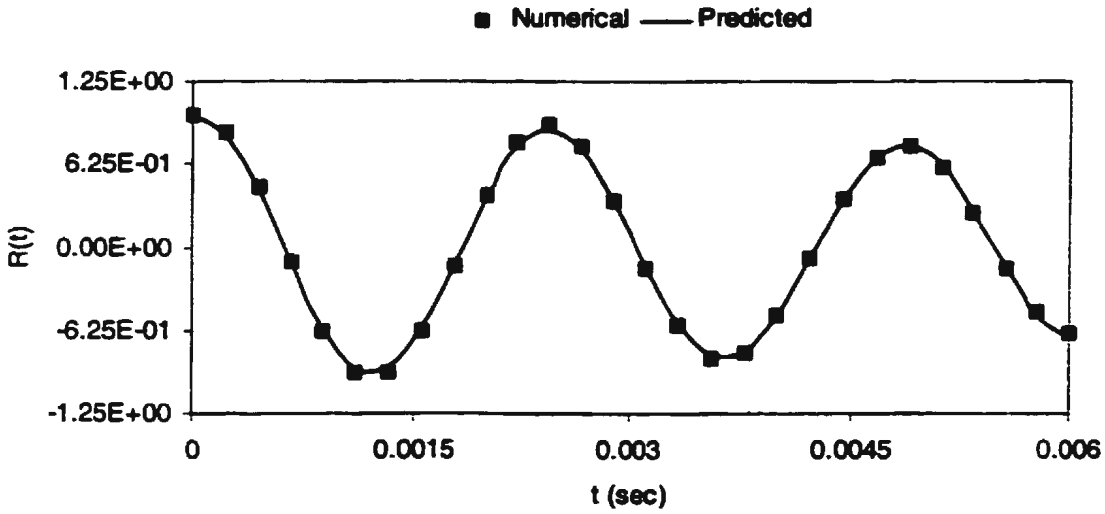

E.1.a: Crack length = 0.40 inch

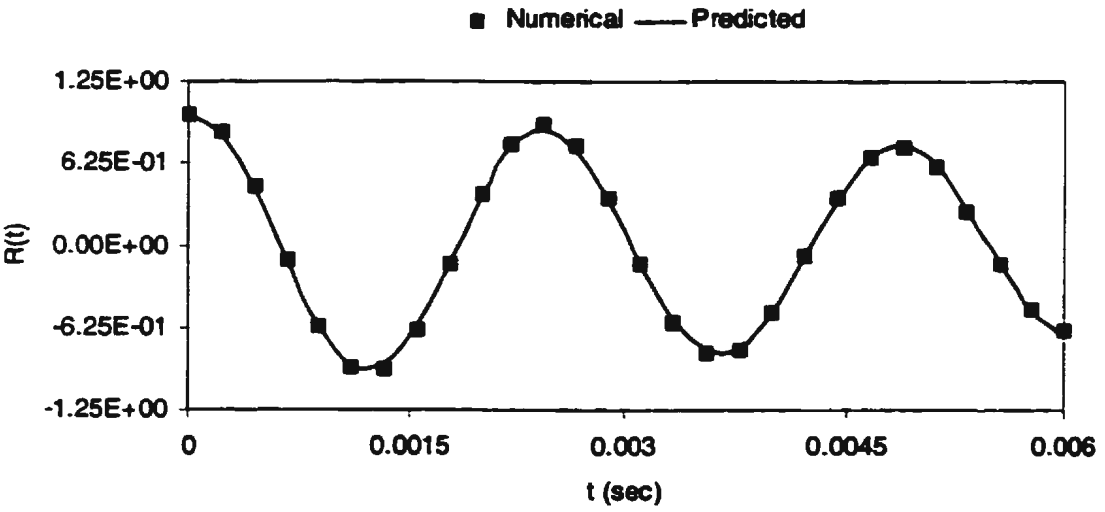

E.1.b: Crack length = 0.80 inch

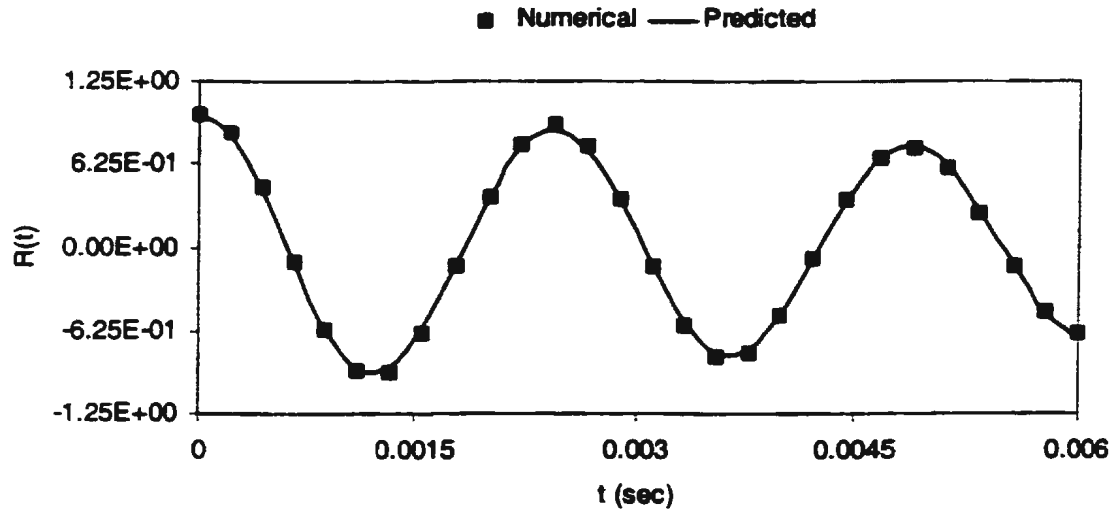

E.1.c: Crack length = 1.20 inch

Figure E.1: Comparison between the Autocorrelation Functions and Predicted Curves obtained using the Neural Network (Numerical, Damaged, Crack at 0.90 inch away from the center)

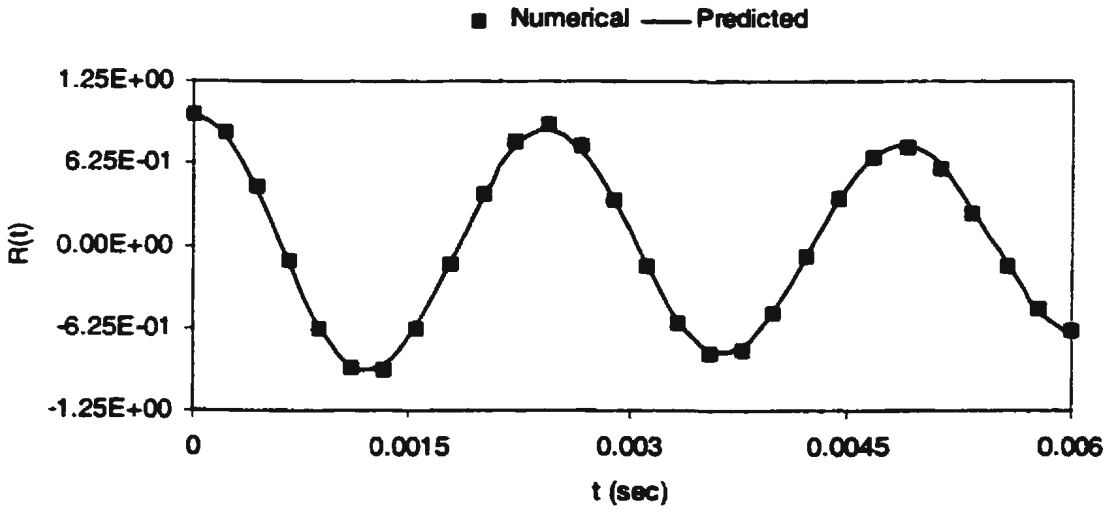

E.2.a: Crack length = 0.40 inch

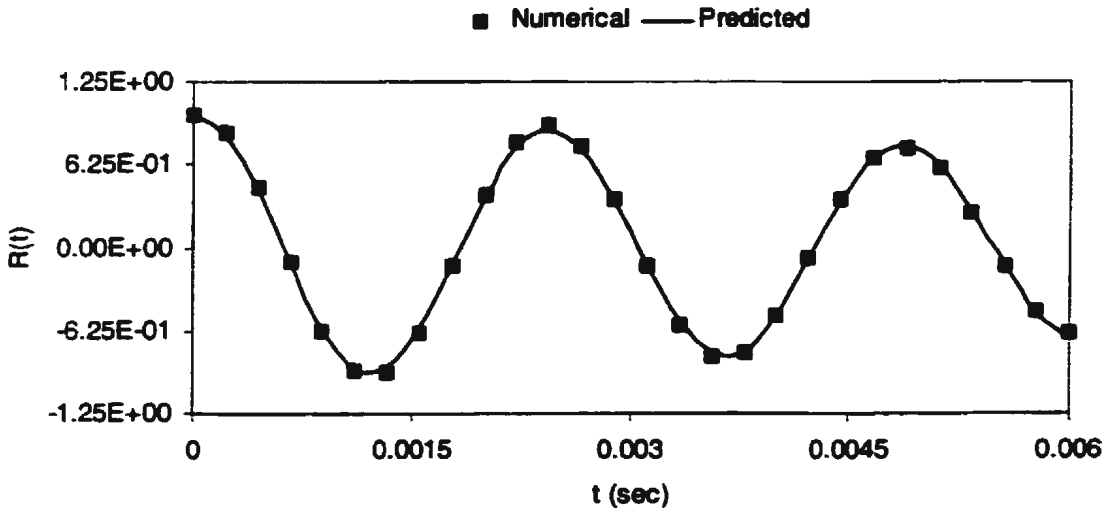

E.2.b: Crack length = 0.80 inch

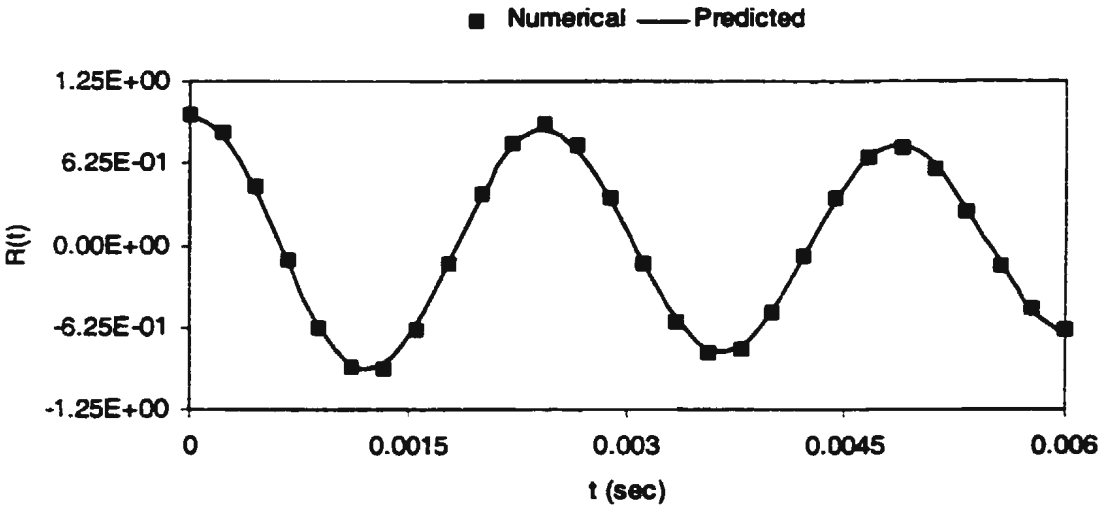

E.2.c: Crack length = 1.20 inch

Figure E.2: Comparison between the Autocorrelation Functions and Predicted Curves obtained using the Neural Network (Numerical, Damaged, Crack at 1.35 inch away from the center)

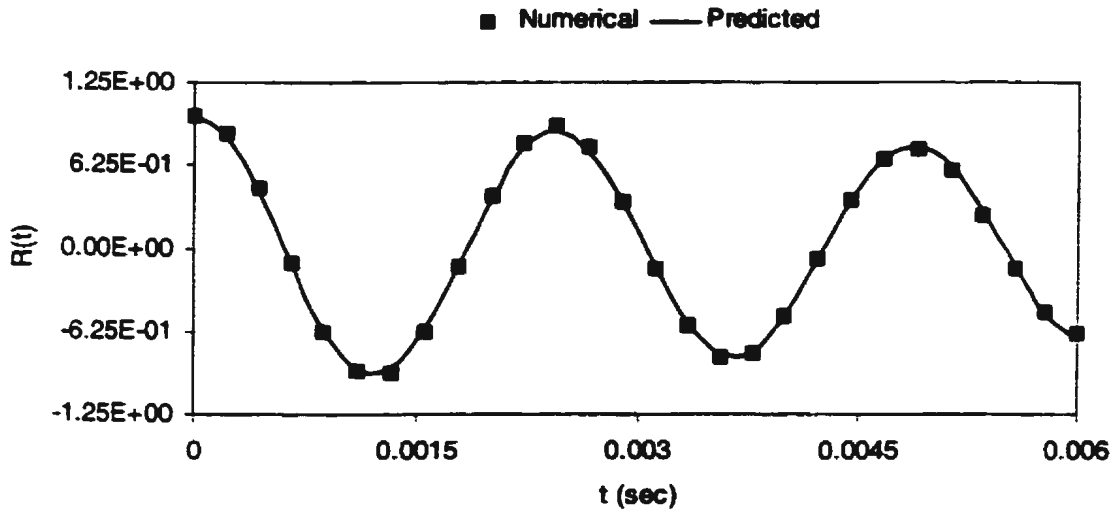

E.3.a: Crack length = 0.40 inch

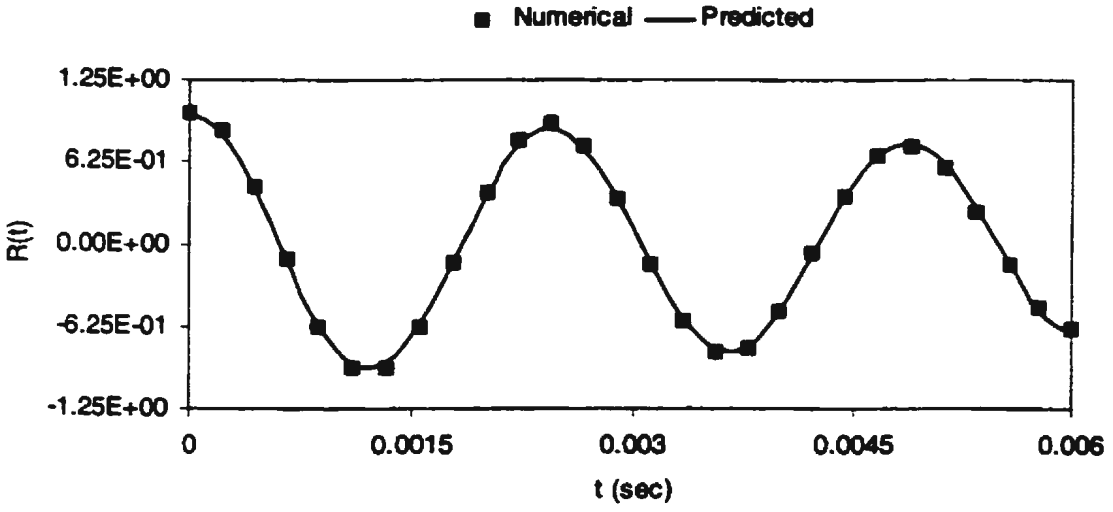

E.3.b: Crack length = 0.80 inch

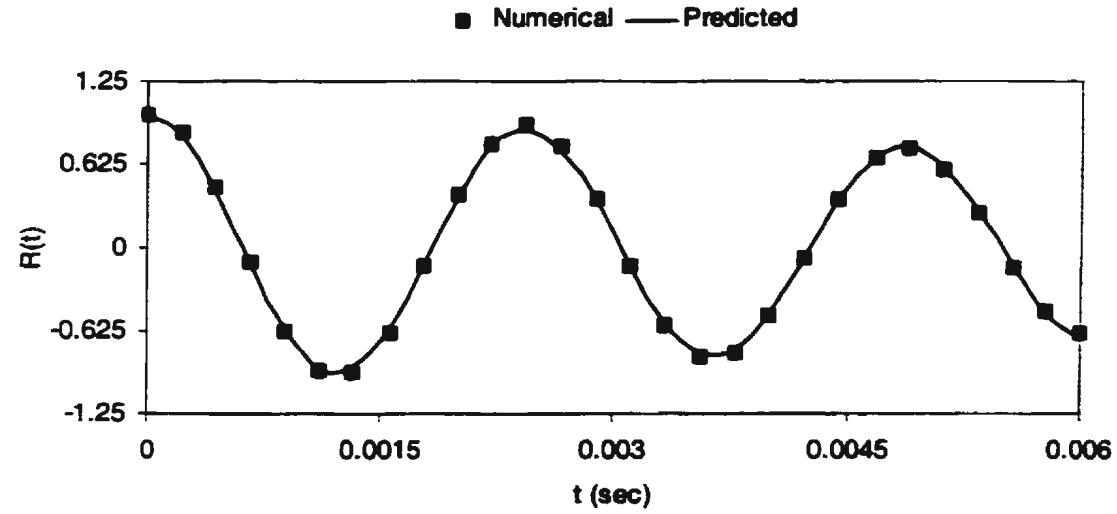

E.3.c: Crack length = 1.20 inch

Figure E.3: Comparison between the Autocorrelation Functions and Predicted Curves obtained using the Neural Network (Numerical, Damaged, Crack at 1.80 inch away from the center)

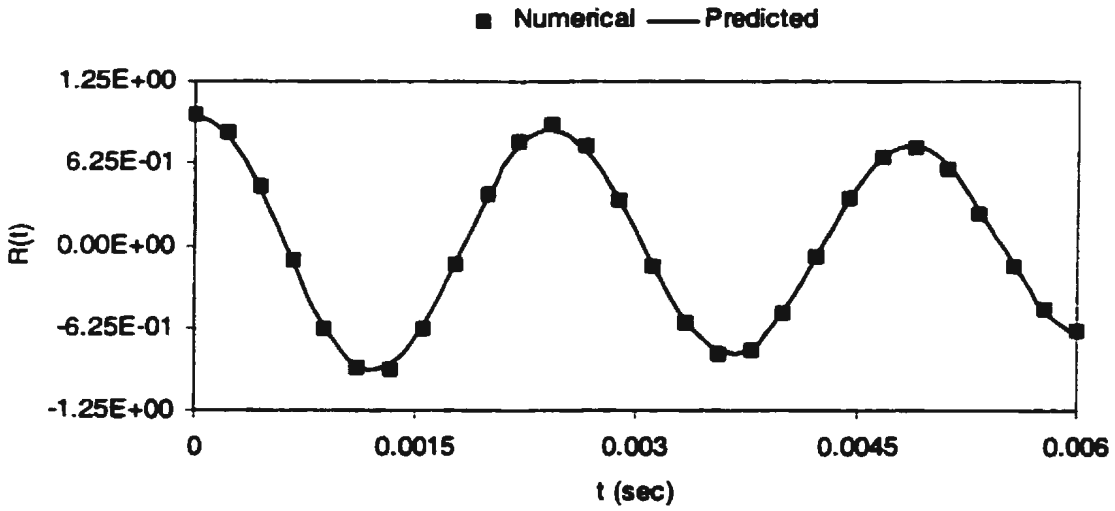

E.4.a: Crack length = 0.40 inch

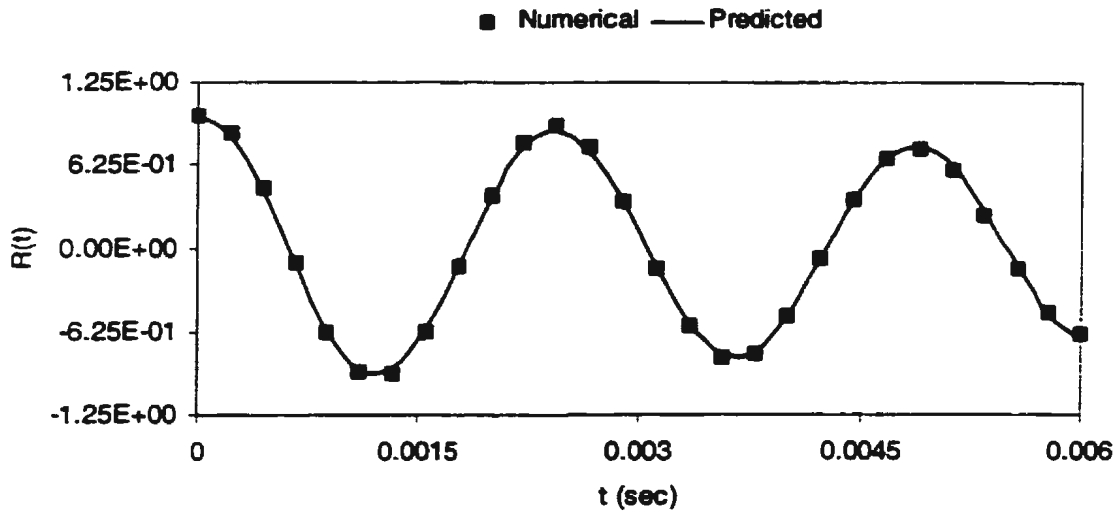

E.4.b: Crack length = 0.80 inch

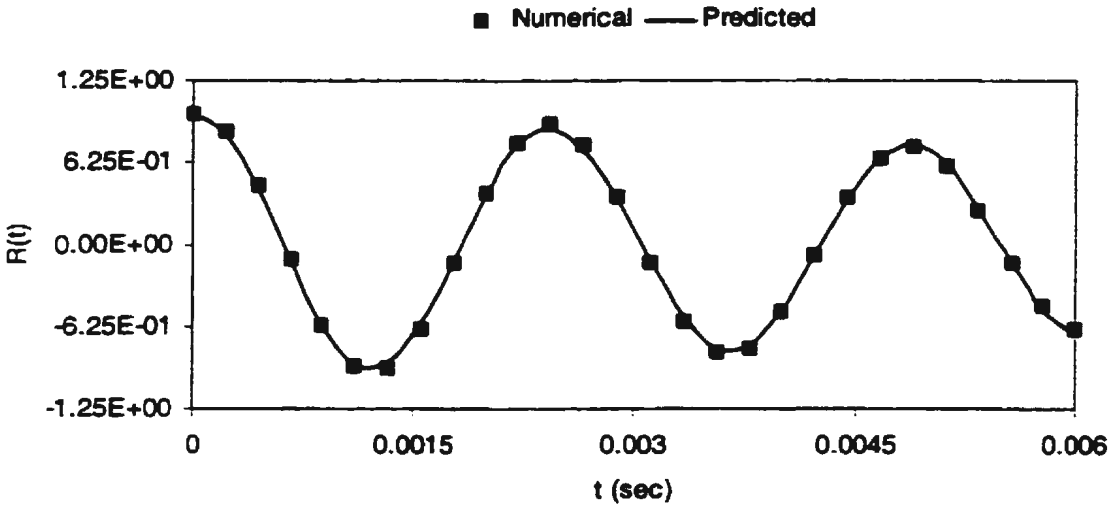

E.4.c: Crack length = 1.20 inch

Figure E.4: Comparison between the Autocorrelation Functions and Predicted Curves obtained using the Neural Network (Numerical, Damaged, Crack at 2.25 inch away from the center)

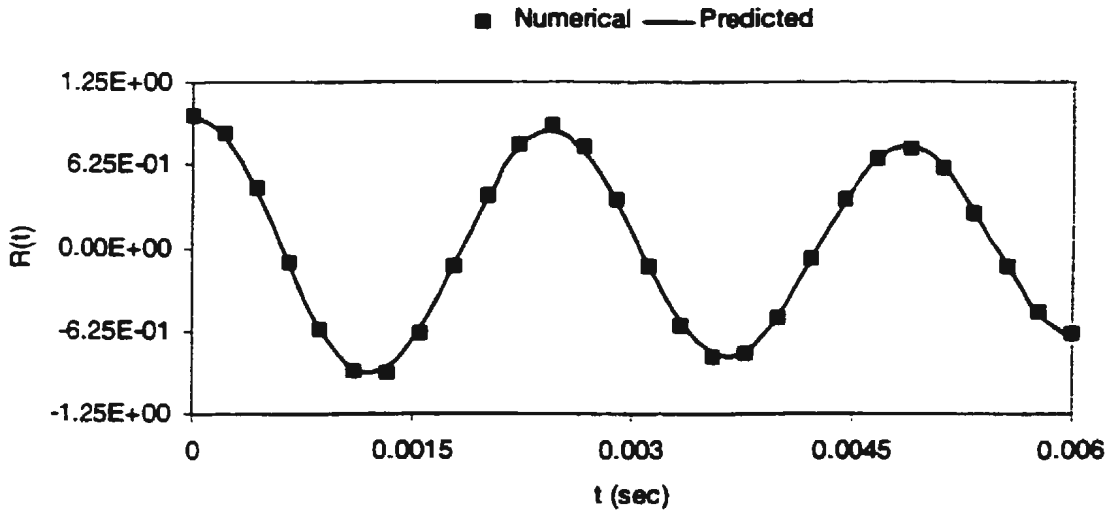

E.5.a: Crack length = 0.40 inch

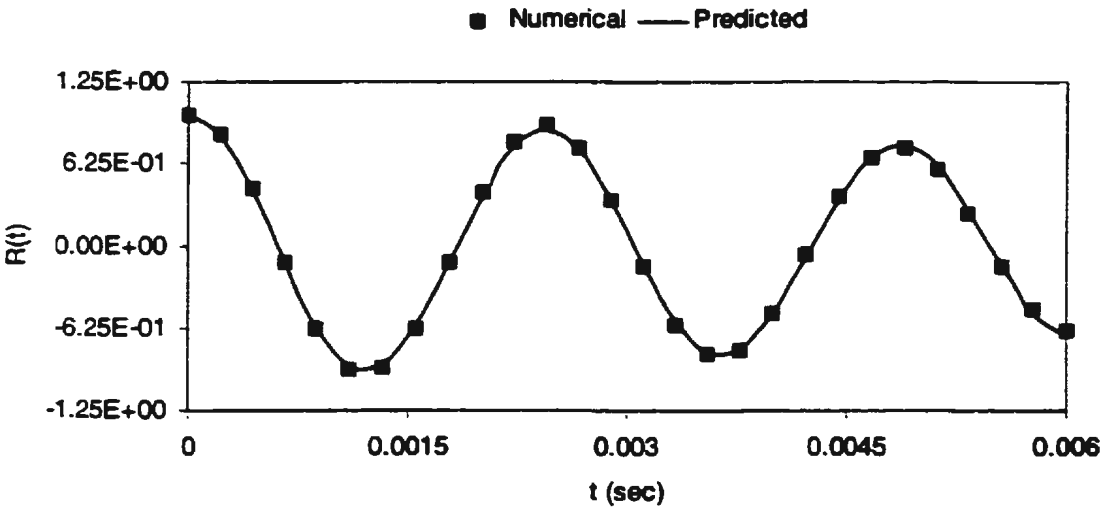

E.5.b: Crack length = 0.80 inch

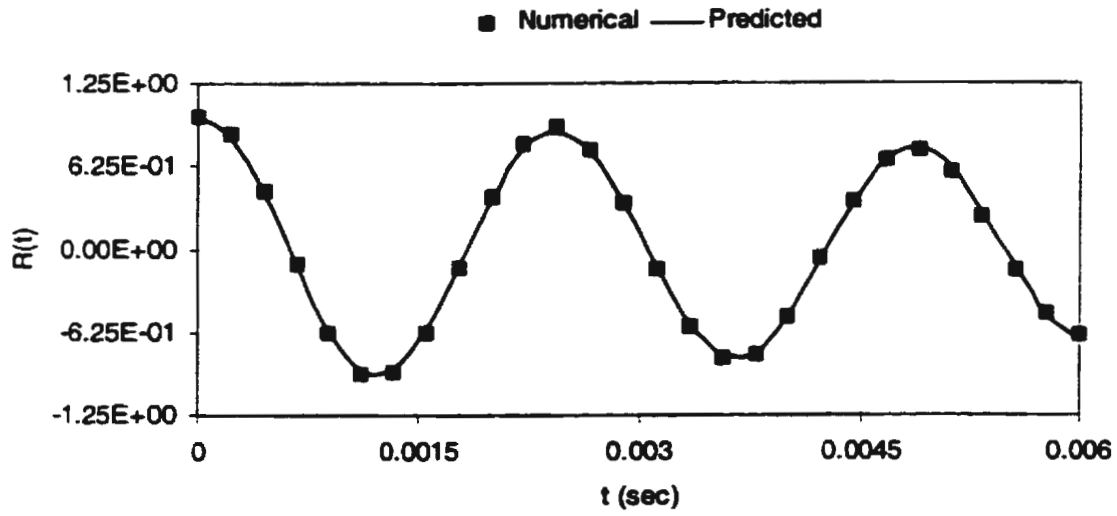

E.5.c: Crack length = 1.20 inch

Figure E.5: Comparison between the Autocorrelation Functions and Predicted Curves obtained using the Neural Network (Numerical, Damaged, Crack at 2.70 inch away from the center)

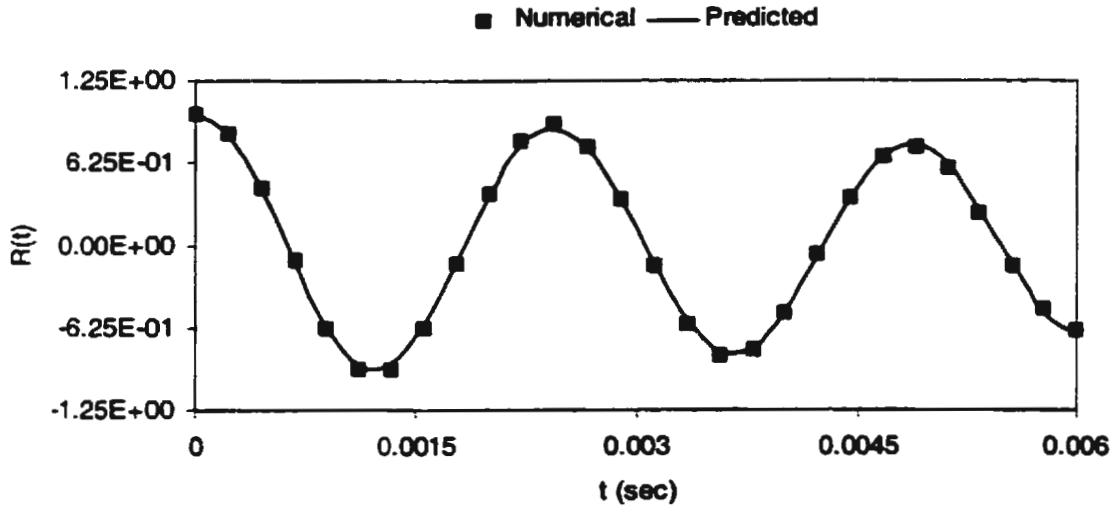

E.6.a: Crack length = 0.40 inch

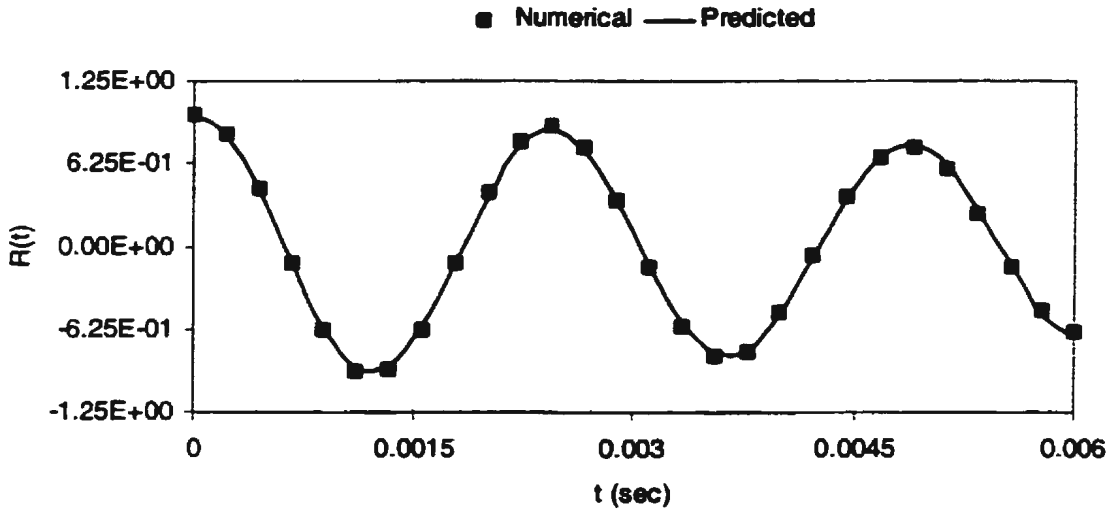

E.6.b: Crack length = 0.80 inch

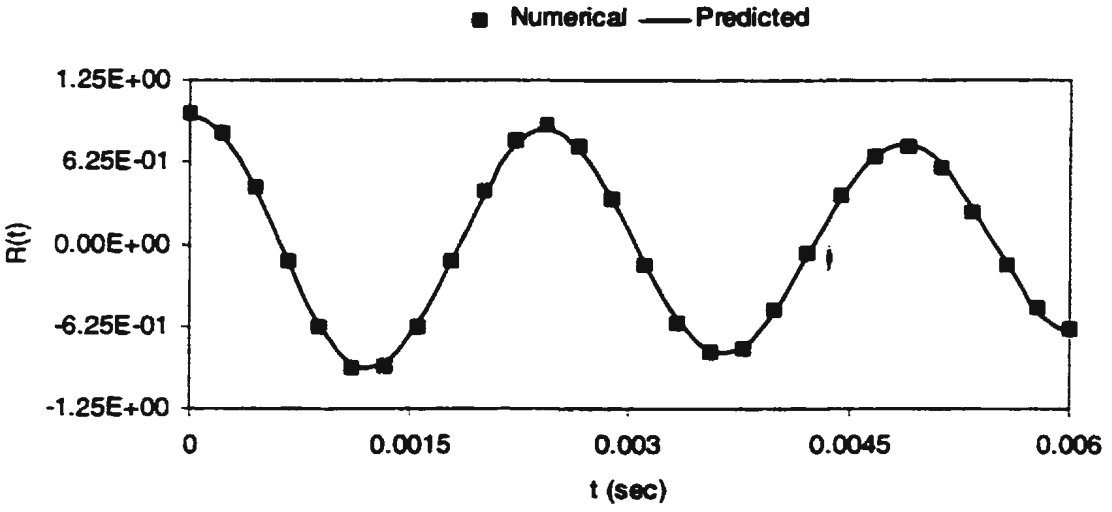

E.6.c: Crack length = 1.20 inch

Figure E.6: Comparison between the Autocorrelation Functions and Predicted Curves obtained using the Neural Network (Numerical, Damaged, Crack at 3.15 inch away from the center)

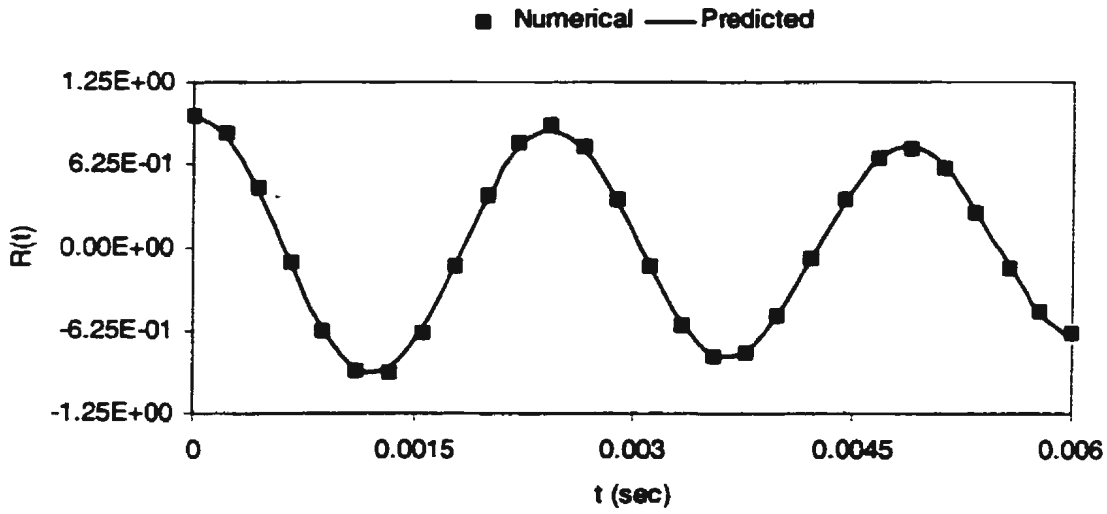

E.7.a: Crack length = 0.40 inch

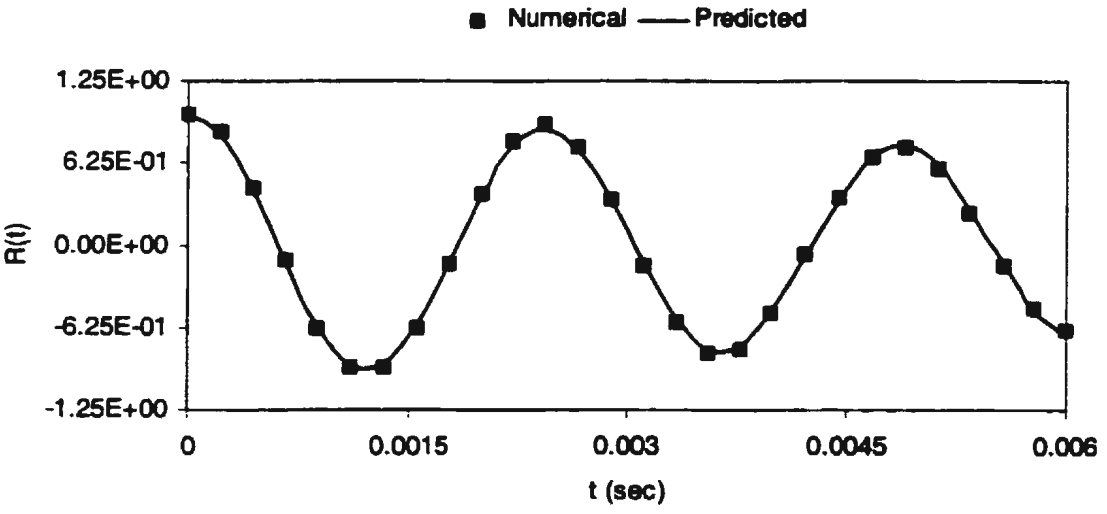

E.7.b: Crack length = 0.80 inch

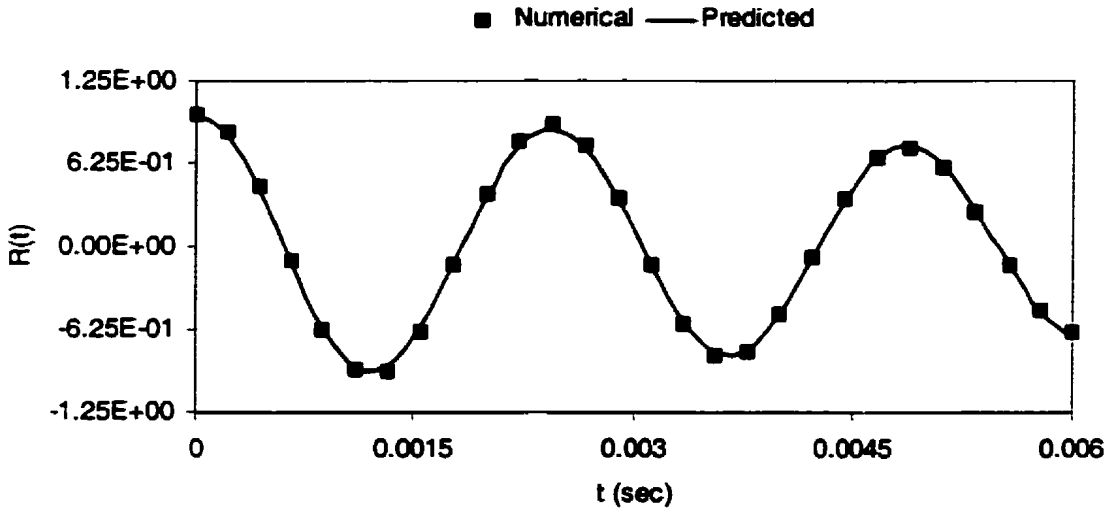

E.7.c: Crack length = 1.20 inch

Figure E.7: Comparison between the Autocorrelation Functions and Predicted Curves obtained using the Neural Network (Numerical, Damaged, Crack at 3.60 inch away from the center)